


UNIVERSITY OF
BIRMINGHAM

# Investigating the seasonal variability of electromagnetic soil properties using field monitoring data from Time-Domain Reflectometry probes

**By**

**Giulio Curioni**

**A thesis submitted to**
**The University of Birmingham**
**For the degree of**
**DOCTOR OF PHILOSOPHY**

**School of Civil Engineering**
**College of Engineering and Physical Sciences**
**University of Birmingham**
**May 2013**

UNIVERSITY OF
BIRMINGHAM

## University of Birmingham Research Archive

### e-theses repository

This unpublished thesis/dissertation is copyright of the author and/or third parties. The intellectual property rights of the author or third parties in respect of this work are as defined by The Copyright Designs and Patents Act 1988 or as modified by any successor legislation.

Any use made of information contained in this thesis/dissertation must be in accordance with that legislation and must be properly acknowledged. Further distribution or reproduction in any format is prohibited without the permission of the copyright holder.

# ABSTRACT

Shallow geophysical techniques such as Ground Penetrating Radar (GPR) have been widely used to detect buried utilities. However, these techniques are influenced by the properties of the ground, in the case of GPR by its electromagnetic (EM) and geotechnical properties. The EM soil properties are dynamic and have the potential to change dramatically with different seasons. Therefore, this research focussed on the long-term monitoring of these soil properties in the field in order to establish the amount, and the causes of variation and their impact on GPR results. A Time-Domain Reflectometry (TDR) monitoring station was developed and was installed in an anthropogenic sandy soil at the University of Birmingham campus (UK). A rigorous methodology was defined and tested in the laboratory before field installation, demonstrating the reliability of the instrumentation. The parameters measured by TDR were the soil apparent permittivity and the bulk electrical conductivity (BEC) up to a depth of approximately 1 m. The monitoring lasted approximately 22 months, during which GPR surveys were conducted over specifically buried targets. The results indicated a significant seasonal variation of the EM soil properties, particularly for apparent permittivity. The variation was found to be strongly dependent on the amount of rainfall and only marginally related to the variation of soil temperature. Greater variability was measured in the topsoil and in a more clayey soil horizon, suggesting that the variation of the EM soil properties could be higher for organic and clayey soils. A time lag of several hours up to several days from rainfall events and changes in EM soil properties was measured depending on the depth. Prolonged periods of dry and wet conditions were shown to be responsible for the seasonal variation in the EM soil properties. Field validation of an empirical calibration relating apparent permittivity and volumetric water content was conducted by means of the Soil-Plant-Air-Water (SPAW)

model, which proved an effective tool for simulating the soil water content in the field. The variation in the EM soil properties was shown to affect the GPR results. During wet periods and soon after rainfall events the quality of the GPR images reduced considerably, making it difficult to distinguish some of the buried targets. Care should be taken when using typical soil apparent permittivity (or velocity) values in case accurate target depths are needed, as they can be significantly different during extreme conditions. The seasonal variation in the EM soil properties should be taken into account when planning GPR surveys in order to maximise the detection of buried utilities.

to Serena

# AKNOWLEDGEMENTS

The author greatly acknowledges his academic supervisors, D.N. Chapman and N. Metje, for their continuous guidance, and all the people who provided help and support in the development of the research described in this thesis. In particular, the colleagues of the MTU and DART projects and the Civil Engineering laboratory staff. Very special thanks to C.D.F. Rogers for is leading role in the MTU project, without whom this research would not have been possible, K.Y. Foo, J.D. Cross, H. Tong, P.R. Atkins, A.M. Thomas, H.G. Ollerton, D. Boddice, S.R. Pennock and G. Alli for their important technical support, help and advice. The author gratefully acknowledges the financial support provided by the UK's Engineering and Physical Sciences Research Council (EPSRC). Thanks also to all the people not involved directly in this research but that provided essential support to the author.

# TABLE OF CONTENTS


**CHAPTER 1: INTRODUCTION ..... 1**

**1.1. BACKGROUND ..... 1**

**1.2. AIM AND OBJECTIVES ..... 2**

**1.3. LAYOUT OF THE THESIS ..... 3**

**CHAPTER 2: LITERATURE REVIEW ..... 4**

**2.1. SCOPE ..... 4**

**2.2. SOIL DEFINITION ..... 5**

**2.3. SOIL ELECTROMAGNETIC PARAMETERS ..... 6**

2.3.1. Definition of the soil electromagnetic parameters ..... 6

2.3.2. Soil interactions to electromagnetic signals ..... 11

2.3.2.1. Storage of energy ..... 12

2.3.2.2. Loss mechanisms ..... 13

**2.4. SOIL PARAMETERS AFFECTING THE ELECTROMAGNETIC SIGNALS ..... 19**

2.4.1. Soil water content ..... 19

2.4.1.1. Overview ..... 19

2.4.1.2. Soil water characteristics ..... 22

2.4.2. Impact of temperature and geotechnical properties on the soil EM behaviour ..... 30

2.4.3. Prediction of the electromagnetic soil properties ..... 34

2.4.3.1. Dielectric mixing models ..... 34

2.4.3.2. GPR soil suitability ..... 36

**2.5. SOIL SENSING TECHNIQUES ..... 39**

2.5.1. Soil water measurement techniques ..... 39
2.5.2. Time-Domain Reflectometry (TDR) ..... 44
2.5.2.1. Introduction ..... 44
2.5.2.2. Principles of Time-Domain Reflectometry ..... 47
2.5.2.3. Limitations of Time-Domain Reflectometry ..... 53
2.5.3. Ground Penetrating Radar (GPR) ..... 58
2.5.3.1. Introduction ..... 58
2.5.3.2. Principles of Ground Penetrating Radar ..... 59
2.5.4. TDR and GPR in the field ..... 63

**2.6. SUMMARY AND IDENTIFICATION OF THE KNOWLEDGE GAPS ..... 65**

**CHAPTER 3: METHODOLOGY ..... 68**

**3.1. INTRODUCTION ..... 68**

**3.2. EXPERIMENTAL DEVELOPMENT ..... 68**

3.2.1. Introduction ..... 68
3.2.2. Choice of the sensing technology ..... 69
3.2.3. Equipment setup ..... 70
3.2.4. TDR100 settings ..... 75
3.2.5. Preliminary tests on the TDR equipment ..... 78
3.2.6. Parameters/aspects affecting the TDR measurements ..... 81
3.2.6.1. Temperature effects on the TDR equipment ..... 81
3.2.6.2. Insulation of the cables ..... 85
3.2.6.3. Multiplexer effects ..... 85
3.2.7. Calibration for apparent permittivity ..... 89
3.2.8. Calibration for BEC (bulk electrical conductivity) ..... 95
3.2.8.1. Considerations on the calibration for BEC ..... 100
3.2.9. TDR waveform analysis ..... 104

3.2.10. Accuracy of TDR after calibration: tests in reference materials ..... 107
3.2.10.1. Introduction ..... 107
3.2.10.2. Accuracy for apparent permittivity ..... 108
3.2.10.3. Accuracy for bulk electrical conductivity (BEC) ..... 113
3.2.11. Temperature sensor calibration and accuracy ..... 116

**3.3. FIELD METHODOLOGY ..... 117**
3.3.1. University of Birmingham test site ..... 117
3.3.2. Field installation ..... 120
3.3.3. Field monitoring ..... 126
3.3.4. Considerations on the data collected by the field TDR monitoring station ..... 129
3.3.5. Methods of soil characterisation ..... 132
3.3.6. Empirical calibration (apparent permittivity *versus* volumetric water content) ..... 133
3.3.7. GPR analysis ..... 135

**3.4. SPAW MODEL ..... 138**
3.4.1. Introduction ..... 138
3.4.2. SPAW inputs ..... 138

**CHAPTER 4: RESULTS AND DISCUSSION ..... 142**

**4.1. INTRODUCTION ..... 142**

**4.2. SOIL CHARACTERISATION ..... 142**

**4.3. FIELD MONITORING ..... 147**
4.3.1. Introduction ..... 147
4.3.2. Seasonal variations ..... 147
4.3.2.1. Variation of weather parameters ..... 147
4.3.2.2. Variation of soil EM properties ..... 150
4.3.2.3. Variation of temperature ..... 173

4.3.3. Daily variations ..... 177

4.3.4. Field monitoring: summary ..... 183

**4.4. FACTORS AFFECTING THE SOIL ELECTROMAGNETIC PROPERTIES ..... 184**

4.4.1. Introduction ..... 184

4.4.2. Time-domain cross correlation ..... 184

4.4.2.1. Selected rainfall event ..... 185

4.4.2.2. Selected dry event ..... 189

4.4.3. Correlation between parameters ..... 193

4.4.4. Empirical calibration (apparent permittivity *versus* volumetric water content) ..... 203

4.4.5. Factors affecting the soil electromagnetic properties: summary ..... 208

**4.5. SOIL SIMULATION WITH SPAW ..... 209**

4.5.1. Introduction ..... 209

4.5.2. SPAW results ..... 209

4.5.3. SPAW sensitivity analysis ..... 215

4.5.4. Soil simulation with SPAW: summary ..... 218

**4.6. IMPACT OF WEATHER ON GPR ..... 219**

4.6.1. GPR performance at extreme seasonal conditions ..... 219

4.6.2. GPR performance before and after rainfall events ..... 225

4.6.3. Comparison between TDR and GPR ..... 230

4.6.4. Impact of weather on GPR: Summary ..... 233

**CHAPTER 5: CONCLUSIONS AND RECOMMENDATIONS ..... 236**

**5.1. CONCLUSIONS ..... 236**

**5.2. RECOMMENDATIONS FOR FUTURE WORK ..... 241**

**REFERENCES ..... 243**

**APPENDICES** ..... **256**

**APPENDIX A: genetic soil horizons** ..... **256**

**APPENDIX B: time plots** ..... **258**

**APPENDIX C: correlations between variables** ..... **261**

**APPENDIX D: empirical calibrations (apparent permittivity *versus* volumetric water content)** ..... **267**

**APPENDIX E: SPAW model** ..... **270**

**APPENDIX F: additional GPR results** ..... **277**

# LIST OF FIGURES

Figure 2.1 – (a) Water molecule tetrahedron, (b) and (c) water molecules without and with an external electric field applied, respectively (after Robinson et al., 2003a). ..... 12

Figure 2.2 – Diagram showing the response of a material to an applied external electric field (after Cassidy, 2008). ..... 13

Figure 2.3 – Diagram showing the process of Maxwell-Wagner polarisation in soils saturated with weakly conducting fluid (after Cassidy, 2008). ..... 15

Figure 2.4 – Diagram showing the process of conduction in a material containing movable ions (after Cassidy, 2008)..... 18

Figure 2.5 – Permittivity and EC variations with water content for soils at a wide range of water contents (after Curtis, 2001). ..... 19

Figure 2.6 – The three main forms of water found in the soil (after Foth, 1990)..... 21

Figure 2.7 – Typical soil water characteristic curves for sandy, silty and clayey soils (after Fredlung and Xing, 1994). ..... 24

Figure 2.8 – Graphical computer program that estimates the soil water characteristics using the Saxton and Rawls model (after Saxton and Rawls, 2006). ..... 26

Figure 2.9 – Electromagnetic dispersion of different types of clay measured at saturation with a Vector Network Analyzer (after Thomas et al., 2008a). ..... 32

Figure 2.10 – Relationship between liquid limit and apparent permittivity for 11 fine-grained soils measured at a range of frequencies by a VNA (after Thomas et al., 2010a). ..... 33

Figure 2.11 – Relationship between linear shrinkage and the magnitude of the EM dispersion for 11 fine-grained soils (after Thomas et al., 2010a). .....33

Figure 2.12 – Apparent permittivity corrected for dry density, in the gravimetric water content domain for (a) London Clay and (b) English China Clay (after Thomas et al., 2010b). [Note: $W_L$, $W_P$, DD are the liquid limit, plastic limit and dry density respectively.] .....34

Figure 2.13 – Knowledge Based System (KBS) for multi-sensor utility detection (after Foo et al., 2011). .....38

Figure 2.14 – Example of EM probes used for soil water determinations. From left to right: Acclima Digital TDT Sensor, three-rod TDR probe, CS616, ECH$_2$O Probe, Hydra Probe, and Theta Probe (after Blonquist et al., 2005). .....43

Figure 2.15 – Schematic of the TDR arrangement and two examples of TDR waveforms (i.e., reflection coefficient *versus* apparent length) taken in air and water. .....48

Figure 2.16 – Steady-state reflection coefficient at long apparent distances measured by TDR in KCl solutions with different EC values. .....51

Figure 2.17 – Measurement of the rise time ($t_r$) from the 10 % to 90 % increase in the reflection coefficient at the end of the TDR probe (after Robinson et al., 2005). .....55

Figure 2.18 – TDR waveforms taken in solutions with different EC (after Jones et al., 2002). .....57

Figure 2.19 – Common midpoint (CMP) and wide angle reflection and refraction (WARR) methods of GPR acquisition (after Huisman et al., 2003a). S and R identify the locations of transmitter and receiver respectively. .....61

Figure 2.20 – Diagram of single offset GPR acquisition..... 62

Figure 2.21 – Example of a GPR image (B-scan) showing multiple buried anomalies (after Annan, 2008). ..... 63

Figure 3.1 – TDR100 cable tester manufactured by Campbell Scientific (Logan, UT)..... 71

Figure 3.2 – SDMX50 multiplexer, manufactured by Campbell Scientific. ..... 71

Figure 3.3 – Schematic diagram of the field TDR monitoring station (mux: multiplexer)... 71

Figure 3.4 – Three-rod probe, manufactured by Campbell Scientific. The low-loss cables were insulated with heat shrinkable tubes. ..... 72

Figure 3.5 – Vertical cross-section of the University of Birmingham field TDR monitoring station. Further details on the site installation are described in section 3.3.2. ..... 73

Figure 3.6 – Experimental equipment used on the University of Birmingham test site..... 74

Figure 3.7 – PCTDR display. The software was not used for the monitoring but the cable and waveform parameters were used as shown..... 75

Figure 3.8 – TDR waveforms carried out in air with a varying number of data points. a), b), c) and d) correspond to waveforms taken with 20, 250, 1000 and 2048 data points respectively..... 78

Figure 3.9 – Twenty TDR measurements carried out in air with the same probe with two levels of multiplexers. The probe was kept in a fixed position during the measurements. ..... 80

Figure 3.10 – Twenty TDR waveforms obtained from measurements carried out with the same probe with two levels of multiplexers. The cable was bent at different positions and the probe orientated differently before taking each new measurement.....80

Figure 3.11 – TDR waveforms obtained from measurements in water at a constant temperature of 18.5 °C, and the cable submerged in a water bath with a range of temperatures. [Note: only some of the data points were selected from each of the original waveforms in an attempt to make the comparison between waveforms clearer.] .....82

Figure 3.12 – TDR waveforms obtained from air measurements carried out in an incubator for a range of temperatures. [Note: the number of data points of each waveform has been reduced to facilitate the comparison between waveforms.].....83

Figure 3.13 – TDR measurements in distilled water carried out in an incubator at a range of temperature. [Note: the number of data points has been reduced to facilitate the comparison between waveforms.].....84

Figure 3.14 – Comparison between the TDR measurements in water carried out using insulated and non-insulated cables. [Note: the number of data points has been reduced to facilitate the comparison between the waveforms.].....86

Figure 3.15 – Comparison between three TDR measurements in air using different numbers of multiplexers. .....87

Figure 3.16 – Comparison between three TDR measurements in water using different numbers of multiplexers.....88

Figure 3.17 – TDR probe short circuited with aluminium foil.....90

Figure 3.18 – TDR waveforms obtained from open and short circuited measurements in air taken without using multiplexers. ..... 91

Figure 3.19 – TDR probe inserted in a beaker containing distilled water at 20 °C; a) held in position manually, b) fixed in position using metal weights..... 92

Figure 3.20 – TDR waveform for a measurement in distilled water used in the calibration for apparent permittivity. ..... 94

Figure 3.21 – TDR waveform for a short circuited air measurement used in the calibration of apparent permittivity. ..... 94

Figure 3.22 – Linear fitting of the sample conductance, $1/R_L$ (1/Ω), to the electrical conductivity (S/m) of four low-range KCl solutions used as reference (first calibration step). [Note: the slope corresponds to the inverse of the probe constant, $K_p$ (1/m).].... 99

Figure 3.23 – Combinations of initial $R_c$ (Ω/m) and $R_0$ (Ω) parameters used to minimise the sum of the squared residuals between the measured and modelled EC. ..... 99

Figure 3.24 – Fitting of the electrical conductivity (S/m) of all eight KCl reference solutions to the load resistance measured by TDR (second calibration step)..... 100

Figure 3.25 – Example results for the two-step calibration procedure for BEC using TDR. ..... 101

Figure 3.26 – The first derivative of a TDR waveform shown in (a) is smoothed in (b) in order to identify the maxima corresponding to the points of inflection in the TDR waveform shown in (c) with the fitting tangents added. ..... 106

Figure 3.27 – Comparison between the temperatures measured by a thermocouple after calibrating the sensor offset and the reference temperature of an incubator..... 116

Figure 3.28 – Location of the TDR monitoring station at the University of Birmingham campus, UK. ..... 117

Figure 3.29 – Geological map of the University of Birmingham trial site, courtesy of the British Geological Survey (Geological Map Data © NERC 2012). ..... 118

Figure 3.30 – Phases of the excavations at the University of Birmingham test site; a) and b) excavation of trench 1 used for the TDR installation; c) excavation of trench 2 where the targets were buried; d) from left to right, cubic metre hole where a large soil sample was taken for lab work, trench 2 and trench 1. ..... 121

Figure 3.31 – a), b) and d) Details of the field installation of the TDR probes; c) temperature sensor with insulating cable; e) installation of the box with the equipment. ..... 123

Figure 3.32 – Details of the insertion of the TDR probes. [Note: each probe was inserted approximately parallel to the ground surface] ..... 124

Figure 3.33 – Installation of stainless steel and polyethylene pipes at the University of Birmingham test site (trench 2). ..... 125

Figure 3.34 – Vertical cross-section of the trench 2, at the University of Birmingham test site. ..... 126

Figure 3.35 – Apparent permittivity and BEC vertical profiles obtained from array 1 (a and b) and array 2 (c and d) of the field TDR monitoring station at the University of Birmingham, for a period of 4 days starting from the 1st October 2010. ..... 130

Figure 3.36 – a) Apparent permittivity and b) BEC and temperature measurements from selected probes at specific depths in the field over a period of one week with no rainfall occurring in March 2010.. ..... 132

Figure 3.37 – Experimental setup for the site-specific empirical calibration. ..... 134

Figure 3.38 – Detector Duo GPR (IDS Ingegneria Dei Sistemi S.p.A.). ..... 135

Figure 3.39 – GPR survey on a predefined transect at the University of Birmingham test site. ..... 136

Figure 3.40 – Diagram of the GPR grid defined at the University of Birmingham test site. [Note: not to scale.] ..... 137

Figure 4.1 – Soil profile in the trench dug to install the TDR probes, showing the identified soil horizons. ..... 144

Figure 4.2 – Particle size distributions for the soil samples collected during the TDR field installation at different depths. ..... 146

Figure 4.3 – Particle size percentage distributions with depth. ..... 146

Figure 4.4 – Seasonal variation of rainfall, solar radiation and temperature. ..... 149

Figure 4.5 – TDR measured apparent permittivity over the entire period of field monitoring, from 0.07 and 0.60 m depth. The left column corresponds to array 1, the right column to array 2. ..... 151

Figure 4.6 – TDR measured apparent permittivity over the entire period of field monitoring, from 0.70 and 1.08 m depth. The left column corresponds to array 1, the right column to array 2. ..... 152

Figure 4.7 – TDR measured bulk electrical conductivity (BEC) over the entire period of field monitoring, from 0.07 and 0.60 m depth. The left column corresponds to array 1, the right column to array 2. .....153

Figure 4.8 – TDR measured bulk electrical conductivity (BEC) over the entire period of field monitoring, from 0.70 and 1.08 m depth. The left column corresponds to array 1, the right column to array 2. .....154

Figure 4.9 – Variation of the seasonal mean soil apparent permittivity and BEC. .....156

Figure 4.10 – Variability of the soil apparent permittivity measured by the TDR probes for each array during the field monitoring. .....157

Figure 4.11 – Variability of the soil BEC measured by the TDR probes for each array during the field monitoring. .....157

Figure 4.12 – Variation of the daily apparent permittivity for the three main soil horizons. .....159

Figure 4.13 – Variation of the daily BEC for the three main soil horizons.....159

Figure 4.14 – Frequency of the daily apparent permittivity values for the topsoil, subsoil 1 and subsoil 2 horizons during the entire monitoring period. .....161

Figure 4.15 – Frequency of the daily BEC values for the topsoil, subsoil 1 and subsoil 2 horizons during the entire monitoring period. .....162

Figure 4.16 – TDR measured apparent permittivity during Winter 2011, from 0.07 and 0.60 m depth. The left column corresponds to array 1 and the right column to array 2. The circles in the topleft plot show the gaps in the dataset caused by problems with the batteries. .....164

Figure 4.17 – TDR measured apparent permittivity during Winter 2011, from 0.70 and 1.08 m depth. The left column corresponds to array 1 and the right column to array 2. ..... 165

Figure 4.18 – TDR measured bulk electrical conductivity (BEC) during Winter 2011, from 0.07 and 0.60 m depth. The left column corresponds to array 1 and the right column to array 2. ..... 166

Figure 4.19 – TDR measured bulk electrical conductivity (BEC) during Winter 2011, from 0.70 and 1.08 m depth. The left column corresponds to array 1 and the right column to array 2. ..... 167

Figure 4.20 – TDR measured apparent permittivity during Summer 2011, from 0.07 and 0.60 m depth. The left column corresponds to array 1 and the right column to array 2. ..... 170

Figure 4.21 – TDR measured bulk electrical conductivity (BEC) during Summer 2011, from 0.07 and 0.60 m depth. The left column corresponds to array 1 and the right column to array 2. ..... 171

Figure 4.22 – TDR measured apparent permittivity during Autumn 2011, from 0.07 and 0.25 m depth. The left column corresponds to array 1 and the right column to array 2. ..... 172

Figure 4.23 – TDR measured bulk electrical conductivity (BEC) during Autumn 2011, from 0.07 and 0.25 m depth. The left column corresponds to array 1 and the right column to array 2. ..... 172

Figure 4.24 – Variation of hourly soil and air temperature during the entire period of field monitoring. ..... 174

Figure 4.25 – Variation of soil and air hourly temperature during Winter 2011. .....176

Figure 4.26 – Variation of soil and air hourly temperature during Summer 2011. .....176

Figure 4.27 – Daily variation of the soil parameters (apparent permittivity, left and BEC, right) in the upper part of the soil profile for a selected period of dry conditions occurring in Spring 2011. [Note: the thin dots represent the rainfall, the thick dots are the apparent permittivity or the BEC] .....178

Figure 4.28 – Daily variation of the soil parameters (apparent permittivity, left and BEC, right) in the lower part of the soil profile for a selected period of dry conditions occurring in Spring 2011. [Note: the thin dots represent the rainfall, the thick dots are the apparent permittivity or the BEC] .....179

Figure 4.29 – Daily variation of the soil parameters (apparent permittivity, left and BEC, right) in the upper part of the soil profile for a selected period of wet conditions occurring in Spring 2012. .....181

Figure 4.30 – Daily variation of the soil parameters (apparent permittivity, left and BEC, right) in the lower part of the soil profile for a selected period of wet conditions occurring in Spring 2012. .....182

Figure 4.31 – Selected rainfall event occurring in February 2011, corresponding to a cumulative rainfall of 10.2 mm in 10 hours. .....185

Figure 4.32 – Time-domain cross correlation between the apparent permittivity measured by the TDR probes in array 1, up to 0.60 m depth, and a rainfall event occurring in February 2011. [Note: the horizontal dashed lines represent the limits above which the absolute cross correlations are significant with a confidence level of 90 %] .....187

Figure 4.33 – Time-domain cross correlation between the apparent permittivity measured by the TDR probes in array 1, from 0.70 to 1.08 m depth, and a rainfall event occurring in February 2011. [Note: the horizontal dashed lines represent the limits above which the absolute cross correlations are significant with a confidence level of 90 %]..... 188

Figure 4.34 – Diurnal variation of air and soil temperature for a selected dry day (21st April 2011)..... 189

Figure 4.35 – Time-domain cross correlation between the soil temperature at different depths and the air temperature of the 21st April 2011. [Note: the horizontal dashed lines represent the limits above which the absolute cross correlations are significant with a confidence level of 90 %]..... 190

Figure 4.36 – Time-domain cross correlation between BEC measured by the TDR probes in array 1, up to 0.60 m depth, and the air temperature of the 21st April 2011. [Note: the horizontal dashed lines represent the limits above which the absolute cross correlations are significant with a confidence level of 90 %]..... 191

Figure 4.37 – Time-domain cross correlation between BEC measured by the TDR probes in array 1, from 0.70 to 1.08 m depth, and the air temperature of the 21st April 2011. [Note: the horizontal dashed lines represent the limits above which the absolute cross correlations are significant with a confidence level of 90 %]..... 192

Figure 4.38 – Correlation coefficients calculated between pairs of soil parameters for the entire period of field monitoring and for all the TDR probes. ..... 194

Figure 4.39 – Correlation coefficients calculated between pairs of soil parameters for Spring 2011 and for all the TDR probes. ..... 195

Figure 4.40 – Correlation coefficients calculated between pairs of soil parameters for Spring 2012 and for all the TDR probes. .....195

Figure 4.41 – Scatterplot matrix of the topsoil apparent permittivity, BEC (mS/m) and soil temperature, soil.T (° C), for the entire period of field monitoring. .....197

Figure 4.42 – Scatterplot matrix of the shallow subsoil (subsoil 1) apparent permittivity, BEC (mS/m) and soil temperature, soil.T (° C), for the entire period of field monitoring. .....197

Figure 4.43 – Scatterplot matrix of the deep subsoil (subsoil 2) apparent permittivity, BEC (mS/m) and soil temperature, soil.T (° C), for the entire period of field monitoring. ..198

Figure 4.44 – (a) Biplot and (b) scree plot of the principal component analysis conducted on the measured soil properties. .....202

Figure 4.45 – Scatterplot matrix of the soil parameters measured during the empirical calibration: temperature, T, gravimetric water content, gwc, volumetric water content, vwc, apparent permittivity, $\varepsilon_a$.....205

Figure 4.46 – Site specific polynomial model ($R^2$ = 97.34 %) relating the soil volumetric water content to the apparent permittivity measured by TDR. .....206

Figure 4.47 – Site specific polynomial models at the specific temperatures generally measured in the field. .....207

Figure 4.48 – Simulated (by SPAW) and calculated (by Equation (4.1)) daily volumetric water content for January 2011. .....211

Figure 4.49 – Simulated (by SPAW) and calculated (by Equation (4.1)) daily volumetric water content for April 2011. .....211

Figure 4.50 – Simulated (by SPAW) and calculated (by Equation (4.1)) daily volumetric water content for July 2011. ..... 212

Figure 4.51 – Simulated (by SPAW) and calculated (by Equation (4.1)) daily volumetric water content for October 2011. ..... 212

Figure 4.52 – Mean absolute difference (i.e., error) and its standard deviation between simulated and calculated soil water contents for the topsoil. ..... 213

Figure 4.53 – Mean absolute difference (i.e., error) and its standard deviation between simulated and calculated soil water contents for the subsoil 1. ..... 214

Figure 4.54 – Mean absolute difference (i.e., error) and standard deviation of the error between simulated and calculated soil water contents for the subsoil 2. ..... 214

Figure 4.55 – Mean absolute difference of the SPAW output for the topsoil, when the input volumetric water content was changed by ±3 %. ..... 216

Figure 4.56 – Mean absolute difference of the SPAW output for the subsoil 1, when the input volumetric water content was changed by ±3 %. ..... 217

Figure 4.57 – Mean absolute difference of the SPAW output for the subsoil 2, when the input volumetric water content was changed by ±3 %. ..... 217

Figure 4.58 – B-scans obtained by the Detector Duo GPR at the University of Birmingham test site, corresponding to (a) wet and (b) dry extremes, with centre frequency of 250 MHz. [Note: the vertical lines approximately correspond to the apex of the hyperbolae.] ..... 221

Figure 4.59 – B-scans obtained by the Detector Duo GPR at the University of Birmingham test site, corresponding to (a) wet and (b) dry extremes, with centre frequency of 700 MHz.....222

Figure 4.60 – B-scans obtained with a 250 MHz antenna on (a) the 4th of October 2011 and (b) on the 6th of October 2011, before and after a rainfall event, respectively. [Note: the vertical lines indicate the approximate position of the plastic targets.] .....226

Figure 4.61 – B-scans obtained with a 700 MHz antenna on (a) the 4th of October 2011 and (b) on the 6th of October 2011, before and after a rainfall event, respectively. .....227

Figure 4.62 – B-scans obtained with a 250 MHz antenna (a) on the 18th of February 2011 and (b) on the 19th of February 2011, before and after a rainfall event, respectively. ..228

Figure 4.63 – B-scans obtained with a 700 MHz antenna (a) on the 18th of February 2011 and (b) on the 19th of February 2011, before and after a rainfall event, respectively. ..229

Figure B.1 – Historic rainfall data (a) and temperature maxima and minima (b) measured by the MetOffice weather station at Shawbury (UK). .....258

Figure B.2 – (a) Unfiltered and (b) filtered apparent permittivity data corresponding to a selected TDR probe.....259

Figure B.3 – (a) Unfiltered and (b) filtered BEC data corresponding to a selected TDR probe.....260

Figure C.1 – Time-domain cross correlation between the BEC measured by TDR probes in array 1, up to 0.60 m depth, and a rainfall event occurring in February 2011.....261

Figure C.2 – Time-domain cross correlation between the BEC measured by TDR probes in array 1, from 0.70 and 1.08 m depth, and a rainfall event occurring in February 2011262

Figure C.3 – Time-domain cross correlation between the apparent permittivity measured by TDR probes in array 1, up to 0.60 m depth, and the air temperature of the 21st April 2011. ..... 263

Figure C.4 – Time-domain cross correlation between the apparent permittivity measured by TDR probes in array 1, from 0.70 m and 1.08 m depth, and the air temperature of the 21st April 2011. ..... 264

Figure C.5 – Scatterplot matrix of the topsoil apparent permittivity, BEC (mS/m) and temperature, soil.T (° C), for the year 2011. ..... 265

Figure C.6 – Scatterplot matrix of the subsoil 1 apparent permittivity, BEC (mS/m) and temperature, soil.T (° C), for the year 2011. ..... 265

Figure C.7 – Scatterplot matrix of the subsoil 2 apparent permittivity, BEC (mS/m) and temperature, soil.T (° C), for the year 2011. ..... 266

Figure E.1 – Soil Water Characteristic Curves calculated by the SPAW model for the topsoil. ..... 270

Figure E.2 – Soil Water Characteristic Curves calculated by the SPAW model for the subsoil 1. ..... 271

Figure E.3 – Soil Water Characteristic Curves calculated by the SPAW model for the subsoil 2. ..... 272

Figure E.4 – Simulated (by SPAW) and calculated (by the Topp model) daily volumetric water contents for January 2011. .....273

Figure E.5 – Simulated (by SPAW) and calculated (by the Topp model) daily volumetric water contents for April 2011. .....273

Figure E.6 – Simulated (by SPAW) and calculated (by the Topp model) daily volumetric water contents for July 2011. .....274

Figure E.7 – Simulated (by SPAW) and calculated (by the Topp model) daily volumetric water contents for October 2011. .....274

Figure E.8 – Simulated (by SPAW) and calculated (by Equation (4.1)) daily volumetric water contents for Winter 2011. .....275

Figure E.9 – Simulated (by SPAW) and calculated (by Equation (4.1)) daily volumetric water contents for Spring 2011. .....275

Figure E.10 – Simulated (by SPAW) and calculated (by Equation (4.1)) daily volumetric water contents for Summer 2011. .....276

Figure E.11 – Simulated (by SPAW) and calculated (by Equation (4.1)) daily volumetric water contents for Autumn 2011. .....276

Figure F.1 – GPR B-scans obtained with a 250 MHz antenna (a) before and (b) after a rainfall event occurring in June 2011. .....277

Figure F.2 – GPR B-scans obtained with a 700 MHz antenna (a) before and (b) after a rainfall event occurring in June 2011. .....278

# LIST OF TABLES

Table 2.1 – Summary of the equations for estimating the soil water characteristics as reported by Saxton and Rawls (2006). ..... 27

Table 2.2 – Definition of the symbols and terms shown in Table 2.1 (after Saxton and Rawls, 2006)..... 28

Table 2.3 – Surrogate measures used by different soil water sensors (after IAEA, 2008).... 42

Table 3.1 – Comparison of different TDR devices and features (after Robinson et al., 2003a). ..... 70

Table 3.2 – Approximate KCl concentration (M=mol/L) and corresponding electrical conductivity (S/m) of eight solutions used for calibrating TDR for BEC..... 97

Table 3.3 – Probe constant ($K_p$), initial and optimised resistance parameters ($R_c$ and $R_0$), with their mean and standard deviation for the 16 probes of the monitoring setup. ..... 103

Table 3.4 – Variability and accuracy of apparent permittivity measurements for the 16 probes used in the field monitoring station. The accuracy is expressed as the mean difference between measurement and reference for the 16 probes. ..... 108

Table 3.5 – Precision and accuracy of apparent permittivity measurements carried out in 10 repetitions with a single probe, with no multiplexers (mux0) and with two levels of multiplexers (mux2), with manual and automatic analysis of the waveforms. ..... 110

Table 3.6 – Mean standard deviation and mean error (expressed as a difference compared to the reference value) of measurements carried out 10 times in reference materials for

four probes, with no multiplexer (mux0) and with two levels of multiplexers (mux2). .....112

Table 3.7 – Accuracy of TDR for BEC measurements of the 16 probes used in the field monitoring station for a range of potassium chloride (KCl) and soil solutions (ECC: English China Clay). .....115

Table 3.8 – Probe identifier and depth (m) of the TDR and temperature sensors installed at the University of Birmingham field monitoring station. .....124

Table 3.9 – Monthly evapotranspiration values calculated by DailyET using the Penman-Monteith method. .....139

Table 3.10 – Input (in bold) and output soil parameters by SPAW (Saxton and Rawls, 2006; see also Table 2.1 and 2.2, and Figure 2.8). .....141

Table 4.1 – List of laboratory results obtained from soil samples collected from the University of Birmingham test site. [Note: particle size percentages are by weight]...145

Table 4.2 – Summary of the environmental variables measured by a weather station over the period of field monitoring. .....148

Table 4.3 – Basic statistics of the soil EM properties measured by each TDR probe calculated on the period of field monitoring. .....158

Table 4.4 – Basic temperature statistics calculated over the entire period of field monitoring. .....174

Table 4.5 – Matrix of the data used to perform the principal component analysis (probe ID and depth excluded). .....199

Table 4.6 – Mean difference and its standard deviation between simulated and calculated soil water content for the Topp model and the site specific UoB empirical model. .... 215

Table 4.7 – Velocity and apparent permittivity with their standard deviations measured at wet and dry extremes by fitting the hyperbola of a metal target buried at approximately 0.5 m depth. ..... 223

Table 4.8 – Variation of the estimated target depth (m) using different values of input permittivity: a typical value of 10, and the wet and dry extremes measured in the field by GPR at 250 MHz. ..... 224

Table 4.9 – Attenuation coefficient and attenuation loss at 1 m depth for the wet and dry extremes. ..... 225

Table 4.10 – Variation of velocity and apparent permittivity before and after three rainfall events occurring in 2011. ..... 230

Table 4.11 – Apparent permittivity values measured by fitting hyperbolae at different depths from GPR data and by TDR probes. ..... 232

# ABBREVIATIONS

| | |
|---|---|
| BEC | Bulk Electrical Conductivity |
| BGS | British Geological Survey |
| BSI | British Standards Institution |
| CEC | Cation Exchange Capacity |
| CMP | Common Mid-Point |
| DART | Detection of Archaeological Residues using Remote sensing Techniques |
| EC | Electrical Conductivity |
| ECC | English China Clay |
| EM | Electromagnetic |
| FC | Field Capacity |
| FFT | Fast Fourier Transform |
| GPR | Ground Penetrating Radar |
| GWC | Gravimetric Water Content |
| IAEA | International Atomic Energy Agency |
| IDS | Ingegneria Dei Sistemi |
| KBS | Knowledge Based System |
| MTU | Mapping The Underworld |
| mux | multiplexer |
| NRCS | Natural Resources Conservation Service |
| OM | Organic Matter |
| ORFEUS | Optimised Radar to Find Every Utility in the Street |
| PCA | Principal Component Analysis |
| REV | representative elemental volume |
| Sat | Saturation water content |
| Sat Cond | Saturation hydraulic Conductivity |
| SCS | Soil Conservation Service |
| SPAW | Soil Plant Air Water |
| SSA | Specific Surface Area |
| SWCC | Soil Water Characteristic Curve |
| TDR | Time-Domain Reflectometry |
| UoB | University of Birmingham |
| USDA | United States Department of Agriculture |
| VNA | Vector Network Analyzer |
| VWC | Volumetric Water Content |
| WARR | Wide Angle Reflection and Refraction |
| WP | Wilting Point |

# NOTATION

| | |
|---|---|
| $\alpha$ | attenuation coefficient |
| $\varepsilon$ | dielectric permittivity |
| $\mu$ | magnetic permeability |
| $\rho$ | density (bulk, dry); reflection coefficient |
| $\sigma$ | electrical conductivity |
| $\tau$ | relaxation time |
| $\omega$ | angular frequency |
| c | speed of light in free space |
| D | distance |
| f | frequency |
| $K_p$ | probe constant |
| $L_a$ | attenuation loss |
| L | length |
| R | electrical resistance; distance |
| t | time |
| T | temperature |
| v | velocity |
| Z | impedance |

# CHAPTER 1: INTRODUCTION

## 1.1. BACKGROUND

Shallow geophysical techniques have been increasingly used for engineering applications. Among these techniques, EM methods such as Ground Penetrating Radar (GPR) are versatile, quick to deploy and non-destructive, and therefore can be utilised for a range of applications. Typical application examples include subsurface characterisation and location of manmade objects such as buried utilities (Anderson et al., 2008).

Each geophysical signal has to travel through the ground and the ability to detect anomalies (e.g., in the case of buried utilities, pipes and cables) depends on their contrast with the surrounding medium. Therefore the ground properties are important and can have great impact on the performance of the geophysical techniques. Different methods work better in certain types of soils and perform worse in others. An attempt to address this issue and to significantly improve the detection of underground utilities was examined at by the Mapping The Underworld (MTU) project (www.mappingtheunderworld.ac.uk), funded by EPSRC in the UK (see Metje et al., 2007; Metje et al., 2008; Rogers, 2008; Rogers et al., 2008; Royal et al., 2010; Royal et al., 2011). MTU combine four different shallow geophysical methods, namely GPR, low-frequency electromagnetic, vibro-acoustic and passive magnetic sensors in order to maximise detection rates.

Field and laboratory testing were undertaken as part of the MTU project and the research described in this thesis represents one aspect of this programme. In particular, it was considered important by the author and the MTU team to further understand the variation of the EM soil properties in the field with seasons and with depth. Time-Domain Reflectometry (TDR) was chosen as an appropriate measurement technique to provide this

information and was used in combination with GPR to understand the impact of changing soil conditions on GPR surveys.

## 1.2. AIM AND OBJECTIVES

The main aim of this research was to investigate the seasonal variability of the EM soil properties and their influencing factors in the field by means of TDR in order to better understand their impact on GPR surveys for buried utility detection. In order to achieve this aim, the following objectives were identified:

- To investigate the current knowledge of EM soil properties and the techniques used to measure them through a comprehensive literature review.
- To define a rigorous TDR methodology for long-term field monitoring covering different seasons based on relatively inexpensive commercial equipment and to verify the most recent findings on TDR calibration.
- To monitor the seasonal variation of the EM soil properties in a field case study for an anthropogenic soil and to thoroughly analyse the causes of this variation, including the relationships between EM soil properties and weather and geotechnical parameters.
- To conduct hydrological simulations in order to validate the results obtained by TDR.
- To establish the impact of the variation of the EM soil properties on GPR surveys for the detection of buried utilities.

# 1.3. LAYOUT OF THE THESIS

This thesis is organised in five chapters. Chapter 1 introduces the subject of the thesis and puts into context the scope of the research undertaken. It also states the aim and objectives of the research. A detailed literature review of the soil properties relevant to shallow geophysical techniques is described in Chapter 2. This chapter also includes a critical review of some of the geophysical techniques used to measure the EM soil properties and describes the models used for their prediction. Chapter 2 concludes by identifying the gaps in knowledge. Chapter 3 describes the methodology used for the construction and calibration of a field TDR monitoring station, including tests on the equipment and verification of its accuracy. It also describes the TDR installation in the field and the methodology associated with the GPR testing. Chapter 3 concludes by introducing the Soil-Plant-Air-Water (SPAW) used for hydrological simulations. Chapter 4 presents the findings obtained during this research and discusses the results. These comprise the characterisation of the soil studied, a description of the variability of the measured soil and weather parameters and their relationship, the results of hydrological simulations by the SPAW model, and the analysis of the seasonal and weather impact on GPR surveys. Each section contains a summary of the main results and findings. Finally, Chapter 5 reports the main conclusions of this research and includes some recommendations for further work.

# CHAPTER 2: LITERATURE REVIEW

## 2.1. SCOPE

Many of the essential services that support the modern human life such as water, gas, electricity and communication are provided by means of a complex system of pipes and cables that run beneath the ground surface. It is important to know the position of the existing buried utilities when new excavations are undertaken, for example when new installations are planned or when services need repair or replacement. A range of shallow geophysical technologies can be employed to locate the buried infrastructure without the need for excavation. In order to optimise the detection it is important to understand the impact of the soil as all geophysical signals need to travel through the ground), in terms of its geotechnical and geophysical properties. Therefore, this literature review focuses on some relevant soil properties, critically assesses recent technological advances to measure them and introduces models used for their prediction. One common experimental technique used to examine the EM properties of the ground is TDR, which is investigated in detail. GPR is also critically reviewed since it is a common shallow geophysical technique used to locate buried utilities, and is strongly affected by the EM soil properties. The potential to predict GPR soil suitability with a better understanding and knowledge of the EM properties of the soil is also investigated. The literature review concludes with a summary highlighting the gaps in knowledge identified that provide the basis for the research described in this thesis.

# 2.2. SOIL DEFINITION

Soil can be defined in several ways. However, there is no generally accepted definition. Jenny (1941) defines the soil as "*a natural body, differentiated into horizons of mineral and organic constituents, usually unconsolidated, of variable depth, which differs from the parent material below in morphology, physical properties and constitution, chemical properties and composition, and biological characteristics*". The main factors influencing the formation of a soil are described by Equation (2.1), according to Jenny (1941).

$$S = f(cl, o, p, r, t) \tag{2.1}$$

where **S** represents the soil system as a function of five parameters: **cl**imate, living **o**rganisms, **p**arent material, **r**elief (i.e., topography) and **t**ime. Natural soils follow specific processes of pedogenesis depending on the combination of these factors, resulting in a large number of soil types.

To the geotechnical engineer the soil can be defined as "*any uncemented or weakly cemented accumulation of mineral particles formed by the weathering of rocks, the void space between the particles containing water and/or air*" (Craig, 2004).

In the context of this thesis, the porous medium where the buried utilities are embedded is referred to as *soil* or simply *ground*. Such a definition includes made grounds and the porous materials buried beneath continuous cemented surfaces, such as roads. It is important to note that no matter their origin, soils are dynamic bodies and that their properties change over time.

In the case of natural or semi-natural[1] soils, the soil can be distinguished as topsoil and subsoil (Foth, 1990). The topsoil represents the shallower layer and it generally has higher organic matter content (commonly 2-10 %) and small amounts of gravel (particles dimension > 2 mm) compared to the subsoil. It normally corresponds to the O and A genetic horizons used in soil science (see appendix A for further details on the genetic horizons). In natural and semi-natural soils, the subsoil shows peculiar characteristics depending on its state of weathering, for instance the accumulation of clay particles caused by leaching. The subsoil normally corresponds to the B and possibly C genetic horizons used in soil science (Foth, 1990; FAO/ISRIC/ISSS, 1998).

This distinction is significant because the topsoil and subsoil generally show dissimilar properties, such as density, particle size distribution, structure, organic matter content. This has important implications when EM techniques are employed in shallow geophysical surveys, since the interactions between signals and soil layers can be affected by this change in soil properties from topsoil to subsoil.

# 2.3. SOIL ELECTROMAGNETIC PARAMETERS

## 2.3.1. Definition of the soil electromagnetic parameters

The key EM parameters associated with TDR and GPR are the signal velocity, $v$ (m/s), and the signal attenuation coefficient, $\alpha$ (i.e., the degree to which the signal decays with distance, Np/m). These two properties are governed by three fundamental EM parameters: dielectric permittivity, electrical conductivity (EC) and magnetic permeability.

[1] In the context of this thesis semi-natural soils refer to anthropogenic soils not covered by a hard surface and characterised by both topsoil and subsoil.

In this section these properties are introduced and defined, with further considerations on their implications with respect to soils being discussed in section 2.3.2.

**Dielectric permittivity (ε):** This is a measure of the ability of a material to transmit (or 'permit') an electric field. It represents the signal energy that can be stored in a material, through separation of charges (e.g., ions, protons, electrons). Dielectric permittivity is a frequency dependent complex number ($\varepsilon^*$), with a real part representing the storage of energy ($\varepsilon'$) and an imaginary part describing the loss mechanisms that degrade energy storage ($\varepsilon''$). The dielectric permittivity of a material is normally expressed as its ratio to the dielectric permittivity of free space ($\varepsilon_0$, $8.854 \times 10^{-12}$ F/m) and is named *relative dielectric permittivity* ($\varepsilon_r$). Hereafter the terms 'relative' and 'dielectric' will be omitted and 'relative dielectric permittivity' will be simply referred to 'permittivity'. The frequency dependency of the permittivity will also be assumed implicitly, even when not directly specified. The complex permittivity, $\varepsilon^*(f)$, is given by Equation (2.2) (Robinson et al., 2003a).

$$\varepsilon^*(f) = \varepsilon'(f) - j\left(\varepsilon_p''(f) + \frac{\sigma_{dc}}{2\pi f \varepsilon_0}\right) \tag{2.2}$$

where $\varepsilon'(f)$ is the real part of the complex permittivity, $\varepsilon_p''(f)$ represents the dipolar losses due to relaxation, $\sigma_{dc}$ is the static electrical conductivity (S/m), $f$ is the frequency (Hz) and $j$ is the imaginary number $\sqrt{-1}$. The imaginary part of the complex permittivity, $\varepsilon''(f)$, is described by Equation (2.3) (Robinson et al., 2003a).

$$\varepsilon''(f) = \varepsilon_p''(f) + \frac{\sigma_{dc}}{2\pi f \varepsilon_0} \tag{2.3}$$

The ratio between the imaginary part, $\varepsilon''(f)$, and the real part, $\varepsilon'(f)$, of the complex permittivity is described by the *loss tangent* given in Equation (2.4), and is an important parameter describing the degree of energy loss associated with a material (Robinson et al., 2003a).

$$tan\,\delta = \frac{\varepsilon_p''(f) + \frac{\sigma_{dc}}{2\pi f \varepsilon_0}}{\varepsilon'(f)} \tag{2.4}$$

The once common term *dielectric constant* is a synonym of the real part of the complex permittivity. This term is now considered inappropriate because the permittivity of a material is in fact not constant, but varies with varying frequency (Evett and Parkin, 2005).

Another common way of expressing permittivity is the so called *apparent permittivity*, $\varepsilon_a$, which in the context of this thesis is the value obtained from TDR or GPR measurements. Further explanations on the apparent permittivity are described later in section 2.5.2.2.

**Electrical conductivity ($\sigma$, EC):** This is a measure of the ability of a material to conduct electric current (S/m). In most soils the EC is ionic and so dependent on the concentration of salts in the pore water. EC is a key factor affecting the signal attenuation and is related to the complex permittivity by Equation (2.2). EC is a frequency dependent quantity, and the direct current EC (or $\sigma_{dc}$) corresponds to the EC at zero frequency. $\sigma_{dc}$ is a term of the imaginary part of the complex permittivity (Equation (2.3))

The EC effects are more significant in the low frequency range of the order of kHz up to a few tens of MHz (Campbell, 1990). In this frequency range the losses due to conductivity are predominant over the dipolar losses. In the TDR and GPR frequency range

(approximately 10 MHz – 1 GHz) EC can be described by a real number because its imaginary component is generally considered insignificant (Cassidy, 2008).

It is important to introduce the concept of *bulk electrical conductivity* (BEC), since it is the parameter measured by TDR. The BEC comprises the contributions to the EC of the pore water and of the surface conduction among soil particles. The accepted method for measuring the BEC by TDR gives an estimation of the direct current bulk electrical conductivity (Lin et al., 2008). The direct current BEC will hereafter be referred to BEC for simplicity (see section 2.5.2.2).

**Magnetic permeability (μ):** This is a measure of the ability of a material to be magnetised when exposed to a magnetic field. It is expressed by a complex quantity, the real part ($\mu'$) describing the storage of energy due to the lining up of atomic and sub-atomic spin directions, and the imaginary part ($\mu''$) describing the losses of energy. It is usually expressed as *relative permeability* ($\mu_r$), i.e., the ratio between the absolute permeability of a material and the permeability of free space ($\mu_0$, $1.2564 \times 10^{-6}$ H/m). In soils the imaginary component is generally neglected because of its minor contribution to the total losses and $\mu_r$ is often assumed to be equal to 1 in the TDR and GPR frequency range (Huisman et al., 2003a). However, this assumption is not valid in soils with high magnetic permeability such as anthropogenic soils rich in iron-oxide components (e.g., crushed bricks, reinforced concrete, smelting waste) and in certain natural soils rich in magnetic minerals (e.g., magnetite-rich igneous rocks, hematitic sands) (Cassidy, 2007, 2008).

As mentioned at the beginning of this section it is possible to determine the signal propagation velocity and the signal attenuation from the knowledge of the complex

permittivity, BEC and $\mu_r$. Since it is relevant in order to understand the principles of TDR the definition of the signal propagation velocity, *v*, is given later in section 2.5.2.2.

The **attenuation coefficient** ($\alpha$) of a material (Np/m) can be determined using Equation (2.5) (Cassidy, 2008).

$$\alpha = \omega \sqrt{\frac{\mu\varepsilon}{2}\left(\sqrt{1+\left(\frac{\varepsilon''}{\varepsilon'}\right)^2}-1\right)} \tag{2.5}$$

where $\omega$ is the radian frequency ($\omega=2\pi f$), $\mu$ is the absolute magnetic permeability and $\varepsilon$ is the absolute permittivity (real component).

By knowing the attenuation coefficient it is possible to calculate the reduction in the signal amplitude with distance using Equation (2.6) (Annan, 2008).

$$A_2 = A_1 e^{-\alpha R} \tag{2.6}$$

where $A_1$ is the initial signal amplitude and $A_2$ is the amplitude after a distance *R* (m).

The attenuation coefficient can also be used to determine the *attenuation loss*, $L_a$ (dB), of a material at a certain depth, *R*, from Equation (2.7) (Daniels, 2004):

$$L_a = 8.686 \times 2 \times R \times \alpha \tag{2.7}$$

## 2.3.2. Soil interactions to electromagnetic signals

Soil can be treated as a porous medium, with different volumetric percentages of air, water and solid particles (Dobson et al., 1985). When an EM signal is injected into the soil, the interactions are complex and depend on the soil type and on parameters such as the amount of water, the pore water EC and the temperature. In particular, water is the key parameter that affects the propagation of EM signals since it directly affects the soil permittivity and BEC.

In order to better understand the importance of water it is useful to briefly describe the structure of the water molecule and its dipolar nature. The water molecule is made of two atoms of hydrogen linked to an atom of oxygen and separated by an angle of 104.5° in order to keep the most stable molecular configuration (Ball, 1999). The molecule is actually a tetrahedron, with the two atoms of hydrogen and two pair of electrons forming the four vertices surrounding the atom of oxygen (Figure 2.1a). This structure confers the dipolar nature of the water molecule, generated by the tendency of the oxygen to attract electrons and leaving the atoms of hydrogen partially positively charged (Ball, 1999). Several molecules of water in the liquid form tend to bond together by creating hydrogen bonds, which are connections between the partially positive atoms of hydrogen and the negative lone pairs of electrons. These bonds keep forming and breaking continuously, at a pace mainly determined by temperature. In its gaseous and solid phases water shows very different characteristics, with the absence of the hydrogen bonds and by assuming a crystalline form in the solid state. These properties make the molecule of water peculiar and the response of water to applied EM signals very complex.

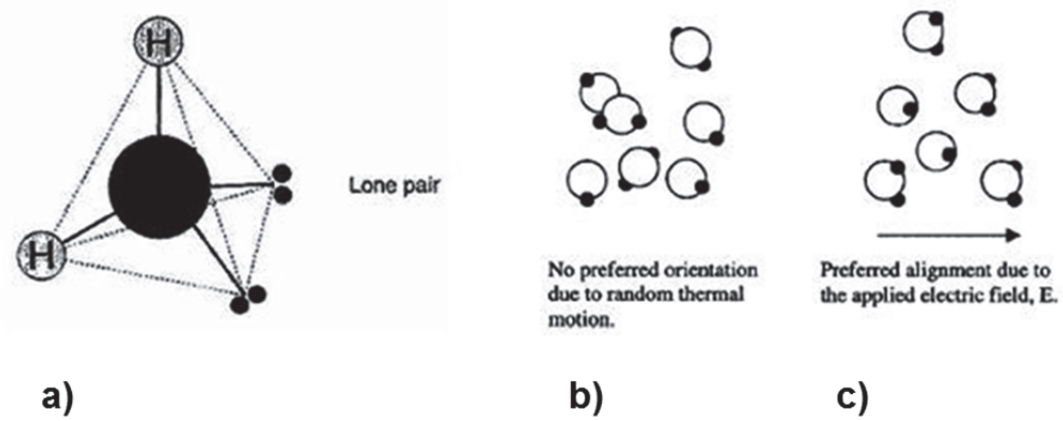



Figure 2.1 – (a) Water molecule tetrahedron, (b) and (c) water molecules without and with an external electric field applied, respectively (after Robinson et al., 2003a).

### 2.3.2.1. Storage of energy

**Real part of the permittivity**

In the absence of an external EM field the water molecules are randomly distributed according to the temperature and the hydrogen bonds (Figure 2.1b). When an EM signal is applied, the water molecules rotate in response to the signal and tend to align to the signal propagation direction (Figure 2.1c). This separation of charges stores electrical energy and is described by the real part of the complex permittivity. The applied energy is then released as the signal proceeds in its path, and is used to separate the neighbouring particles along the signal propagation direction (Cassidy, 2008). The process is illustrated in Figure 2.2.

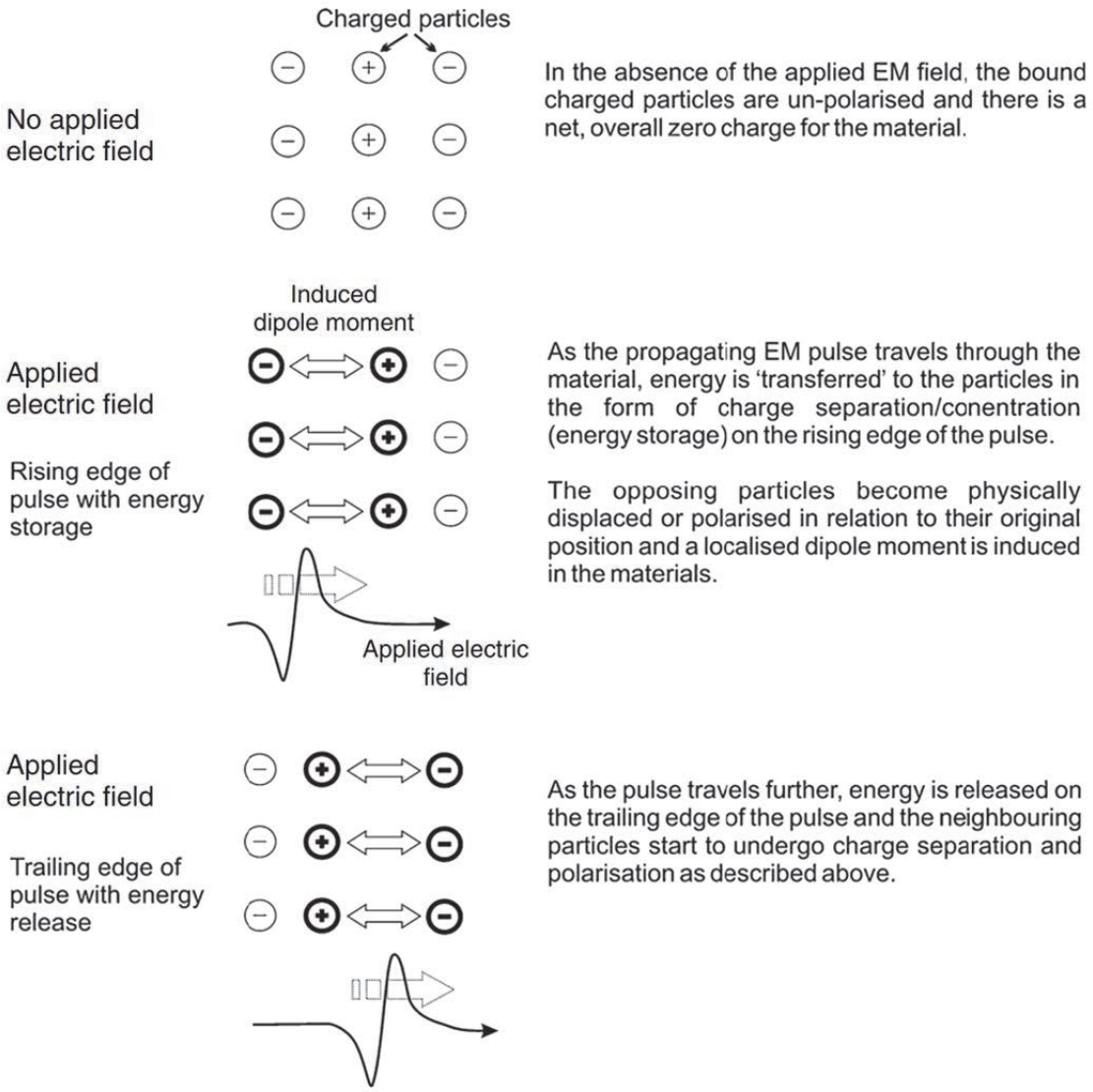



Figure 2.2 – Diagram showing the response of a material to an applied external electric field (after Cassidy, 2008).

## 2.3.2.2. Loss mechanisms

**Dipolar (or relaxation) losses**

Because of the friction that occurs during the displacement of charges a portion of the applied energy is dissipated as heat and is described by the dipolar losses term in the imaginary part of the complex permittivity. This phenomenon, called *relaxation*, shows a maximum at a specific *relaxation frequency*.

There are different types of polarisation: *electronic, atomic, dipolar* and *Maxwell-Wagner* (Cassidy, 2008).

The *electronic and atomic polarisations* are related to the displacement of electron clouds and individual bonded atoms respectively. These types of polarisation provide a high-frequency limit for the value of permittivity (also known as optical permittivity) and are important in dry solid materials and in glacial environments, where it is the only visible polarisation process (Cassidy, 2008).

The *Maxwell-Wagner polarisation* (i.e., free charge and interfacial polarisation) consists in the accumulation of free charges at material barriers or in the preferential distribution of charge along material faces. In soils, this effect occurs only at very low frequencies (below 10 MHz), for fine-grained, saturated soils. When an electric field is applied, the free charges in the saturated pore spaces are displaced and form an induced dipole moment (Cassidy, 2008). Figure 2.3 describes the process of Maxwell-Wagner polarisation.

In the frequency range between 10 MHz and 1 GHz (i.e., the GPR and TDR frequency range) the most relevant form of polarisation is the *dipolar polarisation* (Cassidy, 2008). Due to thermal agitation and molecular inertia, the water molecules oppose the separation of charges caused by an applied EM signal, resulting in a time delay before the maximum net polarisation is reached. The time taken for the molecules to polarise and revert to a random state after the removal of the applied field is known as the *relaxation time,* $\tau$ (s), and is related to the relaxation frequency, $f_{rel}$ (Hz), by Equation (2.8) (Hamburger, 1930).

$$f_{rel} = \frac{1}{2\pi\tau} \tag{2.8}$$

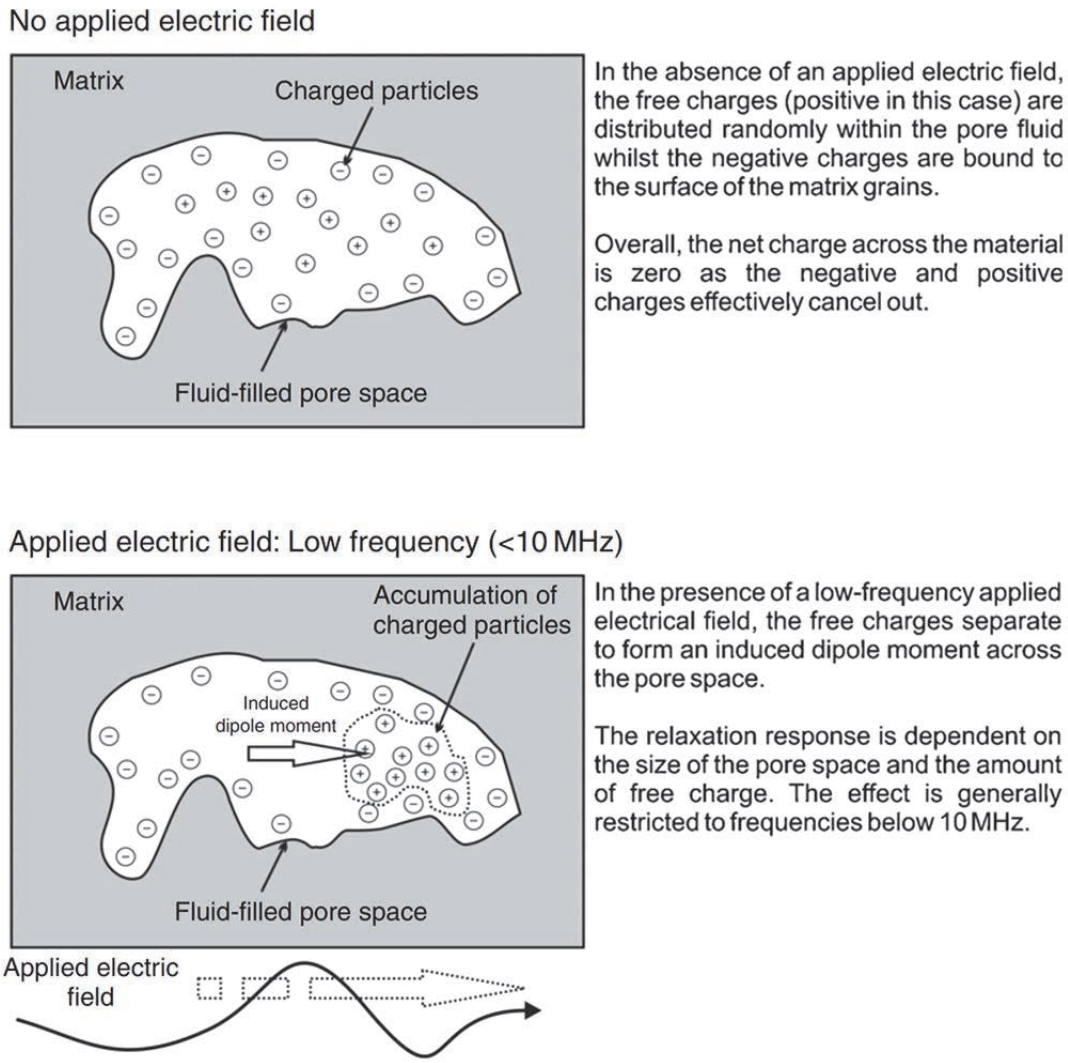



Figure 2.3 – Diagram showing the process of Maxwell-Wagner polarisation in soils saturated with weakly conducting fluid (after Cassidy, 2008).

When the frequency of the applied signal is much lower than the relaxation frequency, the dipolar orientations do not lag the field variations and the energy is stored in the separation of charges. When the frequency increases, the time delay in the particle orientation increases and less energy is stored, a great portion being dissipated as heat through molecular collisions. This effect is visible in a reduction of the real part of the permittivity and in a higher imaginary component. The losses reach a maximum at the relaxation frequency. After this point the signal frequency becomes too fast for the water

molecules to orientate and the net orientation remains in a non-polarised state (Cassidy, 2008). Both the real and imaginary components of the permittivity stabilise at a high frequency value (optical permittivity).

Relaxation phenomena were described by the pioneer work of Debye (1929), who generated a model that explained the polarisation of pure liquids. Cole and Cole (1941) extended the Debye model in order to better describe the polarisation phenomena of solids and mixtures. The Cole and Cole model (Equation (2.9)) is often used to describe the polarisation of soils (Cassidy, 2008).

$$\varepsilon^*(f) = \varepsilon_\infty + \frac{\varepsilon_s - \varepsilon_\infty}{1 + i\left(\frac{f}{f_{rel}}\right)^{1-\beta}} - j\frac{\sigma_{dc}}{2\pi f \varepsilon_0} \tag{2.9}$$

where $\beta$ is a parameter ranging from 0 and 1 accounting for a spread in relaxation frequency, $\varepsilon_s$ is the static real part of the permittivity (i.e., at zero frequency) and $\varepsilon_\infty$ represents the real permittivity at frequencies so high that the molecular orientation does not have time to contribute to the polarisation (Huisman et al., 2003a).

Free water can be considered a pure dipolar molecule, but in soils water molecules are hindered in their movements when they are close to the mineral particle surfaces. This condition is generally referred to as *bound water* (Cownie and Palmer, 1952). The importance of the bound water is evident in the dipolar relaxation phenomena: while free water has a relaxation frequency of approximately 17 GHz, bound water shows relaxation at much lower frequency, in the TDR and GPR frequency range. Clayey soils, with a high specific surface area (SSA), can retain more water and therefore show greater losses due to relaxation, especially in wet conditions. The effect of bound water depends on the soil

constituents (percentage of clay particles, mineralogy), on the density and the degree of saturation, on the ions in the pore water and pH (Cassidy, 2008).

**EC losses**

The second term of the imaginary part of the permittivity is related to the losses due to EC. Charge carriers such as ions in the soil pore water quickly accelerate under an applied electric field causing the particles to collide (Robinson et al., 2003a). As a result some energy is dissipated through heat (Figure 2.4; after Cassidy, 2008). The effect of EC is strongly dependent on the temperature, on the soil water content and on the ions content, and is more significant in the frequency range of the kHz up to a few MHz, because the ions can move in phase with the applied signal, resulting in a great portion of energy loss (Campbell, 1990). In this case the EC can be expressed only by a real part, also called static or DC electrical conductivity. As the frequency increases, the ions accumulate a phase lag due to inertia, and the EC can be described by a complex number, with the imaginary part corresponding to the out of phase component that stores electrical energy. In the TDR and GPR range of frequencies, this imaginary component of EC is negligible, and the EC remains associated with energy losses (Cassidy, 2008).

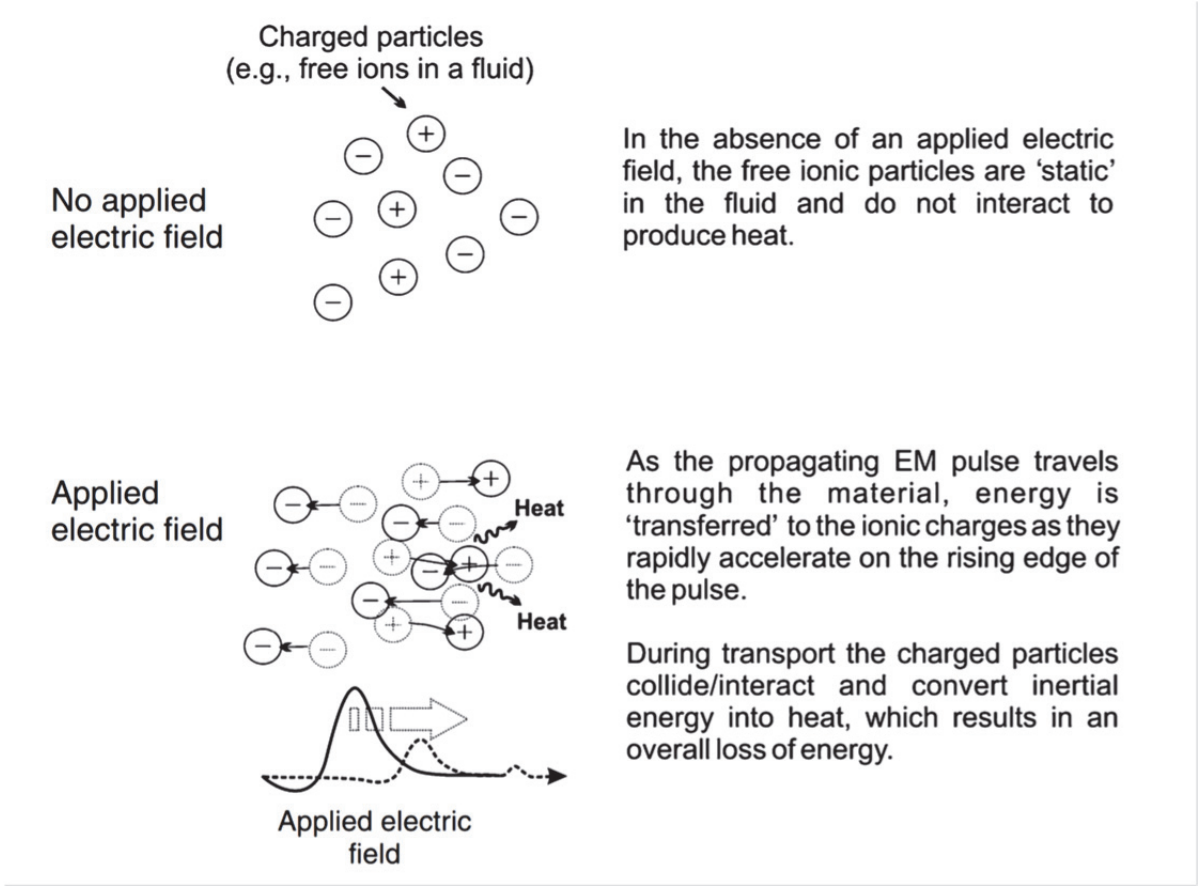



Figure 2.4 – Diagram showing the process of conduction in a material containing movable ions (after Cassidy, 2008).

**Magnetic permeability losses**

Soils are generally considered non-magnetic materials and therefore they are normally described by the real part of the magnetic permeability, which is assumed to be equivalent to the magnetic permeability of free space. However, in some cases such as in magnetite-rich igneous soils, hematitic sands and anthropogenic materials containing large amounts of iron this assumption is not valid and a non-unity value of relative magnetic permeability must be assumed (Cassidy, 2007; Thomas et al., 2008c). The additional losses caused by the magnetic permeability depend on the percentage and type of the ferromagnetic minerals.

# 2.4. SOIL PARAMETERS AFFECTING THE ELECTROMAGNETIC SIGNALS

## 2.4.1. Soil water content

### 2.4.1.1. Overview

The soil water content is a key soil parameter in several fields, such as agriculture, hydrology, geotechnical engineering and environmental science. From a geophysical point of view, based on the discussion of section 2.3.2, the interest in the soil water content rises, amongst others, from its influence on the EM soil properties. This dependence was clearly illustrated by Curtis (2001), who provided extensive measurements of EM parameters for different soils at a wide range of water contents. As shown in Figure 2.5 it is apparent that both permittivity and BEC are strongly affected by the soil volumetric water content.

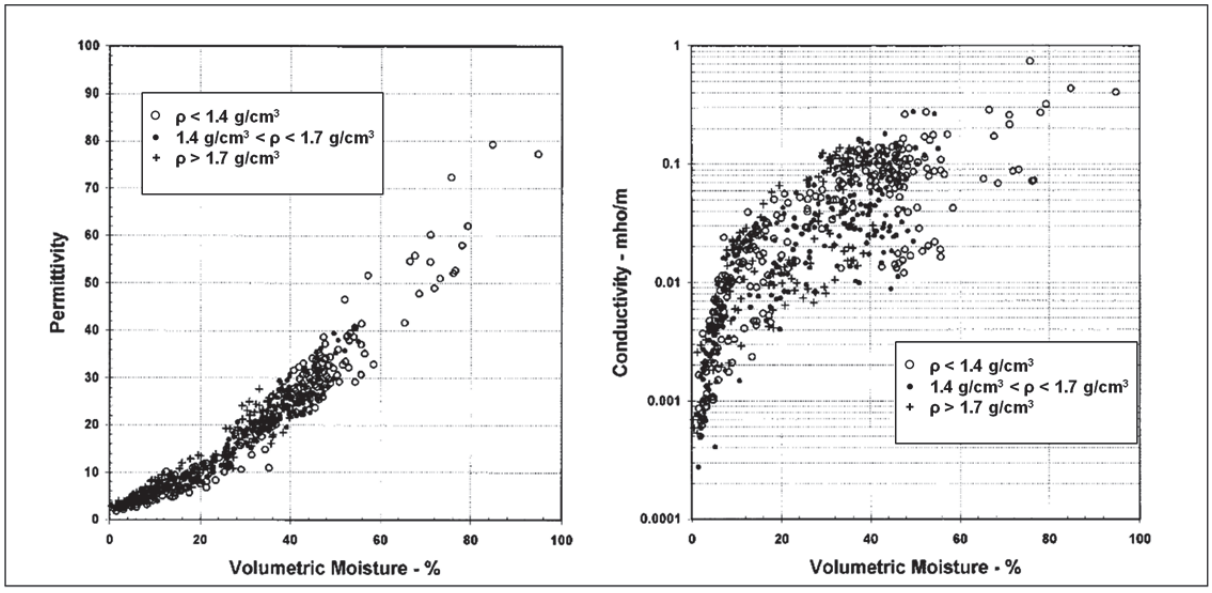



Figure 2.5 – Permittivity and EC variations with water content for soils at a wide range of water contents (after Curtis, 2001).

The dependence of the permittivity to the soil water content was already shown by Smith-Rose (1935), who described the EM dispersion (i.e., variation of the EM properties with frequency) of soils with different amounts of water. Cownie and Palmer (1952) suggested the presence of two distinct forms of water (i.e., bound and free water). However, the water (in its liquid form) is now thought to be present in three main different forms in soils (Foth, 1990, Figure 2.6). The *adhesion water* (i.e., tightly bound water), immobile and strongly adsorbed to the soil particles; the *cohesion water* (also called capillary water), which is held together by the hydrogen bonds between water molecules and is moveable, although it does not respond to gravity; the *gravitational water* (or free water), which is only slightly attracted to the soil particles and whose movement is determined by the gravitational force.

This distinction is useful in agricultural science, since it helps to estimate the water availability to plants. Saarenketo (1998) confirmed this definition by describing the electrical properties of water in a number of silty and clayey soils in the frequency range of 30 MHz to 3 GHz and for volumetric water contents between 0 and approximately 50 %. Saarenketo (1998) concluded that the water in soil can be classified according to its electrical properties. The dielectric dispersion and losses were shown to be mainly associated with the cohesion water. The adhesion water was also deemed to be insensitive to external EM fields unless in the presence of a high cation concentration that would disrupt the ordered structure of the bound water. The gravitational water molecules were shown to be free to move and therefore do not show relaxation in the TDR and GPR frequency range.

It is important to note that this description refers only to the liquid water, but water can exist in the soil in the form of solid (i.e., ice) or vapour, each with very different dielectric properties (i.e., low permittivity ranging from 1 to 5) of liquid water (i.e., permittivity of approximately 80 at 20 °C).

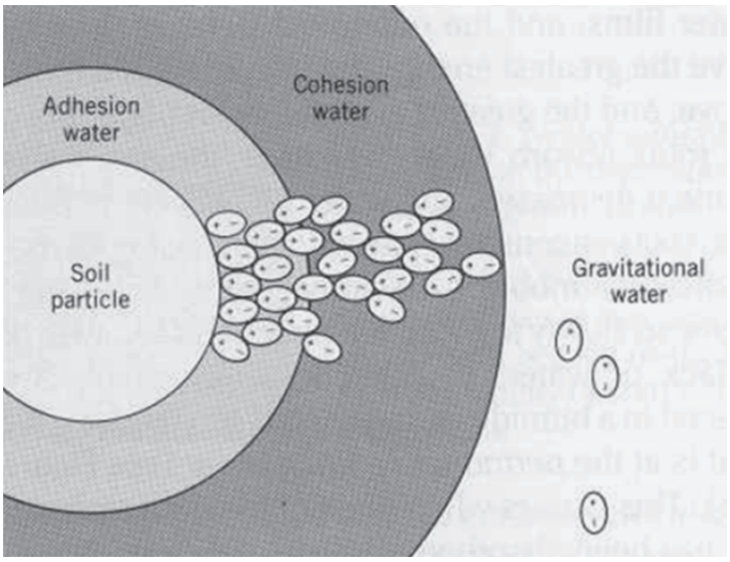



Figure 2.6 – The three main forms of water found in the soil (after Foth, 1990).

In general, the soil water content can be described in two main ways, depending if it is expressed in units of mass or volume. The percentage of the gravimetric water content, *GWC*, is calculated as the ratio between the mass of water, $M_w$, and the mass of the dry soil particles, $M_s$, both expressed in grams (g) (Equation (2.10)). The gravimetric expression is the usual way of describing the soil water in geotechnical engineering (BS 1377-2, 1990).

$$GWC = \frac{M_w}{M_s} 100 \tag{2.10}$$

The volumetric definition (*VWC*) consists of the ratio between the mass of water and the volume of the soil sampled, $V_s$, expressed in g and $cm^3$ respectively[2] (Equation (2.11)).

$$VWC = \frac{M_w}{V_s} 100 \tag{2.11}$$

[2] This definition corresponds to the ratio between volume of water and volume of sample, assuming a density of water of 1 $g/cm^3$.

where *VWC* is the volumetric water content expressed as a percentage. The gravimetric and volumetric expressions can be interchanged by means of the dry density, $\rho_{dry}$ (g/cm$^3$) of the soil sample, according to Equation (2.12).

$$VWC = \rho_{dry} GWC \tag{2.12}$$

In geophysics the soil water content is usually expressed on a volumetric basis, therefore the knowledge of the dry density becomes important in case gravimetric water contents are needed from volumetric water content measurements (Thomas et al., 2008b).

### 2.4.1.2. Soil water characteristics

A combination of soil properties determines the water holding capacity of the soil and therefore its hydraulic conductivity (i.e., ability of the soil to transmit water). The ability of the water to move through a soil is related to its energy level. Adhesion water has a low energy level and tends to remain immobile, while gravitational water has a high energy level and will tend to move by gravity. It is convenient to describe the energy state in terms of water potential (Foth, 1990).

The **soil water potential** is defined as the work needed to move water from a reference pool of pure water to a point in the soil profile and is expressed by pressure units (e.g., kPa, bar, cm of water). The water potential is the sum of its components, the *gravitational potential*, the *matric potential* (also called tension or suction) due to adsorptive and capillary forces, and the *osmotic potential* due to the presence of solutes (Foth, 1990). The gravitational potential has a positive value since it measures the work that must be done to move water from a reference pool at the sea level to a position situated at a higher elevation. Matric and osmotic potential have a negative sign, since no energy input is

required to move water to soil particles, due to adsorptive and capillary forces, and to hydrate ions. The water potential in soils goes from positive value at saturation to a negative value, down to $-10^6$ kPa (Fredlund and Xing, 1994), the more negative the value, the higher the work to move water. Common reference values of water potentials are 0 kPa at saturation (i.e., when all the soil pores are filled with water), −33 kPa at field capacity (i.e., the soil water content after all the gravitational water has drained), and −1500 kPa at the permanent wilting point (i.e., the soil water content that cannot be extracted by plants, which approximately corresponds to the adhesion water). The actual field capacity and wilting point vary with different soils, but the water content at these potentials is useful in the determination of the soil water characteristics (see for example Saxton et al., 1986). Another important level of water potential is the air-entry potential (or bubbling pressure), which corresponds to the matric potential when air starts to enter the largest pores in the soil (Fredlund and Xing, 1994).

The soil water holding capacity is described by the soil water characteristic curves (SWCC) that define the relationship between water content and potential (Fredlund and Xing, 1994). As explained earlier, at higher potential (more negative) the soil tends to retain the water more strongly. The SWCC is primarily determined by the pore-size distribution of the soil which in turn is related to the particle size distribution of the soil particles, the bulk density and the soil structure. Figure 2.7 shows typical SWCC for sandy, silty and clayey soils, as reported by Fredlund and Xing (1994).

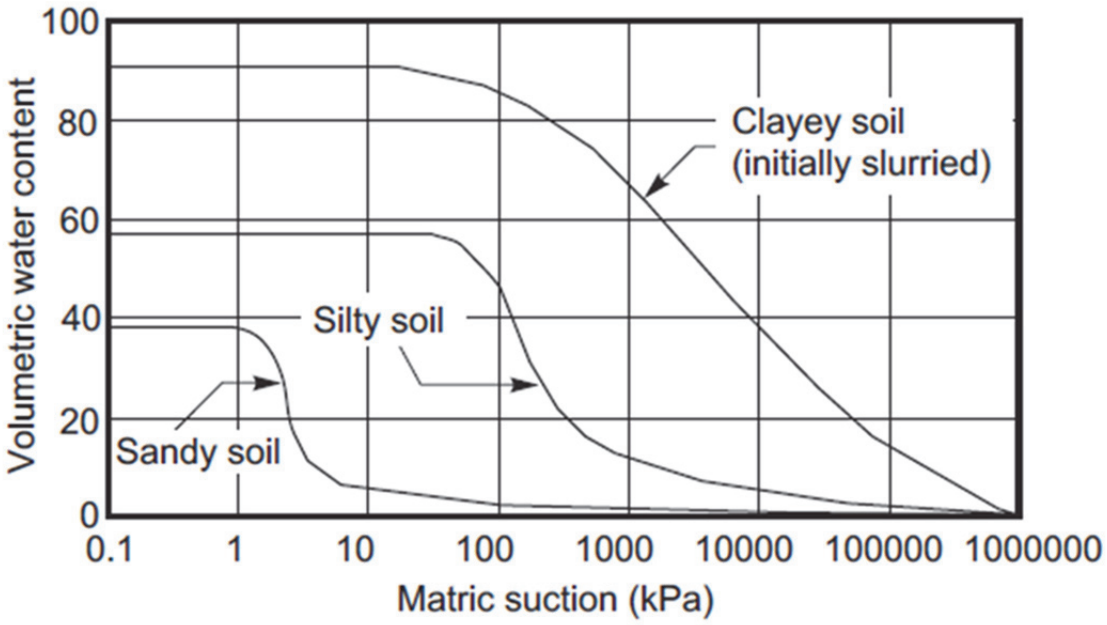



Figure 2.7 – Typical soil water characteristic curves for sandy, silty and clayey soils (after Fredlung and Xing, 1994).

Several empirical equations have been proposed to simulate the SWCC (e.g., van Genuchten, 1980), but despite being commonly used they remain empirical and therefore they may not apply well to all soils. In an attempt to identify more general relationships, Fredlund and Xing (1994) proposed an equation that predicted the SWCC from the pore-size distribution of the soil, but knowledge of this parameter is required in order to apply the model. An empirical approach was followed by Saxton et al. (1986), who suggested a range of equations based on an extensive dataset of agricultural soils in North America. In order to simulate the full water-potential range three potential segments were identified of 1500 kPa – 33 kPa, 33 kPa – air-entry potential, and air-entry potential – 0 kPa. Each of these segments was estimated by a different set of equations in order to obtain a better fit to the data. These equations provided good estimations of the soil water characteristics (water-potential estimations plus hydraulic conductivity) and covered a wide range of soil types,

water potentials and hydraulic conductivities. However, the model can only be applied for soils with up to approximately 60 % of clay and 95 % of sand (see Figure 2.8). An advantage of this model is its minimal input requirements, namely the particle size distribution of the soil (i.e., percentage of sand, silt and clay). Gijsmann et al. (2003), while comparing different models, concluded that the model by Saxton et al. (1986) overall performed better than the others. More recently, the same model was improved by Saxton and Rawls (2006) by also including in the inputs the organic matter content. Unlike the previous model, the new model incorporates the effects of compaction by adjusting the bulk density using a weighting factor from 0.9 to 1.3. It also accounts for a gravel effect, which decreases the hydraulic conductivity, and a salinity effect, which increases the water content at −1500 kPa and reduces the water availability to plants.

Table 2.1 and 2.2 list all the equations and definitions reported by Saxton and Rawls (2006) for estimating the soil water characteristics. A graphical computer implementation of the model was also described in Saxton and Rawls (2006) and is illustrated in Figure 2.8.

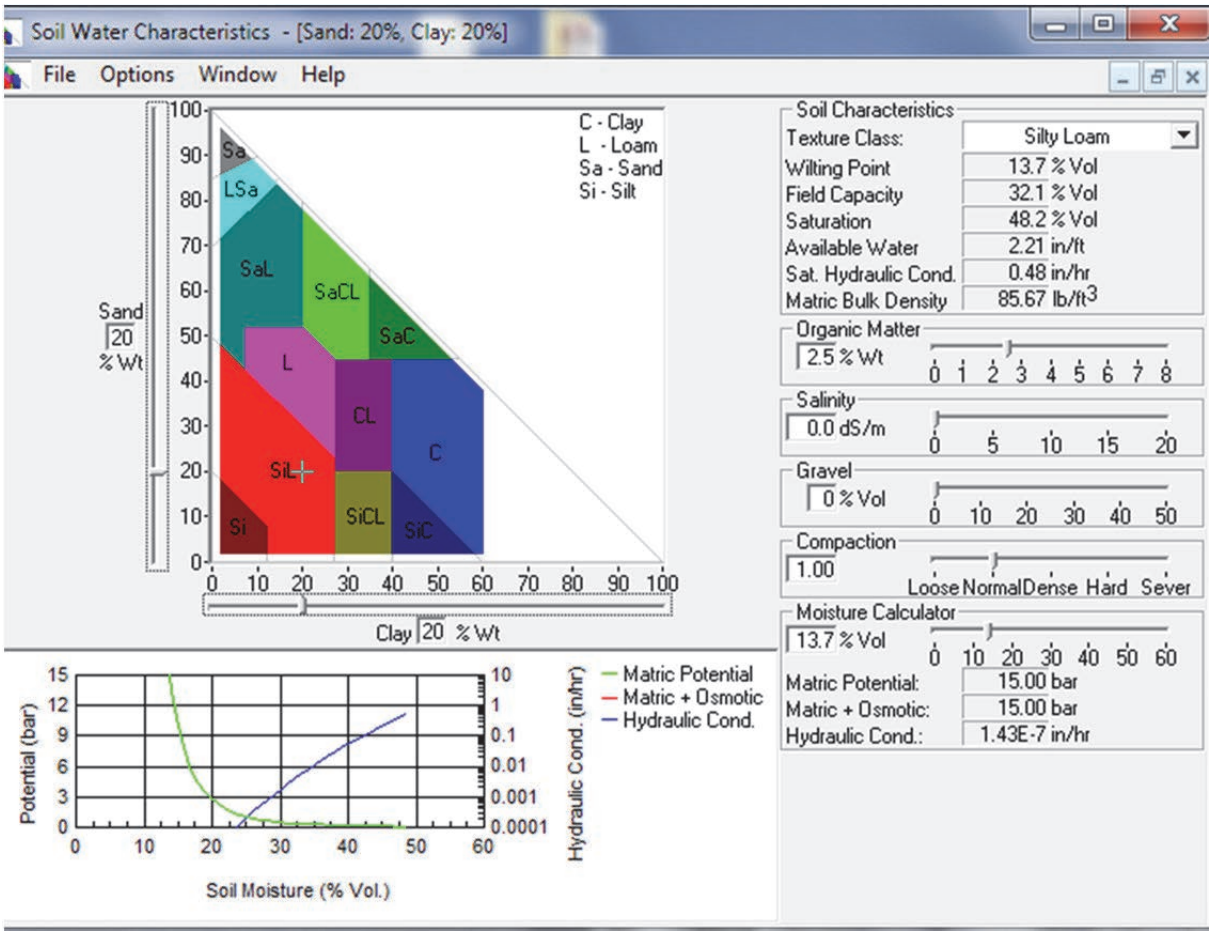



Figure 2.8 – Graphical computer program that estimates the soil water characteristics using the Saxton and Rawls model (after Saxton and Rawls, 2006).

Table 2.1 – Summary of the equations for estimating the soil water characteristics as reported by Saxton and Rawls (2006).

| Variable | Equation | $R^2$/$S_e$ | Eq. |
|---|---|---|---|
| | **Moisture Regressions** | | |
| $\theta_{1500}$ | $\theta_{1500} = \theta_{1500t} + (0.14 \times \theta_{1500t} - 0.02)$ | 0.86/0.02 | 1 |
| | $\theta_{1500t} = -0.024S + 0.487C + 0.006OM + 0.005(S \times OM) - 0.013(C \times OM) + 0.068(S \times C) + 0.031$ | | |
| $\theta_{33}$ | $\theta_{33} = \theta_{33t} + [1.283(\theta_{33t})^2 - 0.374(\theta_{33t}) - 0.015]$ | 0.63/0.05 | 2 |
| | $\theta_{33t} = -0.251S + 0.195C + 0.011OM + 0.006(S \times OM) - 0.027(C \times OM) + 0.452(S \times C) + 0.299$ | | |
| $\theta_{(S-33)}$ | $\theta_{S-33} = \theta_{(S-33)t} + (0.6360_{(S-33)t} - 0.107)$ | 0.36/0.06 | 3 |
| | $\theta_{(S-33)t} = 0.278S + 0.034C + 0.022OM - 0.018(S \times OM) - 0.027(C \times OM) - 0.584(S \times C) + 0.078$ | | |
| $\psi_e$ | $\psi_e = \psi_{et} + (0.02\psi_{et}^2 - 0.113\psi_{et} - 0.70)$ | 0.78/2.9 | 4 |
| | $\psi_{et} = -21.67S - 27.93C - 81.97\theta_{S-33} + 71.12(S \times \theta_{S-33}) + 8.29(C \times \theta_{S-33}) + 14.05(S \times C) + 27.16$ | | |
| $\theta_S$ | $\theta_S = \theta_{33} + \theta_{(S-33)} - 0.097S + 0.043$ | 0.29/0.04 | 5 |
| $\rho_N$ | $\rho_N = (1 - \theta_S)2.65$ | | 6 |
| | **Density Effects** | | |
| $\rho_{DF}$ | $\rho_{DF} = \rho_N \times DF$ | | 7 |
| $\theta_{S-DF}$ | $\theta_{S-DF} = 1 - (\rho_{DF}/2.65)$ | | 8 |
| $\theta_{33-DF}$ | $\theta_{33-DF} = \theta_{33} - 0.2(\theta_S - \theta_{S-DF})$ | | 9 |
| $\theta_{(S-33)DF}$ | $\theta_{(S-33)DF} = \theta_{S-DF} - \theta_{33-DF}$ | | 10 |
| | **Moisture-Tension** | | |
| $\psi_{(1500-33)}$ | $\psi_\theta = A(\theta)^{-B}$ | | 11 |
| $\psi_{(33-\psi e)}$ | $\psi_\theta = 33.0 - [(\theta - \theta_{33})(33.0 - \psi_e)/(\theta_S - \theta_{33})]$ | | 12 |
| $\theta_{(\psi e-0)}$ | $\theta = \theta_S$ | | 13 |
| A | $A = \exp(\ln 33 + B\ln\theta_{33})$ | | 14 |
| B | $B = [\ln(1500) - \ln(33)]/[\ln(\theta_{33}) - \ln(\theta_{1500})]$ | | 15 |
| | **Moisture–Conductivity** | | |
| $K_S$ | $K_S = 1930(\theta_s - \theta_{33})^{(3-\lambda)}$ | | 16 |
| $K_\theta$ | $K_\theta = K_S(\theta/\theta_S)^{[3+(2/\lambda)]}$ | | 17 |
| $\lambda$ | $\lambda = 1/B$ | | 18 |
| | **Gravel Effects** | | |
| $R_v$ | $R_v = (\alpha R_w)/[1 - R_w(1 - \alpha)]$ | | 19 |
| $\rho_B$ | $\rho_B = \rho_N(1 - R_v) + (R_v \times 2.65)$ | | 20 |
| $PAW_B$ | $PAW_B = PAW(1 - R_v)$ | | 21 |
| $K_b/K_s$ | $K_b/K_s = \dfrac{1 - R_w}{[1 - R_w(1 - 3\alpha/2)]}$ | | 22 |
| | **Salinity Effects** | | |
| $\Psi_O$ | $\Psi_O = 36EC$ | | 23 |
| $\Psi_{O\theta}$ | $\Psi_{O\theta} = \dfrac{\theta_S}{\theta}(36EC)$ | | 24 |

Table 2.2 – Definition of the symbols and terms shown in Table 2.1 (after Saxton and Rawls, 2006).

| Symbol | Definition |
|---|---|
| A, B | Coefficients of moisture-tension, Eq. [11] |
| C | Clay, %w |
| DF | Density adjustment Factor (0.9–1.3) |
| EC | Electrical conductance of a saturated soil extract, dS $m^{-1}$ (dS/m = mili-mho $cm^{-1}$) |
| FC | Field Capacity moisture (33 kPa), %v |
| OM | Organic Matter, %w |
| PAW | Plant Avail. moisture (33–1500 kPa, matric soil), %v |
| $PAW_B$ | Plant Avail. moisture (33–1500 kPa, bulk soil), %v |
| S | Sand, %w |
| SAT | Saturation moisture (0 kPa), %v |
| WP | Wilting point moisture (1500 kPa), %v |
| $\theta_\psi$ | Moisture at tension $\psi$, %v |
| $\theta_{1500t}$ | 1500 kPa moisture, first solution, %v |
| $\theta_{1500}$ | 1500 kPa moisture, %v |
| $\theta_{33t}$ | 33 kPa moisture, first solution, %v |
| $\theta_{33}$ | 33 kPa moisture, normal density, %v |
| $\theta_{33\text{-}DF}$ | 33 kPa moisture, adjusted density, %v |
| $\theta_{(S\text{-}33)t}$ | SAT-33 kPa moisture, first solution, %v |
| $\theta_{(S\text{-}33)}$ | SAT-33 kPa moisture, normal density %v |
| $\theta_{(S\text{-}33)DF}$ | SAT-33 kPa moisture, adjusted density, %v |
| $\theta_S$ | Saturated moisture (0 kPa), normal density, %v |
| $\theta_{S\text{-}DF}$ | Saturated moisture (0 kPa), adjusted density, %v |
| $\psi_\theta$ | Tension at moisture $\theta$, kPa |
| $\psi_{et}$ | Tension at air entry, first solution, kPa |
| $\psi_e$ | Tension at air entry (bubbling pressure), kPa |
| $K_S$ | Saturated conductivity (matric soil), mm $h^{-1}$ |
| $K_b$ | Saturated conductivity (bulk soil), mm $h^{-1}$ |
| $K_\theta$ | Unsaturated conductivity at moisture $\theta$, mm $h^{-1}$ |
| $\rho_N$ | Normal density, g $cm^{-3}$ |
| $\rho_B$ | Bulk soil density (matric plus gravel), g $cm^{-3}$ |
| $\rho_{DF}$ | Adjusted density, g $cm^{-3}$ |
| $\lambda$ | Slope of logarithmic tension-moisture curve |
| $\alpha$ | Matric soil density/gravel density (2.65) = $\rho/2.65$ |
| Rv | Volume fraction of gravel (decimal), g $cm^{-3}$ |
| Rw | Weight fraction of gravel (decimal), g $g^{-1}$ |
| $\Psi_O$ | Osmotic potential at $\theta = \theta_S$, kPa |
| $\Psi_{O\theta}$ | Osmotic potential at $\theta < \theta_S$, kPa |

The Saxton and Rawls model has been used successfully in combination with the Soil-Plant-Air-Water (SPAW) computer model for agricultural field hydrological simulations (Saxton et al., 1974; Saxton and Willey, 2006; Saxton et al., 2006). The SPAW model simulates the daily hydrological water budget considering all the major hydrological processes such as runoff, infiltration and evapotranspiration. The SPAW model internally estimates the runoff (i.e., the portion of the rainfall that does not infiltrate into the soil), by means of the USDA Soil Conservation Service Runoff Curve Number (SCS-CN) method (for further details see Ponce et al., 1996 and Saxton and Willey, 2006). The soil water vertical distribution across the soil profile is calculated by means of a simplified finite difference form of the Darcy equation (Saxton and Willey, 2006). Evapotranspiration is not calculated internally by the software, but the user can input this information manually. The SPAW model predicts the soil water content based on a relatively few inputs such as the cumulative daily rainfall, the daily maxima and minima air temperatures, the soil water characteristics, and the field management (Saxton and Willey, 2006; for further details see section 3.4.2).

Despite the SPAW model being developed for agricultural fields it can be applied in a wider context involving hydrological simulations. Foo et al. (2011) implemented the SPAW model within a Knowledge Based System (KBS) aimed at the prediction of the geophysical soil properties from geotechnical data[3]. In this case the hydrological model accounts for the seasonal variation of the soil properties and allows the temporal variation of the soil water content (and therefore of the soil permittivity, see section 2.4.2) to be simulated.

[3] This KBS was developed in parallel to this research as part of the Mapping The Underworld project (http://www.mappingtheunderworld.ac.uk).

### 2.4.2. Impact of temperature and geotechnical properties on the soil EM behaviour

In addition to the soil water there are other soil properties that affect the response of the soil to applied EM signals. However, most of these properties are related to the soil water content. Topp et al. (1980) proposed an empirical relationship between the soil apparent permittivity measured by TDR and the soil water content and found it to be independent of the soil type, soil density, soil temperature and soluble salt content. This was later shown not to be valid in some circumstances, for example for clayey and organic soils (e.g., Roth et al., 1990; Herkelrath et al., 1991).

Soils with a high concentration of soluble salts have a large pore water EC, and this affects the complex permittivity of the soil (Equation (2.2)). Since the EC of the soil solution is known to be dependent on temperature (e.g., Rhoades and Vanschilfgaarde, 1976; Heimovaara et al., 1995), the temperature can become an important factor affecting the dielectric properties of the soil. The relationship between soil temperature and soil permittivity is not straightforward. Wraith and Or (1999) tested four different soils at a range of water contents and temperatures in an attempt to establish a relationship between the soil permittivity and the temperature. They found a mixed response. Soils with a high specific surface area (SSA, i.e., surface per unit of mass or volume) and/or low water content showed an increase in permittivity with temperature, and the soils with low SSA and/or high water content showed a decrease in permittivity with increasing temperature. The permittivity of water is known to decrease with increasing temperature (Weast, 1972), but at higher temperature it is thought to release a portion of the bound water and therefore increase the bulk soil permittivity. Logsdon (2000) also measured positive temperature correlations in soils with high SSA and suggested that a temperature correction factor should be used when converting the soil permittivity into soil water. However, Logsdon (2000)

concluded that this is only necessary for soils with large amounts of bound water and that a temperature correction factor is not necessary for sandy soils and for clays with relatively low SSA (e.g., kaolinite). Or and Wraith (1999) reported an equation by Weast (1986) relating the permittivity of free water ($\varepsilon_w$) to temperature, and normalizing the values at 25 °C (Equation (2.13)).

$$\varepsilon_w(T) = 78.54[1 - 4.579 \times 10^{-3}(T - 25) + 1.19 \times 10^{-5}(T - 25)^2 - 2.8 \times 10^{-8}(T - 25)^3] \quad (2.13)$$

From section 2.4.1 and the above discussion it is apparent that both temperature and water content are important in defining the EM behaviour of the soil. These parameters are related to the geotechnical characteristics of the soil. As shown in section 2.4.1.2 the water holding capacity is mainly determined by the particle size distribution, and therefore the soil type is fundamental in governing the soil EM properties. However, it is important to note that, in addition to their size, the SSA of the soil particles is also significant, since it governs the amount of bound water present in the soil. As a consequence, different clay types (i.e., with varying SSA) show different relaxations, as shown in Figure 2.9 (Thomas et al., 2008a). In addition, soils with a high SSA show higher cation exchange capacity (CEC) and therefore higher BEC, which in turn reflects a larger dependency on the soil temperature.

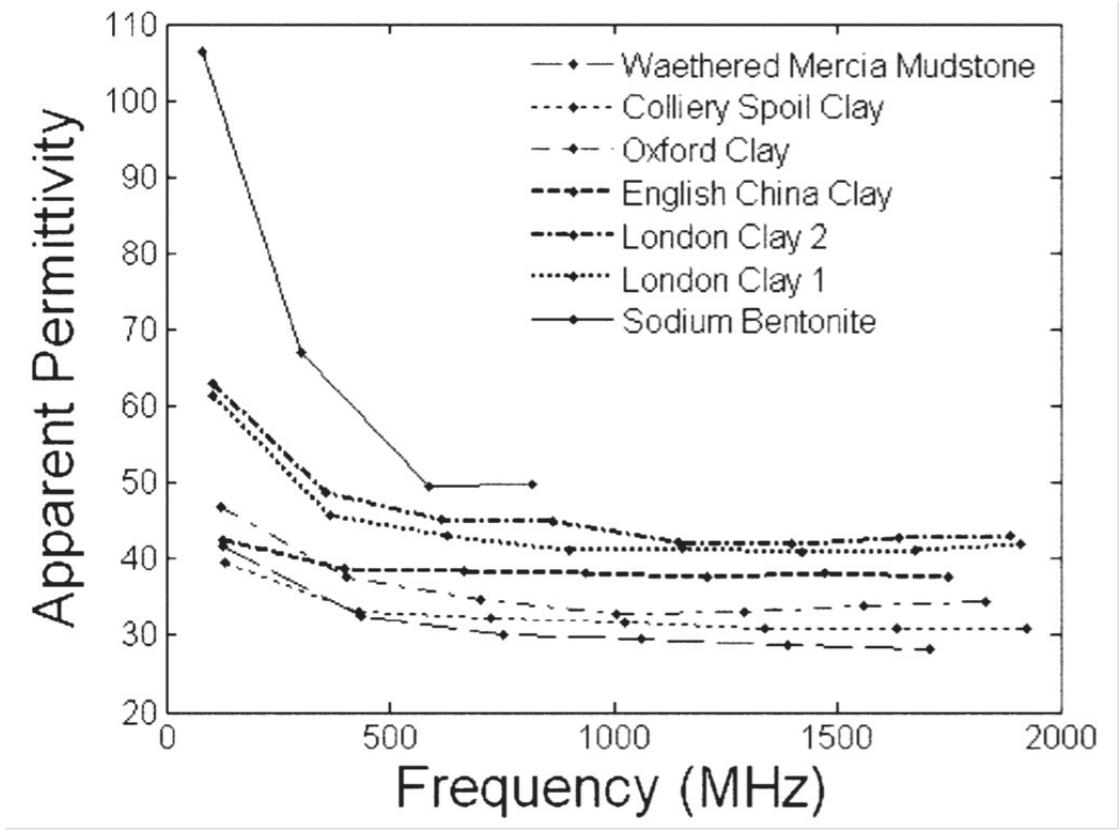



Figure 2.9 – Electromagnetic dispersion of different types of clay measured at saturation with a Vector Network Analyzer (after Thomas et al., 2008a).

Basic geotechnical parameters are known to be related to the EM soil properties. For example, the liquid limit[4] and plastic limit[5] are known to be related to the SSA (Mitchell and Soga, 2005). Thomas et al. (2010a) described in detail the relationships between geotechnical and EM properties for eleven fine-grained soils (i.e., with grain sizes < 425 μm) characterised by different liquid limits. The liquid limit of these soils was related to the frequency-dependent dielectric properties obtained by quarter-wavelength analysis using a Vector Network Analyzer (VNA; details on the methodology are reported in Thomas et al., 2008a). They found a linear relationship between the soil apparent

[4] Liquid limit: the moisture content at which a soil passes from the liquid to the plastic state (BS 1377-1, 1990).
[5] Plastic limit: the mositure content at which a soil becomes too dry to be in a plastic condition (BS 1377-1, 1990).

permittivity measured at high frequency and the liquid limit for the soils tested (Figure 2.10). In addition, the magnitude of the EM dispersion, defined as the absolute difference in apparent permittivity between 100 MHz and 1 GHz, was found to increase with the liquid limit (Figure 2.10) and with the linear shrinkage of the soil (Figure 2.11).

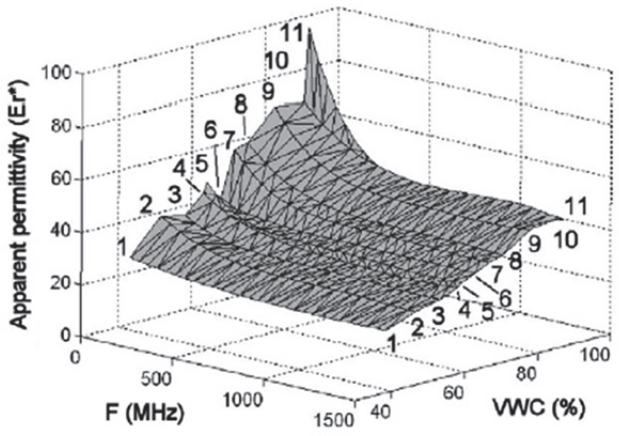



Figure 2.10 – Relationship between liquid limit and apparent permittivity for 11 fine-grained soils measured at a range of frequencies by a VNA (after Thomas et al., 2010a).

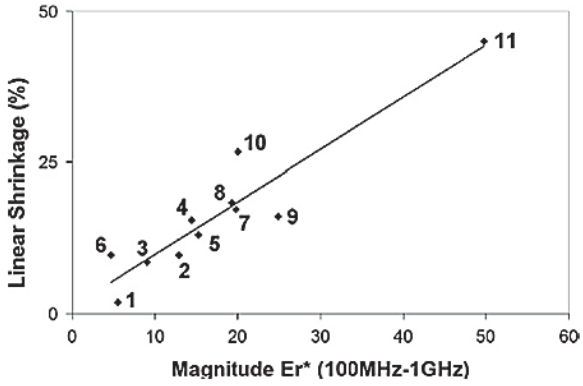



Figure 2.11 – Relationship between linear shrinkage and the magnitude of the EM dispersion for 11 fine-grained soils (after Thomas et al., 2010a).

In a second paper, Thomas et al. (2010b) investigated two selected fine-grained soils (i.e., London Clay and English China Clay) with dissimilar SSA over a range of water

contents. For both soils they found that the magnitude of the EM dispersion corrected for dry density was linearly related to the corrected volumetric water content (i.e., gravimetric water content, see Equation (2.12)) above the plastic limit, as shown in Figure 2.12. The dry density was known to affect the SSA of the soil particles (Saarenketo, 1998). In particular, the surface area of the soil particles per unit of volume decreases if the dry density decreases. Figure 2.12 confirms that the EM dispersion is a function of the SSA since for both the soils analysed, showing different SSA, the relationship between corrected apparent permittivity and gravimetric water content was linear.

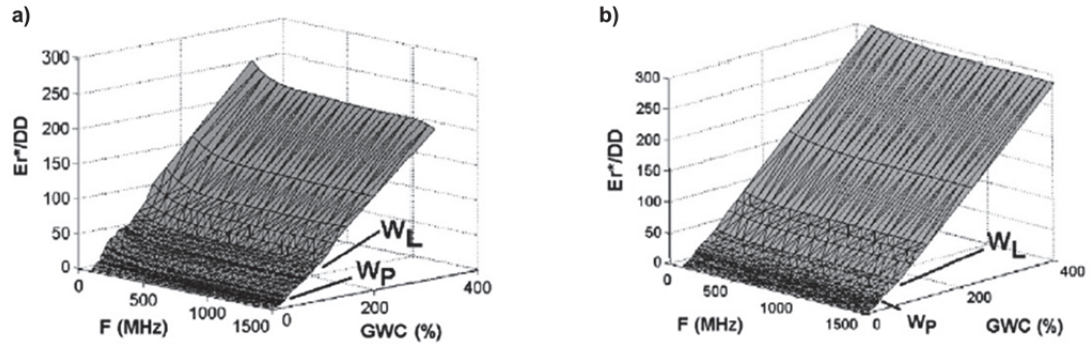



Figure 2.12 – Apparent permittivity corrected for dry density, in the gravimetric water content domain for (a) London Clay and (b) English China Clay (after Thomas et al., 2010b). [Note: $W_L$, $W_P$, DD are the liquid limit, plastic limit and dry density respectively.]

## 2.4.3. Prediction of the electromagnetic soil properties

### 2.4.3.1. Dielectric mixing models

Because of the relationships between geotechnical and EM soil properties, several models have been developed in order to estimate EM soil parameters from commonly available data, such as the particle size distribution. Due to the strong relationship between soil permittivity and volumetric water content, models have been widely used in order to

estimate the soil water from measured permittivity values. van Dam (2005) reported a review of 22 methods for predicting the soil dielectric properties. They included theoretical (e.g., De Loor, 1968), empirical (e.g., Topp et al., 1980), and semi-empirical (e.g., Dobson et al., 1985) methods. The semi-empirical models are normally based on theoretical physical models, but they also contain empirical fitting parameters. For example, Dobson et al. (1985) identified a volumetric mixing model able to predict the real and imaginary parts of the soil complex permittivity in the frequency range between 1.4 GHz and 18 GHz. Peplinski et al. (1995a and b) extended the Dobson model to include the frequency range of 0.3 GHz and 1.3 GHz. These models are called dielectric mixing models because they predict the bulk soil permittivity from the sum of the permittivity of the different soil components (i.e., air, solids, water). Water can be additionally separated in bound and free fractions, each with its volume and dielectric properties (Dobson et al., 1985). The Dobson/Peplinski model only requires the percentage of sand, clay and the soil density to be known and therefore, when this information is available, it can be used effectively in place of empirical models.

A problem with all these models is that they were built from a relatively limited soil dataset and therefore they might suffer from higher inaccuracies if applied to soils dissimilar to those used to build the models. Following this argument, Mironov et al. (2009) described a semi-empirical model based on a very large soil dataset reported by Curtis et al. (1995). Mironov et al. (2009) reported improved results compared to the Dobson/Peplinski model with the advantage of only requiring the percentage of clay and volumetric water content as inputs. In fact, by including the percentage of sand in their model, Mironov et al. (2009) did not obtain improved predictions of the soil EM properties.

The Dobson/Peplinski and the Mironov models offer key advantages over other models because they have a physical foundation and they are relatively easy to implement

(van Dam, 2005). However, with the wide choice offered by the literature it is difficult to select the right model for a specific application. For certain circumstances, depending on the soil studied and the desired level of accuracy, it might be preferable to conduct a soil-type specific water-permittivity calibration.

### 2.4.3.2. GPR soil suitability

As mentioned in section 2.4.2 and described in detail in Thomas et al. (2008a) and in Thomas et al. (2010a and b), in addition to the particle size distribution, there are other important relationships between geotechnical and geophysical properties that could be exploited for predictive purposes. For example, as shown in section 2.4.2 the magnitude of the EM dispersion of a number of fine-grained soils has been shown to be proportional to their liquid limit, SSA and linear shrinkage. To the GPR practitioners, it is valuable to have prior information on the ground conditions before carrying out a survey, since this could improve the planning and outcome of the survey. However, the information of the EM soil properties is sparse and incomplete. Thus, the development of predictive systems based on commonly recorded soil properties is highly desirable (Rogers et al., 2009).

GPR soil suitability maps of the United States, based on physical and chemical soil properties, have been created by the United States Department of Agriculture-Natural Resources Conservation Service (USDA-NRCS) in recent years (Doolittle and Collins, 1995; Doolittle et al., 2007; Doolittle et al., 2010). These maps offer users unfamiliar with soils an indication of the suitability of soils for GPR within broadly defined areas (scale 1:250,000). Larger scale maps of 1:12,000 to 1:63,360 were produced for single States and can be accessed at http://soils.usda.gov/ (Doolittle et al., 2010). The parameters considered in producing these maps were: soil taxonomic classification (based on the Soil Taxonomy classification system, Soil Survey Staff, 1999), clay content, pore water EC, sodium

absorption ratio, calcium carbonate and sulphate content. The main purpose for producing these maps was to facilitate the use of GPR as a tool for soil investigation (e.g., identification of soil horizons and lithologic layers). Different potentials were associated with soils, with the higher potentials identifying soils presenting little attenuation and therefore well suited to GPR, such as sandy soils. At the other extreme there are saline (saturated extract $EC \geq 4$ dS/m), sodic (sodium absorption ratio $\geq 13$) and clayey (clay content > 60 %) soils, which are classified 'unsuited' to GPR because of their high attenuation (Doolittle et al., 2010).

One issue with these maps is that they do not generally include information on urban land since they were developed mainly for soil survey investigations and they were based on soil databases that did not include comprehensive data from urban areas. However, in urban areas, geotechnical information is often available that could be exploited to produce GPR soil suitability maps via construction related site investigation. This would have obvious advantages for improving planning and interpretation of utility location surveys.

An attempt to create a predictive system for geophysical soil properties in urban areas was carried out in the UK by the Mapping The Underworld project (http://www.mappingtheunderworld.ac.uk/), which was aiming to improve the detection of underground utilities by combining different sensing techniques (for more information on the techniques see Metje et al., 2007). The geological and geotechnical databases held by the British Geological Survey (BGS) is a potential source of soil information for predicting geophysical soil properties (Thomas et al., 2008b; Rogers et al., 2008; Rogers et al., 2009). Even if not used to directly predict the values of the geophysical soil properties, the BGS databases could be used effectively to better plan shallow geophysical surveys, and therefore to minimise the risks of survey failure (Jordan, 2009).

The Mapping the Underworld initiated the development of a Knowledge Based System (Foo et al., 2011), which includes inputs from several sources (Figure 2.13) in order to improve the ability of detection of underground utilities by multi-sensor devices.

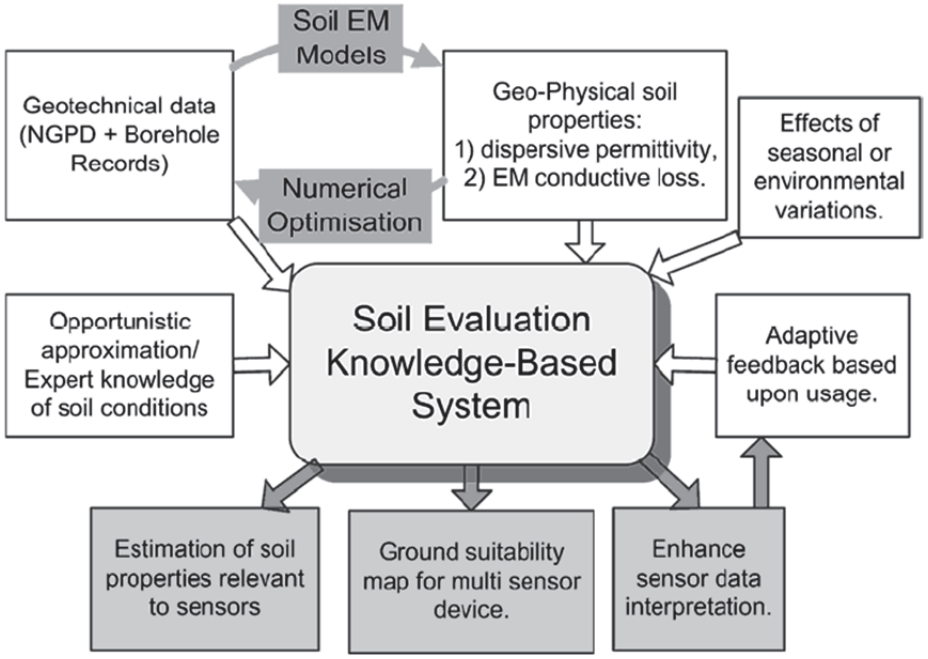



Figure 2.13 – Knowledge Based System (KBS) for multi-sensor utility detection (after Foo et al., 2011).

It is important to note that among the inputs included in the KBS there are the seasonal variations in environmental variables (e.g., rainfall, temperature), which were not considered in the production of GPR soil suitability maps by the USDA-NRSC. However, Doolittle et al. (1995) reported results from a field study aimed at understanding the soil-water table fluctuations over the seasons and established that these variations affect the GPR interpretations of soil properties. In addition, as part of the European funded ORFEUS project (Optimised Radar to Find Every Utility in the Street, http://www.orfeus-project.eu/), whose aim was to advance the state–of-the-art GPR performance, field studies have been conducted in order to establish the seasonal variability of the EM properties of different

soils. It was found that these properties can change by more than 100 % during the year, within the first metre below the ground surface (Slob et al., 2009; Rogers et al., 2009). Other studies involving electrical resistivity tomography showed large variations of BEC over the seasons within the shallow subsurface (e.g., Seger et al., 2010; Musgrave and Binley, 2011). This demonstrates the need to consider the seasonal variation of the soil EM properties to improve their prediction.

# 2.5. SOIL SENSING TECHNIQUES

## 2.5.1. Soil water measurement techniques

The only direct way of measuring the soil water content is the gravimetric method, which consists in weighing the sample before and after drying it in an oven at 105 °C until the mass remains constant (e.g., for 24 hours). This is the standard and most reliable method for measuring the soil water content in the laboratory (BS 1377-2, 1990). However, it is time consuming and cannot be applied in field monitoring. For field use, alternative techniques have been developed that actually measure surrogate parameters from which the water content is inferred by means of known relationships (IAEA, 2008). These techniques generally provide a quick and non-destructive way of estimating the soil water, making it possible to employ them directly in the field for real-time estimation and long-term monitoring. However, there are a series of disadvantages in applying such surrogate methods. Additional sources of error are expected, because of the relationship between the surrogate parameter and the soil water (i.e., calibration) is always affected by factors other than the soil water. In addition, the calibration is generally valid for a certain range of water contents and it might become less accurate outside this range. Another problem lies within the concept of the representative elemental volume (REV), which is the minimum soil

sample volume below which the variability of a soil property increases sharply (IAEA, 2008). It is well known that the soil generally shows a high spatial variability for most of its properties. The size of the REV cannot be generalised because it is dependent upon the soil type and on the property of interest. Many of the surrogate techniques measure samples that are smaller than the REV, providing larger variability that is in fact not relevant at the scale required by most applications.

The EM methods (e.g., capacitance methods, TDR, GPR) estimate the soil water from a measurement of the soil permittivity. However, they are affected by other parameters such as the soil salinity, temperature and the presence of magnetic minerals. They are also influenced by the soil bulk density and by the measurement frequency, which in turn depends on the instrument used and on the dispersive nature of the soil. It is important to note that the final estimation of the water content also depends on the quality of the calibration that relates the permittivity to the volumetric water content.

Table 2.3 shows a summary of some of the available surrogate techniques, with a brief description, as reported by IAEA (2008). As it can be seen there is a wide range of methods that can be used to estimate the soil water. Among these, the neutron water probe was the most widely used technique in the 1970s and 1980s, due to the high accuracy achieved in the measurement of the volumetric water content (< 1 %). The main problem associated with this method lies with the potential radiation hazard caused by the use of a radioactive source. It also becomes imprecise near the soil surface due to difficulties of measurement (Evett et al., 1993) and cannot be multiplexed. However, neutron probes are still convenient for soil deep profiling (Robinson et al., 2003a) and can be used as a reference technique in order to validate results from alternative sensors.

Following the seminal work of Topp et al. (1980) on TDR (see section 2.5.2.1), the EM techniques grew in popularity. It is difficult to compare the different EM methods since

they operate at different frequencies and are based on different principles. However, attempts to characterise these techniques have been made. For example, Jones et al. (2005) tested different EM methods in reference liquids and proposed a methodology for comparison. In a companion paper, Blonquist et al. (2005) applied this method to compare the permittivity measurement ability of seven different EM sensors (Figure 2.14) in reference liquids and established that they generally provide similar performance. However, the systems working at low frequency (< 100 MHz) were generally more sensitive to the EC of the solutions. Other authors studied the impact of the measurement frequency on the estimation of permittivity and suggested that systems working at higher frequency (> 500 MHz) should considerably improve the estimation of the soil water content from permittivity (Kelleners et al., 2005; Chung and Lin, 2009).

Table 2.3 – Surrogate measures used by different soil water sensors (after IAEA, 2008).

| Method | Surrogate Measurement | Explanation |
|---|---|---|
| Neutron moisture meter | Count of slow neutrons around a source of fast neutrons | A radioactive source emits fast neutrons (5 MeV), which lose energy as they collide with other atoms, in particular hydrogen. The surrogate is the concentration of slow neutrons. Since the only rapidly changing source of hydrogen in the soil is water, $\theta_v$ can be calibrated vs. the count of slow neutrons. |
| Thermal sensors | Heat conductivity or heat capacity of the soil | A pulse of heat is generated and the subsequent rise or fall in temperature of adjacent soil is measured over time. Soil is a poor conductor of heat, and water a good one, so the amount of heat or rate of heat transmission is closely related to $\theta_v$. |
| Time domain reflectometer (TDR) | Travel time of an electromagnetic pulse | A fast rise time electromagnetic pulse is injected into a waveguide inserted into or buried in the soil. The time required for the pulse to travel along the metal rods of the waveguide is determined by the bulk electrical permittivity of the soil. The $\theta_v$ is a major factor influencing the bulk permittivity (BEC). True TDR involves capture of a waveform and analysis to find the travel time of the highest frequency part of the pulse. |
| Campbell FDR | Repetition time for a fast rise time electromagnetic pulse | See TDR sensors; same, except reliance on reflected pulse reaching a set voltage rather than waveform analysis causes the method to be more influenced by BEC and temperature. |
| Capacitive sensors | Frequency of an oscillating circuit | An oscillating current is induced in a circuit, part of which is a capacitor that is arranged so that the soil becomes part of the dielectric medium affected by the electromagnetic field between the capacitor's electrodes. The $\theta_v$ influences the electrical permittivity of the soil, which in turn affects the capacitance, causing the frequency of oscillation to shift. |
| Conductivity sensors (e.g., granular matrix sensors and gypsum blocks) | Electrical conductivity of a porous medium in contact with the soil | An alternating current voltage is placed on two electrodes in a porous material in contact with the soil, and the amount of current is a measure of the conductivity and amount of water in the porous material between the electrodes. These are used for estimation of soil water tension (suction), not $\theta_v$. |
| Tensiometers | Matric and gravitational soil water potential components | Capillary forces retaining water in the soil pores are connected through the soil water to water in a porous cup connected to a tube filled with water. This generates a negative pressure within the tube, which can be measured with a vacuum gauge. These are used for estimation of soil water tension (suction), not $\theta_v$. |

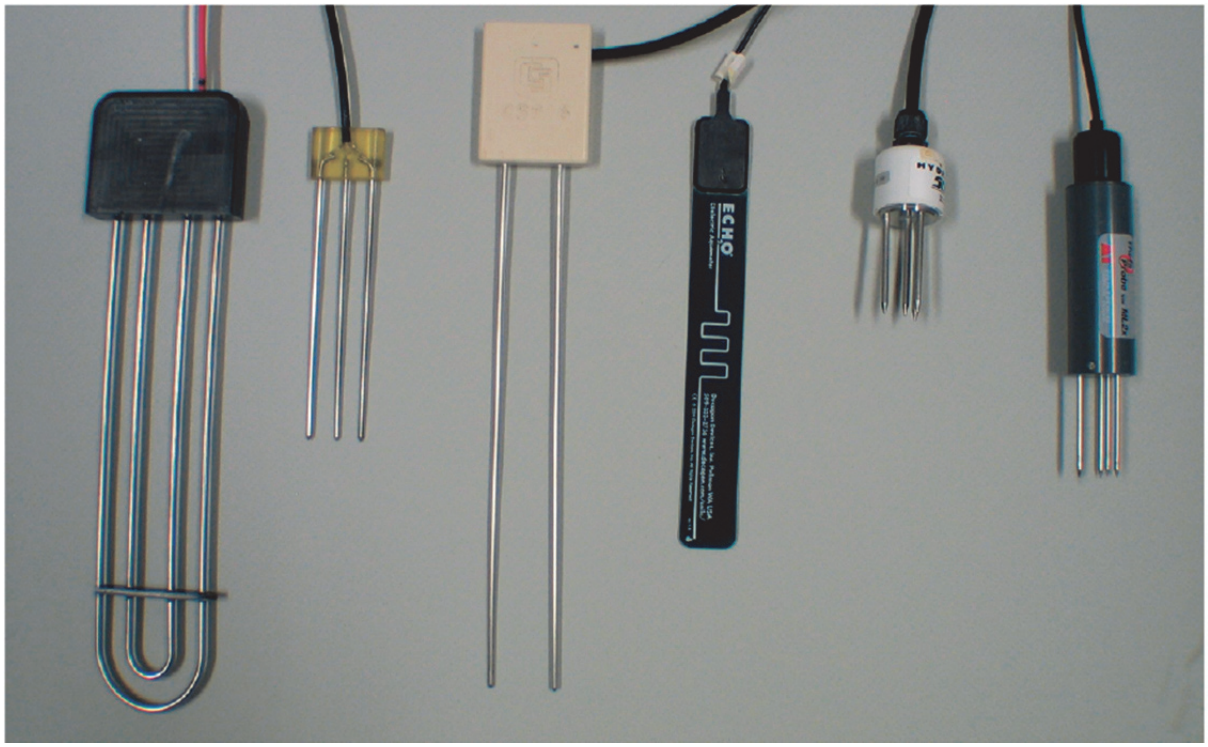



Figure 2.14 – Example of EM probes used for soil water determinations. From left to right: Acclima Digital TDT Sensor, three-rod TDR probe, CS616, $ECH_2O$ Probe, Hydra Probe, and Theta Probe (after Blonquist et al., 2005).

Among the EM techniques, TDR is able to achieve good accuracy (< 2 %) for volumetric water content estimation (Jones et al., 2002) and is less affected by temperature and salinity compared to the capacitance sensors, because it works at higher frequencies (Evett and Parkin, 2005). TDR works at a frequency bandwidth similar to the common GPR commercial units (approximately 10 MHz – 1 GHz), and it provides the possibility of measuring both permittivity and BEC. It can therefore be used effectively for *in situ* soil geophysical measurements involving GPR (Huisman et al., 2003a).

GPR has relatively recently been used to estimate the soil water content (e.g., Weiler et al., 1998; Huisman et al., 2001; Huisman et al., 2003b; Grote et al., 2003). The reason for this is mainly due to the more difficult behaviour of the GPR unconfined signal and also due to the difficulty of interpreting the GPR data. An excellent review on the use

of GPR for measuring the soil water is provided by Huisman et al., (2003a). There are different ways of using GPR for this purpose and they are dependent on the type of GPR used (see section 2.5.4 for more details). In the case of buried utilities, it is sufficient to detect a clear target in order to estimate the average soil permittivity (and therefore water content) above the target. This can be very useful to estimate the soil conditions during surveys, but obviously clear visible targets are required.

GPR and TDR work on similar principles and therefore their combined use could be beneficial in order to validate the measurements of soil water at a catchment scale provided by GPR with point measurements provided by TDR. Both GPR and TDR can be used to supply ground truth conditions when the soil water is estimated by microwave remote sensing techniques at a larger scale (Topp, 2003).

## 2.5.2. Time-Domain Reflectometry (TDR)

### 2.5.2.1. Introduction

TDR is a technique normally used to locate faults in transmission lines (Jones et al., 2002). A short rise time voltage pulse (≈ 150 ps) is sent from a TDR source generator (also called cable tester). In response to a change in impedance along the transmission line, caused for instance by a damaged portion in the line, a reflection is generated and sent back to the TDR source, where the voltage of the reflected signals is measured. From the time taken by the signal to travel through the line and be reflected back it is possible to determine the location of the fault.

Since the Second World War the TDR technique has been increasingly used to measure the soil water content (Robinson et al., 2003a). For instance, Hoekstra and Delaney (1974) used coaxial transmission lines filled with soil and found that both clay and sand exhibited EM dispersion that could be described by the Debye model. The 1970s saw the

earliest application of parallel transmission lines with soils, and the work carried out by Topp, Davis and Annan culminated in a seminal paper (Topp et al., 1980) that can be considered a turning point in the application of TDR in soil science.

In their study, Topp et al. (1980) used TDR in order to determine the volumetric water content of different soils with different particle size distributions and organic contents. They found a general empirical relationship that could be used to relate the permittivity measured by TDR to the soil volumetric water content, successively known as the Topp model and given by Equation (2.14) (Topp et al., 1980).

$$VWC = -5.3 \text{ x } 10^{-2} + 2.92 \text{ x } 10^{-1}\varepsilon_a - 5.5 \text{ x } 10^{-4}\varepsilon_a^2 + 4.3 \text{ x } 10^{-6}\varepsilon_a^3 \qquad (2.14)$$

where *VWC* is the soil volumetric water content ($m^3/m^3$) and $\varepsilon_a$ is the soil apparent permittivity measured by TDR.

This empirical model is widely used in the literature, but it does not apply well to dispersive soils, such as organic and clayey soils, whose apparent permittivity varies with frequency (Roth et al., 1990; Herkelrath et al., 1991; Jones et al., 2002). Equation (2.14) was mainly used for a range of agricultural soils, for volumetric water contents not exceeding 50 %. It has been widely used as a comparative reference when applying new models linking apparent permittivity to water content (e.g., Roth et al., 1990; Dirksen and Dasberg, 1993; Malicki et al., 1996). However, for many applications not involving 'difficult' soils Equation (2.14) can still provide an easy way of measuring the soil water content using TDR.

Since its use in the early 1980s many other studies have been completed, which have advanced the TDR methodology further and helped to overcome the initial general scepticism of the scientific community (Topp et al., 1982a and b; Topp et al., 2003).

Advances in technology, in particular the advent of digital cable testers and the development of data logger systems and electronically operated multiplexers have made the TDR a commercially tempting solution to monitor the soil water in the field (Topp et al., 2003).

At the present time TDR has become one of the standard techniques to measure the soil water content in the field (Robinson et al., 2003a; IAEA, 2008; Herkelrath et al., 1991; Rajkai and Ryden, 1992; Stangl et al., 2009). TDR offers good reliability in the estimation of the soil volumetric water content, with accuracies of ± 1-2 % (Jones et al., 2002; Ledieu et al., 1986), simple measurements, minimal calibration requirements (depending on the soil type and the desired accuracy) and the possibility of continuous measurements through automation and multiplexing (Baker and Allmaras, 1990; Heimovaara and Bouten, 1990; Herkelrath et al., 1991; Logsdon, 2006).

An additional advantage of the TDR technique is that it can measure the soil BEC in addition to the soil apparent permittivity in the same soil sample, making it a convenient method for soil science applications (Robinson et al., 2003a; Jones et al., 2002). Dalton et al. (1984) were the first to evaluate the possibility of measuring simultaneously both apparent permittivity and BEC by TDR and developed a method of waveform analysis for this purpose. Subsequently alternative methods have been proposed (e.g., Yanuka et al., 1988; Topp et al., 1988; Zegelin et al., 1989). However, Nadler et al. (1991) rediscovered a previous method proposed by Giese and Tiemann (1975) and obtained from the thin sample theory, which provided more reliable estimates than the other methods (see also Topp et al., 2000; Lin et al., 2007). The Giese-Tiemann method is now considered the standard method for calculating BEC from TDR measurements (Lin et al., 2007; Huisman et al., 2008).

The Giese-Tiemann method was improved by Heimovaara et al. (1995), who proposed that the load resistance (i.e., soil sample resistance) measured by TDR was the sum of the sample resistance and the additional resistance due to the cables and connectors. The

inclusion of these extra resistances, named $R_{cable}$ (Ω), improved the accuracy in the determination of the soil BEC, especially for BEC above 0.2 S/m. Reece (1998) suggested an easy method to directly measure the cable resistance, but Huisman et al. (1999) found some discrepancies between measured and fitted parameters (i.e., probe constant, $K_p$ (1/m) and cable resistance, $R_{cable}$ (Ω); see section 3.2.8). As a consequence, researchers reconsidered the idea of a series resistor model, for example Castiglione and Shouse (2003) and (2006), who proposed an alternative method for calibrating TDR probes. However, recent findings by Lin et al. (2007) and (2008) established that the series resistor model suggested by Heimovaara et al. (1995) is actually physically sound and the discrepancies between theory and measurements were caused by issues related to the cable tester. This resulted in the proposal of new methodologies for calibrating the probes in order to increase the accuracy of BEC measurements by TDR (Huisman et al., 2008; Bechtold et al., 2010).

### 2.5.2.2. Principles of Time-Domain Reflectometry

**Measurement of the apparent permittivity**

TDR involves injecting a short electromagnetic pulse into a coaxial transmission line consisting of a coaxial cable and a multi-rod probe and measures the reflected signals from the start and the end of the rods (Figure 2.15). Reflections occur in correspondence of changes in impedance, according to Equation (2.15) (Yanuka et al., 1988).

$$\text{Reflection coefficient, } \rho = \frac{Z_s - Z_{out}}{Z_s + Z_{out}} \qquad (2.15)$$

where $Z_{out}$ is the output impedance (Ω) of the TDR unit and $Z_s$ is the impedance of the soil sample.

The TDR output consists of a waveform (also called trace) showing the measured reflection coefficient *versus* time or apparent distance (Figure 2.15). Further details on the term 'apparent' are given later in this section.

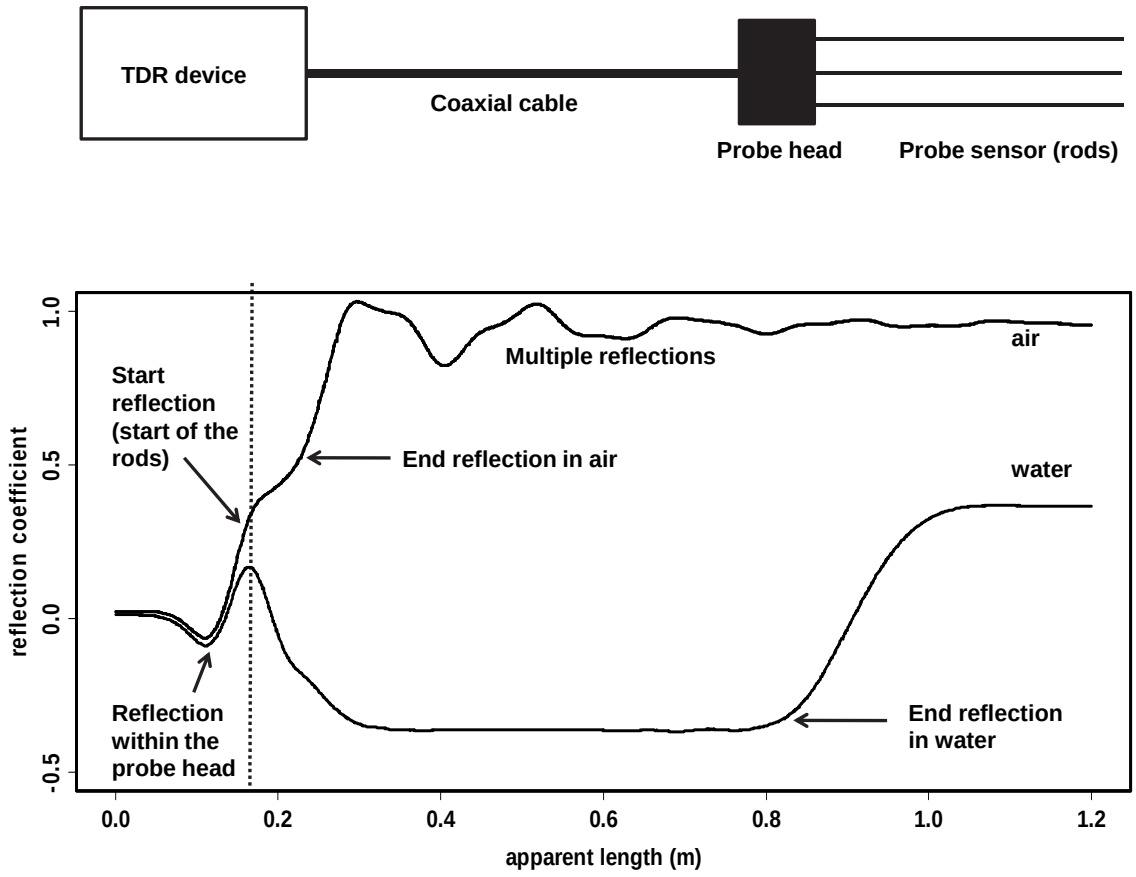



Figure 2.15 – Schematic of the TDR arrangement and two examples of TDR waveforms (i.e., reflection coefficient *versus* apparent length) taken in air and water.

The frequency dependent propagation velocity, *v(f)*, of the electromagnetic signals is described by Equation (2.16) (Von Hippel, 1954).

$$v(f) = \frac{c}{\sqrt{\varepsilon'(f)\mu_r \frac{1+\sqrt{1+tan^2\delta}}{2}}} \tag{2.16}$$

where $c$ is the speed of light in free space ($3 \times 10^8$ m/s), $f$ is the frequency of the electromagnetic wave (Hz), $\varepsilon'(f)$ is the real part of the complex permittivity, $\mu_r$ is the relative magnetic permeability and $\tan \delta$, given by Equation (2.4), is the loss tangent representing the ratio of the imaginary to the real part of the complex dielectric permittivity.

With the exception of some igneous rocks and soils rich in ferromagnetic materials (Cassidy, 2007), the relative magnetic permeability is assumed to be equal to 1 (Huisman et al., 2003a). In low conductive soils with modest clay content, the loss tangent becomes negligible in the TDR frequency range (approximately 10 MHz – 1 GHz) and Equation (2.16) can be simplified to Equation (2.17).

$$v(f) = \frac{c}{\sqrt{\varepsilon_a}} \tag{2.17}$$

where $\varepsilon_a$ is the apparent permittivity measured by TDR and described by Equation (2.18) (Robinson et al., 2003a).

$$\varepsilon_a = \frac{\varepsilon'(f)\mu_r}{2}\left(1 + \sqrt{1 + \left(\frac{\varepsilon_p''(f) + \frac{\sigma_{dc}}{2\pi f \varepsilon_0}}{\varepsilon'(f)}\right)^2}\right) \tag{2.18}$$

The term ‘apparent’ is used to identify the permittivity measured by TDR, which is approximated to the real permittivity for practical applications but also comprises the losses due to conductivity and the dipolar losses caused by the bound water present in the soil (Topp et al., 2000). The apparent permittivity is also affected by cable length, probe design, soil bulk density and particle size distribution as shown by, among others, Lin (2003) and Chung and Lin (2009).

The speed of the signal propagation along the probe rods (transmitted and reflected) is given by Equation (2.19) (Robinson et al., 2003a).

$$v(f) = \frac{2L_{cal}}{t} \tag{2.19}$$

where $L_{cal}$ is the calibrated length (m) of the rods. $L_{cal}$ is obtained after measurements in reference materials with known permittivity and is very similar to the physical length of the rods (see section 3.2.7). Equation (2.17) can therefore be rearranged into Equation (2.20) (Robinson et al., 2003a).

$$\varepsilon_a = \left(\frac{ct}{2L_{cal}}\right)^2 \tag{2.20}$$

The distance between the two points corresponding to the reflections occurring at the start and at the end of the probe rods ($ct_1/2 - ct_2/2$) is called apparent distance, $L_{app}$ (m), because a propagation velocity factor (ratio between the actual signal velocity and the speed of light in free space) is assumed equal to 1 for convenience in the analysis. Equation (2.21) is thus used to determine the apparent permittivity measured by TDR (Robinson et al., 2003a).

$$\varepsilon_a = \left(\frac{L_{app}}{L_{cal}}\right)^2 \tag{2.21}$$

**Measurement of the bulk electrical conductivity (BEC)**

The signal attenuation caused by the electrical conductivity of the material being tested is a potential problem for apparent permittivity measurements because it can cause the end reflection to become non-detectable. This reduction of the reflection coefficient at long apparent distances can be exploited to measure the soil BEC.

According to the method proposed by Giese and Tiemann (1975) the resistance of the sample, load resistance $R_L$ (Ω), can be determined using Equation (2.22).

$$R_L = Z_{out}\frac{1+\rho_\infty}{1-\rho_\infty} \tag{2.22}$$

where $Z_{out}$ is the output impedance of the TDR device (≈ 50 Ω) and $\rho_\infty$ is the reflection coefficient at long distances, i.e., where the multiple reflections have levelled out and the high frequencies have attenuated (Figure 2.16).

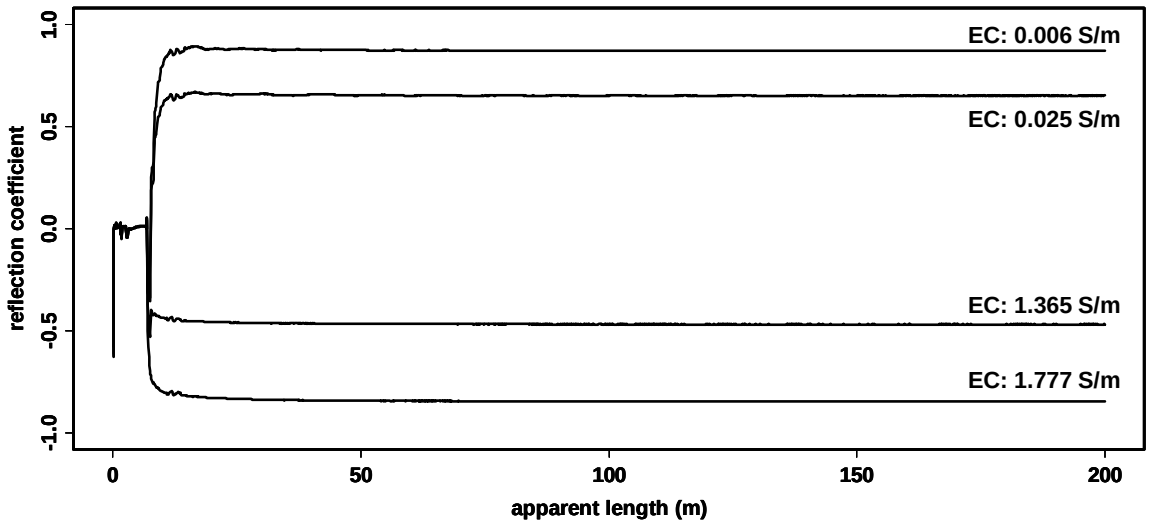



Figure 2.16 – Steady-state reflection coefficient at long apparent distances measured by TDR in KCl solutions with different EC values.

Lin et al. (2008) demonstrated the necessity of correcting the reflection coefficient at long distances using Equation (2.23) to account for deviations from optimal open-circuit measurements. For example, these are known to vary between 0.96 and 1.00 for the TDR100 cable tester manufactured by Campbell Scientific, Logan (UT).

$$\rho_{corr} = \frac{2(\rho_{meas} + 1)}{\rho_{open} + 1} - 1 \tag{2.23}$$

where $\rho_{open}$ is the reflection coefficient of an open-circuit measurement, $\rho_{meas}$ is the measured reflection coefficient at long distances and $\rho_{corr}$ is the corrected reflection coefficient to be used in Equation (2.22).

As mentioned in section 2.5.2.1, Heimovaara et al. (1995) proposed a series resistor model, which included the additional resistance parameters due to cables, connectors and multiplexers in the calculation of the sample BEC. According to this model, the soil BEC is calculated by Equation (2.24) (Huisman et al., 2008).

$$BEC = \frac{K_P}{R_L - (DR_c + R_0)} \tag{2.24}$$

where $D$ is the cable length (m), $R_c$ is the cable resistance (Ω/m), $R_0$ are the extra resistances (Ω) caused by the TDR device, connectors, multiplexers and probe head, and $K_p$ is the probe constant (1/m), which is a geometrical factor defined by Equation (2.25) (Huisman et al., 2008).

$$K_p = \frac{\varepsilon_0 c Z_0}{L} \tag{2.25}$$

where $Z_0$ is the characteristic impedance of the probe (Ω) and $L$ is the physical length of the probe rods (m).

After calibrating $K_p$, $R_c$ and $R_0$ in reference solutions with different electrical conductivities (see section 3.2.8), it is possible to determine the sample BEC by measuring $\rho_{meas}$ from the TDR waveforms and applying Equations (2.23), (2.22) and (2.24) in sequence (Huisman et al., 2008; Bechtold et al., 2010).

### 2.5.2.3. Limitations of Time-Domain Reflectometry

Due to the extensive research carried out in the past thirty years, TDR has become a mature technology in soil science applications (Topp, 2003). However, it presents limitations that must be understood for it to be used correctly.

In their work, Topp et al. (1980) assumed that $\varepsilon'' << \varepsilon'$, which is a general approximation but it is not valid in every circumstance, such as in soils with high BEC and in clayey and organic soils (e.g., Topp et al., 2000). For these soils the calibration between apparent permittivity and volumetric water content becomes more complex, since the losses become non-negligible, and in this case TDR can provide soil water estimations with variable accuracy. This is an important issue to be considered when applying the TDR technique to estimate the soil water content.

Wyseure et al. (1997) showed that the TDR consistently overestimated the volumetric water content in soils with BEC > 0.2 S/m. Bittelli et al. (2008) also showed similar results, with volumetric water contents overestimated by up to 20 % in soils with BEC > 0.25 S/m. Several authors proposed methodologies for accounting for the imaginary part of the permittivity. Correction procedures based on the separation of $\varepsilon'$ and $\varepsilon''$ from $\varepsilon_a$

were suggested, for example, by Topp et al. (2000) and Bittelli et al. (2008). These corrections involved the determination of an effective conductivity comprising both the relaxation and conductivity losses and the subtraction of this quantity from the measured $\varepsilon_a$ in order to obtain $\varepsilon'$, which could then be more correctly related to the volumetric water content. Another approach was followed by Evett et al. (2005), who proposed an empirical calibration model relating the volumetric water content to the apparent permittivity and the BEC.

However, all these methods depend on the estimation of an effective frequency. This effective frequency can be defined in several ways. The most common definition describes it as the frequency containing the majority of the energy of the signal (Robinson et al., 2003a). A common method for estimating the effective frequency is based on the determination of the rise time at the end of the TDR probe (e.g., Topp et al., 2000; Robinson et al., 2005). The rise time ($t_r$) is generally calculated from the 10 % to 90 % increase of the reflection coefficient at the end of the probe (Equation (2.26) and Figure 2.17) (Robinson et al., 2003a).

$$f_{eff} = \frac{ln\left(\frac{0.9}{0.1}\right)}{2\pi t_r} \tag{2.26}$$

However, as pointed out by Evett et al. (2005), the estimation of the effective frequency by Equation (2.26) and using tangent lines (see Figure 2.17) is not easy in practice, as multiple reflections at the end of the probe could make it difficult to define the maximum value.

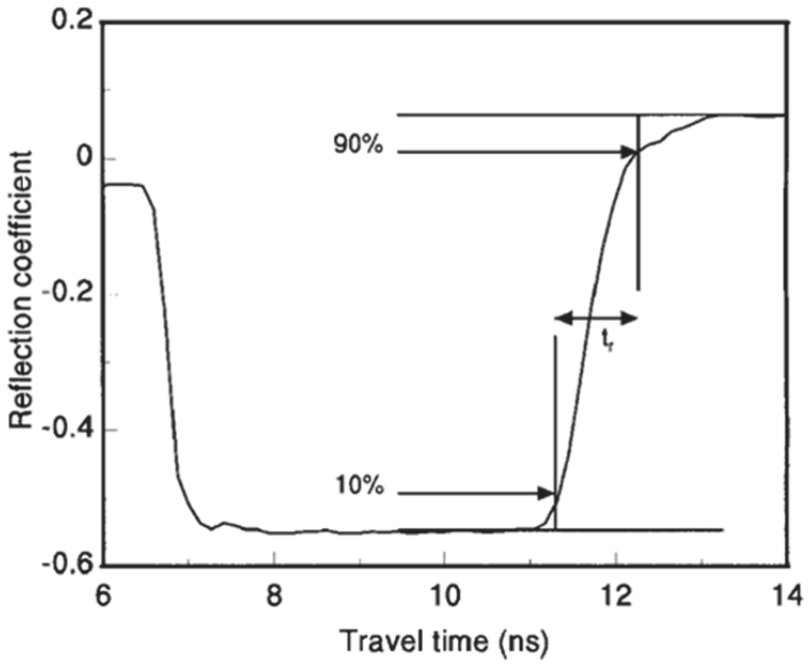



Figure 2.17 – Measurement of the rise time ($t_r$) from the 10 % to 90 % increase in the reflection coefficient at the end of the TDR probe (after Robinson et al., 2005).

Another way of estimating the effective frequency is by fitting simulated waveforms with frequency dependent parameters (i.e., obtained by using dielectric mixing models or by using Debye-type equations) to the measured waveforms (e.g., Lin, 2003). In this case, the effective frequency is selected when the calculated apparent permittivity by Equation (2.18) matches the measured value. However, simulating TDR waveforms is not straightforward since it requires each individual section of the transmission line to be modelled (Lin, 2003), and this is difficult in practical applications involving multiplexers or other attachments.

In addition, the use of the effective frequency in order to compensate for relaxation and conductive losses was shown to be theoretically unfeasible by Chung and Lin (2009). In their work, they used simulated TDR waveforms to study the effects of cable length, EC and relaxation on the apparent permittivity and showed that changes in these parameters have divergent effects on the relationship between apparent permittivity and effective frequency. In other words, there was no consistent trend between the change in apparent

permittivity and effective frequency as the influencing factors varied and therefore using the effective frequency to account for those factors seems incorrect.

When measuring soil water by TDR, the same water content may result in different apparent permittivity due to differences in EC, cable length and EM dispersion (Chung and Lin, 2009). This happens because the imaginary permittivity can become non-negligible when varying these factors. It is important to note that long cables, poor quality connectors and multiplexers significantly affect the TDR waveforms. Among other authors, the experimental work by Logsdon (2000; 2005 and 2006) showed that TDR readings are affected by cable length and the presence of attachments (e.g., multiplexers, balancing transformers). Each attachment causes further signal attenuation and impedance mismatches that produce unwanted reflections and noise. The attenuation causes the reflection coefficient to be reduced and the waveforms to be rounded, which can complicate their interpretation (i.e., identification of the start and end reflections). The use of attachments and long cables causes the pulse rise time to increase and the frequency bandwidth to decrease, by acting as a low-pass filter (Heimovaara, 1993). In dispersive soils, this is a problem since the losses due to relaxation and conductivity become more important in the low frequency range (Kelleners et al., 2005).

In addition, in highly conductive soils, the signal can be attenuated to the point that the end reflection at the end of the probe becomes undetectable (Jones et al., 2002, see Figure 2.18). In these cases TDR cannot provide an estimation of the apparent permittivity and therefore water content.

As for the other EM sensors, the reliability of TDR also depends on the correct installation of the probes in the soil. In particular, the formation of air gaps close to the metal rods can significantly affect the TDR measurements (Topp and Davis, 1985; Ferre' et al, 1996).

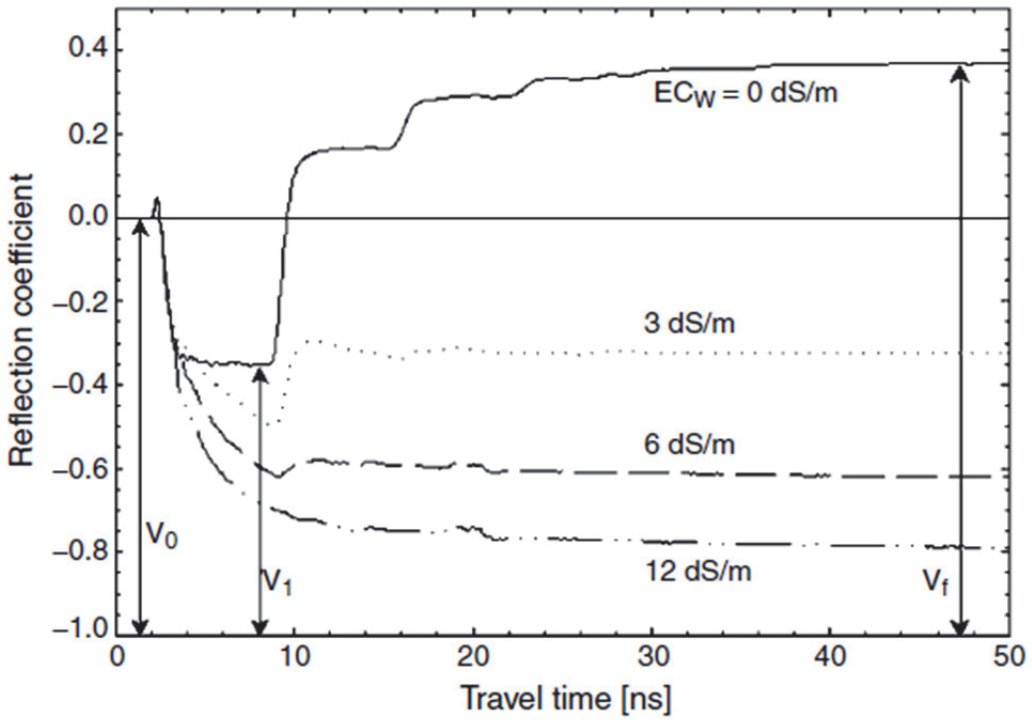



Figure 2.18 – TDR waveforms taken in solutions with different EC (after Jones et al., 2002).

It is apparent from the above discussion that the TDR technology has important limitations. Perhaps the most important drawback results from its undefined measurement frequency. TDR provides a single value of apparent permittivity and therefore it does not give information on the dispersive nature of the soil (Thomas et al., 2008a). In dispersive soils, frequency-domain techniques such as Vector Network Analyzer (VNA) are more informative. However, VNAs are generally more expensive than TDR and require very careful calibrations. Specific probe designs, such that the impedance mismatches between different components is minimised, have been proposed by different studies in the past (Heimovaara, 1994; Heimovaara et al., 1996; Thomas et al., 2008a). In these cases, the conversion from the time domain into the frequency domain can be achieved successfully by using Fast Fourier Transform (FFT) techniques. However, these probes have only been used for research purposes and the proposed inversion methods cannot be used for commercially available probes, which generally have non-separable connectors.

The choice of the experimental equipment has to be carried out carefully, depending on the desired level of accuracy and the soil type. Shorter probes and shorted cable lengths are preferable in conductive soils since the signal is less likely to be totally attenuated and the TDR can still provide measurements of the apparent permittivity.

## 2.5.3. Ground Penetrating Radar (GPR)

### 2.5.3.1. Introduction

Radar techniques have been used since the 1960s for sounding the ground (Annan, 2008). In simple terms, a GPR unit sends a high frequency EM signal (generally between 10 MHz and 1 GHz; see Davis and Annan, 1989) into the ground and measures the portion of the signal reflected as a result of discontinuities (or anomalies; i.e., material with different EM properties compared to the surrounding medium). It operates on a principle similar to TDR (see section 2.5.2.2), but the GPR does not inject the signal along a coaxial transmission line. Instead it sends unguided waves both upwards into the air and downwards into the soil (Huisman et al., 2003a).

GPR has been successfully deployed for diverse purposes, such as to map ice thickness, bedrock depth, soil stratigraphy and water table depth. GPR is also commonly used to detect buried archaeological features and in the past two decades it has been successfully used to monitor the soil water content (Davis and Annan, 1989; Huisman et al., 2003a). Another important application of GPR techniques is the detection of buried objects, such as landmines, buried pipes and cables. In the field of utility detection GPR has recently become one of the most widely used shallow geophysical technique (Rogers et al., 2008). The main advantage of GPR over other shallow geophysical techniques (e.g., resistivity, acoustics) is its ability to survey large areas at high speed, generally offering near real time

interpretations. GPR is a non-invasive technique, which is a key advantage when operating in urban areas in order to reduce disruptions to human activities.

However, GPR is limited by the signal attenuation, which depends on the EM properties of the ground (Davis and Annan, 1989). The attenuation determines the GPR performance in terms of depth resolution, and limits its applicability with respect to detecting buried objects. Attenuation is proportional to the frequency (see Equation (2.5)), i.e., the higher frequencies are more strongly attenuated than the lower frequencies. However, high frequencies have a high spatial resolution and allow smaller discontinuities present in the ground to be detected. As a result, the use of GPR is a balance between obtaining high spatial resolution, but limited penetration depth, by using high-frequency antennas, and obtaining larger penetration depths with lower spatial resolution, by using low-frequency antennas.

#### 2.5.3.2. Principles of Ground Penetrating Radar

There are different types of GPR, the most common one being the impulse GPR, which sends EM pulses into the ground and operates in the time domain. Other types of GPR include the continuous-wave GPR systems, which operate in the frequency domain (Koppenjan, 2008). Continuous-wave GPRs (e.g., stepped-frequency radars) sample signals at frequency increments over a specific frequency bandwidth. The advantage of these systems is that they provide direct control of the operative frequency. However, they involve more complex electronics and digital signal processing and for these reasons only a few of these systems are at present commercially available (Koppenjan, 2008).

GPR characteristics are a compromise between range and spatial resolution. The range (or dynamic range) is defined as the ratio of the maximum receivable signal, $V_{max}$ (in

Volts), to the minimal detectable signal, $V_{min}$, and is expressed in decibels (dB), for a specified frequency bandwidth in Hertz (Equation (2.27); Koppenjan, 2008).

$$dynamic\ range = 20\ log\left(\frac{V_{max}}{V_{min}}\right) \quad (2.27)$$

The dynamic range determines the maximum penetration depth, below which the signal becomes noise. The spatial resolution determines the dimension of the smallest detectable target.

The signal range is inversely proportional to the frequency, but the resolution increases with frequency. Impulse GPR are built to achieve frequency bandwidths that are approximately equal to their centre frequency. For example, a 100 MHz GPR is characterised by a 100 MHz frequency bandwidth centred at the frequency of 100 MHz, with a corresponding pulse width of 10 ns (Annan, 2008). Different centre frequencies are achieved by varying the pulse width, which is inversely proportional to the centre frequency.

GPR systems generally comprise two antennas, one transmitter that emits the EM pulse and one receiver that samples the reflected signals. The most common GPR systems work in a reflection profiling mode (Davis and Annan, 1989). Another configuration is the borehole GPR, which is used to sound the soil by inserting the transmitter and receiver into separate boreholes. In the reflection profiling mode, the antennas are usually placed in a fixed configuration, with a constant separation. This method of GPR deployment is called the single (or common) offset method (Huisman et al., 2003a). Alternative multi-offset configurations are the common mid-point (CMP) and the wide angle reflection and refraction (WARR). In the CMP and WARR methods the antennas are manually separated during a survey. In the first case, the distance between antennas is increased stepwise while keeping a common midpoint (e.g., Greaves et al., 1996). In the WARR configuration only

the receiver is moved stepwise while leaving the transmitter in a fixed position. Figure 2.19 shows the relative positions of the transmitter and receiver in the CMP and WARR methods of acquisition (after Huisman et al., 2003a).

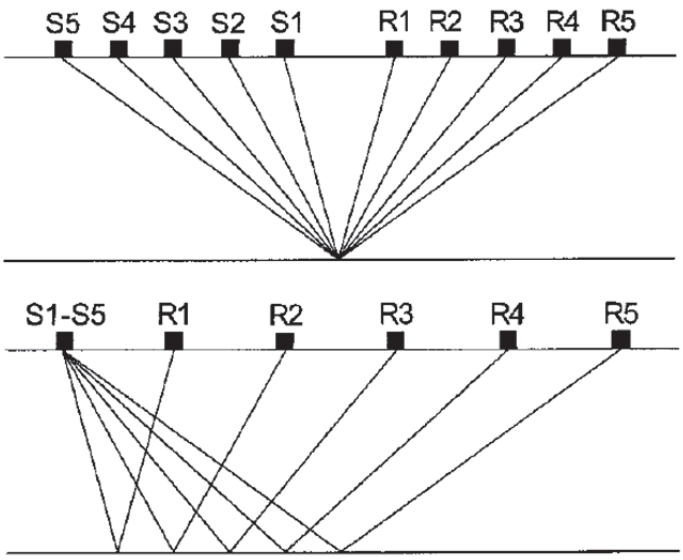



Figure 2.19 – Common midpoint (CMP) and wide angle reflection and refraction (WARR) methods of GPR acquisition (after Huisman et al., 2003a). S and R identify the locations of transmitter and receiver respectively.

Both the single offset and multi-offset techniques allow the determination of the average signal velocity up to the depth of a reflector. From the velocity, a permittivity value can be calculated by using Equation (2.17) and this can potentially be converted to determine the average volumetric water content above the target.

In utility detection applications, the single offset method is the preferred one because it is much faster than the CMP and WARR methods. Since the GPR emits signals in all directions, the reflected energy coming from the buried target is detected before the GPR unit is directly above it. This results in the formation of a hyperbola, since the signals have to travel longer through the soil when the GPR is not directly over the target, as shown in Figure 2.20.

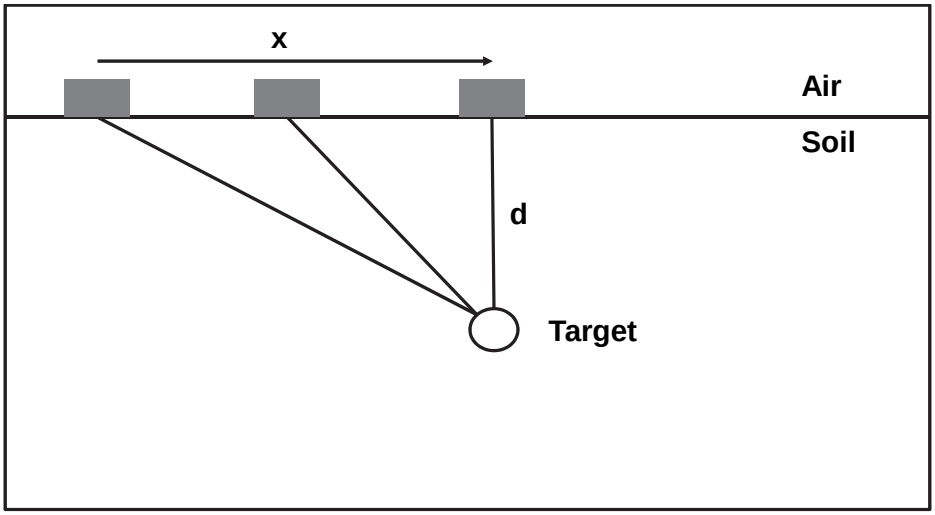



Figure 2.20 – Diagram of single offset GPR acquisition.

In single offset mode, the velocity is calculated by Equation (2.28) (Huisman et al., 2003a).

$$v = \frac{2\sqrt{x^2 + d^2}}{t_{rw,x}} \tag{2.28}$$

where $x$ is the horizontal distance (m) between the GPR and target position (apex of the hyperbola), $d$ is the depth of the target (m) and $t_{rw,x}$ is the arrival time (s) of the reflected wave at position $x$.

The convexity of the reflection hyperbola depends on the average velocity above the target. Common GPR analysis software provides methods to fit the hyperbolae in order to estimate the signal velocity.

During a single offset survey, impulse GPR emits signals at regular steps along the x direction (see Figure 2.20). The vertical traces collected at each step are named A-scans. A combination of A-scans produces an image called B-scan, which is the common GPR data output (Figure 2.21).

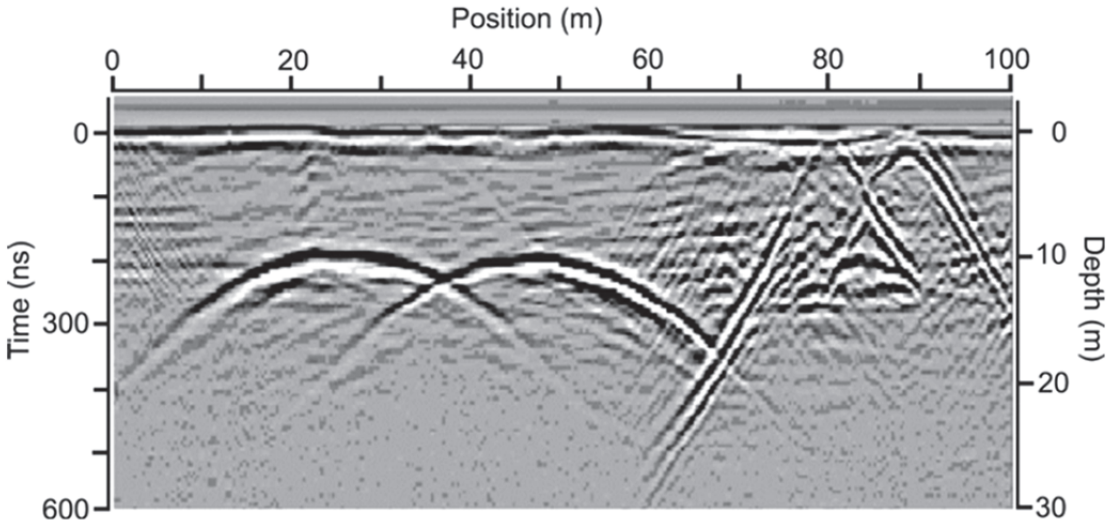



Figure 2.21 – Example of a GPR image (B-scan) showing multiple buried anomalies (after Annan, 2008).

In order to improve the data interpretation a broad range of post-processing procedures is included in GPR software analysis. A discussion on the GPR data processing is not included here[6]. It is sufficient to know that these processing techniques generally tend to decrease the level of noise and to enhance the features in the images, for instance by applying gains and filters.

## 2.5.4. TDR and GPR in the field

TDR has been used by several researchers for monitoring the soil water content and the BEC in the field (e.g., Herkelrath et al., 1991; Menziani et al., 2003; Logsdon, 2005). The advantage of TDR is that it can be left unattended for long periods of time and therefore it can provide *in situ* information of the temporal variability of the EM soil properties. GPR cannot provide continuous monitoring of the soil properties. However, if a number of

[6] Information on GPR processing techniques can be found in GPR manuals, such as Daniels (2004).

surveys is carried out at different times, it is possible to study the variation of the soil properties even with GPR, and for larger areas compared to point measurements by TDR.

The combined use of TDR and GPR in the field has been shown for soil water content measurements, since soil water can be determined and compared by both techniques. For example, Weiler et al., (1998) compared CMP measurements obtained by GPR and point measurements by TDR in a sandy soil and showed that GPR could be used effectively to measure the soil water content in the field. Other authors investigated the ability of GPR to measure the soil water by using the ground wave technique (i.e., EM wave travelling at the interface between the air and soil. See Huisman et al., 2001; Huisman et al., 2003b and Grote et al., 2003). They found that with this method the accuracy of GPR to measure the soil water content was comparable to the accuracy obtained by TDR for the upper few centimetres of the soil. However, these studies were focussed on the measurement of the soil water content, not directly of the electric properties of the soil. As pointed out by Huisman et al. (2001), a direct comparison of permittivity (and not water content) measurements by TDR and GPR would be more meaningful since this would eliminate the error introduced by the calibration model.

Despite comparative studies between GPR and TDR having been conducted in the last two decades (Huisman et al., 2003a), they did not generally include long-term field monitoring. An example of field monitoring was given by Boll et al. (1996), who conducted regular GPR surveys over a period of five months in order to identify the optimal time to detect layers in a sandy soil. The results of this study showed that the different sandy layers (coarse and fine sands) were distinguishable when the soil was not too dry or too wet, that is when it did not present homogeneous characteristics. In fact, for the GPR to be successful, it is necessary to have good contrast between the anomaly and the surrounding medium. Such contrast varies with time as the EM soil properties change, mainly because of varying

water contents. This result obtained by Boll et al. (1996) is significant, because it demonstrates that the seasonal variation of EM soil properties can affect the GPR performance to the point of causing it to fail to detect anomalies. Although the study by Boll et al. (1996) did not involve buried utilities, the same considerations can be applied to the field of utility detection. For example, common plastics have a permittivity ranging between approximately 2 and 8 (Weast, 1972), which corresponds to the permittivity of the most common dry mineral soil particles. Thus, these pipes are likely to become more or less visible to GPR depending on the season (i.e., wet/dry conditions).

## 2.6. SUMMARY AND IDENTIFICATION OF THE KNOWLEDGE GAPS

From the examination of the literature discussed above, several knowledge gaps have been identified. It is apparent that the EM soil properties depend on a number of factors, in particular on the soil water content, the temperature and geotechnical soil properties such as the particle size distribution, the bulk density and the SSA. Relationships between these parameters have been identified and could potentially be used to predict the EM soil properties. For GPR applications, there is a real benefit from further understanding the factors affecting the EM soil behaviour, since the GPR performance depends on these. The development of predictive systems has been investigated in the past with the creation of GPR soil suitability maps for the United States of America. However, there is the potential to significantly improve the predictions of EM soil properties by using geotechnical datasets, such as those held by the British Geological Survey in the UK. Furthermore, seasonal variations of the EM soil properties have not been extensively studied in the field and were not included in previous predictive systems. Knowledge of the links between geophysical

and geotechnical soil properties and their seasonal variation could considerably improve the planning and use of GPR techniques in the detection of buried utilities. Considering this context, the identified gaps of knowledge are described as follows.

- The relationships between geotechnical, geochemical and EM soil properties have not been extensively tested in the field. In order to improve our understanding of the soil and its interactions with EM signals, there is a need for further field testing, by means of case studies that should reflect commonly encountered real situations. These include measuring the EM soil properties of anthropogenic urban soils, which have been generally excluded from the past literature.
- The need for field testing is also valuable in order to better understand the seasonal variations of the EM soil properties and their relationship with environmental variables such as rainfall and temperature. In this regard, long-term monitoring covering several seasons of the EM soil properties has not been commonly carried out in the past.
- Existing soil hydrological models can be used to simulate the variation of the soil water content with time. Simulations can be used to validate these models and confirm the experimental results from field monitoring. In addition, they could provide field validation of calibration relationships between permittivity and soil water.
- To the knowledge of the author, no extensive, long-term field studies involving both TDR and GPR have been conducted in order to assess the seasonal and weather impact on GPR, for the purpose of utility detection. The combined use of TDR and GPR should provide more insights on the effects of the seasonal variation of the EM soil properties on GPR performance to detect buried utilities.
- Finally, the TDR technology has been used extensively in soil science in the past three decades. However, its main application concerned the measurement and monitoring of

the soil water content and not directly of the EM soil properties. The definition of clear methodologies for the construction and calibration of a commercial TDR system could be helpful to facilitate its use in geophysical soil monitoring.

# CHAPTER 3: METHODOLOGY

## 3.1. INTRODUCTION

This chapter gives a detailed description of the methodology used in this research. Based on the knowledge gaps identified in Chapter 2, the focus of the research is on the development of a field monitoring station in order to provide information of the EM soil properties that affect shallow geophysical surveys such as GPR. This information was related to the geotechnical soil properties measured in the laboratory to further understand the links between geophysical and geotechnical properties of soils. Therefore, this chapter describes the techniques used for these purposes in two main sections called ‘experimental development’ and ‘field methodology’. The chapter concludes with a section dedicated to the application of the SPAW model.

## 3.2. EXPERIMENTAL DEVELOPMENT

### 3.2.1. Introduction

This section initially explains the chosen technology and the construction and settings of the monitoring station setup. This is followed by some preliminary analyses carried out on the equipment and finally it will illustrate the calibrations and methods of analysis. The results of the tests performed to verify the accuracy of the instrumentation after calibrations are also reported here.

### 3.2.2. Choice of the sensing technology

As explained in Chapter 2 there are a number of different techniques that can measure the EM properties of the soil (see section 2.5). These methods are generally used as surrogate measurements of the soil water content. Among these techniques, conventional TDR was chosen because it is an established method able to provide better performance compared to other techniques (e.g., capacitance sensors), mainly because of the higher operational frequency, which makes the TDR less affected by conductivity losses (Evett et al., 2005; Kelleners et al., 2005). For the purposes of this research the TDR was considered more suitable because it works on a similar frequency bandwidth of the common commercial GPR units (10 MHz – 1 GHz), and therefore it was the obvious choice in case of comparisons between the two methods. In fact, detectable buried targets allow the GPR to estimate the soil apparent permittivity, which can be directly compared with the TDR measurements.

Table 3.1 provides a list of commercial TDR equipment, as reported by Robinson et al. (2003a). The Campbell Scientific TDR100 cable tester was chosen for a number of reasons. The main advantage over other units was that it could provide both apparent permittivity and BEC, which were the main foci of this research. In addition, it allowed the user to have more control on the analysis since it produced waveforms as output that could be saved and processed by user-developed scripts. The TDR100 was also cheaper compared to other devices.

Table 3.1 – Comparison of different TDR devices and features (after Robinson et al., 2003a).

| Feature | TDRANA† | PCTDR†§ | Viewpoint† | WINTDR† | TACQ¶ | WinTrase† |
|---|---|---|---|---|---|---|
| DOS | ✓ | | ✓ | | ✓ | |
| Windows 3.x | | | | ✓ | | ✓ |
| Windows 95/98 | | ✓ | | ✓ | | ✓ |
| Windows 2000 | | | | ✓ | | ✓ |
| Windows NT | | ✓ | | ✓ | | ✓ |
| Proprietary software | | ✓ | ✓ | | | ✓ |
| TDR interface capability | 1502 | TDR100 | MP-917 | 1502/TDR100 | 1502 | 6050X1 |
| Cost | $0 | $0 | $410 | $0 | $0 | $1400 |
| Waveform display | ✓ | ✓ | ✓ | ✓ | ✓ | ✓ |
| Detection of 1st reflection‡ | A, M | A | A | A, M | A | A |
| Detection of 2nd reflection‡ | A | A | A | A, M | A | A |
| θ analysis‡ | A, M | M | A, M | A, M | A | A, M |
| EC analysis‡ | A | A | A | A | A | None |
| θ, ε, EC, WF storage‡ | ✓ | ✓ | No EC | ✓ | ✓ | No EC |
| User-defined calib. Eq. | ✓ | ✓ | | ✓ | ✓ | ✓ |
| Probe parameter input | ✓ | ✓ | ✓ | ✓ | ✓ | ✓ |
| Multiplexer control | ✓ | ✓ | | ✓ | ✓ | ✓ |
| Waveform averaging | ✓ | ✓ | ✓ | ✓ | ✓ | ✓ |
| Automated readings | ✓ | DL req. | ✓ | ✓ | ✓ | ✓ |

† TDRANA, www.frw.uva.nl/soil/software.html; PCTDR, www.campbellsci.com; Viewpoint, www.esica.com; WINTDR, soilphysics.usu.edu; TACQ, www.cprl.ars.usda.gov/programs/; WinTrase, www.soilmoisture.com.
‡ θ = water content, ε = permittivity, EC = electrical conductivity, DL = datalogger, *M* = manual operation, A = automatic operation.
§ TDR100 performs the waveform analysis internally, PCTDR serves mainly as a laboratory calibration tool.
¶ TACQ operates under a DOS shell in Windows 3.1 or Windows 95.

## 3.2.3. Equipment setup

This section focuses on the experimental setup used for the field test site at the University of Birmingham, UK. More details on the site as well as the actual installation of the probes are presented in sections 3.3.1 and 3.3.2. In this section, only the instruments used and their connections are described.

A total of sixteen probes were connected to a Campbell Scientific (Logan, UT) TDR100 cable tester (Figure 3.1) using two levels of SDMX50 multiplexer (Figure 3.2). RG58, 50 Ω, 0.5 m long coaxial cables were used to connect the multiplexers to the TDR100. In order to install sixteen probes, the TDR100 was connected to one multiplexer which was then connected to the other two using the RG58 cables, thus representing two levels of multiplexers, as shown schematically in Figure 3.3. Each multiplexer has eight channels therefore two levels of multiplexer were necessary in order to connect sixteen TDR probes.




Figure 3.1 – TDR100 cable tester manufactured by Campbell Scientific (Logan, UT).




Figure 3.2 – SDMX50 multiplexer, manufactured by Campbell Scientific.

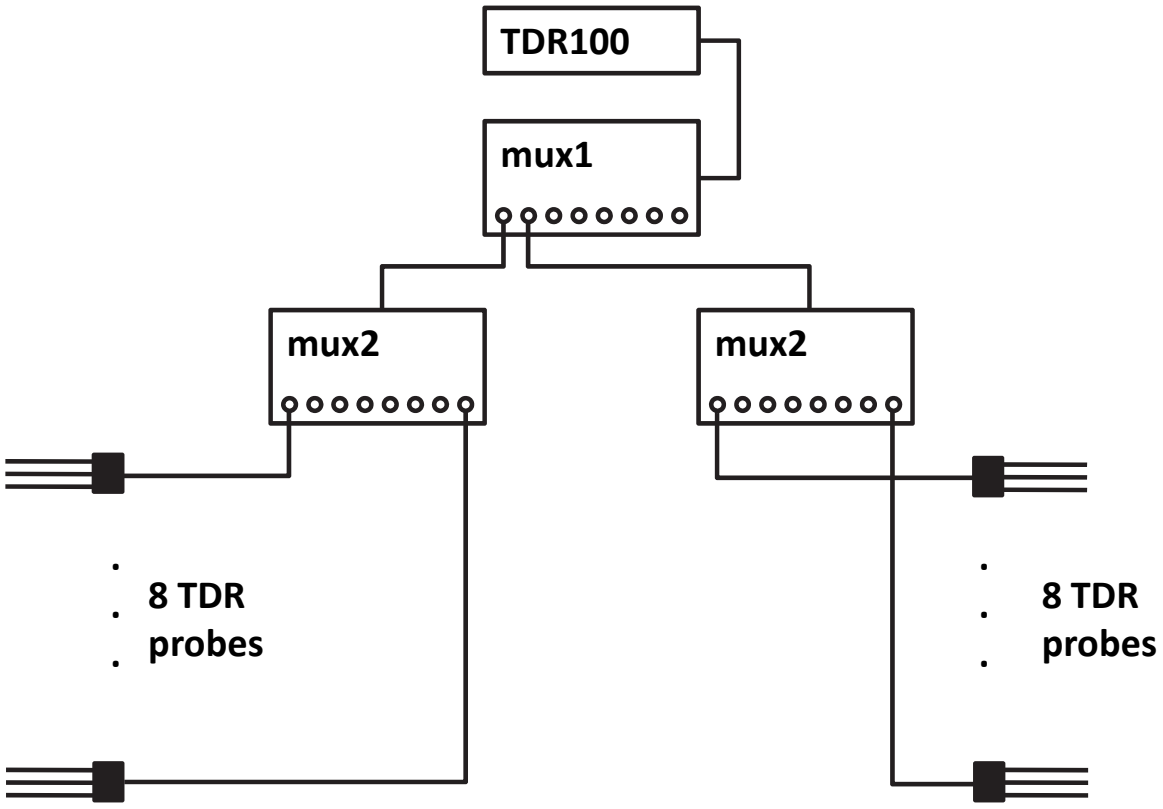



Figure 3.3 – Schematic diagram of the field TDR monitoring station (mux: multiplexer).

In order to switch channels and to provide electrical power, the multiplexers and the TDR100 were also connected using 5-conductor cables. All the equipment was then

grounded to the same grounding point. The probes' cables were of the low-loss type (LMR200DB) and were approximately 3 m long. Three-rod CS645 probes (rod length: 75 mm, Figure 3.4) were inserted horizontally into the ground at eight different depths up to a maximum depth of 1.08 m, in order to obtain detailed information of the vertical profile of the geophysical soil properties (Figure 3.5). The probes were inserted by hand and with the rods' plane parallel to the ground surface (see section 3.3.2). Two installations in the same soil, approximately one metre apart, were considered necessary as a back-up and to provide cross-validation of the results. Three USB thermocouples (model HSTC-TT-KI-24S, by Omega Engineering, UK) were buried at different depths to measure the variations in soil temperature.

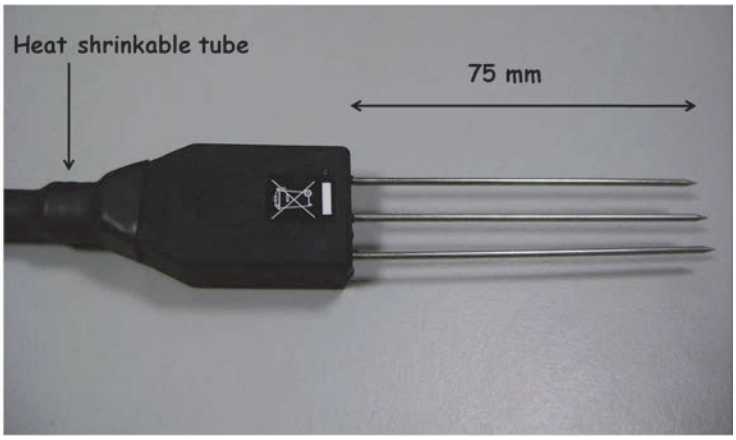



Figure 3.4 – Three-rod probe, manufactured by Campbell Scientific. The low-loss cables were insulated with heat shrinkable tubes.

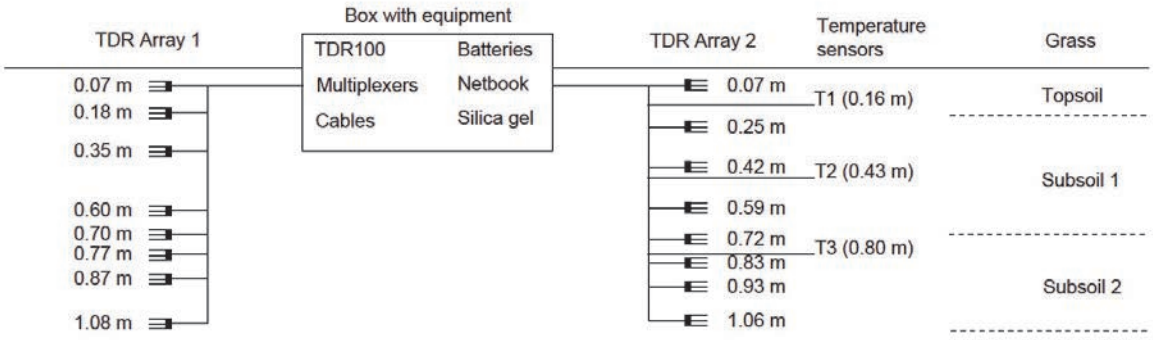



Figure 3.5 – Vertical cross-section of the University of Birmingham field TDR monitoring station. Further details on the site installation are described in section 3.3.2.

A netbook was used to automatically collect and save the TDR measurements by running a script written in Matlab (courtesy of Dr Foo). Each waveform was saved in a separate .mat file named after the date and time of the measurement. The original idea of remotely controlling the monitoring station using RF Solutions Typhoon radio modems was discarded after multiple failed attempts to communicate with the TDR100. A netbook was considered an easier alternative compared to a datalogger.

The three temperature sensors were connected to the netbook by using a USB 4-port hub. The Omega Engineering TRH software was used to automatically collect measurements at regular intervals.

In order to provide electrical power 110 AH, 12 V deep cycling batteries were used, one connected to the TDR100 and three connected together in parallel to the netbook. With this setup the batteries lasted up to eight days.

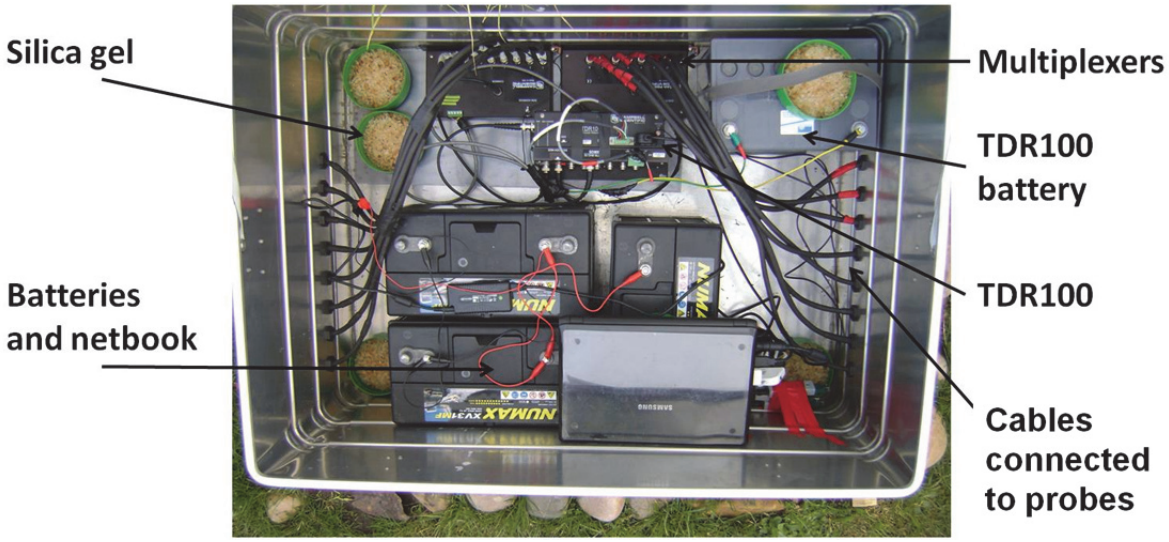



Figure 3.6 – Experimental equipment used on the University of Birmingham test site.

In order to build a monitoring station able to withstand the harsh outdoor environment, it was necessary to make the equipment waterproof and more resistant to physical and chemical damage. All the equipment was put into a lockable, sealed aluminium box manufactured by Zarges, UK (900 long × 640 wide × 450 deep, dimensions in mm). A layer of silicon sealant was added to the inner edges to further improve the waterproofing. To avoid condensation several plastic containers containing silica gel were left inside the box to reduce the humidity. Sixteen holes were drilled in the walls of the box to allow the cable BNC connectors to pass through and were sealed using IP68 cable glands and silicon sealant. The cable protection was very important to avoid communication failures and the introduction of possible unwanted noise in the measurements. For this purpose polyolefin heat shrinkable tubes manufactured by Ultraflex Interconnect were used. Their shrinking ratio was 4:1, to allow the tubes to pass through a BNC connector. This approach was preferred compared to the use of rigid conduits because of its greater flexibility. This proved important during the field installation since it allowed the position of the probes to be altered in case an obstruction was encountered in the ground (e.g., large particles such as gravel) making the insertion impossible. These heat shrinkable tubes are

specifically designed to provide waterproofing and additional insulation against temperature variations. They are also a barrier against physical or chemical damage. A thinner type of heat shrinkable tube was used to protect the cables for the temperature sensors.

### 3.2.4. TDR100 settings

This section describes the parameters that must be set in order to take measurements with the TDR100. Figure 3.7 shows the display of the Campbell Scientific software PCTDR, with all the possible parameters that can be set. However, PCTDR is not suitable for continuous monitoring and a script written in Matlab was used instead. The same parameters as shown in Figure 3.7 had to be set in the Matlab programme to get good quality measurements. The sampling rate in the field was set in the Matlab script to one measurement per probe every hour, both for apparent permittivity and BEC. This sampling rate was shown to be sufficient to detect daily variations of these properties (see section 3.3.4).

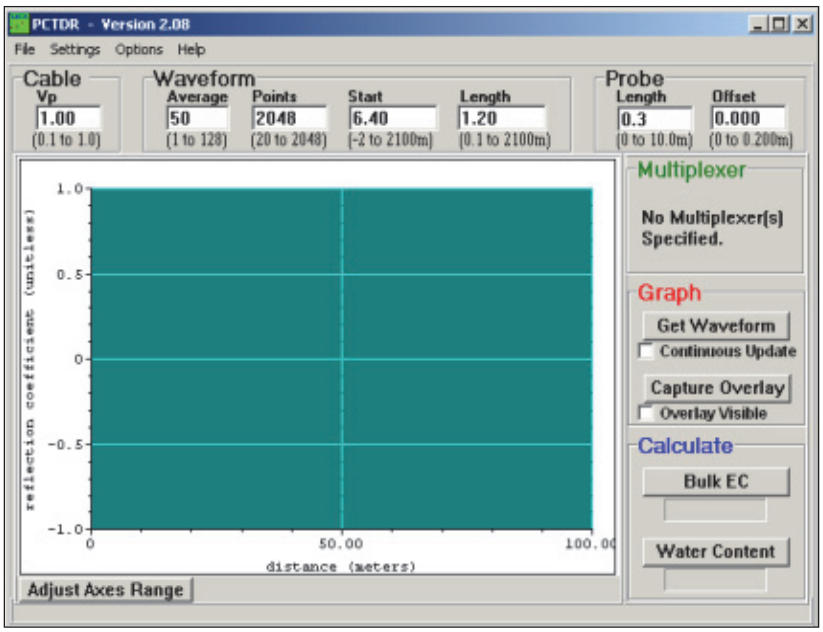



Figure 3.7 – PCTDR display. The software was not used for the monitoring but the cable and waveform parameters were used as shown.

The parameters to be specified to obtain the TDR measurements were:

1) **Velocity propagation factor ($V_p$)**, for simplicity this value was set to unity in order to use apparent distances instead of actual distances. $V_p$ represents the ratio between the actual signal velocity, $v$ (m/s), and the speed of light in free space, $c$, and depends on the transmission line properties, such as the permittivity of the insulating material of the inner conductor. In a vacuum $v = c$, therefore $V_p$ is equal to 1, in other mediums the value is lower depending on the permittivity of the material. This factor was set to 1 to simplify the data analysis, by working on apparent distances instead of real distances. The apparent distance (also called apparent length) is obtained assuming that the actual signal velocity was equal to the speed of light in a vacuum.

2) **Number of averages**, ranging from 1 up to 128 for the TDR100. It was set to 50 as a compromise between obtaining smooth waveforms and the time necessary to take one measurement. A single waveform obtained without averaging multiple waveforms is slightly rougher and noisier. Averaging a large number of waveforms results in a final smooth waveform, but this requires a longer time to take one measurement. In addition, as shown in Bechtold et al. (2010), a minimum number of 16 waveforms are required in order to obtain accurate BEC measurements. As a compromise it was decided to average 50 waveforms per measurement. With this setup, a measurement was obtained in approximately 30 seconds.

3) **Number of data points** in each waveform. This was set to 2048, the maximum allowed by the TDR100, in order to get more detailed waveforms (Figure 3.8). A smaller number of data points reduces the time to take a measurement and it requires

less memory to be stored. These were not considered relevant issues, in particular the storage was not a problem since the netbook could potentially store millions of waveforms in separate files, using the Matlab script (one file corresponding to a waveform obtained with 50 averages and 2048 data points required up to 6 Kb of memory). As shown in Figure 3.8 a choice of 250 or 1000 data points seem to produce detailed waveforms, nevertheless it was decided to use the maximum number allowed by the TDR100 since this allowed the possibility to smooth over the waveforms subsequently, if necessary. The initial choice of a smaller number of data points would not allow the reverse process.

4) ***Start*** and ***Length*** of the waveform plot. These values were empirically determined for apparent permittivity measurements with two levels of multiplexers and set to 6.4 m and 1.2 m of apparent length respectively. For other tests carried out in the laboratory with one or zero levels of multiplexers, the *Start* value was empirically set to either 5.2 m or 4.1 m respectively and the *Length* value was kept equal to 1.2 m. With these values the waveform plot contained all the elements of interest (e.g., reflection in the probe head and end reflection). The BEC measurements used a *Start* value of 0 and a *Length* value of 200 m of apparent length, in accordance with Huisman et al. (2008) and Bechtold et al. (2010).

5) **Channel** of the multiplexer/probe. Each probe was connected to a specific channel on the second level of multiplexer, which in turn was connected to a specific channel on the first level of multiplexer, as shown earlier in Figure 3.3.

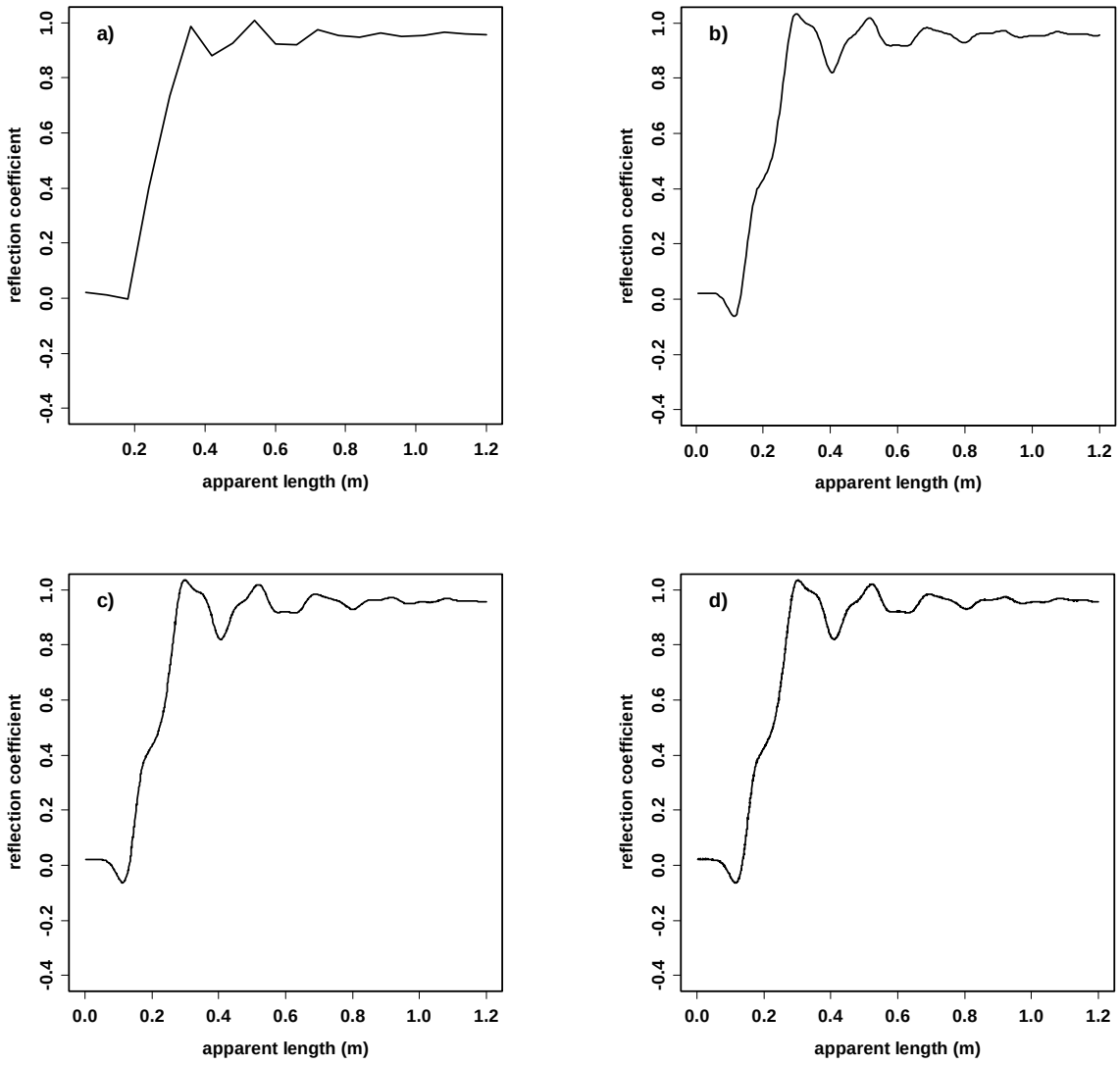



Figure 3.8 – TDR waveforms carried out in air with a varying number of data points. a), b), c) and d) correspond to waveforms taken with 20, 250, 1000 and 2048 data points respectively.

## 3.2.5. Preliminary tests on the TDR equipment

This section reports a number of simple tests carried out on the TDR preliminary laboratory setup in order to find and solve potential problems before assembling the monitoring station.

Several repeat TDR waveforms were collected in air. It was found that a visible shift in the waveforms occurred, apparently with random behaviour. However, it seemed that the shift was not influencing the apparent permittivity and BEC measurements because it was the whole waveform that moved, without changing the shape. Figures 3.9 and 3.10 show twenty measurements carried out in air with the same probe, with two levels of multiplexers. The measurements were carried out at $20 \pm 1$ °C room temperature in a temperature controlled room. As can be seen, the waveforms do not overlay exactly, but they are slightly shifted for each repeat measurement as indicated by the larger line thickness. Figure 3.9 shows the waveforms for twenty measurements carried out with the probe in a fixed position. Figure 3.10 shows the waveforms for another twenty measurements with the same probe, but each time orientated in a different position with the cable bent. No significant differences were noticed in the results obtained by the two data sets. The shift is not relevant for conductivity measurements because only the last part of the waveform is used, but it is important to take this into account when applying an automatic method of waveform analysis for the apparent permittivity measurements. In this case even the start reflection point corresponding to the start of the rods must be identified for each measurement and should not be fixed in any case, even after performing the calibration.

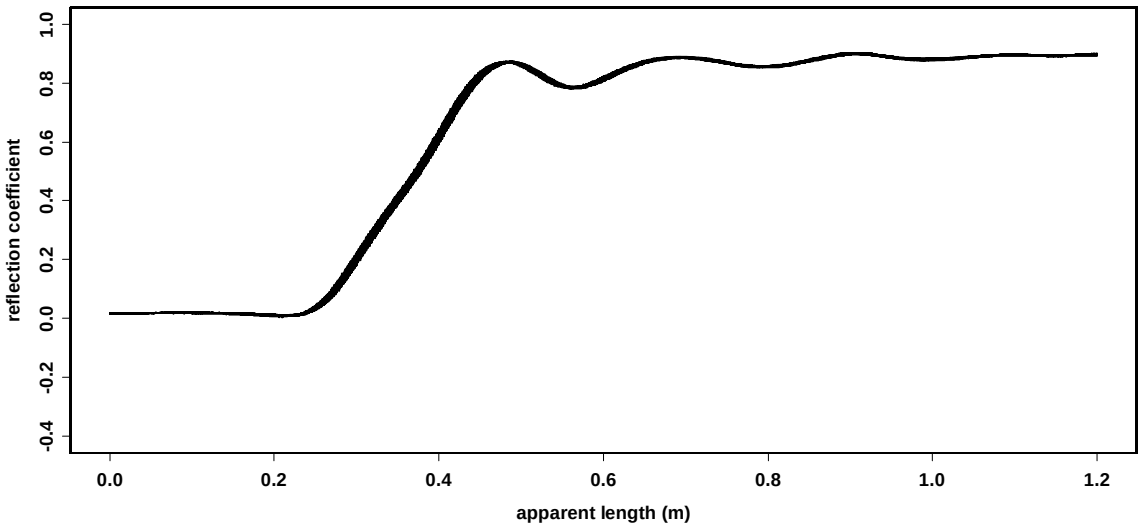



Figure 3.9 – Twenty TDR measurements carried out in air with the same probe with two levels of multiplexers. The probe was kept in a fixed position during the measurements.

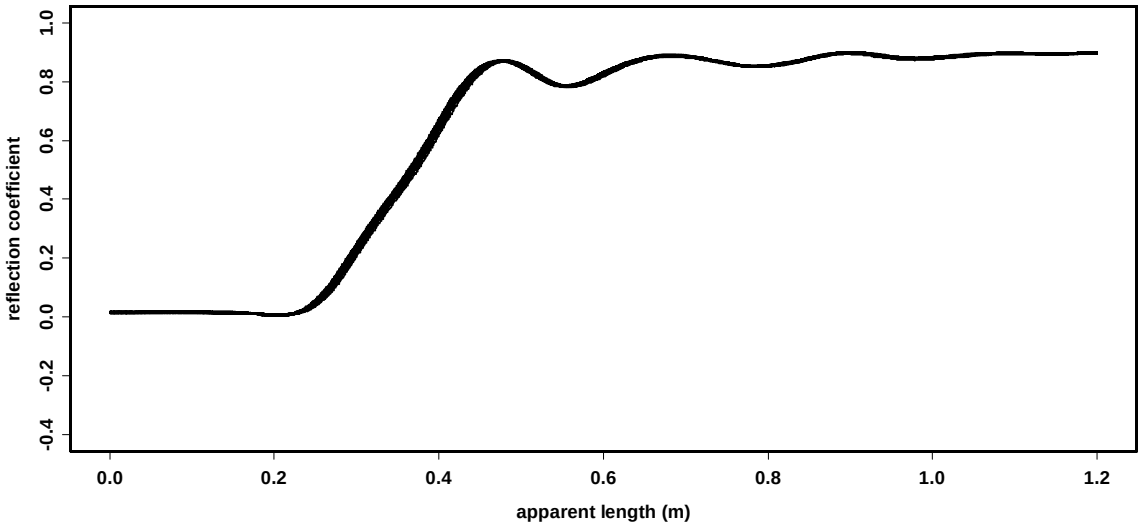



Figure 3.10 – Twenty TDR waveforms obtained from measurements carried out with the same probe with two levels of multiplexers. The cable was bent at different positions and the probe orientated differently before taking each new measurement.

## 3.2.6. Parameters/aspects affecting the TDR measurements

### 3.2.6.1. Temperature effects on the TDR equipment

The performance of the TDR100, the cables and the multiplexers could be affected by environmental factors such as temperature. A rigorous study of these factors and their effects on the instrumentation was beyond the scope of this work, however a few simple tests were carried out on the equipment at different temperatures and are described in this section.

The range of temperature for which the instrumentation was used was well within the tolerance limits established by the manufacturer (i.e., -40 to +55 °C for TDR100). The first test was conducted without multiplexers, with a probe inserted in a beaker containing 1 L of distilled water at a constant temperature of 18.5 °C, and the cable submerged into a water bath. The temperature of the water bath was varied from 19.5 to 42.2 °C, and TDR measurements were taken within this range of temperature at increments of approximately 2 °C, allowing several minutes between one measurement and the next. The whole experiment was carried out in a constant temperature room at 20 ±1 °C. Figure 3.11 shows the result of this test. To make the plot slightly clearer, only some of the data points were selected from each of the original waveforms and then plotted. The shift in the waveforms explained in section 3.2.5 was evident for some waveforms (e.g., the waveform taken at 19.5 °C). However, there seems to be no clear relationship between the shift and the temperature, and there is no apparent difference in the shape of the waveforms with varying temperature.

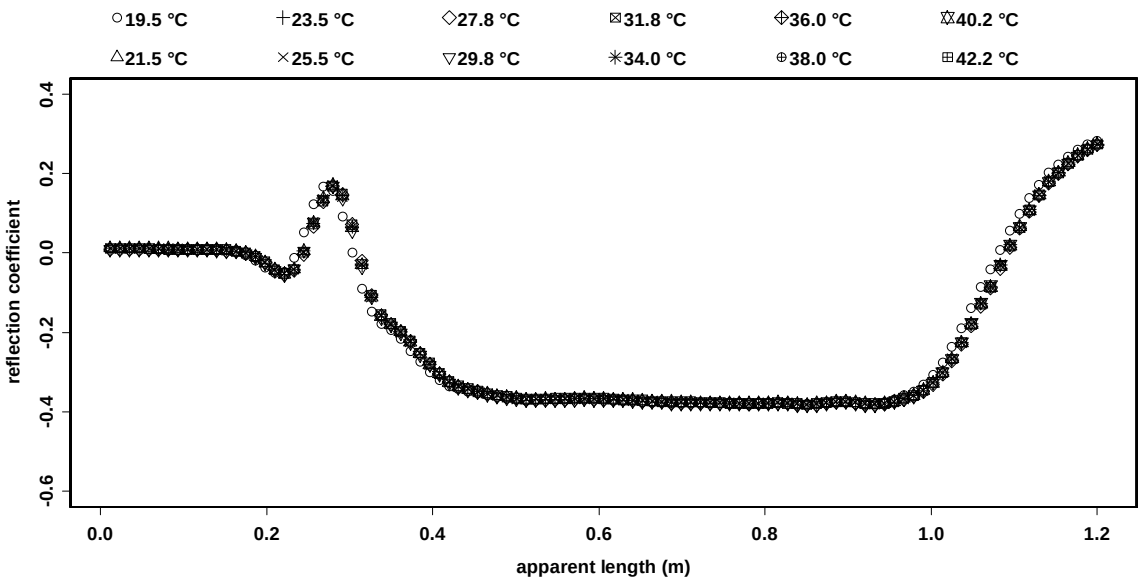



Figure 3.11 – TDR waveforms obtained from measurements in water at a constant temperature of 18.5 °C, and the cable submerged in a water bath with a range of temperatures. [Note: only some of the data points were selected from each of the original waveforms in an attempt to make the comparison between waveforms clearer.]

A second experiment was carried out in an incubator that made it possible to select a wider range of temperatures and reach more stable values compared to the temperature controlled room and the water bath. In this case the TDR100, a multiplexer and a probe with its cable were left inside the incubator at a specific temperature. A netbook was used to carry out the measurements, but was left outside the incubator together with the battery connected to the TDR100. Silica gel was used in order to reduce the formation of condensation. It was not possible to use two levels of multiplexers because of the limited space inside the incubator. The temperature was varied from 1 to 30 °C, allowing at least a couple of hours between one measurement and the next. For each temperature five measurements were taken in air.

Figure 3.12 shows the waveforms obtained from this test. In the interest of clarity, only the first of the five measurement repetitions has been plotted. The number of data

points per waveform has also been reduced to just 41 from 2048, to make the comparison clearer. Figure 3.12 seems to indicate that there is no evident effect due to the temperature, since the shift in the waveforms does not correspond to an increase or decrease in temperature.

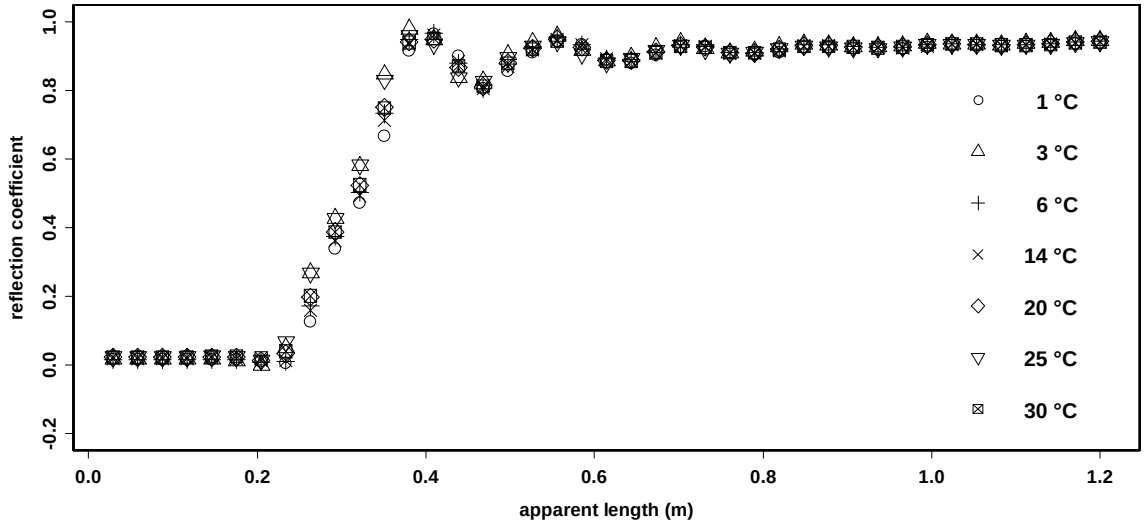



Figure 3.12 – TDR waveforms obtained from air measurements carried out in an incubator for a range of temperatures. [Note: the number of data points of each waveform has been reduced to facilitate the comparison between waveforms.]

A potential problem with this test was the possible presence of humidity inside the incubator. Silica gel was used, but this might not have been sufficient to avoid some water condensing on the equipment and, in particular, on the probe. However, no condensed water was observed during the experiment.

To show how water at varying temperatures might affect the TDR waveforms, a test was carried out using a beaker of distilled water left in the incubator, following the same procedure reported for air. As explained in Chapter 2 the permittivity of water varies with temperature, in particular it increases with decreasing temperature (down to 0 °C). This is evident in the waveforms illustrated in Figure 3.13, which shows the result of the test in

distilled water, at a range of temperatures. At 1 °C, for example, the apparent length within the probe sensor (approximately indicated by the distance between the peak close to 0.2 m of apparent length and the rising limb corresponding to approximately 0.8 m of apparent length) was substantially greater than the apparent length corresponding to the higher temperatures, indicating a greater apparent permittivity.

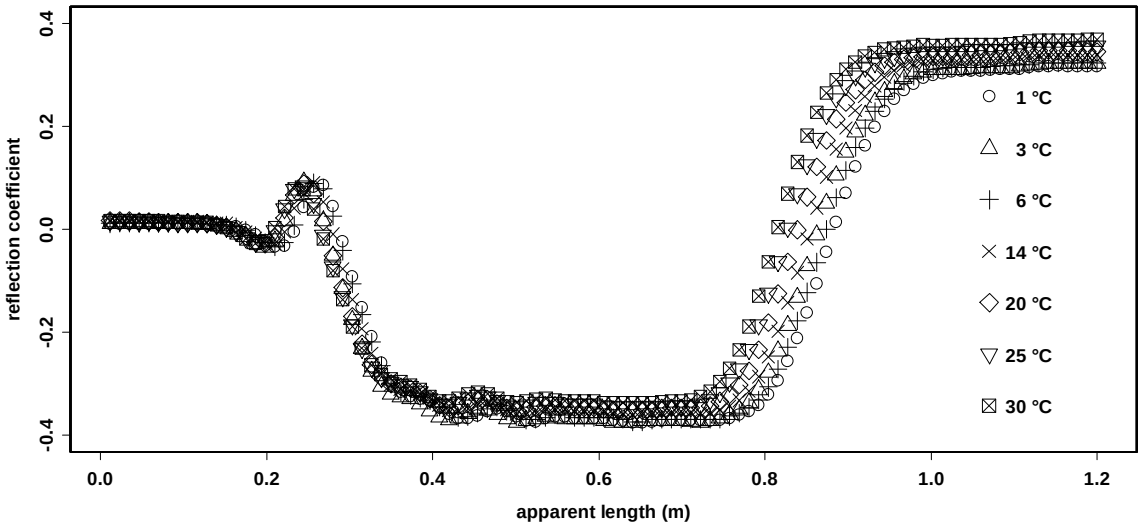



Figure 3.13 – TDR measurements in distilled water carried out in an incubator at a range of temperature. [Note: the number of data points has been reduced to facilitate the comparison between waveforms.]

By observing these data it was not possible to identify any effect on the equipment due to temperature variations, at least within the range tested of 1 °C to 42 °C. Temperature might of course contribute to causing the shift in the waveforms, but no clear relationship between temperature and the amount of the shift was found.

### 3.2.6.2. Insulation of the cables

A few tests were carried out to evaluate possible effects on the TDR measurements related to the use of heat shrinkable tubes. These tubes needed to be heated up to a few hundred degrees in order to shrink and stick to the cables. If the process is conducted with care this should not affect the performance of the cables, but in case by mistake a tube was heated up for too long the cable inside is at risk of melting. Therefore some measurements were taken in distilled water by using non-insulated and insulated cables, and the results compared. The measurements were taken under the same conditions, over a short period of time. There was no evident effect in the waveforms after insulating the cables with the heat shrinkable tubes.

Figure 3.14 shows an example of the waveforms acquired during this test. It can be seen that the waveforms obtained using the insulated cables did not differ from the ones obtained using the non-insulated cables. It can therefore be concluded that the application of the heat shrinkable tubes did not introduce any visible additional noise into the waveforms. It is apparent in Figure 3.14 that the presence of the shift observed in other tests and described earlier in sections 3.2.5 and 3.2.6.1, is also present in these results.

### 3.2.6.3. Multiplexer effects

As mentioned in Chapter 2, using long cables or adding levels of multiplexers results in the introduction of noise and attenuation to the signals sent by a TDR device (Logsdon, 2000; Logsdon, 2006). The multiplexers allow the connection of multiple probes to the same TDR unit and are necessary when several probes are to be used together at the same site. The SDMX50 multiplexers used in the test setup have an impedance of 50 Ω matching the cables' impedance in order to minimise the signal noise and attenuation. This type of multiplexer allows up to eight probes to be connected to the same TDR source.

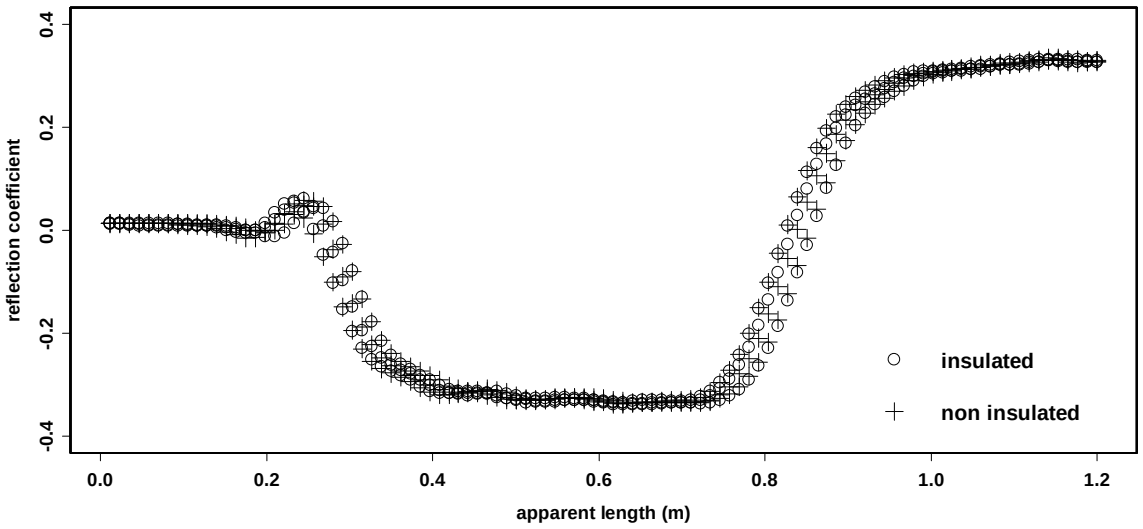



Figure 3.14 – Comparison between the TDR measurements in water carried out using insulated and non-insulated cables. [Note: the number of data points has been reduced to facilitate the comparison between the waveforms.]

The effect of the attenuation caused by the multiplexers is clearly visible in Figure 3.15, which shows three TDR measurements in air taken with zero, one and two levels of multiplexers respectively. It can be noted that the introduction of two levels of multiplexers smooth over the waveform, making the end reflection indistinguishable and reducing the reflection coefficient with distance. In addition, it can be seen that the slope of the rising parts of the waveform corresponding to reflections, for example after the end reflection, decreases with the introduction of multiplexers. This happens because cables and multiplexers act as low-pass filters, attenuating the higher frequencies first and therefore increasing the signal rise time (Evett et al., 2005). The shift shown in Figure 3.15 between the three waveforms does not indicate the presence of a real shift because an accurate waveform overlay was not possible. In fact the selection of the start parameter differed according to the number of levels of multiplexers (see section 3.2.4), resulting in a slightly different plot for each setup.

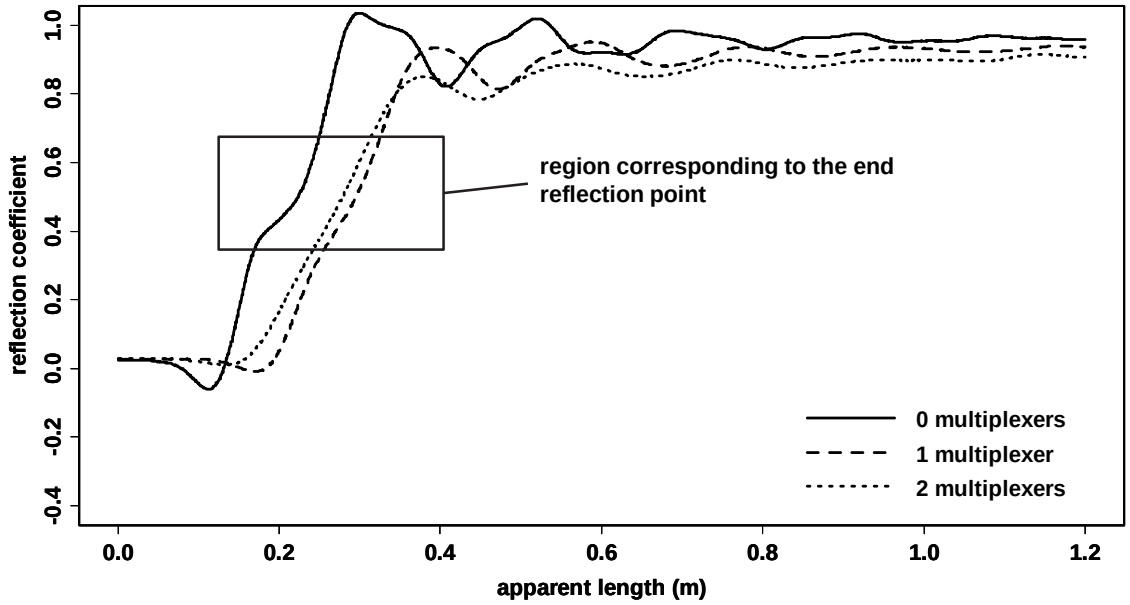



Figure 3.15 – Comparison between three TDR measurements in air using different numbers of multiplexers.

Figure 3.16 shows the same comparison but with the TDR probe in distilled water. In this case, because of the greater permittivity of water, the signal travels at a lower speed compared to air, and has the time to reach a steady state along the rods before being reflected from the end of the sensor. Thus, in distilled water the end reflection remains visible despite the addition of multiplexers. However, the attenuation caused by the multiplexers is still evident in the reduced reflection coefficient range and in the increased rise time after reflections, indicated by the more gentle slopes associated with the increasing sections of the waveforms.

It is important to note that in the current study, the use of two levels of multiplexers combined with a total of approximately 4 m of cable length and 75 mm probes was found not to affect the apparent permittivity measurements as long as the end reflection was easily

recognisable. The apparent permittivity values measured with or without multiplexers were in fact very similar, as shown later in section 3.2.10.

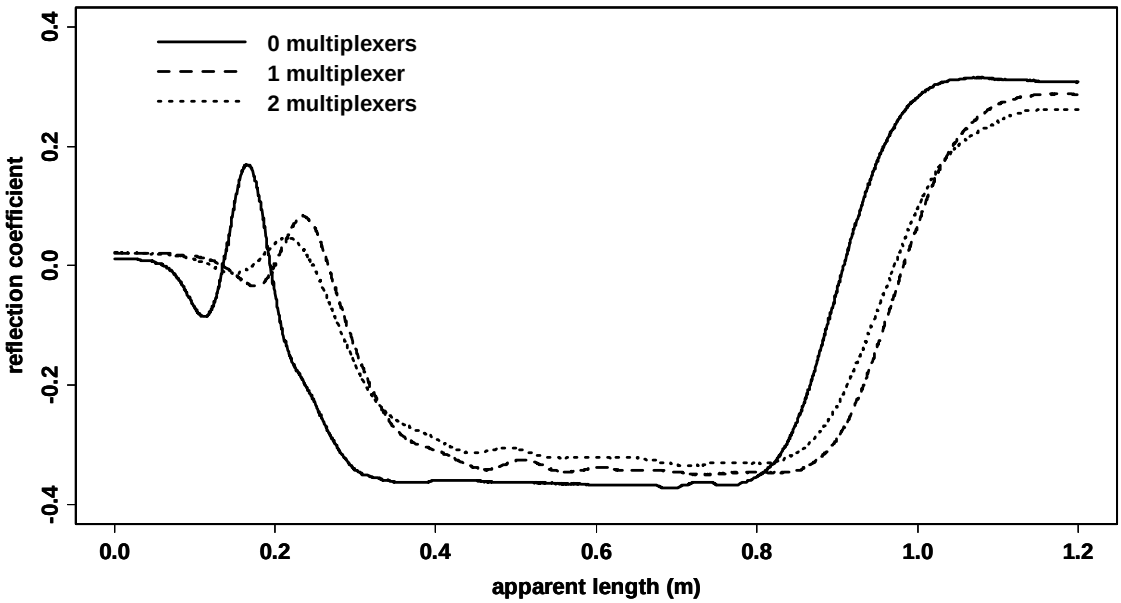



Figure 3.16 – Comparison between three TDR measurements in water using different numbers of multiplexers.

Although the introduction of multiplexers did not to have a large influence on the apparent permittivity measurements, this was not the case for the BEC measurements. In order to measure BEC, the reflection coefficient at long distances must be evaluated from the TDR trace. A reduction in the reflection coefficient due to the addition of one or more multiplexers was found to create inaccuracies and inconsistent results. In order to overcome this problem, a calibration had to be carried out with all the multiplexers and pieces of hardware attached (Logsdon, 2000; Huisman et al., 2008; Bechtold et al., 2010, see section 3.2.8). It is important to note that the calibration is only valid for measurements taken with the same setup and is not reliable if modifications to the hardware are made at a later stage.

## 3.2.7. Calibration for apparent permittivity

This section reports the procedure for calibrating the TDR probes for apparent permittivity. In order to calculate apparent permittivity values using a TDR it is necessary to perform a calibration using the same setup that is used when taking the actual measurements. This calibration is also called the *basic calibration* to distinguish it from the calibration that relates the measured apparent permittivity to the soil volumetric water content.

The basic calibration is performed in materials with known permittivity, possibly identifying the extremities of the expected values to be measured. In the case of soils, the bulk permittivity can be considered as a combination of the permittivity of air, water and solid components. Air has a $\varepsilon'$ (real component of the complex permittivity) very close to 1, the value for the soil components generally range between 3 and 10 (Huisman et al., 2003a), and the value for distilled water varies from approximately 88 at 0 °C to 78 at 25 °C, with the reference value for water being 80.10 at 20 °C (Weast, 1972). For TDR applications with soils it is therefore suggested to perform a calibration in air and distilled water because these are the two extremes within which the soil bulk permittivity normally lies[7] (Heimovaara, 1993; Robinson et al., 2003b). The advantage of using these materials is also that they are not dangerous, they are always at hand and it has been proven that they provide accurate and reliable calibrations (Robinson et al., 2003b).

The measurements for each probe were conducted in air and distilled water at 20 °C in a temperature controlled room. The probes were numbered and connected to the multiplexers on their final corresponding channel positions, and all the cables used were the same as in the final equipment setup.

[7] Values of $\varepsilon$' higher than 80 have been reported by several authors in dispersive clays (e.g., Campbell et al., 1990, Kelleners et al., 2005, Saarenketo, 1998), where the effective TDR measurement frequency reduces well below 500 MHz.

Since it was not possible to identify the end reflection in air when using two levels of multiplexers combined with approximately 4 m of cable length and 75 mm probes (see section 3.2.6.3), measurements were performed in air with the rods short circuited with aluminium foil (Figure 3.17), as this allowed the end reflection point to be accurately identified.

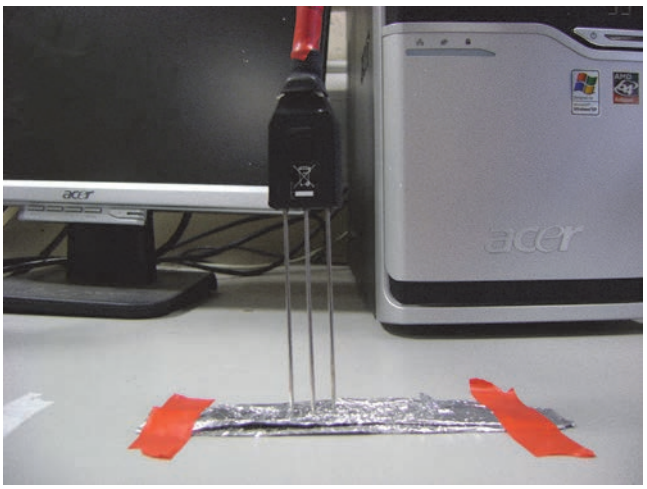



Figure 3.17 – TDR probe short circuited with aluminium foil.

A few measurements were also performed without multiplexers to verify the reliability of this approach. It was found that the end reflection in air corresponded to the intersection of a horizontal line tangent to the largest peak in the waveform and a tangent line to the subsequent descending limb of the short circuited waveform, as shown in Figure 3.18. Figure 3.18 shows that this point corresponds to the same apparent distance of the end reflection point identified with fitting tangents when no multiplexers are used. To overcome the possible inaccuracies associated with a single measurement, four repetitions were taken for each probe and the average values were used.

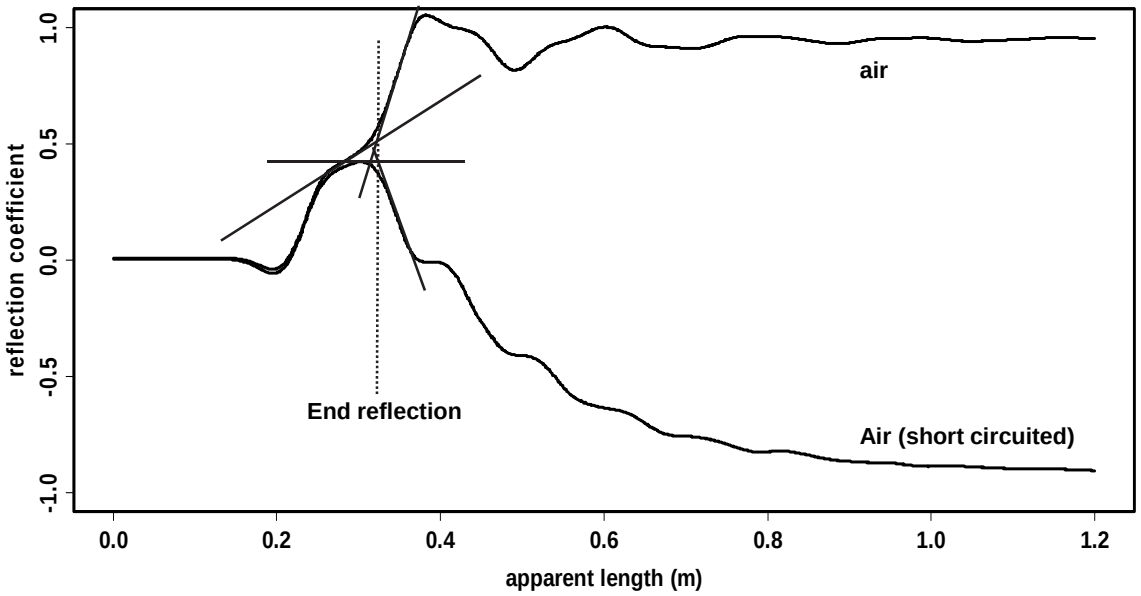



Figure 3.18 – TDR waveforms obtained from open and short circuited measurements in air taken without using multiplexers.

Four repetitions were also performed in distilled water in a 1 L conical beaker (Figure 3.19). The temperature was strictly controlled and kept at 20 °C by putting the beaker in an incubator at a constant temperature. The measurements were taken immediately after in the temperature controlled room and each time the water temperature was measured with a thermometer.

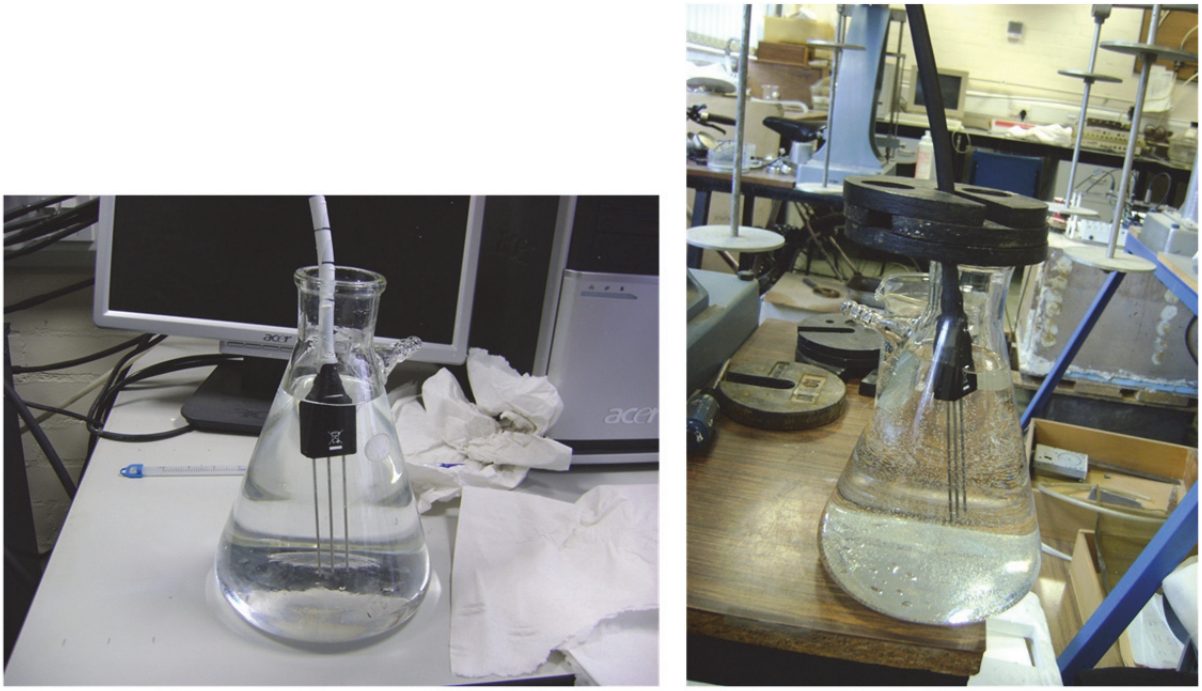



Figure 3.19 – TDR probe inserted in a beaker containing distilled water at 20 °C; a) held in position manually, b) fixed in position using metal weights.

The following describes the calibration procedure for apparent permittivity used in this study based on the principles reported by Heimovaara, 1993 and Robinson et al., 2003b:

1. Two measurements were taken with the same probe in air (short circuited) and distilled water respectively. The measurements were taken at 20 °C and repeated four times for each probe.
2. An easily recognisable reference point in the part of the waveform corresponding to the probe head was found by crossing a base line and a line tangent to the subsequent rising part of the waveform (Figure 3.20). Heimovaara and Bouten (1990) identified this reference point at the interface between the coaxial cable and the probe head, which corresponds to the first reflection after the steady-state level along the coaxial cable. Due to the attenuation introduced by using two levels of multiplexers, this interface was not easily recognisable and it was better to exploit the characteristic dip caused by a

change in impedance inside the Campbell Scientific probe head (Figure 3.20). The position of this reference point should not vary between the different measurements because the geometrical and dielectric properties inside the probe head are fixed.

3. The end reflection point (end of the rods) for the measurements in water was identified by crossing a base line and a line tangent to the subsequent rising portion of the waveform corresponding to the end reflection (Figure 3.20). The end reflection in air (short circuited) was identified as explained previously in this section and is also shown in Figure 3.21.
4. The apparent distance $L_t$ (in Figure 3.20, $L_t = L_0 + L_{app}$) between the reference point and the end reflection point was calculated from the average of the four measurements in air (short circuited) and water. By setting $\varepsilon_a$ to 1.00 for air and to 80.10 for distilled water at 20 °C (Weast, 1972) it was possible to calculate the offset distance within the probe head from the reference point and the start of the rods, $L_0$ (m, Figure 3.20), and the calibrated length of the rods, $L_{cal}$ (m) according to Equation (3.1). $L_{cal}$ obtained after calibration is very similar to the physical length of the rods (Robinson et al., 2003b).

$$L_t = L_0 + L_{cal}\sqrt{\varepsilon_a} \qquad (3.1)$$

All the calibrations were carried out by manually holding the probes. For the short circuited measurements in air this was necessary in order to keep a good contact with the aluminium foil. The measurements in water also required the probes to be held in position because of the difficulty of keeping the cables in a specific position due to the stiffness of the insulation caused by the heat shrinkable tubes.

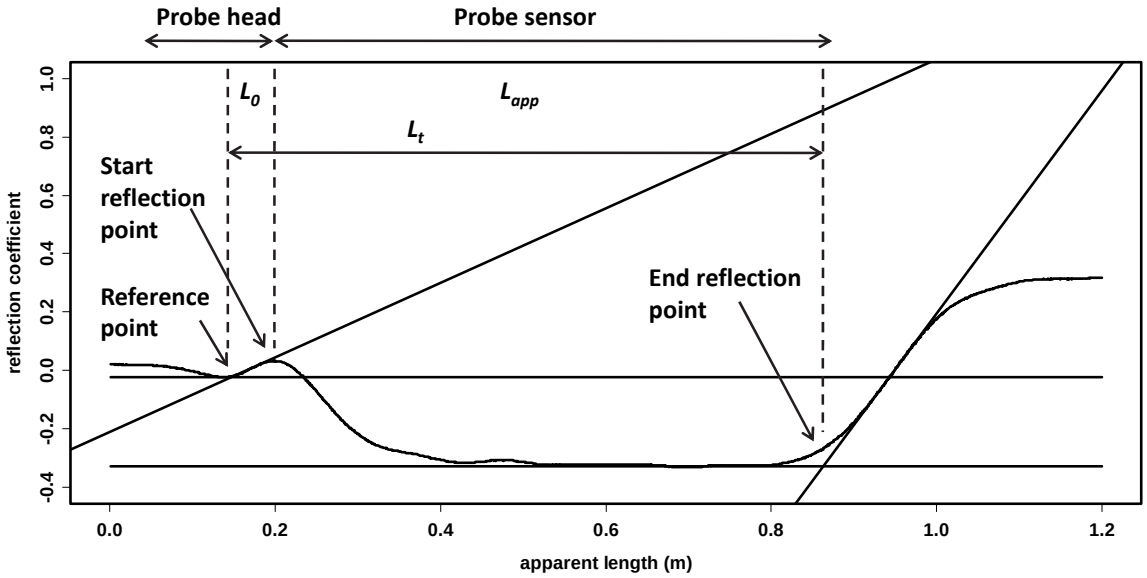



Figure 3.20 – TDR waveform for a measurement in distilled water used in the calibration for apparent permittivity.

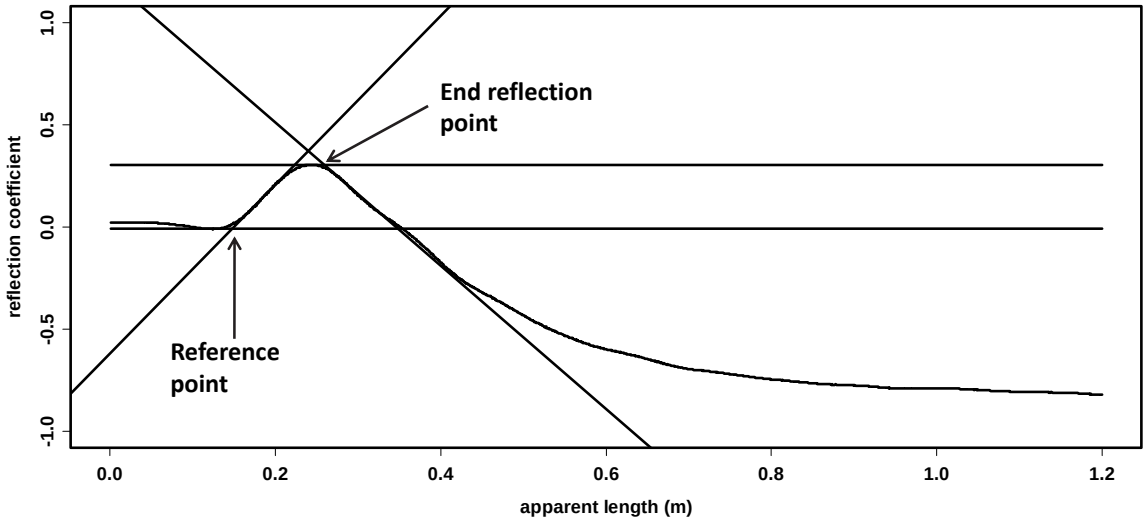



Figure 3.21 – TDR waveform for a short circuited air measurement used in the calibration of apparent permittivity.

A few measurements were taken in order to detect possible edge effect due to the conical beaker. This involved comparison with a second test arrangement using a large

bucket (diameter: 0.3 m, height: 0.4 m) filled with distilled water. No identifiable differences were found between these measurements and those obtained in the conical beaker. It was noted that small differences could arise if the rods touched the edge of the beaker or the bucket. This was carefully avoided during the calibrations by keeping the probe in the middle of the beaker. In addition, comparisons were also carried out between the waveforms taken by manually holding the probe and by keeping it in a fixed position by using metal weights as shown earlier in Figure 3.19b, but no differences were observed.

The accuracy achieved by TDR after this calibration procedure was typically of 1-2 % (see section 3.2.10.2).

## 3.2.8. Calibration for BEC (bulk electrical conductivity)

In this section the calibration for the BEC measurements with TDR is explained in detail. While the basic calibration for apparent permittivity in air and distilled water is widely accepted (Robinson et al., 2003b; Chung and Lin, 2009), the situation is different for the calibration for BEC, since only in recent years has an improved calibration methodology been defined (Heimovaara et al., 1995; Lin et al., 2007 and 2008; Huisman et al., 2008; Bechtold et al., 2010). In the current study the calibration procedure is based on the two-step methodology suggested by Huisman et al. (2008), which allows the accurate determination of the BEC with TDR, based on the original method proposed by Giese and Tiemann (1975). The two-step calibration method allows the probe constant $K_p$ (1/m) and of the additional resistance parameters, $R_c$ (Ω/m) and $R_0$ (Ω) in Equation (3.2) to be determined by using eight reference solutions with known electrical conductivity (see section 2.5.2.2 for further details, although the equations are reported here to facilitate the reader).

$$BEC = \frac{K_P}{R_L - (DR_c + R_0)} \quad (3.2)$$

where $D$ is the cable length (m) and $R_L$ is the load resistance (Ω), as calculated from Equation (3.3).

$$R_L = Z_{out}\frac{1+\rho_\infty}{1-\rho_\infty} \quad (3.3)$$

where $Z_{out}$ is the output impedance of the TDR device (~ 50 Ω) and $\rho_\infty$ is the reflection coefficient at long distances.

As explained in Chapter 2 the reflection coefficient at long distance must be corrected for non-ideal open circuit measurements. The reflection coefficient of an open-circuit measurement, $\rho_{open}$, to be used in Equation (3.4) according to Lin et al. (2008), was calculated as the mean of 96 measurements in air (mean: 0.9629, standard deviation: 0.0010), corresponding to 6 repetitions for each probe with all the multiplexers attached.

$$\rho_{corr} = \frac{2(\rho_{meas}+1)}{\rho_{open}+1} - 1 \quad (3.4)$$

Eight reference solutions with known EC (in solutions BEC is equivalent to EC) were prepared by repeatedly diluting potassium chloride (KCl) solutions, starting from a 0.15 M solution prepared by adding 11.183 g KCl to 1 L of distilled water. The approximate final concentration (M) and EC (S/m) measured with a conventional conductivity meter (HI 9033, Hanna Instruments) are reported in Table 3.2. The values are only indicative because small changes in temperature and potential contamination of the solutions might have changed the reference EC slightly, after they were first measured. For

this reason the reference EC was measured with the conductivity meter every time a new set of TDR probes was calibrated.

Table 3.2 – Approximate KCl concentration (M=mol/L) and corresponding electrical conductivity (S/m) of eight solutions used for calibrating TDR for BEC.

| **Approx. [KCl] (M)** | 0.15 | 0.10 | 0.075 | 0.03 | 0.00375 | 0.001875 | 0.0010 | 0.00046875 |
|---|---|---|---|---|---|---|---|---|
| **Approx. BEC (S/m)** | 1.7963 | 1.1910 | 0.8830 | 0.3667 | 0.0248 | 0.0124 | 0.0078 | 0.0063 |

Each day a calibration was performed, every solution was tested three times by both the TDR and the conductivity meter HI 9033, used to obtain the average reference EC. The measurements were taken at a constant temperature of 21 °C, carefully measured and adjusted with the use of an incubator. The *Start* and *Length* parameters defining the dimension of the waveform plot were set to 0 m and 200 m of apparent length respectively (see section 3.2.4). The reflection coefficient at long distances was determined by averaging the last portion of the waveform between 193 m and 200 m of apparent length (Huisman et al., 2008 and Bechtold et al., 2010) corresponding to the 75 data points between data points 1973 and 2048.

In the first step of the calibration, four low-conductivity solutions with EC ranging from ≈ 0.006 S/m to ≈ 0.025 S/m (Table 3.2) were used to determine the probe constant, $K_p$, by setting $R_c$ and $R_0$ equal to zero in Equation (3.2), which simplifies into Equation (3.5).

$$BEC = \frac{K_P}{R_L} \tag{3.5}$$

The reflection coefficient corresponding to these low conductivities ranged between 0.5 and 1.0 making it possible to neglect the cable and extra resistance parameters (Huisman et al., 2008). According to Equation (3.5), the inverse of the probe constant, $1/K_p$, was resolved from the plot of the TDR sample conductance (i.e., the inverse of the load resistance, $1/R_L$) against the EC of the low conductivity solutions (Figure 3.22).

In the second step, the calculated $K_p$ was fixed in Equation (3.2) and the additional resistance parameters $R_c$ and $R_0$ were estimated by using all eight reference solutions with known EC, with the higher-conductivity ranging from ≈ 0.37 S/m to ≈ 1.80 S/m (Table 3.2). The extra resistance parameters were estimated by minimising the sum of the squared residuals between the measured and modelled EC (Equation (3.2)) using the Simplex optimisation algorithm (Nelder and Mead, 1965; Figure 3.23 and Figure 3.24). The function *optim* was used as implemented in the *stats* package in the software environment R (Venables et al., 2012; Adler, 2010). For each probe, the optimisation was performed on a range of initial $R_c$ and $R_0$ values and the initial pair that provided the best minimisation of the error was selected. As reported in previous studies (Huisman et al., 2008; Lin et al., 2007), $R_c$ and $R_0$ were both expected to be small positive values therefore the evaluated initial values were between 0 and 0.5.

Figure 3.23 shows the combination of initial $R_c$ and $R_0$ values for a selected probe. $R_c$ was increased in increments of 0.01 from 0 and 0.5, and for each of these values $R_0$ was increased from 0 and 0.5 in increments of 0.01.

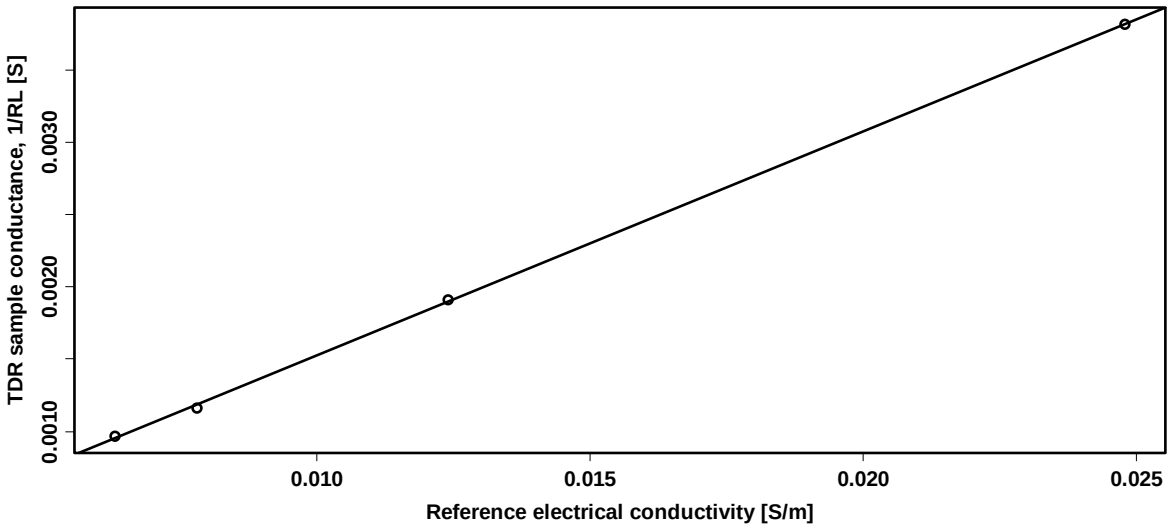



Figure 3.22 – Linear fitting of the sample conductance, $1/R_L$ (1/Ω), to the electrical conductivity (S/m) of four low-range KCl solutions used as reference (first calibration step). [Note: the slope corresponds to the inverse of the probe constant, $K_p$ (1/m).]

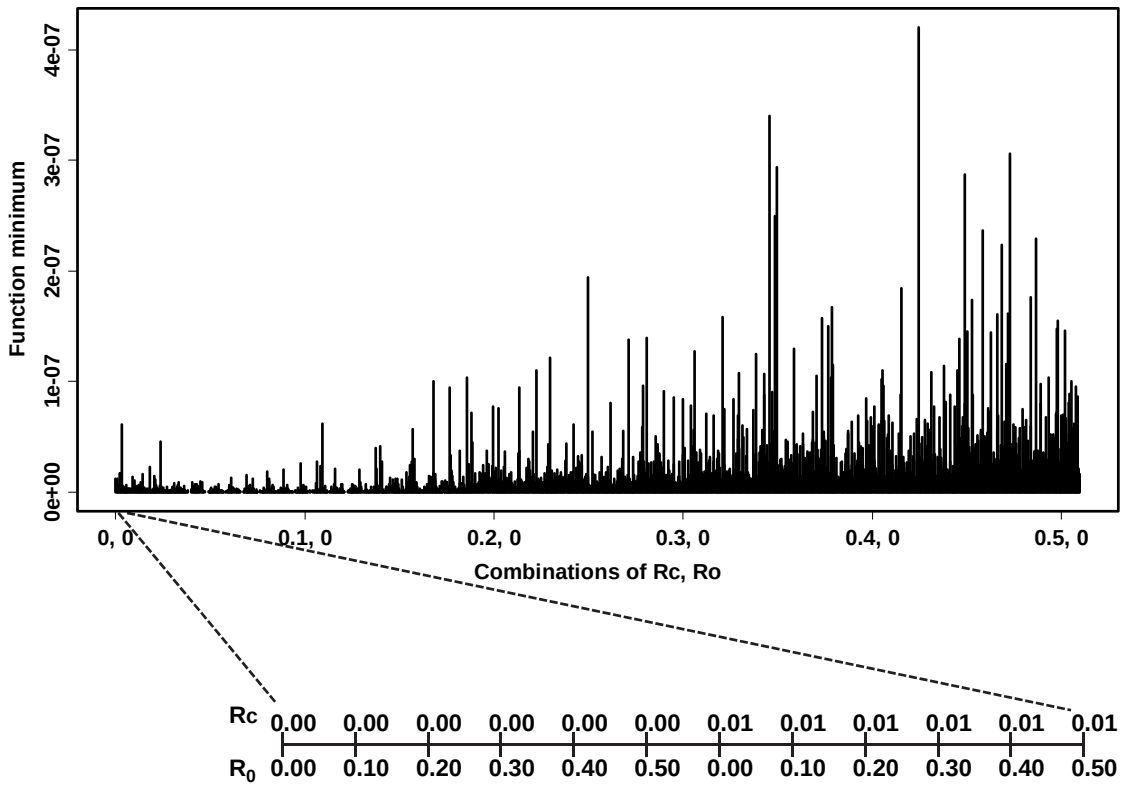



Figure 3.23 – Combinations of initial $R_c$ (Ω/m) and $R_0$ (Ω) parameters used to minimise the sum of the squared residuals between the measured and modelled EC.

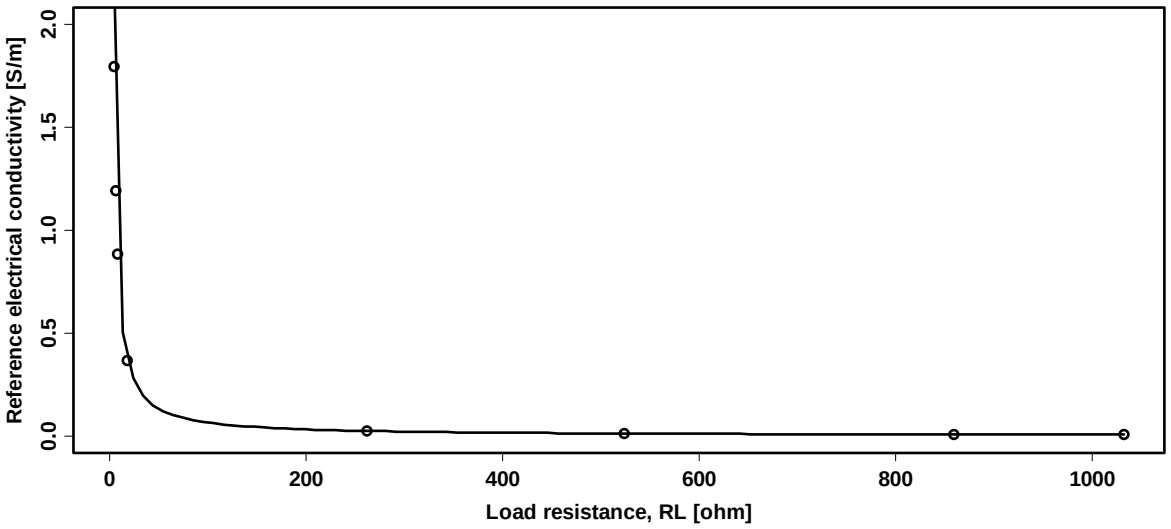



Figure 3.24 – Fitting of the electrical conductivity (S/m) of all eight KCl reference solutions to the load resistance measured by TDR (second calibration step).

### 3.2.8.1. Considerations on the calibration for BEC

This section provides extra details on the calibration for BEC and further supports the chosen methodology.

Figure 3.25 shows the sample conductance ($1/R_L$) measured by a selected TDR probe as a function of the known BEC of all the reference solutions. The Simplex model (dotted line in Figure 3.25) agrees well with the measured sample conductance demonstrating it to be appropriate in the two-step calibration procedure. Compared to the information reported in Huisman et al. (2008) for similar cable lengths, the deviation from linearity at the higher conductivities is more pronounced here because of the extra resistance caused by the two levels of multiplexers.

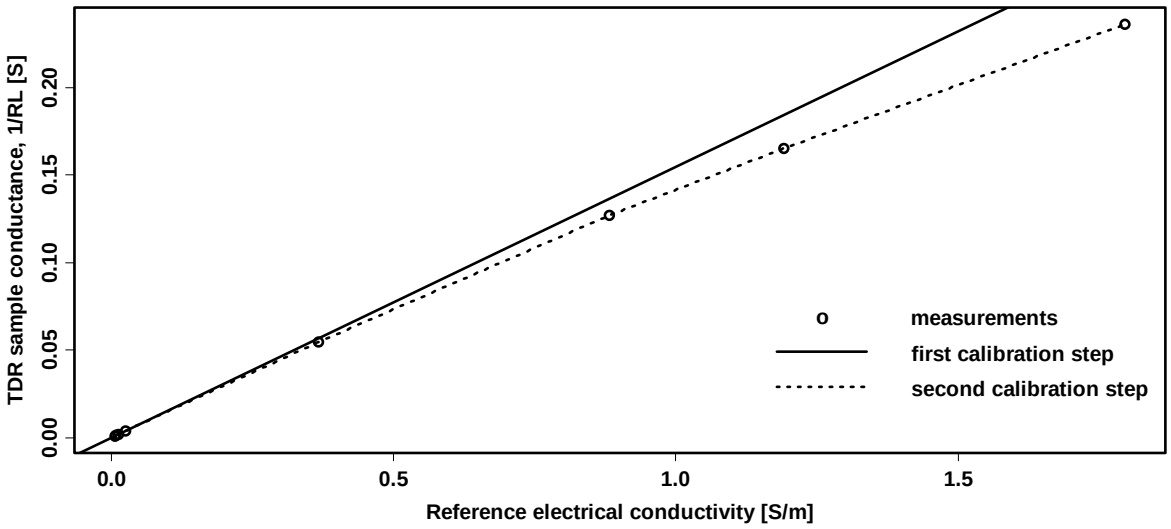



Figure 3.25 – Example results for the two-step calibration procedure for BEC using TDR.

Figure 3.23 shows combinations of initial $R_c$ and $R_0$ values for one probe used as inputs in the Simplex algorithm, noting that an arbitrary selection of these initial parameters can lead to suboptimal minimisations. A similar plot was obtained for all the probes. The best initial pair generally occurred at lower $R_c$ values (< 0.20) and at a range of $R_0$ values. For this reason it is important to test multiple initial $R_c$ and $R_0$ values to find the global minimum, which can then be used in the Simplex optimisation. The global minimum was always found at small initial values of $R_c$ (< 0.50) for each probe. Larger initial values of $R_c$, from 0.50 to 1.00 (not shown), were also tested, but in these cases $R_0$ became negative. For this reason, only the initial values between 0.00 and 0.50 were eventually evaluated.

Table 3.3 summarises the probe constant and the initial and optimised resistance parameters for the 16 probes used in the field monitoring. Both $R_0$ and $R_c$ showed a strong variability with a standard deviation greater than 50 %, and $R_c$ rarely matched the values reported by other authors (Reece, 1998; Huisman et al., 1999; Huisman et al., 2008; Bechtold et al., 2010), and were usually found to be greater than the direct measurements reported by earlier works. These results show that the optimised $R_c$ and $R_0$ values do not

represent the actual physical resistance of the cables and attachments. Huisman et al. (2008) suggested treating $R_0$ as an empirical fitting parameter. From the data collected in this study it appears that both $R_c$ and $R_0$ must be treated as empirical fitting parameters. $R_c$ and $R_0$ are the result of a fitting procedure and therefore their high variability is caused by the uncertainty associated with the fitting (linear fitting for the estimation of $K_p$ and non-linear fitting in the case of the Simplex). The experimental error associated with the measurement of $R_L$ (Equation (3.3)) by TDR and reference BEC (Equation (3.2)) by a standard conductivity meter, are both affecting the quality of the fitting. In addition, as shown in Figure 3.23, there are several pairs of initial resistance parameters that could lead to similar minimisations, but the selection of the initial pair will affect the estimated parameters.

Table 3.3 – Probe constant ($K_p$), initial and optimised resistance parameters ($R_c$ and $R_0$), with their mean and standard deviation for the 16 probes of the monitoring setup.

| Probe | $K_p$ (1/m) | Initial $R_c$ (Ω/m) | Initial $R_0$ (Ω) | Optimised $R_c$ (Ω/m) | Optimised $R_0$ (Ω) |
|---|---|---|---|---|---|
| 1 | 6.55 | 0.06 | 0.37 | 0.0609 | 0.4069 |
| 2 | 6.49 | 0.10 | 0.16 | 0.0985 | 0.1659 |
| 3 | 6.51 | 0.12 | 0.08 | 0.1197 | 0.0812 |
| 4 | 6.61 | 0.15 | 0.02 | 0.1495 | 0.0222 |
| 5 | 6.55 | 0.10 | 0.29 | 0.0983 | 0.2965 |
| 6 | 6.51 | 0.13 | 0.28 | 0.1265 | 0.2889 |
| 7 | 6.50 | 0.14 | 0.10 | 0.1470 | 0.1122 |
| 8 | 6.58 | 0.12 | 0.25 | 0.0522 | 0.2820 |
| 9 | 6.61 | 0.15 | 0.19 | 0.1474 | 0.1906 |
| 10 | 6.63 | 0.13 | 0.13 | 0.1288 | 0.1338 |
| 11 | 6.54 | 0.08 | 0.47 | 0.0582 | 0.4966 |
| 12 | 6.67 | 0.15 | 0.15 | 0.1226 | 0.1683 |
| 13 | 6.57 | 0.15 | 0.01 | 0.1500 | 0.0109 |
| 14 | 6.65 | 0.18 | 0.05 | 0.1717 | 0.0516 |
| 15 | 6.62 | 0.14 | 0.19 | 0.1399 | 0.2092 |
| 16 | 6.65 | 0.40 | 0.22 | 0.3992 | 0.2235 |
| **mean** | **6.58** | **0.14** | **0.19** | **0.1357** | **0.1963** |
| **std. dev.** | **0.06** | **0.07** | **0.13** | **0.0789 (58.14 %)** | **0.1349 (68.72 %)** |

### 3.2.9. TDR waveform analysis

The analysis of the TDR waveforms was carried out using scripts specifically developed in the software environment R.

For BEC measurements the script automatically evaluated Equations (3.4), (3.3) and (3.2) (see section 2.5.2.2 and 3.2.8). The load resistance was computed by averaging the last 75 data points of the waveform as explained in section 3.2.8.

Apparent permittivity was calculated by identifying the points corresponding to crossing tangents (Figure 3.26) and applying Equation (2.21) (see section 2.5.2.2).

The code was based on the methods proposed by Baker and Allmaras (1990) and Menziani et al. (1996). In the literature it was also referred to as the derivative-based method (Timlin and Pachepsky, 1996) and single tangent method (Chung and Lin, 2009).

The script performed the following steps:

1) Compute the first derivative of a waveform and perform a smoothing average on 100 data points in order to reduce its roughness and improve the identification of maxima and minima (Figure 3.26a and b)
2) Find the points of inflection in the original waveform located after the reference reflection point and end reflection point (Figure 3.26c). This step was achieved by splitting the derivative in two sections and finding the maximum in each section corresponding to the respective point of inflection.
3) Empirically identify a suitable range of points before and after the points of inflection and perform a linear fitting across these points to draw tangents. The number of data points used for the fitting was different for each probe and was dependent on the shape of the waveforms. Typically, 70 to 100 data points were used.
4) Find the minima located before the reference point and the end reflection point in the original waveform and plot horizontal tangent lines.

5) Identify the crossing points between tangents, as shown in Figure 3.26c, and calculate their separation, $L_t$. Subtract $L_0$ derived from the air-water calibration from $L_t$ to find $L_{app}$ (Figure 3.20).
6) Evaluate Equation (2.21) to obtain the apparent permittivity by using $L_{app}$ calculated above and $L_{cal}$ derived after the air-water calibration (Equation (3.1)).

As shown in Figure 3.26, the process of smoothing the first derivative of a TDR waveform deleted the first 100 data points. However, this was necessary in order to identify the maximum points. The smoothing also reduced the range of the derivative values on the y-axis and shifted the maxima towards the right (Figure 3.26b). As a consequence, with this method one does not find the real points of inflection corresponding to the change in convexity along the steepest gradients in the TDR waveform, but points close to these. This was not an issue because an empirically selected interval of data points had to be used to perform a linear model and to draw tangents.

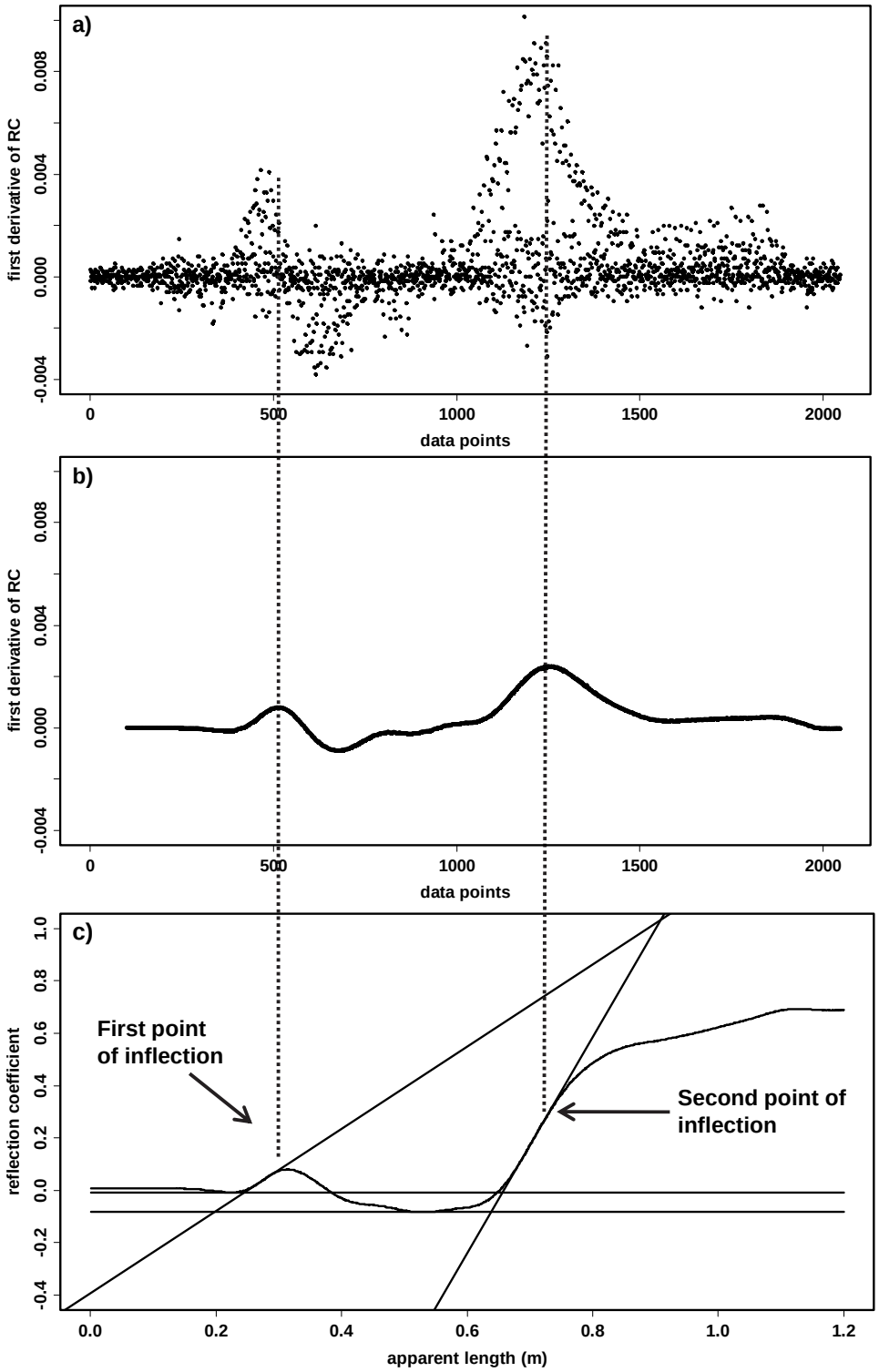



Figure 3.26 – The first derivative of a TDR waveform shown in (a) is smoothed in (b) in order to identify the maxima corresponding to the points of inflection in the TDR waveform shown in (c) with the fitting tangents added.

## 3.2.10. Accuracy of TDR after calibration: tests in reference materials

### 3.2.10.1. Introduction

A number of tests were carried out using TDR in reference materials (i.e., with known EM properties) in order to quantify the precision and the accuracy of the equipment setup and the selected method of analysis. The measurements were carried out in a temperature controlled room on the final equipment setup used in the field, with two levels of multiplexers and the probes connected to their corresponding channel. Four TDR probes of the same type as the ones used in the field monitoring station were also tested with and without multiplexers, and one of these was tested both manually, by drawing tangents in Matlab, and automatically, using the R scripts.

The apparent permittivity measurements were taken in air (short circuited), water at different temperatures and acetone.

BEC measurements were taken in eleven solutions with different electrical conductivities. A HI 9033 (Hannah Instruments, manufacturer claimed accuracy ± 1 %) conventional conductivity meter was used to provide reference EC values. Five of these solutions were obtained by mixing different proportions of the excess of the potassium chloride solutions used for the BEC calibration. The remaining six solutions were made up from different soils, diluted to a ratio of 5:1, using samples of topsoil, sandy subsoil (from the field trial site) and English China clay treated with different quantities of calcium (courtesy of Dr Azhar). The EC of the potassium chloride solutions ranged from 0.0303 S/m to 1.3400 S/m and from 0.0045 S/m to 0.4913 S/m for the soil solutions.

### 3.2.10.2. Accuracy for apparent permittivity

The results of the tests conducted to evaluate the performance of the TDR for obtaining apparent permittivity measurements are presented in this subsection.

Table 3.4 reports the results of the tests carried out to verify the accuracy of the calibration for apparent permittivity on the probes used in the field monitoring station. The variability between the sixteen probes, expressed as standard deviation, is caused by experimental error during the calibration procedure and test (for instance caused by small temperature variations between measurements), error in the waveform analysis and systematic error intrinsic in the TDR measurements. A comprehensive investigation of each of these sources of error was not conducted because of time constraints and because of the practical difficulty in separating the individual sources of uncertainty. However, measurements were taken to minimise these sources of error. The experimental error during calibration and measurements was reduced by using a rigorous laboratory procedure and by averaging at least three measurements every time. The random systematic error associated with the TDR device was minimised by taking the average of fifty measurements for each waveform.

Table 3.4 – Variability and accuracy of apparent permittivity measurements for the 16 probes used in the field monitoring station. The accuracy is expressed as the mean difference between measurement and reference for the 16 probes.

| Material | Std. dev. on the 16 probes | mean difference between measurements and reference (error) | Std. dev. of the error |
|---|---|---|---|
| **acetone (25 °C)** | 0.29 (1.38 %) | 0.28 (1.35 %) | 0.18 (0.90 %) |
| **water (10 °C)** | 0.30 (0.37 %) | 0.38 (0.46 %) | 0.29 (0.35%) |
| **water (25 °C)** | 0.43 (0.55 %) | 0.33 (0.42 %) | 0.26 (0.34 %) |
| **air (shorted)** | 0.06 (6.17 %) | 0.05 (5.10 %) | 0.03 (3.33 %) |
| **Mean** | **0.27 (2.12 %)** | **0.26 (1.83 %)** | **0.19 (1.23 %)** |

Overall, all the TDR probes performed similarly with a mean standard deviation for all the probes of 0.27 (2.12 %). The mean accuracy, which comprises all the sources of error just mentioned, was expressed as the absolute difference between the measured apparent permittivity and reference permittivity values reported in Weast (1972) (acetone at 25 °C: 20.70, water at 10 °C: 83.83, water at 25 °C: 78.54, air: 1.00). The results show that this difference was below 0.38 units of permittivity, and 5.10 % for all the materials.

The higher inaccuracy in air (up to approximately 5 %) is due to the very low permittivity of air, which corresponds to a short apparent length along the rods ($L_{app}$). A small error in the identification of the start and end reflection points will have a greater impact in the calculation of apparent permittivity compared to materials with longer apparent length. In other words the percentage accuracy of the TDR equipment used is reduced in materials with low permittivity.

It is important to note that a rigorous and direct comparison between the reference values and the measured permittivity was not possible because TDR measures an apparent permittivity, while the reference permittivity refers to the real component only, at a specific frequency. Acetone and water were chosen as reference values because they are not dispersive and their imaginary permittivity component is negligible in the TDR frequency range (Robinson et al., 2003b).

As can be seen in Table 3.5, which shows the performance of a selected probe of the same type of the ones used in the field monitoring station, the standard deviation of ten measurements taken in repetitions was generally low, demonstrating a good precision in the TDR measurements. Similar standard deviations, in the order of 0.10, were obtained from measurements in dry Leighton Buzzard sand, wet English China clay and in an unclassified clay-based soil in the field (Bristol Water plc, Blagdon, UK).

When compared to reference values, the absolute error was confirmed on average to be lower than 0.36 (1.69 %). Higher percentage errors were found in air, for the reasons discussed earlier in this section. With the exception of air, the percentage error was always lower than 2 %, and generally being lower than 1 %, which is again an indication of the good accuracy achieved by TDR.

Table 3.5 – Precision and accuracy of apparent permittivity measurements carried out in 10 repetitions with a single probe, with no multiplexers (mux0) and with two levels of multiplexers (mux2), with manual and automatic analysis of the waveforms.

| Material | Std. dev. on 10 repetitions (precision) | | | | mean difference to reference (accuracy) | | | |
|---|---|---|---|---|---|---|---|---|
| | mux0 manual | mux0 script | mux2 manual | mux2 script | mux0 manual | mux0 script | mux2 manual | mux2 script |
| **Acetone (25 °C)** | 0.10 (0.46 %) | 0.10 (0.46 %) | 0.20 (0.98 %) | 0.11 (0.54 %) | 0.13 (0.61 %) | 0.32 (1.54 %) | 0.20 (0.99 %) | 0.12 (0.58 %) |
| **Water (10 °C)** | 0.35 (0.42 %) | 0.38 (0.46 %) | 0.48 (0.58 %) | 0.28 (0.34 %) | 0.83 (0.99 %) | 0.49 (0.58 %) | 0.67 (0.80 %) | 0.25 (0.30 %) |
| **Water (25 °C)** | 0.20 (0.25 %) | 0.11 (0.14 %) | 0.40 (0.52 %) | 0.27 (0.34 %) | 0.20 (0.25 %) | 0.58 (0.73 %) | 0.41 (0.52 %) | 0.22 (0.29 %) |
| **Air (shorted)** | 0.03 (3.31 %) | 0.01 (1.30 %) | 0.03 (3.39 %) | 0.02 (2.23 %) | 0.03 (2.73 %) | 0.04 (3.91 %) | 0.03 (2.66 %) | 0.05 (5.04 %) |
| **Mean** | **0.17 (1.11 %)** | **0.15 (0.59 %)** | **0.28 (1.37 %)** | **0.17 (0.86 %)** | **0.30 (1.15 %)** | **0.36 (1.69 %)** | **0.33 (1.24 %)** | **0.16 (1.55 %)** |

As expected, Table 3.5 indicates that the automatic analysis of the waveforms showed an improvement in precision (lower standard deviations), since it eliminates the error introduced by human interpretation. However, it did not always give better accuracy when compared to manual interpretation. The script was empirically adjusted to draw tangents in the right position by selecting a suitable range of data points around the points of inflection (see section 3.2.9). If the shape of the waveform changed, the range of points used in the linear fitting might have become less adequate, leading to slightly inaccurate

results. However, an automatic analysis of the waveforms was necessary in the field monitoring, in order to cope with the large amounts of data being collected. Regular visual checks of the waveforms and tangents can indicate when it is necessary to adjust the range of data points to be fitted in the script. This allowed flexibility and improved the accuracy of the measurements.

Despite the attenuation caused by two levels of multiplexers, as explained in section 3.2.6.3 and shown for example in Figure 3.15, the use of multiplexers seemed to not have a substantial impact in the precision and accuracy of the measurements. However, Table 3.6, which reports the results obtained by four probes, each tested ten times in reference materials, confirms on average a slight increase in the standard deviation and in the percentage error when two levels of multiplexers were used. With only one exception (probe 2 in acetone in Table 3.6) the percentage error remained lower than 2 % for all materials, except to those in air. It is important to note that despite the standard deviation almost consistently increasing with two levels of multiplexers, this was not always true for the mean difference with respect to the reference value (error). For example probe 1 and probe 4 in Table 3.6 showed a decrease in the absolute and percentage error when two multiplexers were used. In addition, the overall absolute mean error was actually decreasing from 0.30 to 0.23. The increase in the percentage error was mainly due to the higher errors in air.

Table 3.6 – Mean standard deviation and mean error (expressed as a difference compared to the reference value) of measurements carried out 10 times in reference materials for four probes, with no multiplexer (mux0) and with two levels of multiplexers (mux2).

[Note: the waveforms were analysed automatically using the R scripts.]

| | | st. dev. on 10 repetitions (precision) | | mean difference to reference (accuracy) | |
|---|---|---|---|---|---|
| | **Material** | **mux0** | **mux2** | **mux0** | **mux2** |
| **probe1** | **Acetone (25 °C)** | 0.10 (0.46 %) | 0.11 (0.54 %) | 0.32 (1.54 %) | 0.12 (0.58 %) |
| | **Water (10 °C)** | 0.38 (0.46 %) | 0.28 (0.34 %) | 0.49 (0.58 %) | 0.25 (0.30 %) |
| | **Water (25 °C)** | 0.11 (0.14 %) | 0.27 (0.34 %) | 0.58 (0.73 %) | 0.22 (0.29 %) |
| | **Air (shorted)** | 0.01 (1.30 %) | 0.02 (2.23 %) | 0.04 (3.91 %) | 0.05 (5.04 %) |
| | **mean** | **0.15 (0.59 %)** | **0.17 (0.86 %)** | **0.36 (1.69 %)** | **0.16 (1.55 %)** |
| **probe2** | **Acetone (25 °C)** | 0.11 (0.51 %) | 0.10 (0.52 %) | 0.19 (0.92 %) | 0.58 (2.82 %) |
| | **Water (10 °C)** | 0.36 (0.43 %) | 0.24 (0.29 %) | 0.33 (0.40 %) | 0.42 (0.50 %) |
| | **Water (25 °C)** | 0.24 (0.30 %) | 0.36 (0.45 %) | 0.72 (0.92 %) | 0.30 (0.38 %) |
| | **Air (shorted)** | 0.02 (2.33 %) | 0.04 (3.64 %) | 0.02 (1.75 %) | 0.03 (3.08 %) |
| | **mean** | **0.18 (0.89 %)** | **0.18 (1.23 %)** | **0.31 (1.00 %)** | **0.33 (1.70 %)** |
| **probe3** | **Acetone (25 °C)** | 0.12 (0.58 %) | 0.19 (0.93 %) | 0.26 (1.27 %) | 0.30 (1.44 %) |
| | **Water (10 °C)** | 0.24 (0.29 %) | 0.37 (0.44 %) | 0.36 (0.42 %) | 0.41 (0.49 %) |
| | **Water (25 °C)** | 0.22 (0.27 %) | 0.27 (0.34 %) | 0.24 (0.31 %) | 0.25 (0.32 %) |
| | **Air (shorted)** | 0.02 (1.96 %) | 0.03 (2.42 %) | 0.04 (3.92 %) | 0.10 (10.19 %) |
| | **mean** | **0.15 (0.78 %)** | **0.21 (1.03 %)** | **0.22 (1.48 %)** | **0.26 (3.11 %)** |
| **probe4** | **Acetone (25 °C)** | 0.12 (0.56 %) | 0.18 (0.87 %) | 0.15 (0.71 %) | 0.19 (0.92 %) |
| | **Water (10 °C)** | 0.26 (0.31 %) | 0.23 (0.28 %) | 0.21 (0.25 %) | 0.18 (0.21 %) |
| | **Water (25 °C)** | 0.24 (0.30 %) | 0.30 (0.38 %) | 0.76 (0.97 %) | 0.22 (0.28 %) |
| | **Air (shorted)** | 0.02 (1.44 %) | 0.01 (1.34 %) | 0.06 (5.87 %) | 0.04 (3.95 %) |
| | **mean** | **0.16 (0.65 %)** | **0.18 (0.72 %)** | **0.29 (1.95 %)** | **0.16 (1.34 %)** |
| | **MEAN ON 4 PROBES** | **0.16 (0.73 %)** | **0.19 (0.96 %)** | **0.30 (1.53 %)** | **0.23 (1.92 %)** |

In summary, Table 3.5 shows that the automatic analysis of the waveforms improved the precision, but not necessarily the accuracy of the apparent permittivity compared to the manual analysis. Table 3.6 shows that the use of two levels of multiplexers slightly decreased the precision of the TDR and in some cases reduced the accuracy of the apparent permittivity measurements. However, the decrease in accuracy was not consistent for all the

probes and materials tested. The uncertainty associated with the TDR measurements either with no multiplexer or with two levels of multiplexers was comparable and therefore the addition of two levels of multiplexers was not considered a cause for concern.

In conclusion, the following considerations can be made based on the results shown above.

- The TDR can provide a good level of precision for the measurements of apparent permittivity, with a standard deviation generally smaller than 2 %. The work carried out in this study consisted mainly of the monitoring of the temporal changes of the soil EM properties, therefore, it was important to be able to detect these changes through time. In this case, the precision of the apparent permittivity measurements, expressed by the standard deviation, was more important than the absolute accuracy.

- The accuracy (absolute difference to reference values) for apparent permittivity measurements can also be considered good, being lower than 2 % and often lower than 1 %. Higher inaccuracies, up to approximately 5 %, can be found in air, where small uncertainties produce higher percentage errors due to the small reference permittivity value of air. In other words, the accuracy of the TDR equipment in use is reduced in media with very low apparent permittivity.

### 3.2.10.3. Accuracy for bulk electrical conductivity (BEC)

This subsection describes the results of the tests carried out in reference solutions of known EC in order to verify the accuracy of the TDR calibration. Some considerations on the calibration for BEC have already been discussed in section 3.2.8.1.

The standard deviation on a number of BEC measurements carried out in air, Leighton Buzzard dry sand, wet English China clay and in an unclassified clay-based soil in

the field (Bristol Water plc, Blagdon, UK) was 0.0002 S/m, which is an indication of the TDR precision of the BEC measurements.

The two-step calibration procedure previously described in section 3.2.8 provides a good level of accuracy, as shown by the low error values in Table 3.7. A range of potassium chloride solutions and soil solutions (dilution 5:1) were tested with a conventional conductivity meter (HI 9033, Hannah Instruments) and with TDR. The samples represent natural soil collected from the University of Birmingham test site (subsoil and topsoil), pure English China clay (ECC), and potassium chloride (KCl) solutions. The reference EC is the mean of three measurements with HI 9033, the mean TDR is the mean EC of the sixteen probes. The mean corrected reflection coefficient at long distances ($\rho_{corr}$) is also reported. The accuracy was expressed as the mean difference from the measurements with the sixteen TDR probes and the reference values obtained with the conventional conductivity meter.

As shown in Table 3.7 the absolute deviation from the reference values increased substantially with increasing BEC. However, the percentage error always remained relatively low, generally below 3 %, which demonstrates that TDR can achieve good accuracy in EC measurements. This is in accordance with the values reported by Huisman et al. (2008). The low standard deviations also confirm the good precision of the TDR measurements. However, both the difference to the reference values and the standard deviation were higher at very low electrical conductivities (< 0.0100 S/m). This could be related to the sensitivity of the TDR instrument or of the standard conductivity meter.

Table 3.7 – Accuracy of TDR for BEC measurements of the 16 probes used in the field monitoring station for a range of potassium chloride (KCl) and soil solutions (ECC: English China Clay).

| Sample | mean HI 9033 (S/m) | mean TDR (S/m) | mean $\rho_{corr}$ | error: mean difference to reference (S/m) | Std. dev. of the error |
|---|---|---|---|---|---|
| **ECC1** | 0.0045 | 0.0048 | 0.9292 | 0.0003 (7.58 %) | 0.0001 (2.49 %) |
| **subsoil2** | 0.0106 | 0.0098 | 0.8610 | 0.0008 (7.48 %) | 0.0004 (3.99 %) |
| **subsoil1** | 0.0108 | 0.0108 | 0.8483 | 0.0003 (2.51 %) | 0.0001 (1.35 %) |
| **topsoil1** | 0.0257 | 0.0255 | 0.6764 | 0.0004 (1.46 %) | 0.0002 (0.96 %) |
| **topsoil2** | 0.0264 | 0.0259 | 0.6719 | 0.0005 (1.80 %) | 0.0003 (1.27 %) |
| **ECC2** | 0.0458 | 0.0453 | 0.4898 | 0.0005 (1.15 %) | 0.0002 (0.52 %) |
| **ECC3** | 0.4913 | 0.4774 | -0.5493 | 0.0139 (2.83 %) | 0.0059 (1.21 %) |
| **KCl sol1** | 0.0303 | 0.0296 | 0.6336 | 0.0007 (2.40 %) | 0.0003 (0.86 %) |
| **KCl sol2** | 0.0534 | 0.0526 | 0.4312 | 0.0008 (1.57 %) | 0.0004 (0.68 %) |
| **KCl sol3** | 0.1427 | 0.1386 | -0.0182 | 0.0041 (2.85 %) | 0.0008 (0.60 %) |
| **KCl sol4** | 1.3400 | 1.3003 | -0.7912 | 0.0419 (3.13 %) | 0.0207 (1.55 %) |
| | | | **mean** | **3.16 %** | **1.41 %** |

It is worth noting that at EC values higher than ≈ 0.4-0.5 S/m the TDR is unreliable for apparent permittivity measurements, because the end reflection point becomes indistinguishable. In such cases the TDR loses its ability to measure the apparent permittivity but remains a useful tool for measuring the soil BEC.

It is important to note that these tests were carried out in salt solutions in order to measure reference EC values. In this case the BEC is equivalent to the EC of the solutions. This was the easiest, and possibly the only way, of comparing directly the measurements with TDR and another tool used as a reference in the same volume of sample. In order to produce the accuracy values reported in Table 3.7 it was assumed that the conventional conductivity meter HI 9033 provided the true EC values. The accuracy claimed by the manufacturers for this instrument is ± 1 %.

## 3.2.11. Temperature sensor calibration and accuracy

This section describes the calibration of the thermocouples (Omega Engineering, UK) used in the field monitoring station. The accuracy claimed by the manufacturer of these thermocouples is ± 1 °C. The calibration allowed the adjustment of possible measurement offset by comparing the temperature measured by the sensor and the reference temperature. An incubator was used at a range of temperatures (from -3 °C to 27 °C), with increments of approximately 3 °C to provide these reference values. The reference temperature was read from the display of the incubator and compared using a mercury thermometer.

After adjusting the mean offset of each sensor during calibration, the accuracy was tested repeatedly at different times (on separate days). During the calibration and tests the sensors were left in the incubator for a few hours in order to equilibrate at the required temperature.

Figure 3.27 shows the reference temperature against the temperature measured by one of the calibrated sensors and a linear fitting applied to the data. The $R^2$ of this fitted line was 0.9995 demonstrating the good reliability of the measurements after calibrating the sensor offset. Similar $R^2$ values were obtained for the other two thermocouples.

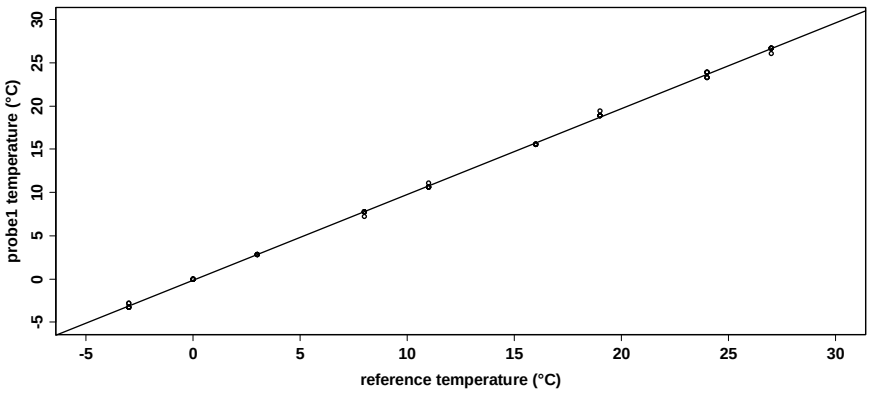



Figure 3.27 – Comparison between the temperatures measured by a thermocouple after calibrating the sensor offset and the reference temperature of an incubator.

# 3.3. FIELD METHODOLOGY

## 3.3.1. University of Birmingham test site

In order to monitor the EM soil properties (i.e., apparent permittivity, BEC), their gradient with depth and their seasonal variation an experimental field monitoring station was developed on campus at the University of Birmingham, UK (Figure 3.28).

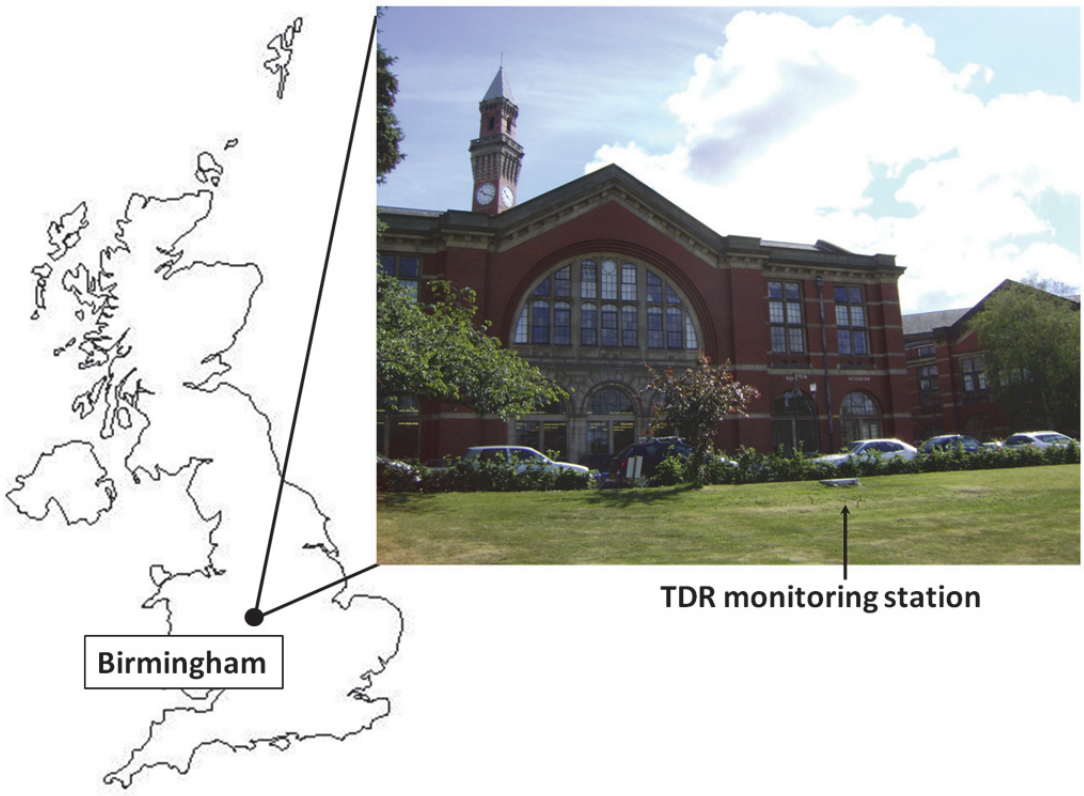



Figure 3.28 – Location of the TDR monitoring station at the University of Birmingham campus, UK.

Figure 3.29 shows the geological map of the area, obtained from the records of the British Geological Survey. The location of the field trial site corresponds to the quaternary glaciofluvial deposits (GFDMP, in light blue) dated to the Middle Pleistocene (0.126 – 0.781 Ma). The deposits are made by sand and gravel.

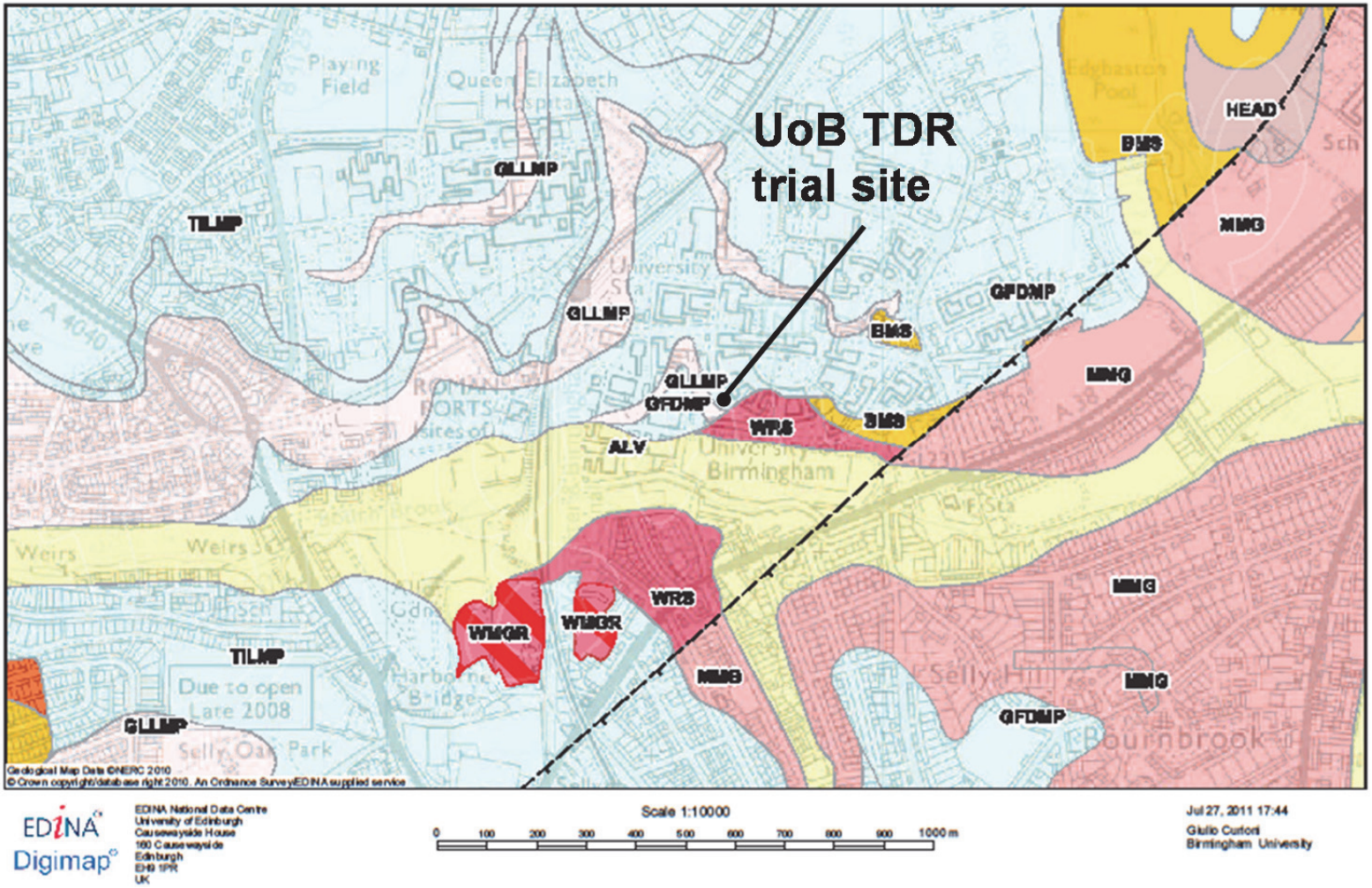



Figure 3.29 – Geological map of the University of Birmingham trial site, courtesy of the British Geological Survey (Geological Map Data © NERC 2012).

# CHAPTER 3: METHODOLOGY

The location was chosen in agreement with the University Estates department. This site was chosen from three possible options as it best satisfied the requirements for this research. The requirements for the site were the followings:

- Grassed flat area, with soil left undisturbed for several decades.
- Enough space to be able to install a monitoring station and bury pipes as reference targets.
- A stable area, i.e., no works to be carried out on the site for the length of the project.
- Easy access. Proximity to the Civil Engineering building.

The selected area was on a sloping grassed area, but the location was chosen to minimise the slope by installing the monitoring station on the top, close to a road. The reason for preferring a flat area derived from the need to minimise the lateral flow of water on the ground surface and within the soil that could further complicate the study of the soil properties. The distance to the road (≈ 3 m) was considered enough so as not to affect in any substantial way the monitoring.

Although the underlying geology in the area of the test was previously stated as being quaternary glaciofluvial deposits, the surface soil deposit was made ground, left undisturbed for four or five decades (Estates personal communication). The water table was known to vary between 6.5 m and 8.0 m depth (Hatzichristodulu et al., 2002). The soil comprised approximately 0.2 m of topsoil rich in organic matter overlying sandy subsoil, rich in coarse particles (gravel and cobbles).

The field description of the soil profile and the soil characterisation carried out in the laboratory are described in section 4.1.

## 3.3.2. Field installation

In this section the methodology for the excavations and installation of the experimental equipment at the University of Birmingham test site is reported. The installation of the field TDR monitoring station was completed in two days, on the 8th and 9th of July 2010. The first day two trenches 2.5 m by 1.3 m and 3 m by 2.5 m large, both approximately 1 m deep, were dug on the selected grassed area. The smaller trench, from now on named trench 1, was used for the TDR installation. The bigger trench (trench 2) was dug on the 8th of July and fully backfilled on the 12th of July. Trench 2 was used for the installation of metal and plastic pipes at a range of depths in order to provide reference targets for the GPR (more details follow later in this section and in section 3.3.7).

Figure 3.30 shows the phases of the excavations. In both trenches the turf and topsoil were removed manually. Trench 1 (top left and right in Figure 3.30) was mainly dug manually and the horizons were separated on plastic sheets during the excavation in order to backfill them in the same order as they were collected. Due to the warm and very dry conditions at the time of the installation, it was decided to use a mechanical digger to dig trench 2 (Figure 3.30c) and the deeper portion of trench 1 (Figure 3.30a). Due to the use of a mechanical digger and because of time constraints only the turf was kept separated from the subsoil in the trench 2.

A third hole was dug (Figure 3.30d) and a cubic metre of bulk subsoil was collected and brought to the laboratory. Smaller quantities of soil samples were also collected at different depths from both trenches 1 and 2 for soil analyses.

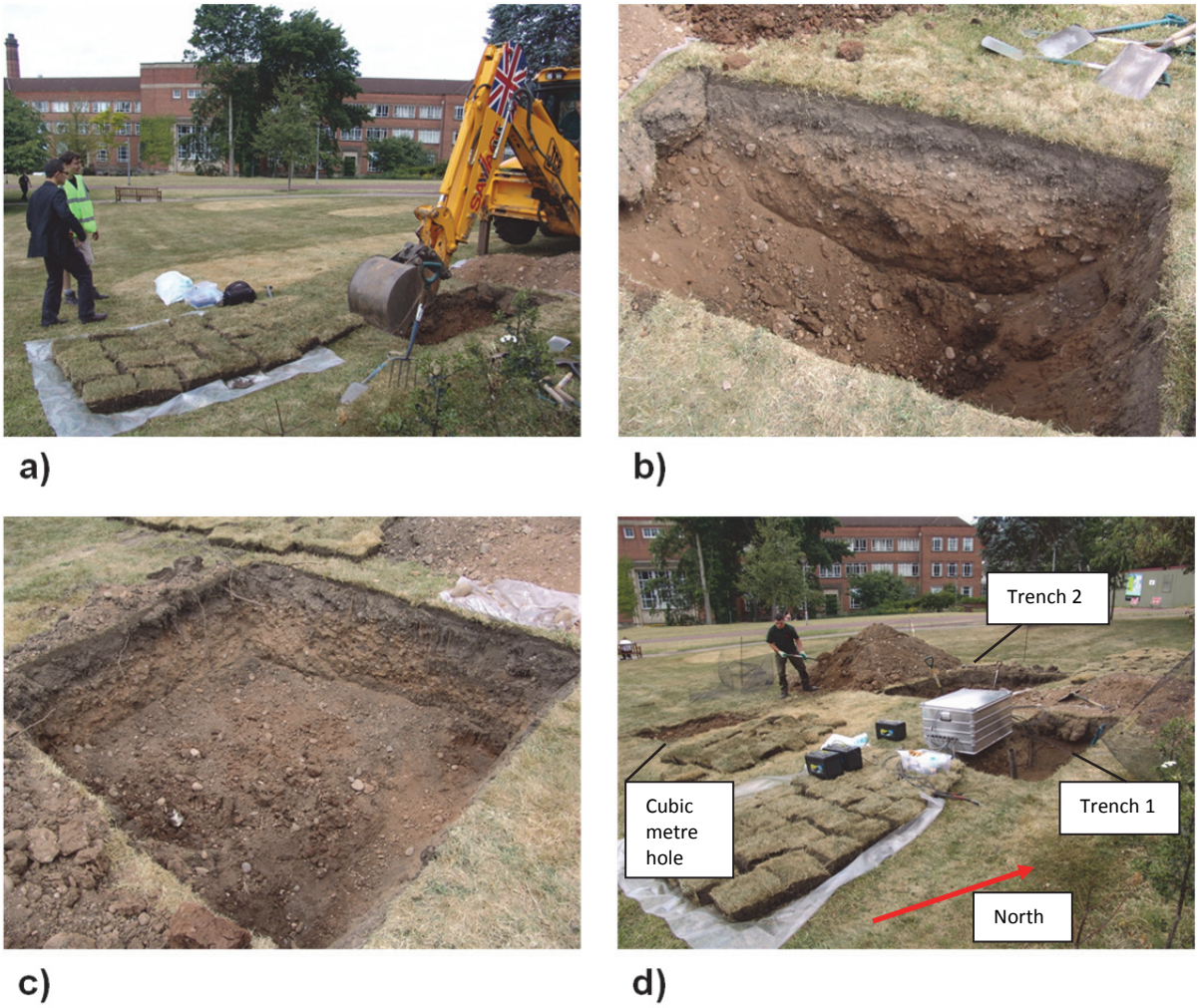



Figure 3.30 – Phases of the excavations at the University of Birmingham test site; a) and b) excavation of trench 1 used for the TDR installation; c) excavation of trench 2 where the targets were buried; d) from left to right, cubic metre hole where a large soil sample was taken for lab work, trench 2 and trench 1.

The excavations took several hours, therefore, it was decided to install the TDR monitoring station the following day, on the 9$^{th}$ of July 2010.

The two vertical arrays of TDR probes were inserted on one side of trench 1, starting from the bottom. **Array 1** was installed on the left side of the trench, looking towards the road in direction N-NE. **Array 2** was installed on the right side of the trench. The arrays were approximately 1 m to 2 m apart. Due to the gravelly conditions of the soil it was not

possible to keep the lateral separation between the two arrays constant, as shown in Figure 3.31a and b. For the same reason, the vertical separation between probes of the same array was not fixed. The flexibility provided by the heat shrinkable tubes proved useful in this occasion because the exact locations of the probes could not be established a priori. The three temperature sensors (Figure 3.31c) were buried on the right side of the trench, close to array 2.

The soil horizons were manually backfilled to their excavated depth. Careful manual compaction of the soil was conducted close to the probes and cables. The rest of the trench was compacted by standing on the soil and by using a spade and a heavy metal tube (visible in Figure 3.31b and d). The compaction was performed in multiple steps approximately every 0.1 m of backfilled material. A mechanical compactor was not used to avoid damage to the probes and cables.

In order to keep the TDR probes' rods parallel during the installation a specifically developed plastic tool was used as a waveguide and it was removed after the probe was completely inserted into the side of the trench, as shown in Figure 3.32. Twelve TDR probes were fully inserted in the soil; probe 6, installed at 0.42 m of depth, was partially inserted; probes 3, 4 and 5, installed at 0.18 m, 0.25 m, 0.35 m of depth respectively, were buried due to the very gravelly conditions of the soil at that depth. Table 3.8 reports the final depths (m) of the TDR and temperature probes installed at the University of Birmingham field monitoring station. The relative numbered names (identifier) of the TDR probes are also shown.




Figure 3.31 – a), b) and d) Details of the field installation of the TDR probes; c) temperature sensor with insulating cable; e) installation of the box with the equipment.

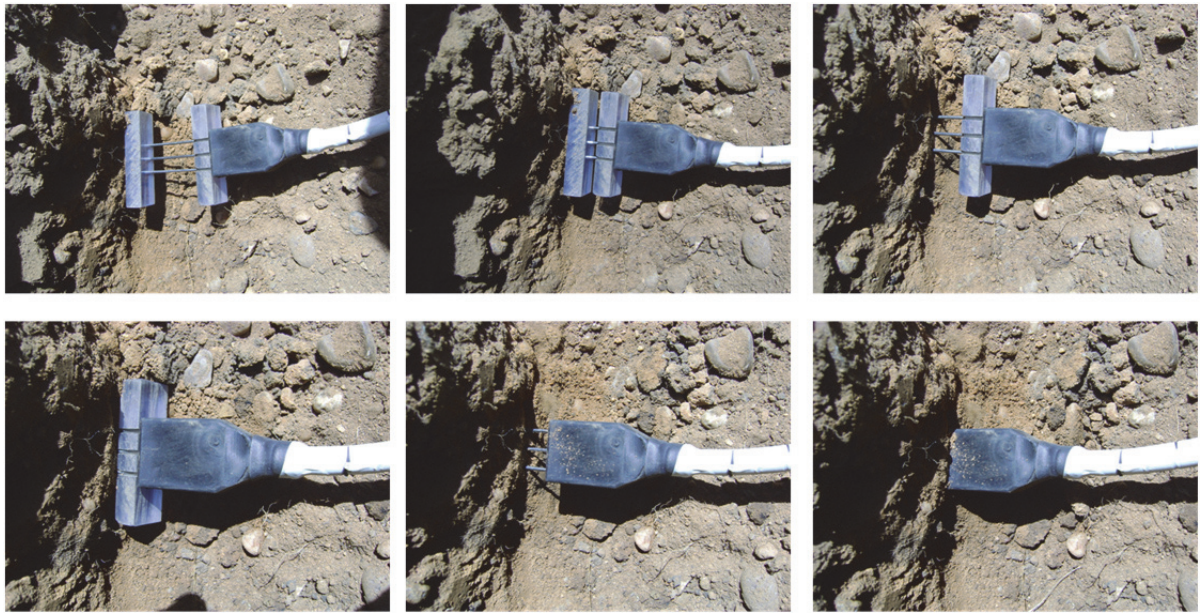


Figure 3.32 – Details of the insertion of the TDR probes. [Note: each probe was inserted approximately parallel to the ground surface]

Table 3.8 – Probe identifier and depth (m) of the TDR and temperature sensors installed at the University of Birmingham field monitoring station.

| array 1 | depth (m) | array 2 | depth (m) | temperature sensors depth (m) |
|---|---|---|---|---|
| probe 1 | 0.07 | probe 2 | 0.07 | 0.16 |
| probe 3 | 0.18 | probe 4 | 0.25 | 0.43 |
| probe 5 | 0.35 | probe 6 | 0.42 | 0.80 |
| probe 7 | 0.60 | probe 8 | 0.59 | |
| probe 9 | 0.70 | probe 10 | 0.72 | |
| probe 11 | 0.77 | probe 12 | 0.83 | |
| probe 13 | 0.87 | probe 14 | 0.93 | |
| probe 15 | 1.08 | probe 16 | 1.06 | |

Five pipes were installed in trench 2 at different depths (Figure 3.33) in order to provide reference targets with known position for the GPR surveys. Three pipes were stainless steel pipes, 2.5 m long and 25 mm in diameter, the other two were polyethylene pipes, 2 m long and 100 mm in diameter. The vertical cross-section of trench 2 is shown in Figure 3.34.

The depth of each pipe was taken from the surface with a measurement tape. The accuracy of the reference depth is deemed to be within a few centimetres, due to the difficulty of measuring the depth in this manner. For example it was very difficult to determine an exact start reference value at the surface because of the irregular micromorphology of the grassed cover. The pipes were buried parallel to the soil surface, but depth differences were measured at each end of the pipes, from the top of the pipes. The mean depth of two measurements taken at the ends of the pipes was used as the reference depth (from left to right in Figure 3.34: pipe 1: (0.32 + 0.32)/2 = 0.32 m; pipe 2 and 3: (0.50 + 0.56)/2 = 0.53 m; pipe 4: (0.92 + 0.94)/2 = 0.93 m; pipe 5: (1.03 + 1.03)/2 = 1.03 m). A problem associated with these reference depths was the soil settling with time. It was clear after some weeks that the soil surface sank by a few centimetres. Following these considerations it seems reasonable to say that the reference depths could vary by a few centimetres. However, it was not possible to quantify this uncertainty value.



Figure 3.33 – Installation of stainless steel and polyethylene pipes at the University of Birmingham test site (trench 2).

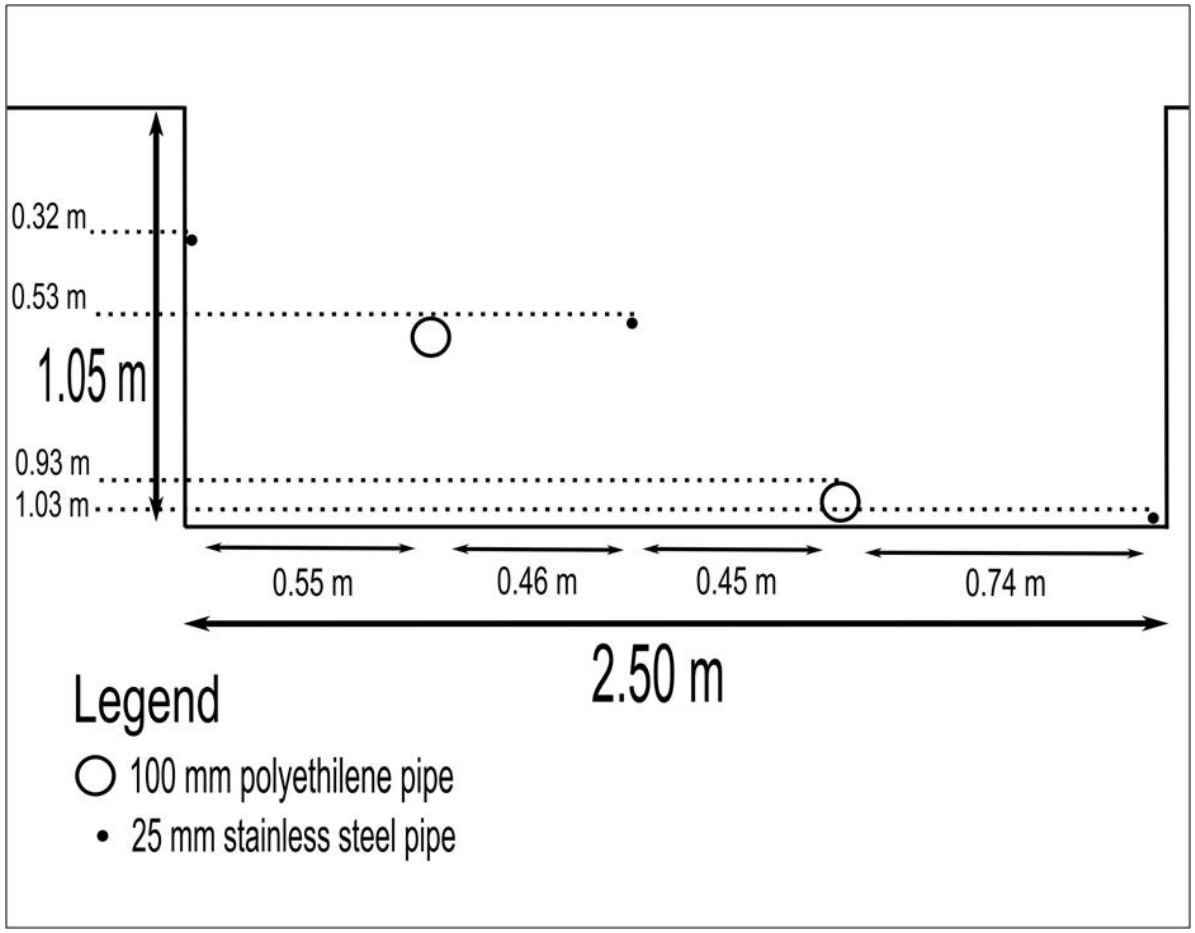



Figure 3.34 – Vertical cross-section of the trench 2, at the University of Birmingham test site.

## 3.3.3. Field monitoring

This section describes the methodology related to the field soil monitoring by TDR. Information on a weather station used to relate the soil data to the weather parameters is also reported. Details such as the sampling rate and issues arisen with the equipment are discussed.

A few measurements were taken during the installation of the TDR probes to check whether the waveforms were sensible and did not show unexpected features such as several multiple reflections across the length of the rods. The soil was left to settle for a period of a few weeks and the proper soil monitoring started on the 20$^{th}$ of August 2010.

The sampling rate in the field was set in the Matlab script to one measurement per probe every hour, both for apparent permittivity and BEC. The first half of an hour 16 measurements of apparent permittivity were taken, followed by 16 measurements of BEC on the second half of an hour. The measurements were taken starting from the probes closer to the surface, that is starting from the shallower probe in the array 1 (probe 1), followed by the shallower probe in array 2 (probe 2) and so on (the probes' identifiers were shown in Table 3.8 in section 3.3.2). In this way two measurements at a similar depth were collected in a short period of time, facilitating the direct comparison between the two arrays. It was convenient to keep this sampling rate for the Matlab script to work without problems (more frequent measurements resulted in errors in the Matlab script and consequently in losses of data). In section 3.3.4 it is demonstrated that this was sufficient to detect temporal variations of the measured soil properties.

The sampling rate of the temperature sensors was set to a measurement every 10 minutes in the Omega Engineering TRH software. The TRH software allowed simultaneous readings of the three temperature probes. Due to the slow rate of change of the soil temperature this sampling rate was considered sufficient to detect temperature variations during the field monitoring.

A weather station (Vaisala Weather Transmitter, WXT520) was installed as part of another doctoral project on the roof of the Civil Engineering building at the University of Birmingham, and the data were kindly made available for this study (courtesy of Dr Jefferson and Ms Doan). The building was approximately 100 m away from the field TDR monitoring station. The parameters collected from the weather station were the wind direction (°), the wind speed (m/s), the rainfall (mm), the air temperature (°C), the relative humidity (%), the barometric pressure (hPa). The weather data were collected every 10 minutes.

During the first months of the field monitoring the Matlab script was not yet completely optimised and failed several times, nearly once per week. As a consequence the data collection was not always continuous, but gaps of a few hours up to a few days occurred regularly until the 21st of October, when the Matlab script was finally fixed. However, some gaps in the data occurred during the whole period of the data collection, for example when the batteries went flat before it was possible to replace them (e.g., during holidays). It also happened a few times that the netbook stopped working for no apparent reason, while the batteries were fully charged. This problem was addressed by restarting the netbook every time the batteries were changed and by checking it almost daily to save the soil temperature data. In fact, it was still possible to access the TDR data up to the moment when the netbook stopped functioning, because the TDR data were automatically saved on separate files on the netbook by the Matlab script. In contrast, the soil temperature data were simply stored on a table in the TRH software and were lost since they were last saved whenever the netbook stopped working. Small temporal gaps in the data of approximately one or two hours occurred weekly, since the data collection had to be stopped for replacing the batteries. Due to the long-term nature of the monitoring these small gaps were not a problem.

The batteries lasted approximately eight days at the start of the monitoring and reduced to seven/six days after one year of monitoring. They were replaced weekly with an identical set of charged batteries. The power consumption of the TDR100 was limited, but the netbook consumed considerably despite having applied the energy saving settings. However, this was not a critical issue due to the vicinity and easy access of the field TDR monitoring station.

### 3.3.4. Considerations on the data collected by the field TDR monitoring station

This section describes a few examples of the data collected from the field TDR monitoring station in order to demonstrate the validity of the selected methodology.

Figure 3.35 shows the profile of apparent permittivity and BEC (mS/m; in the Figure labelled as $EC_b$) with depth of the two arrays installed in the ground. The data refer to a period of 4 days starting from 00:00 on the 1st of October 2010. During this period two main rainfall events occurred and were measured by the nearby weather station. The first rainfall event lasted 17 hours, starting from 00:50 on October the 1st, with a cumulative rainfall of 25.8 mm. The second lasted approximately 10 hours and occurred between 04:35 and 14:00 on October the 3rd, with a cumulative rainfall of 16.6 mm. Figure 3.35a and c show the sudden increase in apparent permittivity for the shallower probes following the rainfall. Also evident is a smaller increase in apparent permittivity measured by the deeper probes. This occurs several hours after the rainfall event and this delay can be seen to increase with increasing depth. In addition, it can be seen in Figure 3.35b and d that the BEC at different depths does not increase uniformly and there seems to be a more conductive layer between 0.80 m and 0.90 m depth. A sampling rate of one measurement per hour allows these changes to be tracked with sufficient detail. Figure 3.35 also shows the need for two vertical arrays of probes to cross validate the results. Since the probes measure small volumes of soil, they are sensitive to the small-scale spatial variability of the soil properties. The two arrays do not provide enough information to study the spatial distribution of these properties, but can demonstrate the existence of similar trends in the data. The use of multiple probes allows the detection of variations with depth. The wetter and more conductive horizon (Figure 3.35b) present between 0.80 m and 0.90 m of depth might not have been detected if a smaller number of probes were used. Installing horizontal

probes has the disadvantage of being laborious and disruptive, but allows more flexibility in the choice of the position of the sensors compared to measurement systems inserted from the ground surface. In addition, horizontal probes are less affected by possible preferential water paths occurring down the side of vertical probes (Topp et al., 2003).

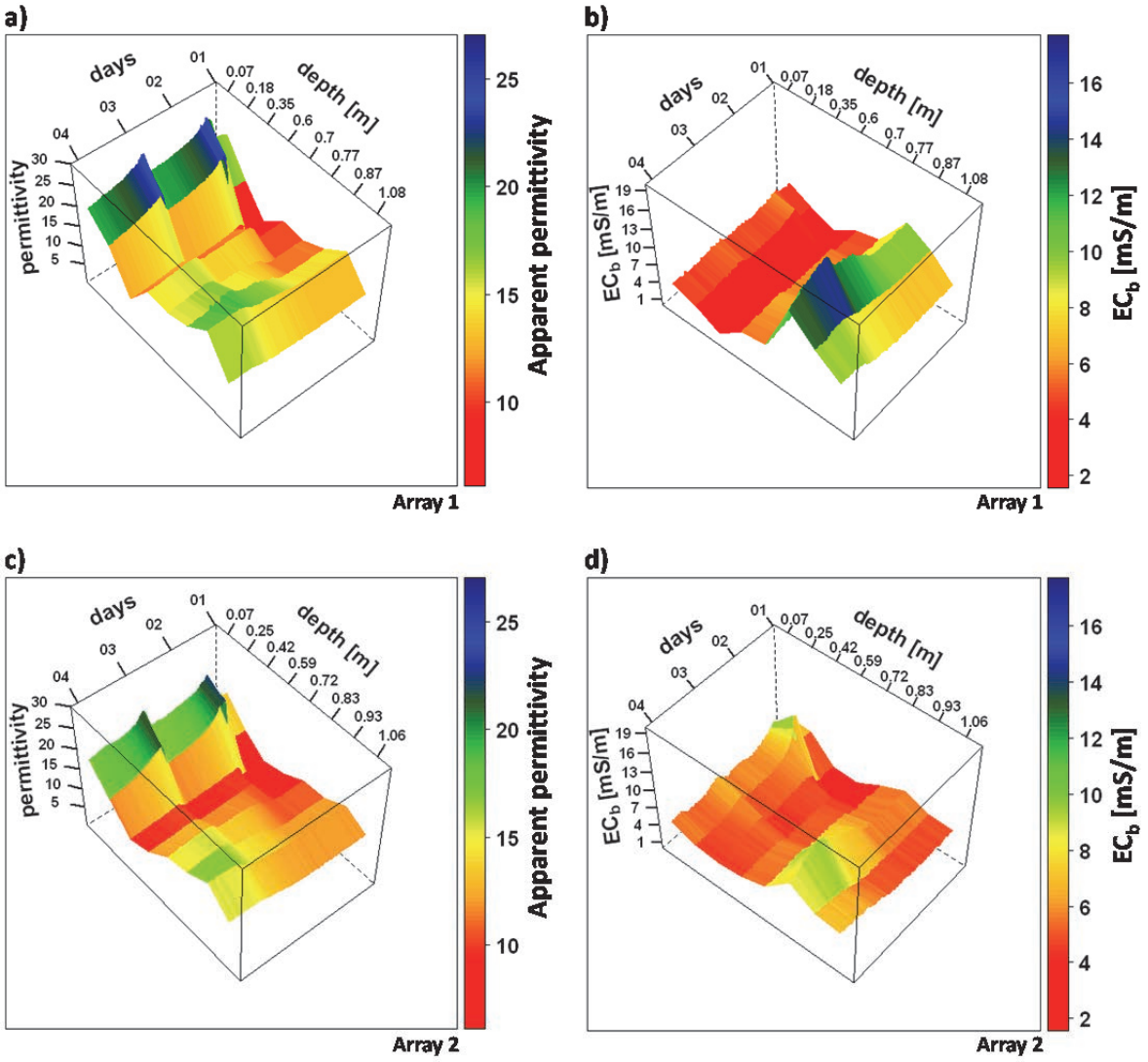



Figure 3.35 – Apparent permittivity and BEC vertical profiles obtained from array 1 (a and b) and array 2 (c and d) of the field TDR monitoring station at the University of Birmingham, for a period of 4 days starting from the 1st October 2010.

Figure 3.36 shows an example of the data obtained from the field TDR monitoring station corresponding to specific depths, for a period of one week where no rain occurred. To test the precision of the apparent permittivity measurements in the field, a linear regression was performed on the data (solid lines in Figure 3.36). The standard error of the residuals was 0.1017, 0.0668 and 0.0556 for the probes at 0.07 m, 0.60 m and 1.08 m depth respectively. These values agree well with the standard errors reported by Heimovaara and Bouten (1990) and Menziani et al. (1996), and demonstrate the high precision that can be obtained using TDR in the field. This means that the TDR can detect changes bigger than 0.1 units of apparent permittivity. In section 3.2.10 higher standard deviations (approximately 0.3) were reported associated with tests conducted in reference materials (acetone, water and air). Even if this higher value is used the TDR remains able to detect changes of 0.3 units of apparent permittivity, which can still be considered very good.

Figure 3.36b shows irregular BEC data for the same period for one set of probes. This is caused by daily temperature variations as shown by the sinusoidal behaviour of both the shallower TDR probe (0.07 m) and the temperature sensor (0.16 m). The influence of temperature reduces with depth as the temperature variability decreases, hence the consistent sinusoidal pattern evident for shallower depths becomes less pronounced, making it more difficult to interpret the relationship between BEC and temperature. As a consequence, the BEC measurements at higher depths become less clear, resulting in a decrease of precision. The standard error of the linear regression performed on the probes at 0.42 m and 1.06 m depth was 0.1116 mS/m and 0.1681 mS/m respectively. However, this is still considered a good level of precision, since the TDR remains able to detect changes of BEC bigger than 0.5 mS/m.

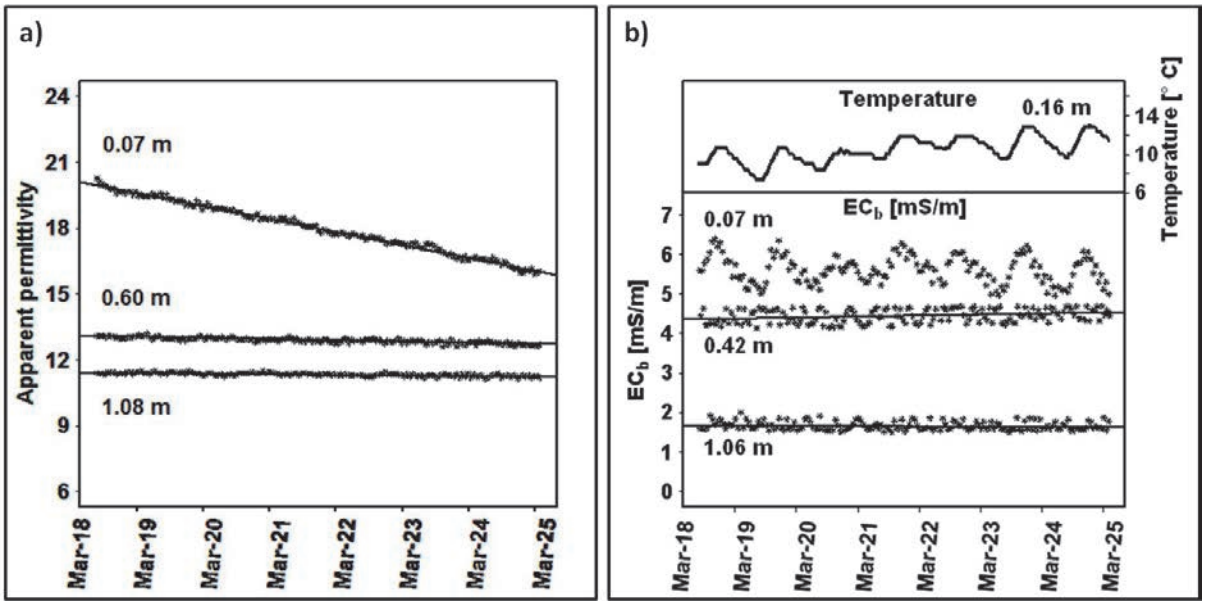



Figure 3.36 – a) Apparent permittivity and b) BEC and temperature measurements from selected probes at specific depths in the field over a period of one week with no rainfall occurring in March 2010..

## 3.3.5. Methods of soil characterisation

In order to characterise the soil a number of soil analyses were conducted in the laboratory on the soil samples collected from the field. The following properties were determined:

- Particle size distribution (BS 1377-2, 1990).
- Gravimetric water content (BS 1377-2, 1990).
- Dry and bulk density (BS 1377-2, 1990).
- Particle density (BS 1377-2, 1990).
- pH (BS 1377-3, 1990).
- Organic matter (BS 1377-3, 1990).
- Electrical conductivity (BS 7755-3.4, 1995).

The experimental methodology was compliant to the British Standard (BS 1377-2, 1990; BS 1377-3, 1990; BS 7755-3.4, 1995). The methods of analysis are described in detail in the British Standard and therefore are not reported here. Each test was conducted at least in duplicates (and often more than twice) and the mean values are reported later in section 4.1.

### 3.3.6. Empirical calibration (apparent permittivity *versus* volumetric water content)

In order to simulate the variation of volumetric water content by the SPAW model (see section 2.4.1.2), it is necessary to input an initial soil water value. To achieve more accurate measurements of soil water content by TDR it is necessary to perform a site-specific calibration relating the apparent permittivity to the volumetric water content (Ponizovsky et al., 1999; Gong et al., 2003; Laurent et al., 2005; Benson and Wang, 2006). Therefore an empirical calibration was performed in the laboratory on a number of subsoil samples collected from the University of Birmingham test site. The soil samples were wetted, manually mixed and then placed into plastic cylinders (0.1 m high, 0.1 cm in diameter) in order to achieve the dry density as measured in the field and specific bulk densities depending on the desired water content (Take et al., 2007; further details on the sample preparation are given in an unpublished MSc report by Ollerton, 2012). The tests were replicated by using two separate cylinders kept under the same conditions. Measurements were taken in an incubator at four different temperatures (i.e., 5, 10, 15, 20 °C) and at nine water contents, ranging from 0 to approximately 18 % of gravimetric water content. Measurements were also taken at higher water contents (i.e., at 21 and 24 %), but were discarded from the analysis because of the formation of a layer of water 25-35 ml thick on top of the soil sample. It was deduced that the saturation level occurred between 18

and 21 %, and therefore that the chosen range covered the soil conditions from completely dry to approximately the saturation level. The TDR probes were of the same type used in the field monitoring station and were inserted vertically in the middle of each cylinder, which were then sealed with tapes to prevent evaporation (Figure 3.37).




Figure 3.37 – Experimental setup for the site-specific empirical calibration.

Eight TDR measurements were taken at a specific temperature, allowing a few hours between one temperature and the next. The temperature was double-checked by means of a thermocouple left inside the incubator. At the end of each test at a specific water content, the soil samples were put in an oven at 105 °C for 24 hours to determine the gravimetric water content. The results of this test are described in section 4.4.4.

## 3.3.7. GPR analysis

Two important objectives of this study were to verify the effects of changing soil conditions on GPR surveys and also to compare the TDR and GPR data in the field. For these purposes, five reference targets were installed in proximity to the field TDR monitoring station at the University of Birmingham, as mentioned previously in section 3.3.2. Stainless steel and polyethylene pipes of different diameter (25 mm and 100 mm respectively) were used. The stainless steel pipes were chosen in order to provide clear reflections and facilitate the data interpretation (e.g., fitting of the hyperbolae). The plastic pipes were buried for comparison.

The GPR system used in this study was the dual-frequency (250-700 MHz) pulse Detector Duo GPR manufactured by IDS Ingegneria Dei Sistemi S.p.A. (Figure 3.38). This GPR has a fixed antenna separation that makes it quick and easy to use. Its ability to scan the soil at two separate frequencies allows different penetration depths and resolutions to be achieved.



Figure 3.38 – Detector Duo GPR (IDS Ingegneria Dei Sistemi S.p.A.).

A regular grid was established on the field nearly perpendicular to the pipes buried at the University of Birmingham campus. Yellow pegs were pushed and left in the ground at

both ends of the grid. In order to scan the same area two wires were fixed in position close to these pegs as shown in Figure 3.39 before conducting a GPR survey.



Figure 3.39 – GPR survey on a predefined transect at the University of Birmingham test site.

The grid consisted of three transects called transect 1, transect 2 and transect 3, as shown in Figure 3.40, each 0.4 m wide and 8.36 m long. Transect 2 and 3 were parallel, while transect 1 ran diagonally across the grid.

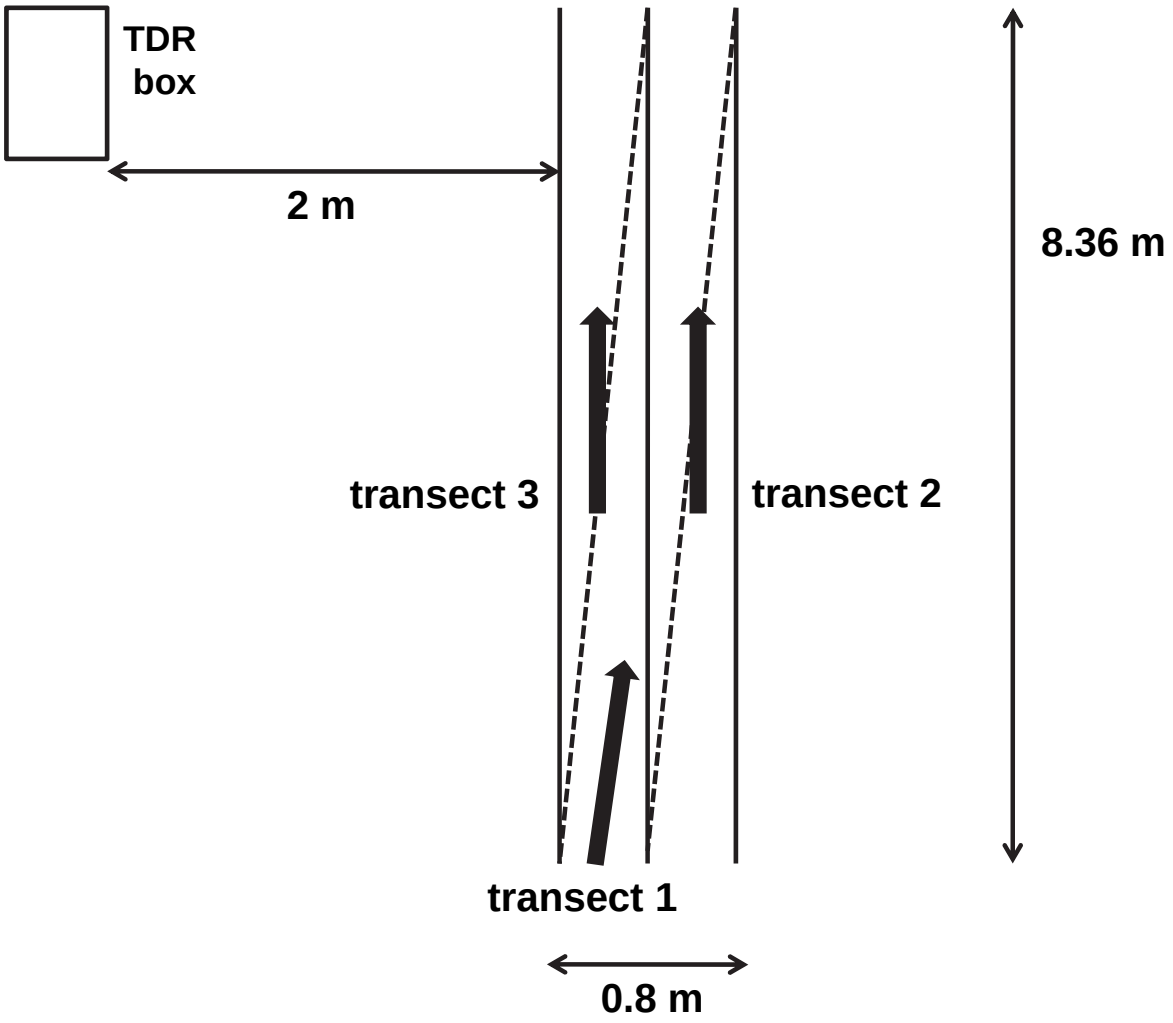



Figure 3.40 – Diagram of the GPR grid defined at the University of Birmingham test site. [Note: not to scale.]

The GPR surveys were carried out almost weekly starting from November 2010 until February 2012. Four scans were normally run for each transect, i.e. a total of 12 scans per survey. Only transect 1 was used in the subsequent GPR analysis because it seemed to give slightly better images and because the data analysis was very time-consuming.

# 3.4. SPAW MODEL

## 3.4.1. Introduction

As explained in section 2.4.1.2 the SPAW (Soil-Plant-Air-Water) model allows the soil water content to be simulated from soil and weather input parameters (Saxton and Willey, 2006; Saxton and Rawls, 2006; Saxton et al., 2006; see also Table 2.1 and 2.2, and Figure 2.8). In the context of this thesis, it was deemed valuable to verify the SPAW model performance by comparing the results from the simulations with the data collected from the TDR monitoring station at the University of Birmingham. Despite the SPAW model being designed for agricultural purposes it will be demonstrated in section 4.5.2 that its use could be extended to other applications, such as modelling the soil water content in semi-natural soils, in this specific case an anthropogenic soil covered by grass. Furthermore, the SPAW model could be a useful tool to validate calibrations between apparent permittivity and volumetric water content directly in the field and to help choose the most appropriate calibration model. Simulating the soil water content with time could provide useful to quantify the potential water content variation for a specific soil given only weather data and initial soil conditions. The SPAW model was chosen because of its effectiveness, simplicity, minimal input requirements and computational time, and not least its free availability (Saxton and Wiley, 2006; Rao and Saxton, 1995; Arora and Gajri, 1996; Lenka et al., 2008). This section describes the application of the SPAW model to the University of Birmingham test site. The results will be discussed in section 4.5.

## 3.4.2. SPAW inputs

The SPAW input data comprise information on the climate, soil and crop type. Rainfall is required for the SPAW model to work. However, additional weather parameters

are necessary to calculate the evapotranspiration, which is not directly calculated by the model. In this study the open source software DailyET developed by Cranfield University (UK) was used to calculate the monthly evapotranspiration from monthly temperature maxima and minima, relative humidity, solar radiation and wind speed (Hess, 1996). Table 3.9 lists the monthly evapotranspiration (cm/month) calculated by DailyET using the standard and widely used Penman-Monteith method (Penman, 1948; Monteith, 1965; Allen et al., 1998; Howell and Evett (undated)). These values were input into the SPAW model as part of the simulations.

Table 3.9 – Monthly evapotranspiration values calculated by DailyET using the Penman-Monteith method.

| month | evapotranspiration (cm/month) |
|---|---|
| 2010-10 | 3.30 |
| 2010-11 | 1.94 |
| 2010-12 | 1.03 |
| 2011-01 | 1.74 |
| 2011-02 | 2.31 |
| 2011-03 | 5.11 |
| 2011-04 | 8.93 |
| 2011-05 | 9.92 |
| 2011-06 | 12.20 |
| 2011-07 | 10.36 |
| 2011-08 | 8.57 |
| 2011-09 | 7.00 |
| 2011-10 | 5.09 |
| 2011-11 | 2.00 |
| 2011-12 | 2.24 |
| 2012-01 | 1.65 |
| 2012-02 | 3.56 |
| 2012-03 | 7.22 |
| 2012-04 | 6.50 |
| 2012-05 | 12.46 |
| 2012-06 | 9.65 |

Table 3.10 shows the input (in bold) and output soil parameters used in the SPAW model. A soil comprising of three horizons was created, with inputs based on the results of the soil characterisation conducted on the University of Birmingham soil (see section 4.2). The SPAW model implements the empirical equations of Saxton and Rawls (2006) (see Table 2.1 and 2.2)[8]. Table 3.10 shows the output texture class (i.e., class of particle size distribution), wilting point (WP), field capacity (FC), saturation water content (Sat) and saturated hydraulic conductivity (Sat Cond), for the studied soil. The SPAW also calculates the soil water characteristic curves (see appendix E) and the relationship between hydraulic conductivity and water content. These relationships, together with weather inputs, are used to simulate the water infiltration into the soil.

The SPAW model was developed for agricultural monitoring, therefore an additional input required by the model is the crop type. For this study, two default typical crops were selected, 'Example pasture – cool season grass' and 'Example pasture – warm season grass'. These crop types were thought to be the best representation of the actual plant cover at the University of Birmingham test site. The first was used as input in the months from October to March, the second for the remaining months. Relevant parameters associated with the crop type are the typical canopy cover (that could intercept rainfall) and typical root depth.

[8] The equations by Saxton and Rawls (2006) were coded in R in order to verify their consistency and the presence of bugs in the SPAW software, which was confirmed to be correct. Due to the complexity of coding the runoff estimates by the SCS-CN method and the Darcy equation, these were not tested independently.

Table 3.10 – Input (in bold) and output soil parameters by SPAW (Saxton and Rawls, 2006; see also Table 2.1 and 2.2, and Figure 2.8).

| **topsoil** | | | | | | | | | | |
|---|---|---|---|---|---|---|---|---|---|---|
| **Sand** | **Clay** | **Silt** | **Gravel** | **Salinity** | **OM** | Texture Class | WP | FC | Sat | Sat Cond |
| **%Wt** | **%Wt** | **%Wt** | **%Wt** | **dS/m** | **%Wt** | | %Vol | %Vol | %Vol | mm/hr |
| **88** | **6** | **6** | **1** | **0** | **4.7** | Sand | 8 | 14.2 | 50.8 | 109.5 |
| **subsoil 1** | | | | | | | | | | |
| **Sand** | **Clay** | **Silt** | **Gravel** | **Salinity** | **OM** | Texture Class | WP | FC | Sat | Sat Cond |
| **%Wt** | **%Wt** | **%Wt** | **%Wt** | **dS/m** | **%Wt** | | %Vol | %Vol | %Vol | mm/hr |
| **95** | **2** | **3** | **49** | **0** | **0.9** | Sand | 1.3 | 5 | 44.3 | 90.7 |
| **subsoil 2** | | | | | | | | | | |
| **Sand** | **Clay** | **Silt** | **Gravel** | **Salinity** | **OM** | Texture Class | WP | FC | Sat | Sat Cond |
| **%Wt** | **%Wt** | **%Wt** | **%Wt** | **dS/m** | **%Wt** | | %Vol | %Vol | %Vol | mm/hr |
| **87** | **7** | **6** | **34** | **0** | **1.3** | Loamy Sand | 3.6 | 7.9 | 43.7 | 75.8 |

# CHAPTER 4: RESULTS AND DISCUSSION

## 4.1. INTRODUCTION

This chapter describes the principal results obtained from this study. The first section gives a field description and laboratory characterisation of the studied soil. The second section describes in detail the data obtained by the TDR monitoring station installed at the University of Birmingham, with focus on both seasonal and diurnal variations of soil and environmental properties. The third section shows the results of statistical analyses aimed at understanding the relationships between the measured parameters with particular attention to the factors affecting the variability of the EM soil properties. A specific section shows the results of the SPAW hydrological modelling and its comparison with the data collected in the field. Finally the last section describes the results obtained by the GPR, including a comparison between TDR and GPR data. A discussion is included in each section.

## 4.2. SOIL CHARACTERISATION

This section focuses on the field description of the soil profile excavated during the TDR installation and the results of the analyses carried out in the laboratory. A discussion of the results is included in this section.

Figure 4.1 summarizes the soil description carried out in the field, following the terminology commonly used in soil science (Foth, 1990; FAO/ISRIC/ISSS, 1998; see also

appendix A for further details). Two A horizons (A1 and A2) were identified below a 0.02 m O horizon, made by partially decomposed organic residues such as grass roots. A1 and A2 seemed to have similar characteristics (black colour and granular structure), but A2 showed more coarse particles and fewer roots than A1. The small distinction between the two did not justify the A2 horizon to be named as a B horizon, which was deemed to be absent. This was not a surprise because the soil consisted of made ground, and laid down too recently for the natural pedological processes to manifest. It was decided to distinguish the subsoil only in two major BC horizons (BC1 and BC2) with similar characteristics, the most peculiar being the very high percentage of coarse material and the lack of structure (i.e., presence of aggregates). The properties of the BC1 horizon slightly changed with depth, for example the soil texture seemed to become sandier and slightly less gravelly with increasing depth. A clearer change was evident at approximately 0.70 m depth, corresponding to the start of the BC2 horizon, which was darker and contained coal residues. BC2 was wetter than the upper horizons, an indication of a higher clay content. Despite these changes, the BC2 horizon lacked a specific soil structure and was predominantly made of sand and gravel as with the BC1 horizon.

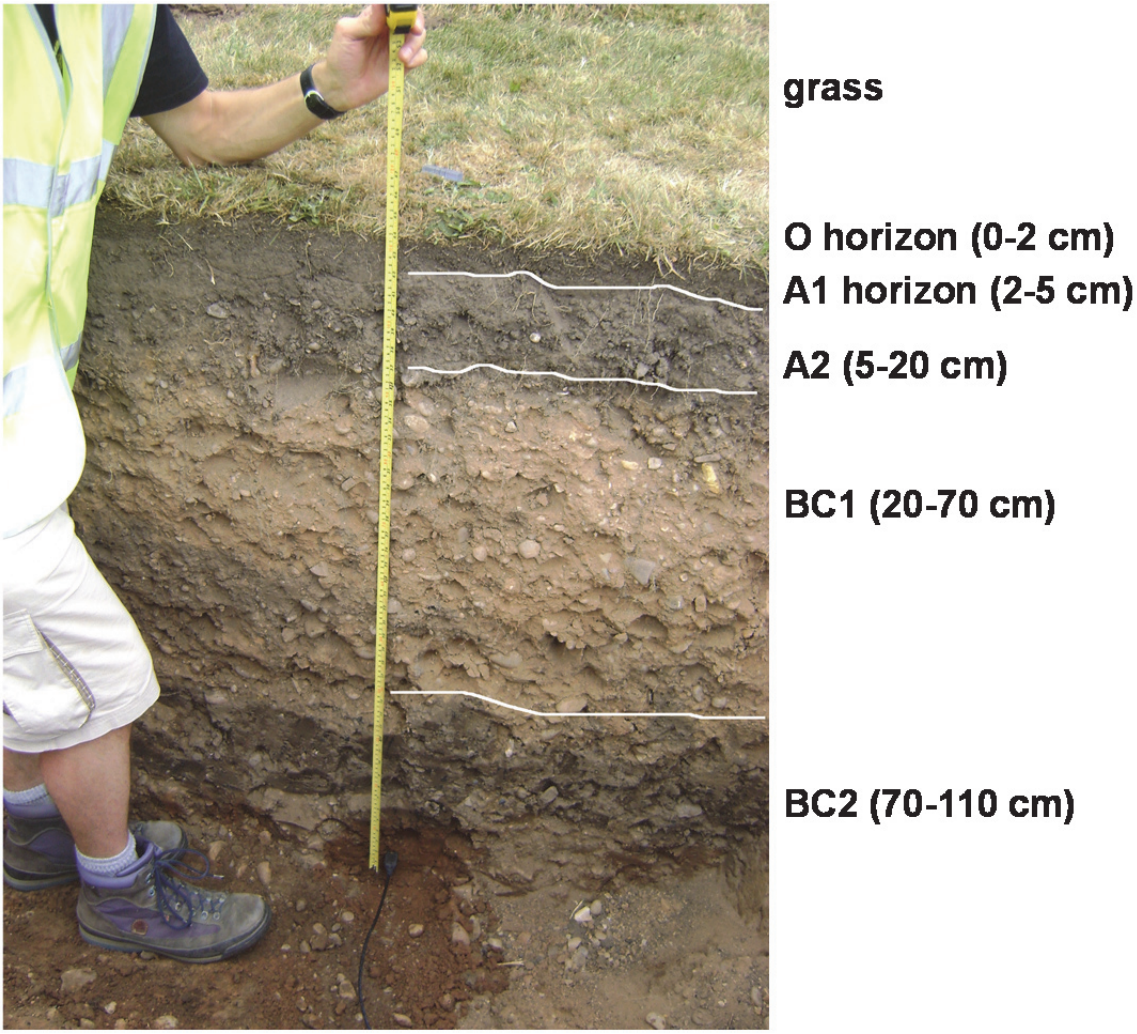



Figure 4.1 – Soil profile in the trench dug to install the TDR probes, showing the identified soil horizons.

The horizons described above correspond to the following, simpler terminology, that will be used in the remainder of this thesis: **topsoil** (A horizons), **subsoil 1** (BC1 horizon) and **subsoil 2** (BC2 horizon).

Table 4.1 lists the laboratory measurements taken on soil samples collected from the field. Due to the very gravelly nature of the soil it was not possible to collect samples exactly corresponding to the horizons identified in the field. Thus, 'bulk' samples were taken at increasing depths. In Table 4.1 the values of particle size distribution, pH, BEC and OM were obtained from the trench dug for the installation of the TDR probes. Density and

oven-dried gravimetric water content (GWC) were measured on samples collected on the 28th of January 2010 (before the TDR installation) in the proximity of the chosen area. The cylinders used for measuring the soil density had a diameter ranging between 16 and 27 mm and a volume ranging from 14 and 57 $cm^3$. Since the hole was dug manually it was not possible to collect samples deeper than approximately 0.5 m.

Table 4.1 – List of laboratory results obtained from soil samples collected from the University of Birmingham test site. [Note: particle size percentages are by weight]

| depth (m) | gravel (> 2 mm, %) | sand (0.063 - 2 mm, %) | silt + clay (< 0.063 mm, %) |
|---|---|---|---|
| 0.05 | 1 | 87 | 12 |
| 0.50 | 48 | 48 | 4 |
| 0.80 | 34 | 57 | 9 |

| depth (m) | dry density ($g/cm^3$) | bulk density ($g/cm^3$) | GWC (%) | particle density ($g/cm^3$) |
|---|---|---|---|---|
| 0.05 | 1.11 | 1.50 | 35.87 | |
| 0.50 | 1.49 | 1.67 | 12.50 | 2.66 |

| depth (m) | pH | BEC HI9033 (mS/m) | OM (%) |
|---|---|---|---|
| 0.05 | 5.94 | 6.53 | 4.7 |
| 0.50 | 6.35 | 2.42 | 0.9 |
| 0.80 | 6.30 | 7.47 | 1.3 |

Figures 4.2 and 4.3 show details of the particle size distribution of the soil samples. It can be seen that the percentage of fine particles (i.e., silt and clay) remains low over the entire soil profile, and is almost absent in the middle portion of the soil profile between 0.3 and 0.6 m of depth. With the exception of the topsoil, gravel is present in large quantities and sand is dominant at all depths. According to the British Standard (BS 5930:1999+2, 2010) the soil is a coarse-grained soil, and can be described as very gravelly SAND.

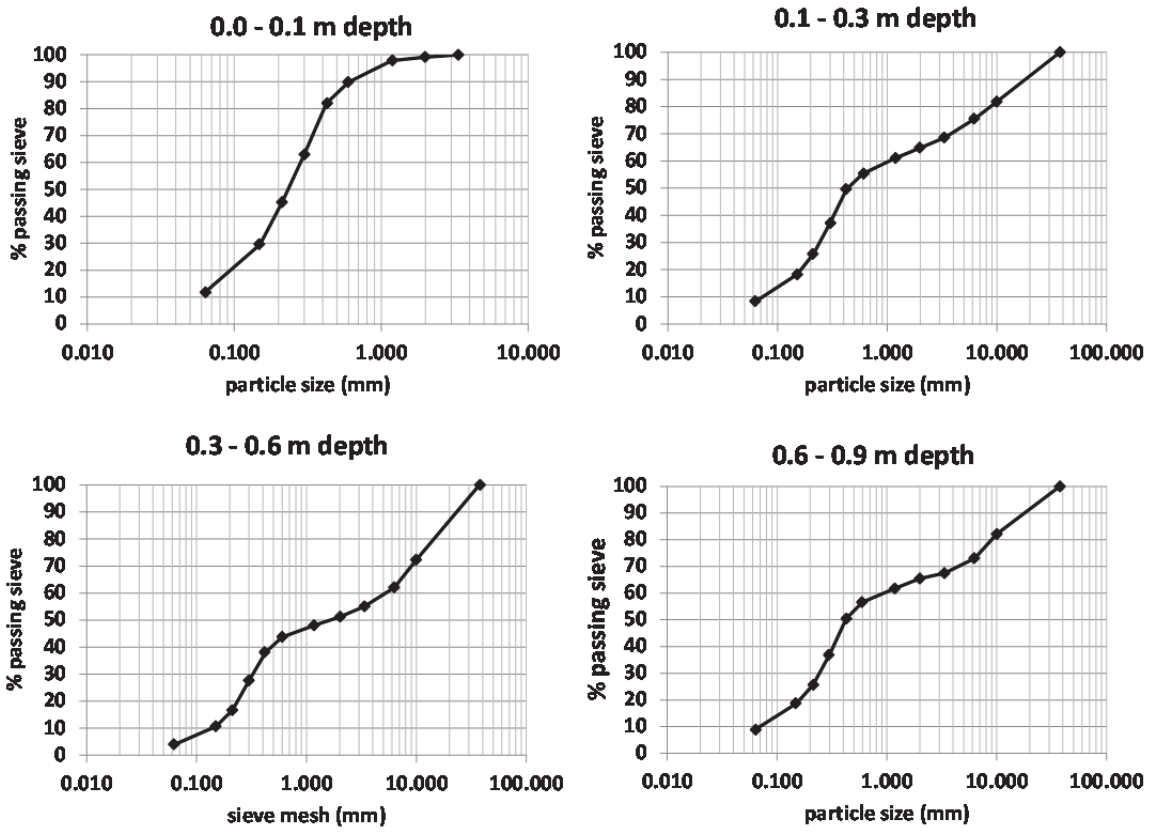



Figure 4.2 – Particle size distributions for the soil samples collected during the TDR field installation at different depths.

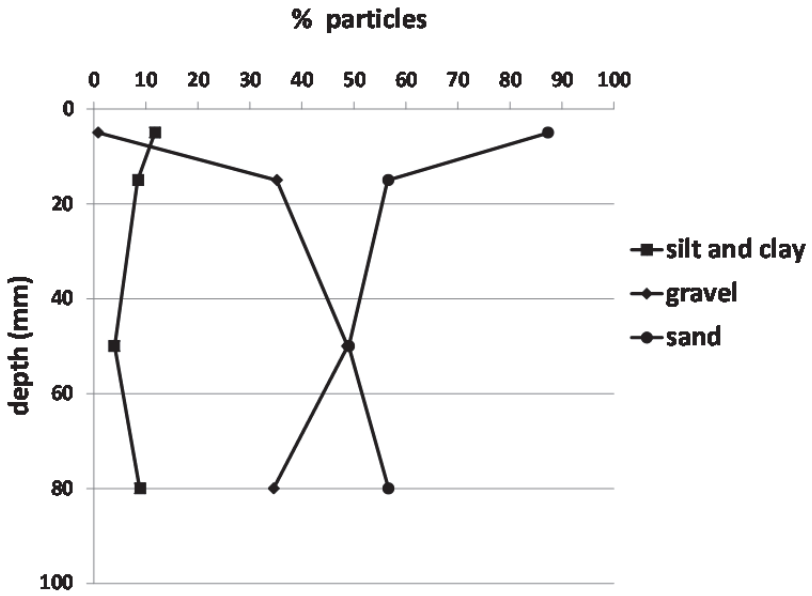



Figure 4.3 – Particle size percentage distributions with depth.

It is interesting to note that both BEC and OM are related to the percentage of fine particles, both showing higher values with increasing clay and silt content (Table 4.1). This is not a surprise since both values are expected to be lower in gravelly and sandy horizons. The increase of percentage of fines and organic matter with depth can be due to natural leaching, or quite likely, to how the backfilling was conducted. Because the soil was made ground, a possibility is that the natural soil present in the area was covered by additional sandy material during backfilling, and the higher OM, fines and BEC values are a residue of this original soil.

# 4.3. FIELD MONITORING

## 4.3.1. Introduction

This section describes the results obtained from the TDR and weather monitoring stations installed at the University of Birmingham. The data correspond to a period of 22 and a half months, starting the 20th of August 2010 and ending the 6th of July 2012. The results show the seasonal and the daily variability of the measured environmental and soil parameters. A summary of the main results is included at the end of the section.

## 4.3.2. Seasonal variations

### 4.3.2.1. Variation of weather parameters

Long-term monitoring data, in this case approximately 22 months, provided information on the seasonal variability of the environmental and soil variables for the University of Birmingham test site. Table 4.2 shows a summary of the environmental parameters measured by the weather station during the entire monitoring period. A seasonal pattern of some of these variables is visible, for example solar radiation and temperature

(Figure 4.4). Rainfall was generally lower in the first months of the year, but did not seem to show a consistent sinusoidal pattern during the period of the investigation. Notably, Spring 2011 showed significantly different characteristics compared to Spring 2012, the first being largely dry and the second very wet (Figure 4.4). The low rainfall values for the months of January and February and the sinusoidal pattern of the air temperature were confirmed by historical data collected by a Met Office weather station located approximately 100 km from the test site (see appendix B; Met Office, 2012).

Table 4.2 – Summary of the environmental variables measured by a weather station over the period of field monitoring.

| | **Oct-Dec10** | **Jan-Mar11** | **Apr-Jun11** | **Jul-Sep11** | **Oct-Dec11** | **Jan-Mar12** | **Apr-Jun12** | **Aug10-Jun12** |
|---|---|---|---|---|---|---|---|---|
| **mean wind direction (°)** | 118 | 131 | 152 | 186 | 197 | 109 | 143 | 147 |
| **mean wind speed (m/s)** | 2.0 | 2.1 | 1.7 | 1.3 | 2.4 | 3.2 | 4.2 | 2.5 |
| **cumulative rainfall (mm)** | 106.8 | 56.2 | 52.8 | 91.8 | 116.7 | 20.1 | 307.4 | 919.9 |
| **min air temperature (°C)** | -9.6 | -4.4 | 3.7 | 7.4 | 0.0 | -5.5 | 0.5 | -9.6 |
| **max air temperature (°C)** | 19.2 | 18.9 | 25.4 | 27.6 | 27.8 | 21.9 | 27.6 | 27.8 |
| **mean air temperature (°C)** | 5.1 | 6.2 | 12.7 | 15.8 | 9.4 | 6.8 | 11.4 | 9.6 |
| **mean humidity (%)** | 82.1 | 77.9 | 64.3 | 67.2 | 77.8 | 75.3 | 71.5 | 74.0 |
| **mean pressure (hPa)** | 994 | 1000 | 1001 | 996 | 997 | 1008 | 994 | 999 |
| **mean solar radiation ($W/m^2$)** | 39.4 | 59.1 | 184.6 | 157.1 | 43.3 | 67.2 | 153.1 | 98.9 |

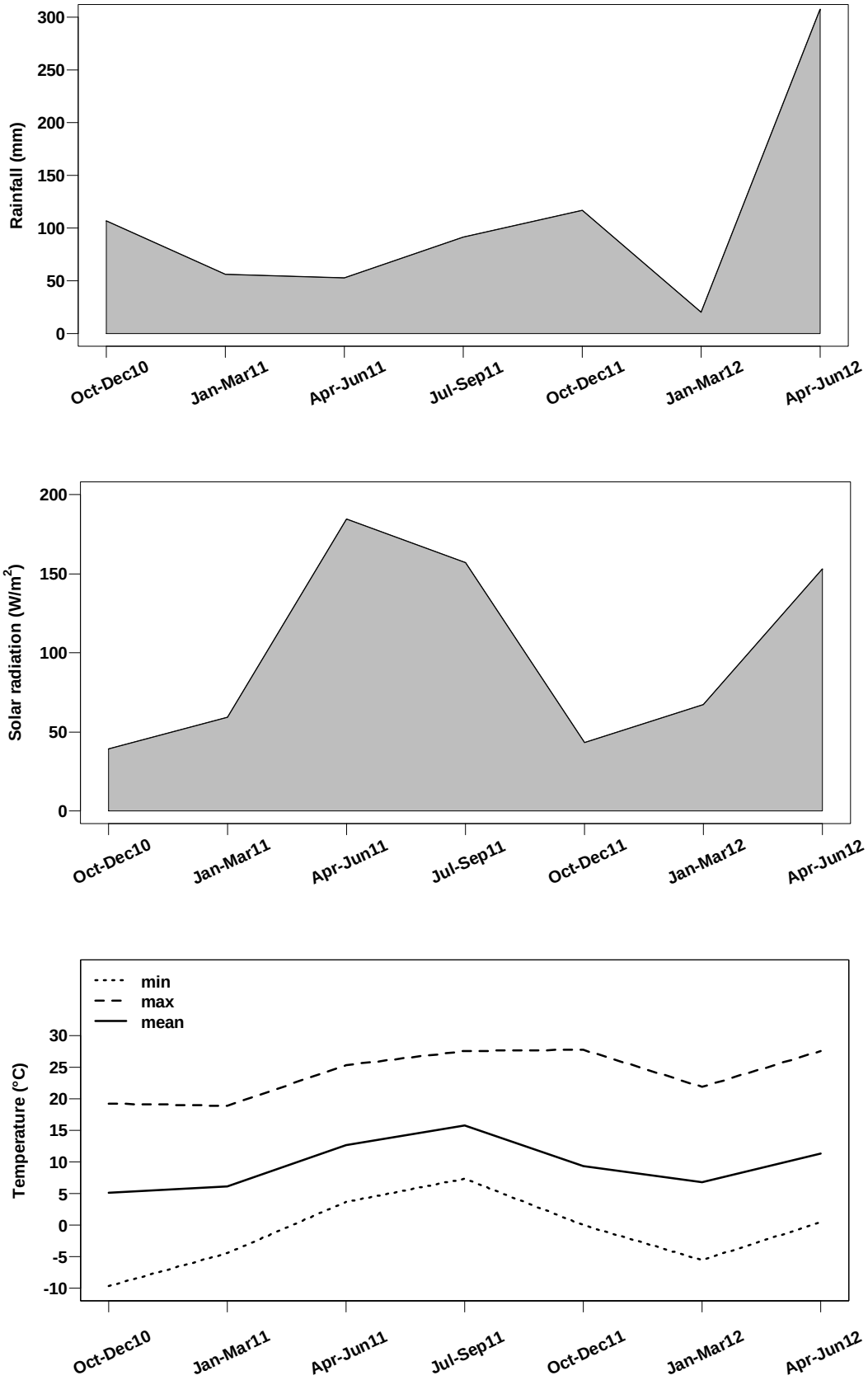



Figure 4.4 – Seasonal variation of rainfall, solar radiation and temperature.

### 4.3.2.2. Variation of soil EM properties

Figures 4.5 and 4.6 show the variation of apparent permittivity for each probe and Figures 4.7 and 4.8 show the variation of BEC (mS/m) with time during the entire monitoring period. Several outliers were removed by a median filter function written in R. However, it was not possible to eliminate all of them (for example plots with and without filtering see appendix B).

Figures 4.5 to 4.8 show that there was a seasonal variation of the EM soil properties and that this variation was highly dependent on the amount of rainfall. The sharp reduction of both apparent permittivity and BEC starting in early Spring 2011 corresponded to a prolonged dry period that caused the soil water content to drop significantly. This drop was more evident for apparent permittivity and for shallower depths. A similar reduction was not recorded during Spring 2012, which was characterised by intense rainfall events.

The data collected in this study show higher values of soil EM properties during the Winter and lower values during the Summer. However, such variation was highly dependent on the amount of rainfall. It is important to note that each peak of rainfall in Figures 4.5 to 4.8 correspond to the rainfall of an hour. Thus single high peaks do not necessarily correspond to a large amount of rainfall infiltrating in the soil because a significant portion of water was likely to be lost as superficial runoff.

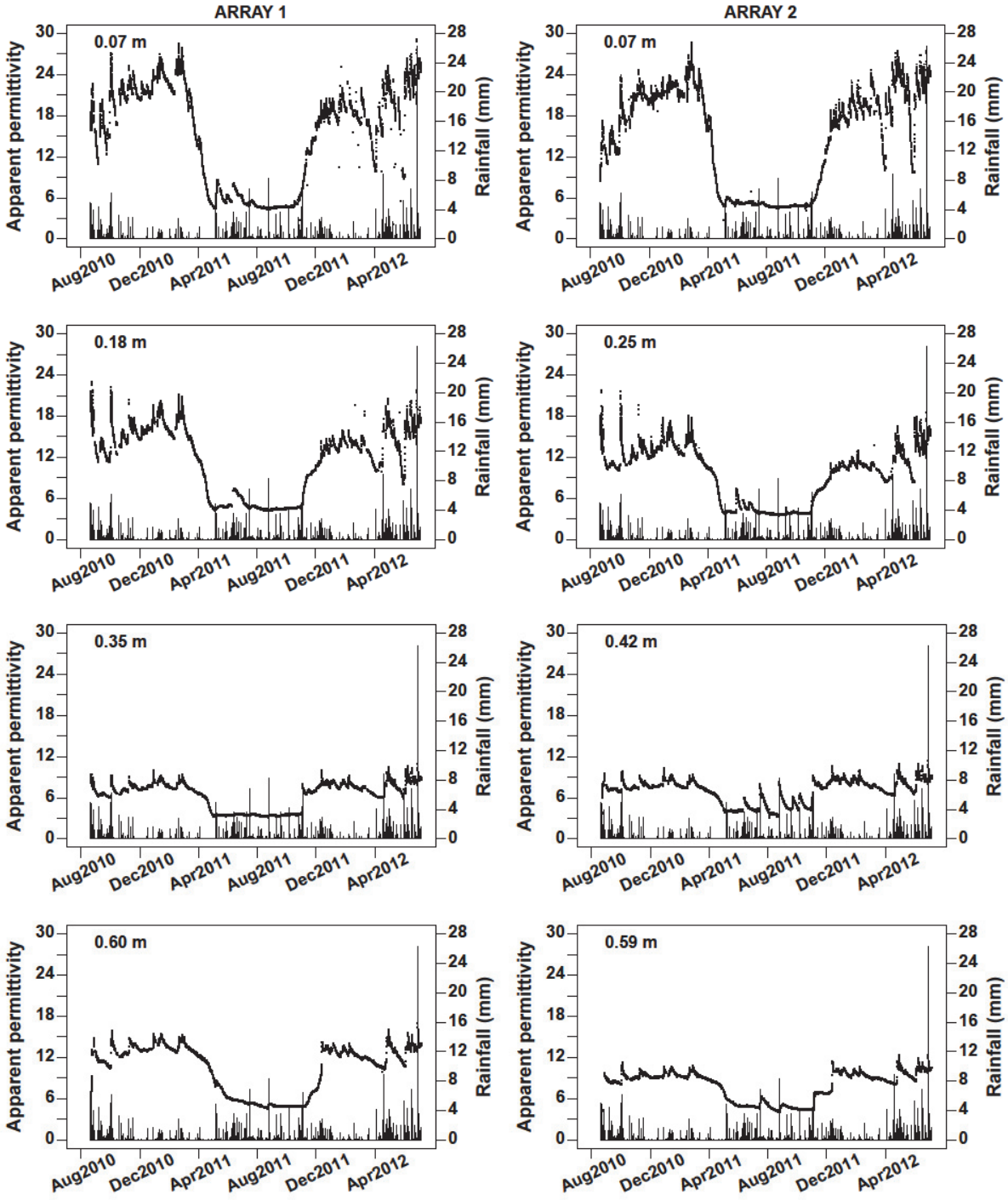



Figure 4.5 – TDR measured apparent permittivity over the entire period of field monitoring, from 0.07 and 0.60 m depth. The left column corresponds to array 1, the right column to array 2.

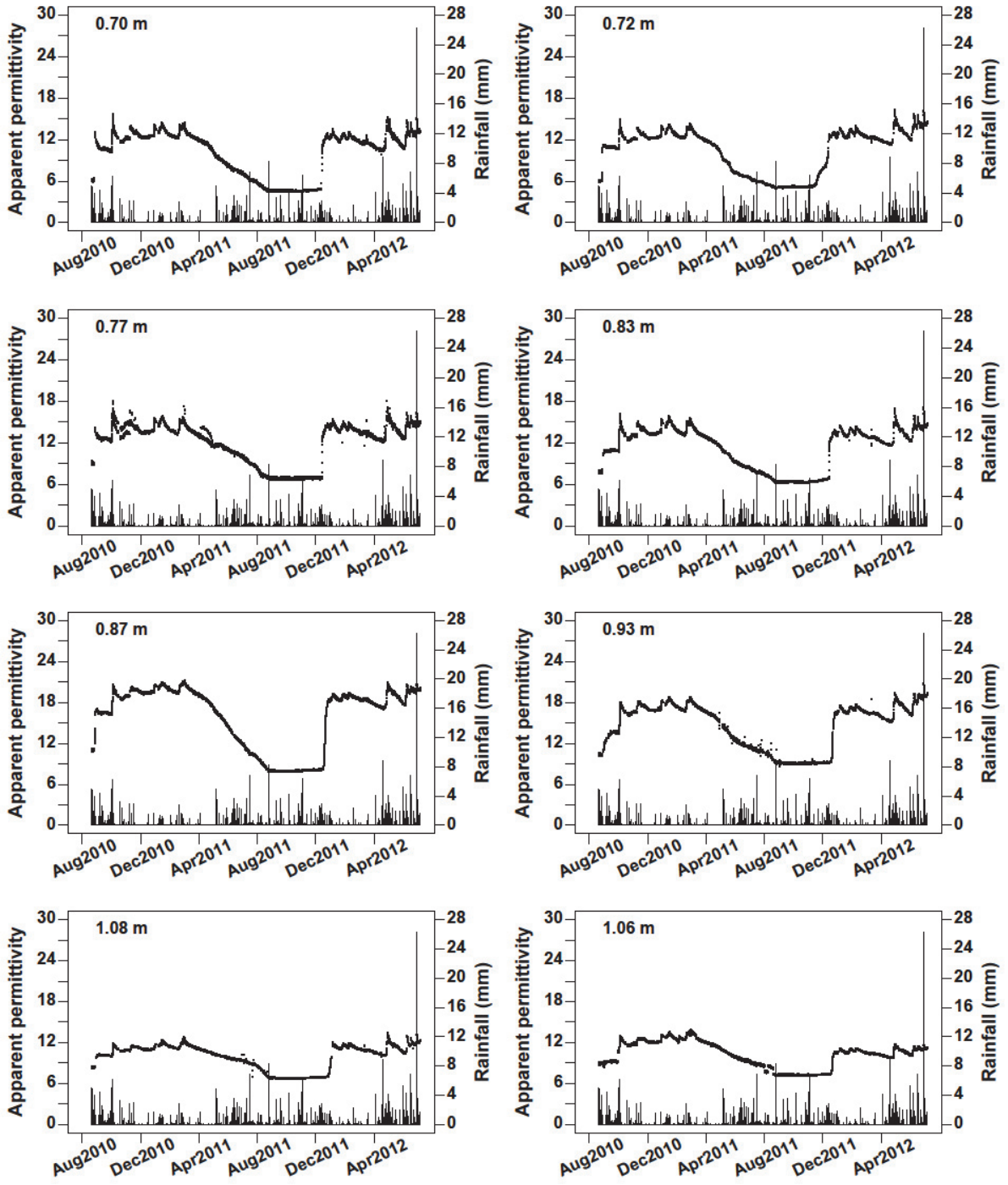



Figure 4.6 – TDR measured apparent permittivity over the entire period of field monitoring, from 0.70 and 1.08 m depth. The left column corresponds to array 1, the right column to array 2.

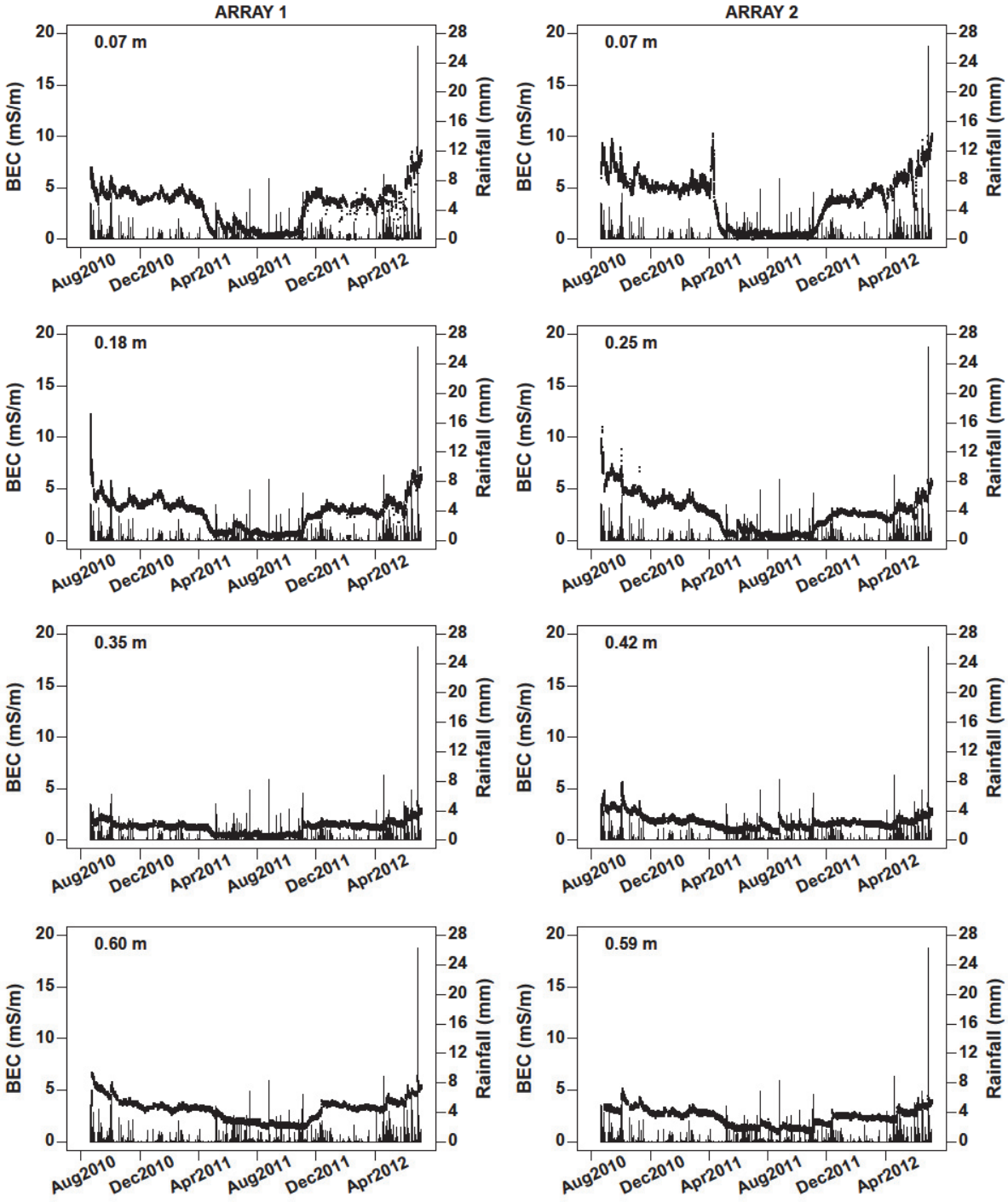



Figure 4.7 – TDR measured bulk electrical conductivity (BEC) over the entire period of field monitoring, from 0.07 and 0.60 m depth. The left column corresponds to array 1, the right column to array 2.

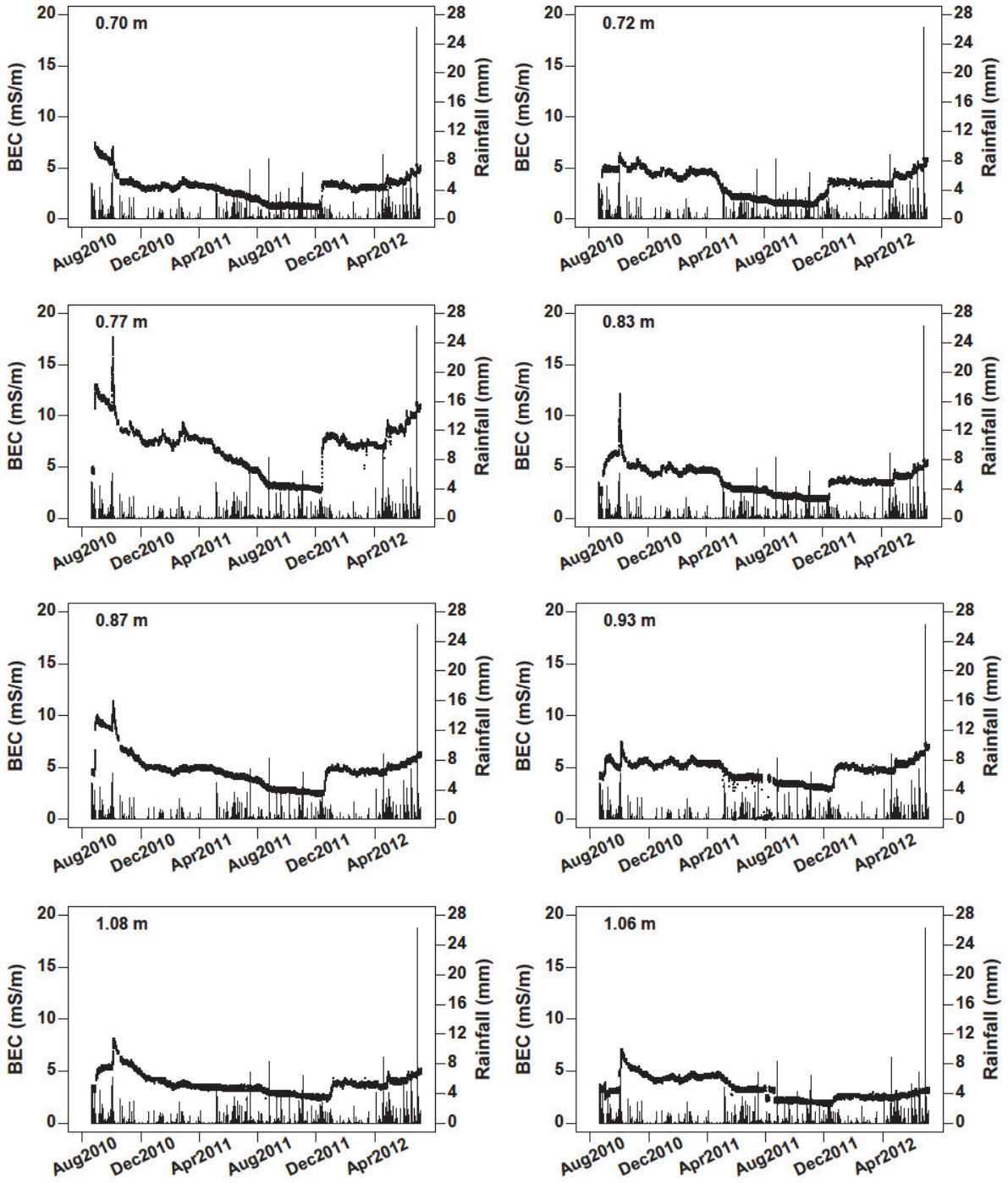



Figure 4.8 – TDR measured bulk electrical conductivity (BEC) over the entire period of field monitoring, from 0.70 and 1.08 m depth. The left column corresponds to array 1, the right column to array 2.

Figures 4.5 to 4.8 also show the variation of the EM soil properties with depth and for the two different arrays. In general, the shallower probes in the topsoil showed greater seasonal variation, with large differences between maxima and minima values, because they were directly affected by rainfall and evaporation events. Similar findings were reported by other authors (e.g., Rajeev et al., 2012; Menziani et al., 2003; Slob et al., 2009). The probes inserted in the very sandy horizon between approximately 0.30 m and 0.60 m showed smaller seasonal variation because of the reduced ability of the soil to retain water.

It is worth noting that despite the small dimension of the TDR probes, which measured small soil samples and therefore were potentially susceptible to the small scale variability in the soil properties (IAEA, 2008), the trends measured by the two arrays were consistent throughout the monitoring period. The absolute values were to some extent different, but both arrays provided a very similar picture of the seasonal trends.

Figure 4.9 shows the variation of the seasonal mean apparent permittivity and BEC up to a depth of 1 m. The seasonal variation of these soil properties is clearly visible, with higher values occurring during the Winter and lower values during the Summer.

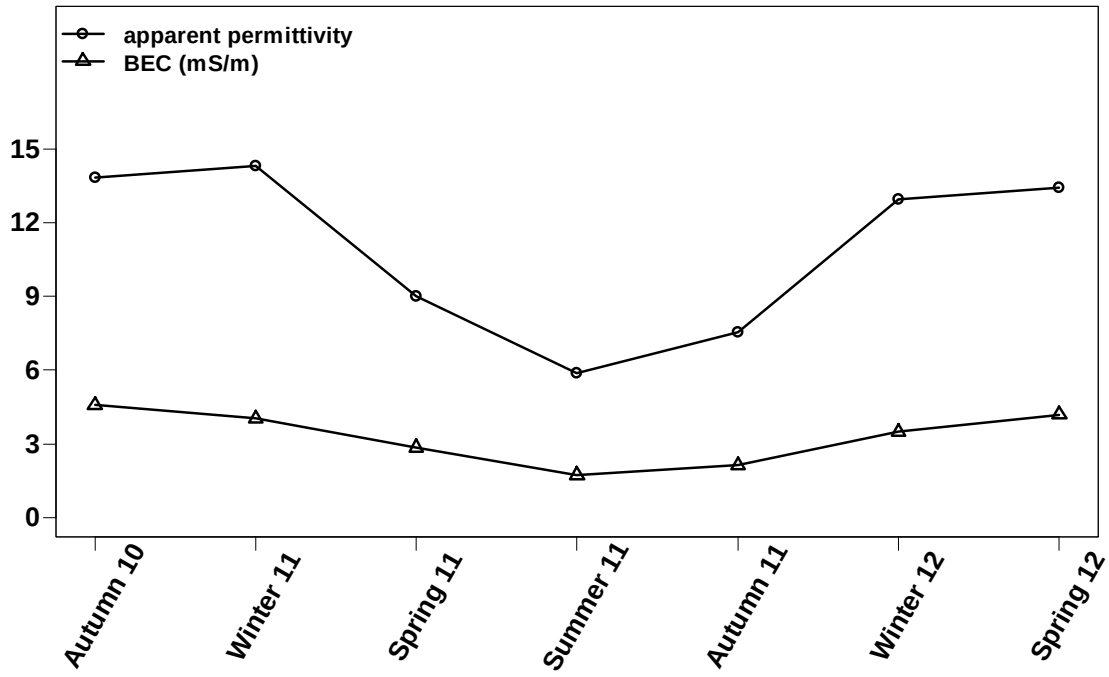



Figure 4.9 – Variation of the seasonal mean soil apparent permittivity and BEC.

Figures 4.10 and 4.11 show the variation of the EM soil properties with depth measured by each TDR probe and for both arrays. The corresponding basic statistics are shown in Table 4.3. The variability between probes, expressed as a difference between maxima and minima[9], decreased at the lower limit of both apparent permittivity and BEC. During dry periods the soil conditions were fairly homogeneous across the depth of the soil profile. On the other hand, wetter conditions, expressed by maxima values of soil EM properties, were more variable between the probes. Higher values were measured by the shallower probes inserted in the topsoil and the deeper probes inserted in the more clayey soil horizon. Figures 4.10 and 4.11 clearly show that both arrays provided similar trends in the data, although the absolute values were not always consistent. The differences in the absolute values measured by the two arrays were not a surprise, since soil properties are well

[9] Standard deviation was not used to estimate the variability of the data because the data are not normally distributed (see Figures 4.14 and 4.15).

known for having a high spatial variability (e.g., Rajkai and Ryden, 1992; Dekker et al., 1999).

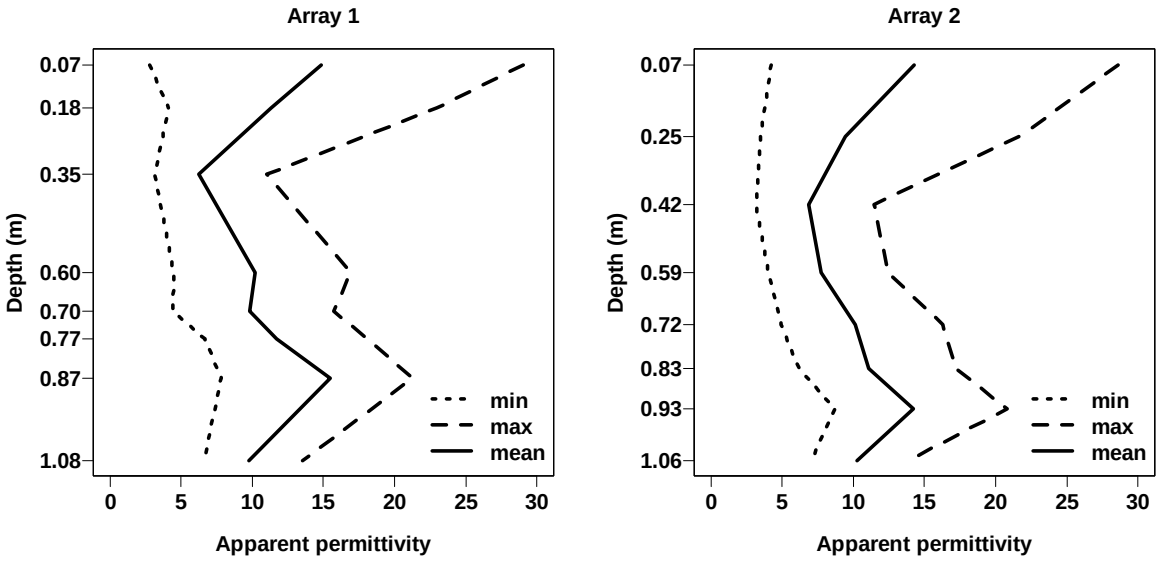



Figure 4.10 – Variability of the soil apparent permittivity measured by the TDR probes for each array during the field monitoring.

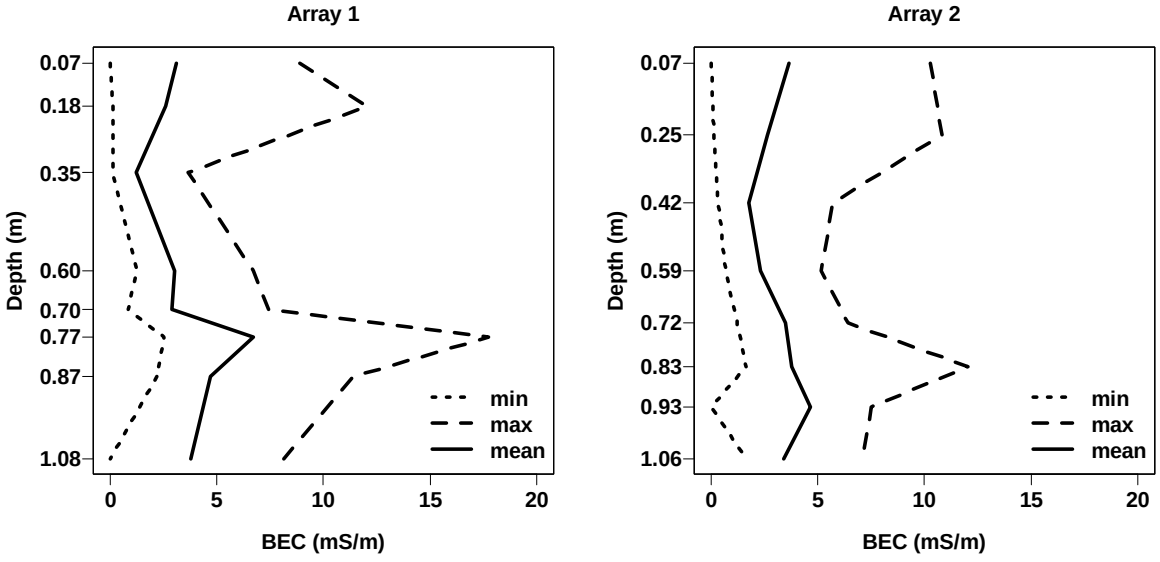



Figure 4.11 – Variability of the soil BEC measured by the TDR probes for each array during the field monitoring.

Table 4.3 – Basic statistics of the soil EM properties measured by each TDR probe calculated on the period of field monitoring.

| | | apparent permittivity | | | BEC (mS/m) | | |
|---|---|---|---|---|---|---|---|
| probe | depth (m) | min | max | mean | min | max | mean |
| 1 | 0.07 | 2.80 | 29.07 | 14.87 | 0.01 | 8.89 | 3.13 |
| 2 | 0.07 | 4.22 | 28.64 | 14.31 | 0.01 | 10.28 | 3.64 |
| 3 | 0.18 | 4.12 | 22.98 | 11.36 | 0.15 | 12.04 | 2.59 |
| 4 | 0.25 | 3.48 | 21.67 | 9.44 | 0.14 | 10.82 | 2.65 |
| 5 | 0.35 | 3.15 | 11.00 | 6.26 | 0.15 | 3.66 | 1.21 |
| 6 | 0.42 | 3.19 | 11.44 | 6.89 | 0.33 | 5.70 | 1.78 |
| 7 | 0.60 | 4.51 | 16.95 | 10.23 | 1.28 | 6.73 | 3.02 |
| 8 | 0.59 | 4.02 | 12.44 | 7.76 | 0.68 | 5.17 | 2.32 |
| 9 | 0.70 | 4.40 | 15.75 | 9.83 | 0.87 | 7.41 | 2.91 |
| 10 | 0.72 | 4.94 | 16.30 | 10.13 | 1.22 | 6.44 | 3.49 |
| 11 | 0.77 | 6.65 | 18.14 | 11.70 | 2.51 | 17.72 | 6.70 |
| 12 | 0.83 | 6.18 | 17.18 | 11.06 | 1.64 | 12.04 | 3.79 |
| 13 | 0.87 | 7.78 | 21.25 | 15.50 | 2.21 | 11.40 | 4.71 |
| 14 | 0.93 | 8.69 | 20.83 | 14.24 | 0.01 | 7.50 | 4.68 |
| 15 | 1.08 | 6.59 | 13.51 | 9.79 | 0.01 | 8.15 | 3.77 |
| 16 | 1.06 | 7.06 | 13.85 | 10.26 | 1.65 | 7.10 | 3.41 |

Figures 4.12 and 4.13 show the seasonal variation for each soil horizon during the monitoring period. The data correspond to the daily means for all the probes in both arrays, organised in the three main soil horizons identified in the field (i.e., topsoil, subsoil 1 and subsoil 2, see section 4.2). It is evident that the shallower and deeper horizons showed greater seasonal variability, with large differences between minima and maxima values. In contrast, the middle horizon (i.e., subsoil 1), which contained negligible amounts of fine particles, showed less variability during the monitoring period. Figures 4.12 and 4.13 also show higher variability for the topsoil in the short period, with more frequent rises and drops corresponding to rainfall events and dry periods, respectively.

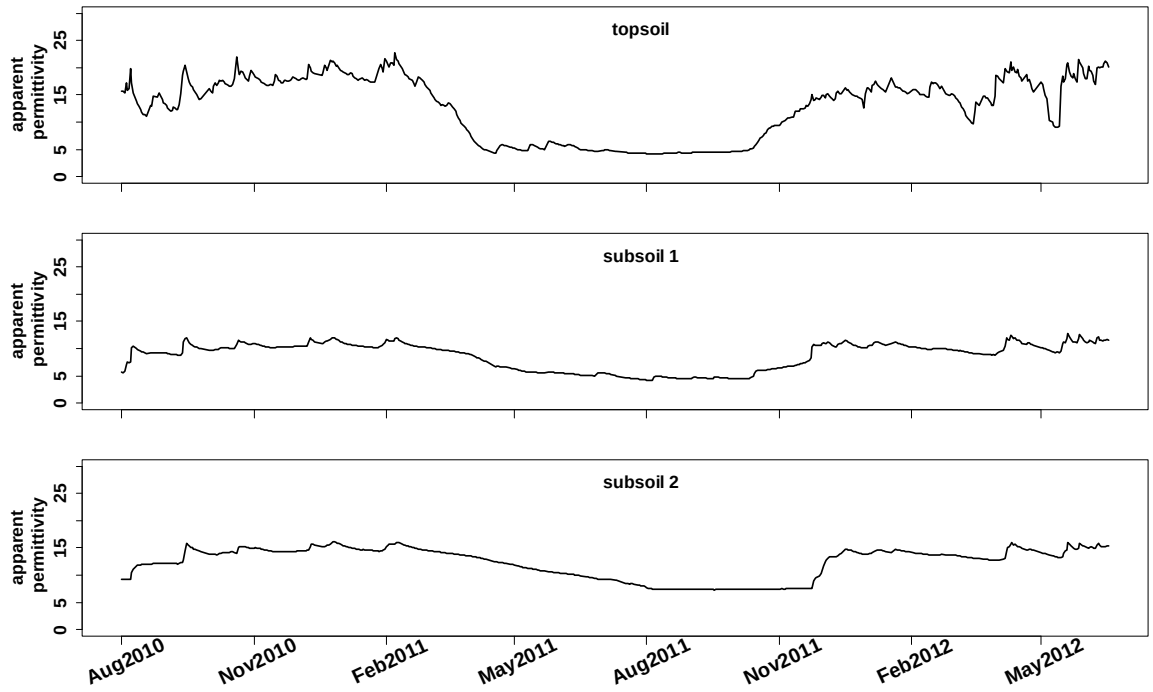



Figure 4.12 – Variation of the daily apparent permittivity for the three main soil horizons.

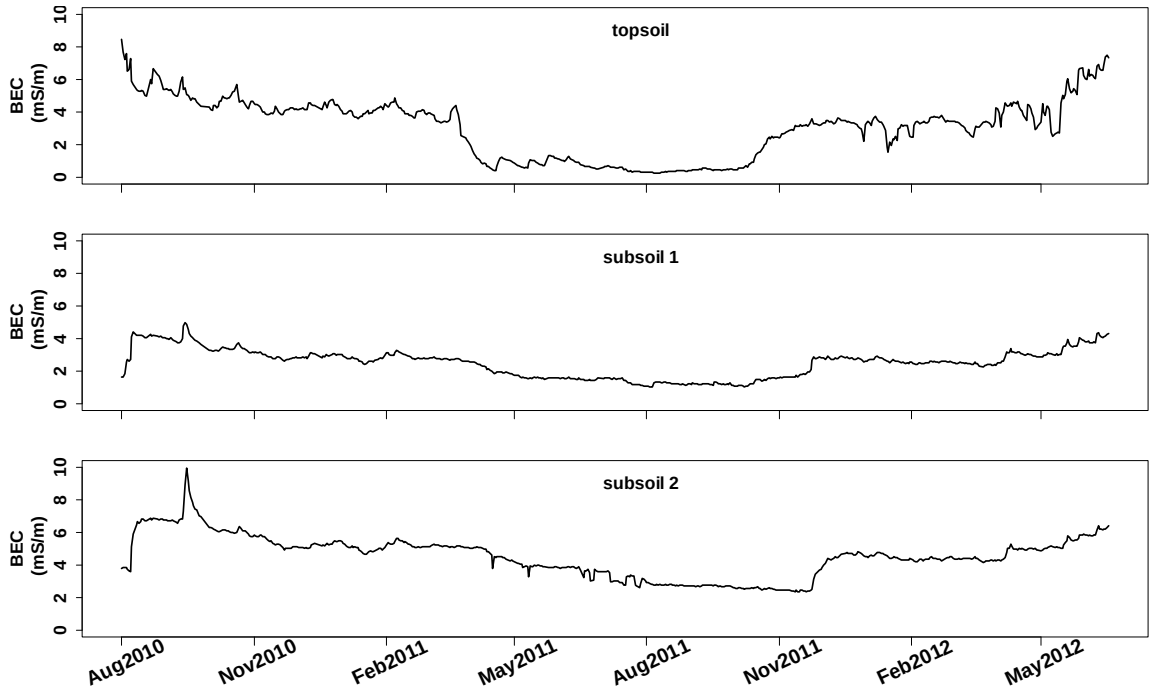



Figure 4.13 – Variation of the daily BEC for the three main soil horizons.

Figures 4.14 and 4.15 show the frequency of the daily values of apparent permittivity and BEC (mS/m) by soil horizon, for both arrays, during the entire monitoring period. It is apparent that the data are not normally distributed and that two approximate peaks can be identified corresponding to dry and wet conditions (i.e., low and high values respectively). This means that the use of an average apparent permittivity or BEC value for the soil studied is not appropriate since the real values can be significantly different during dry and wet conditions. This is particularly true for apparent permittivity. From the frequencies shown in Figure 4.14 it is apparent that the mean apparent permittivity value did not occur often and that it was more likely that the soil had a low or high apparent permittivity.

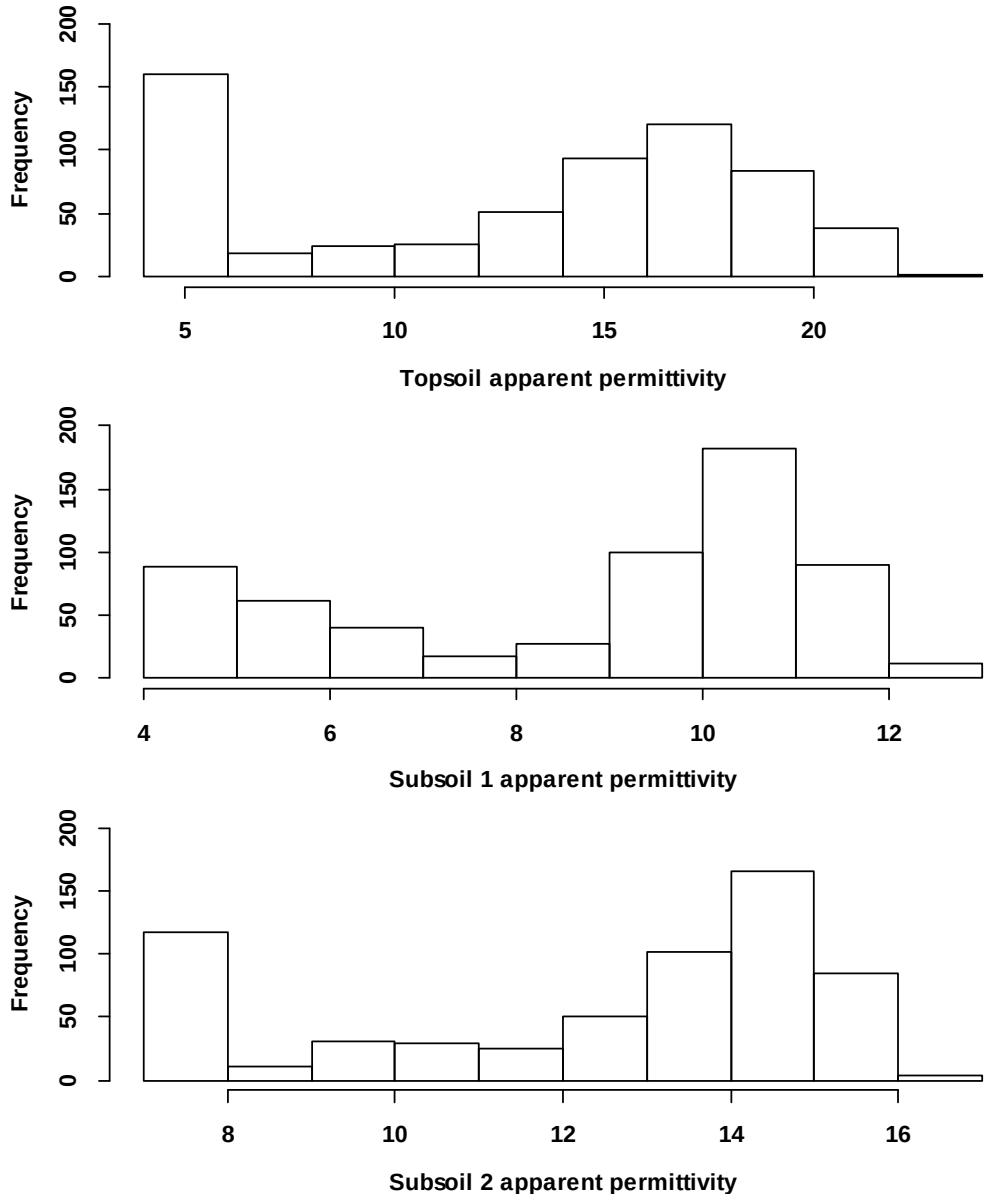



Figure 4.14 – Frequency of the daily apparent permittivity values for the topsoil, subsoil 1 and subsoil 2 horizons during the entire monitoring period.

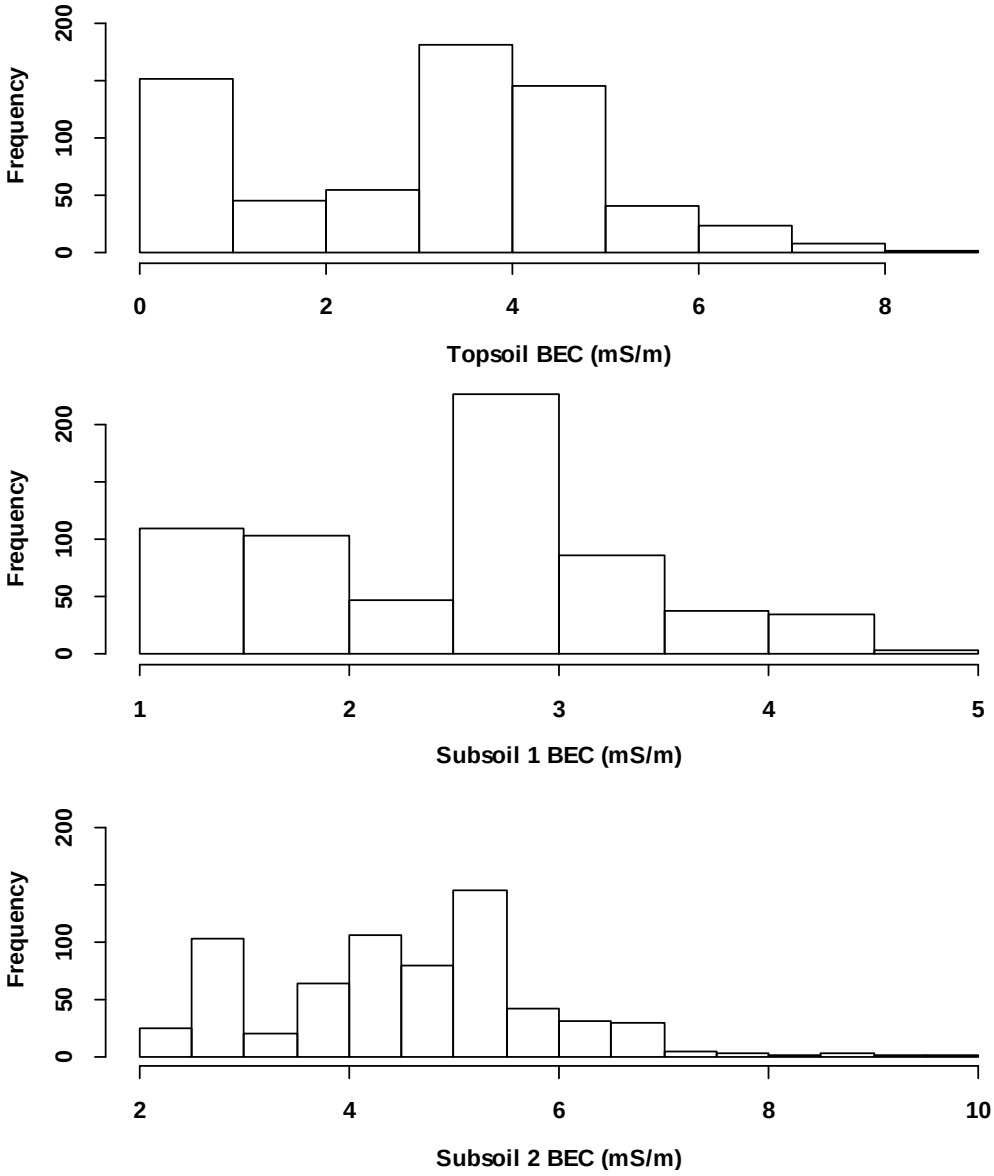



Figure 4.15 – Frequency of the daily BEC values for the topsoil, subsoil 1 and subsoil 2 horizons during the entire monitoring period.

In order to analyse in more detail the variability of the measured soil properties the data corresponding to Winter 2011 were selected and plotted in Figures 4.16 to 4.19. The data collection stopped twice because of issues with the batteries (circles in Figure 4.16). This resulted in gaps of a few days in the dataset.

As it can be seen from Figures 4.16 and 4.17, the soil apparent permittivity increased visibly corresponding to rainfall events. The extent of the increase was greater for the shallower probes compared to the deeper probes. In Figures 4.16 and 4.17 a time lag between the response of the deeper probes compared to the shallower ones is also visible.

Figures 4.18 and 4.19 show the variation of BEC during Winter 2011. Interestingly, BEC values remained low and relatively constant during this period, although slight changes were measured corresponding to rainfall events. This can be explained by the sandy and gravelly nature of the soil. Sandy soils are known to show low ion exchange capacity and BEC (Foth, 1990; Igel et al., 2011), so this result was not unexpected. In addition to the small variations due to rainfall, Figure 4.18 shows that there was a noticeable variation of BEC at shallow depth, in particular at 0.07 m, where the data seem noisier. This was possibly caused by diurnal variation of temperature and was more pronounced in March 2011 when the temperature started to rise.

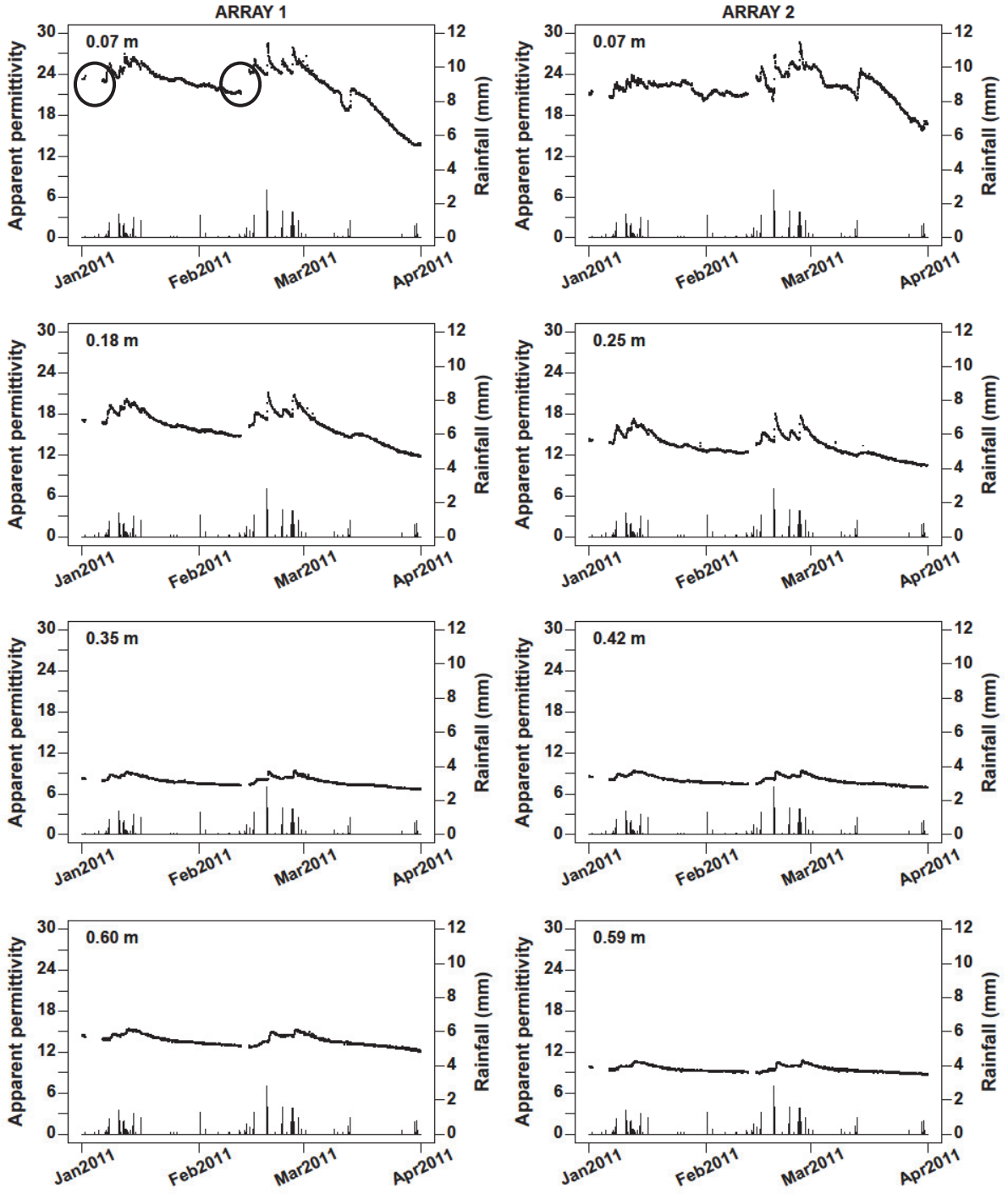



Figure 4.16 – TDR measured apparent permittivity during Winter 2011, from 0.07 and 0.60 m depth. The left column corresponds to array 1 and the right column to array 2. The circles in the topleft plot show the gaps in the dataset caused by problems with the batteries.

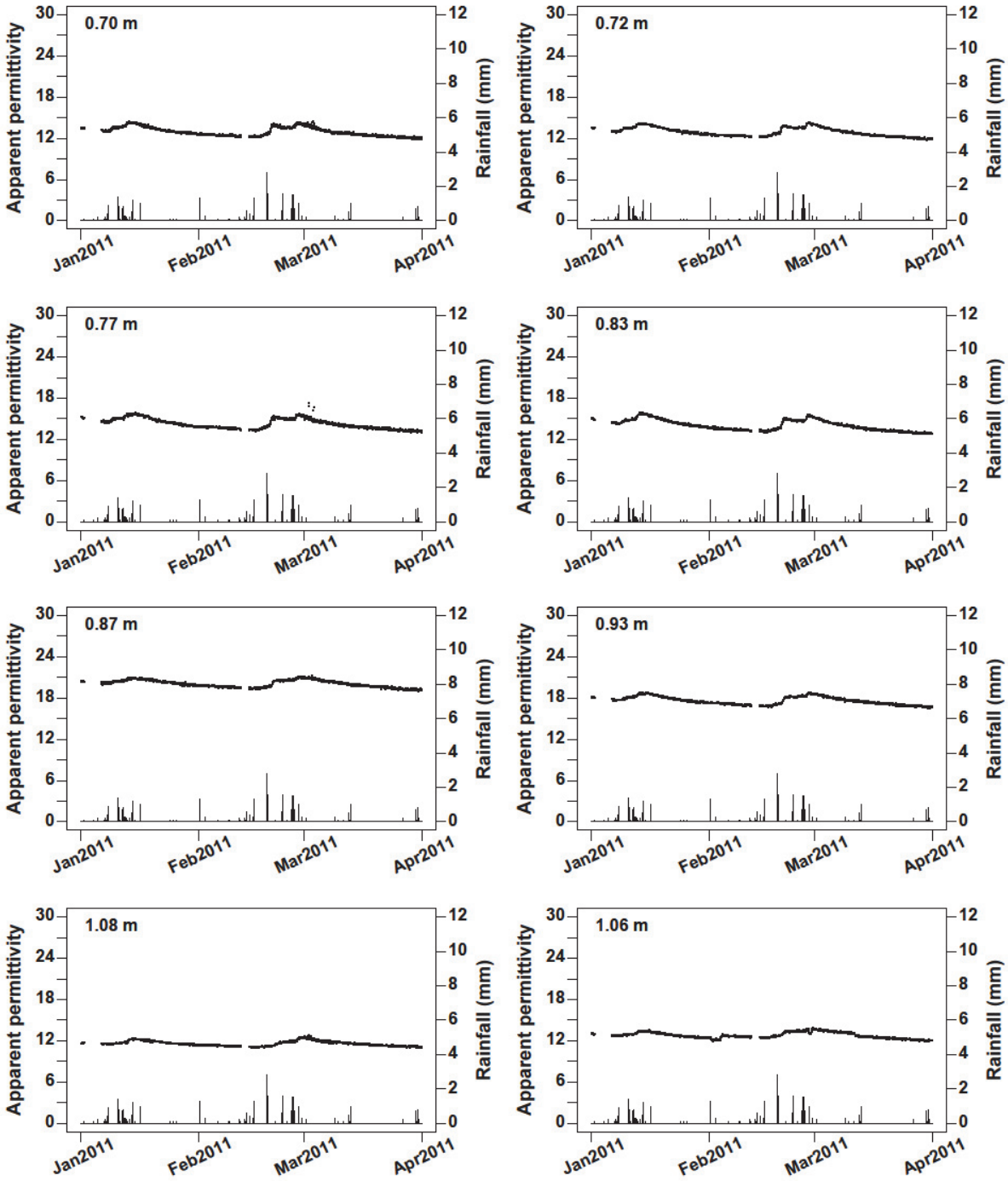



Figure 4.17 – TDR measured apparent permittivity during Winter 2011, from 0.70 and 1.08 m depth. The left column corresponds to array 1 and the right column to array 2.

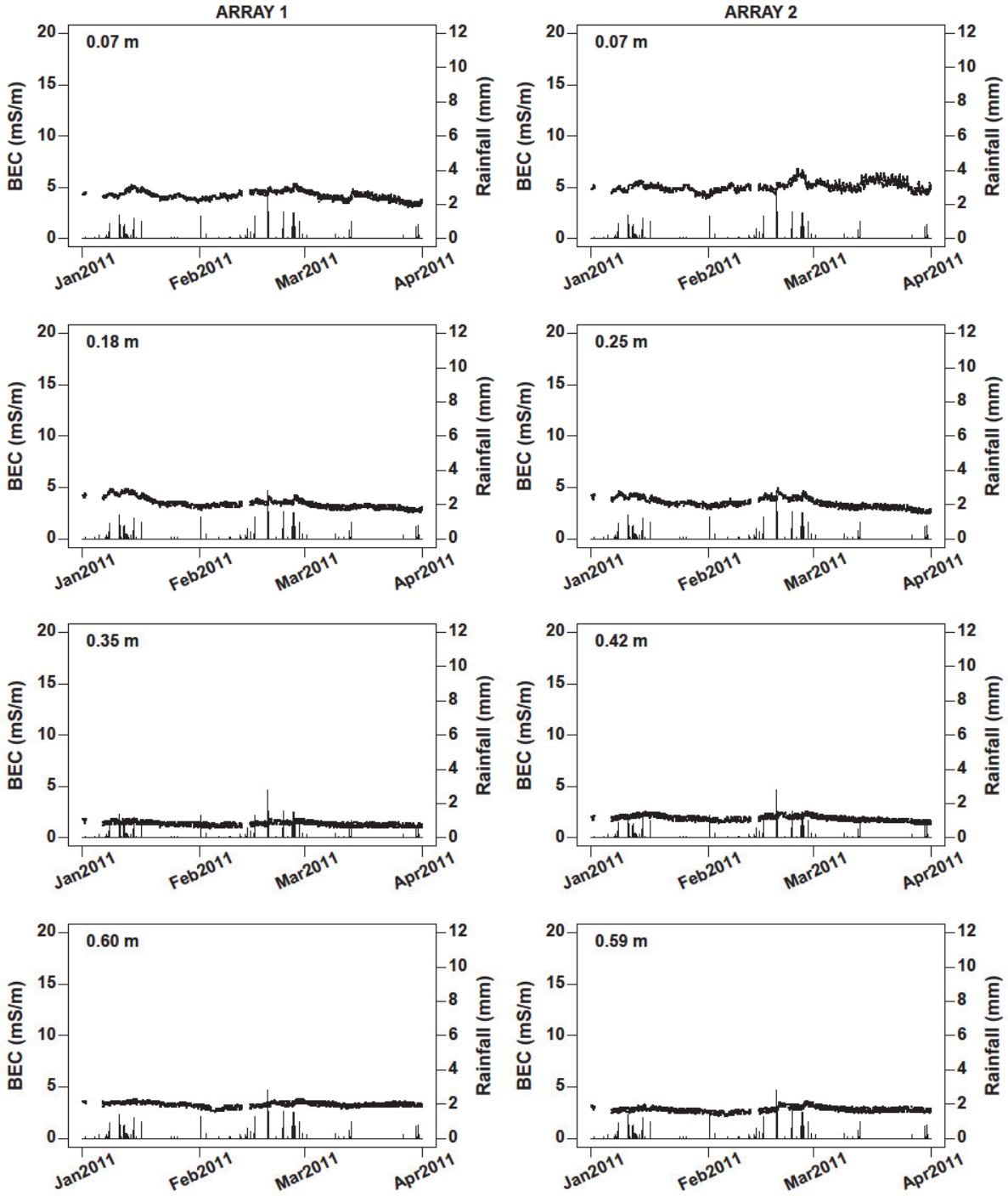



Figure 4.18 – TDR measured bulk electrical conductivity (BEC) during Winter 2011, from 0.07 and 0.60 m depth. The left column corresponds to array 1 and the right column to array 2.

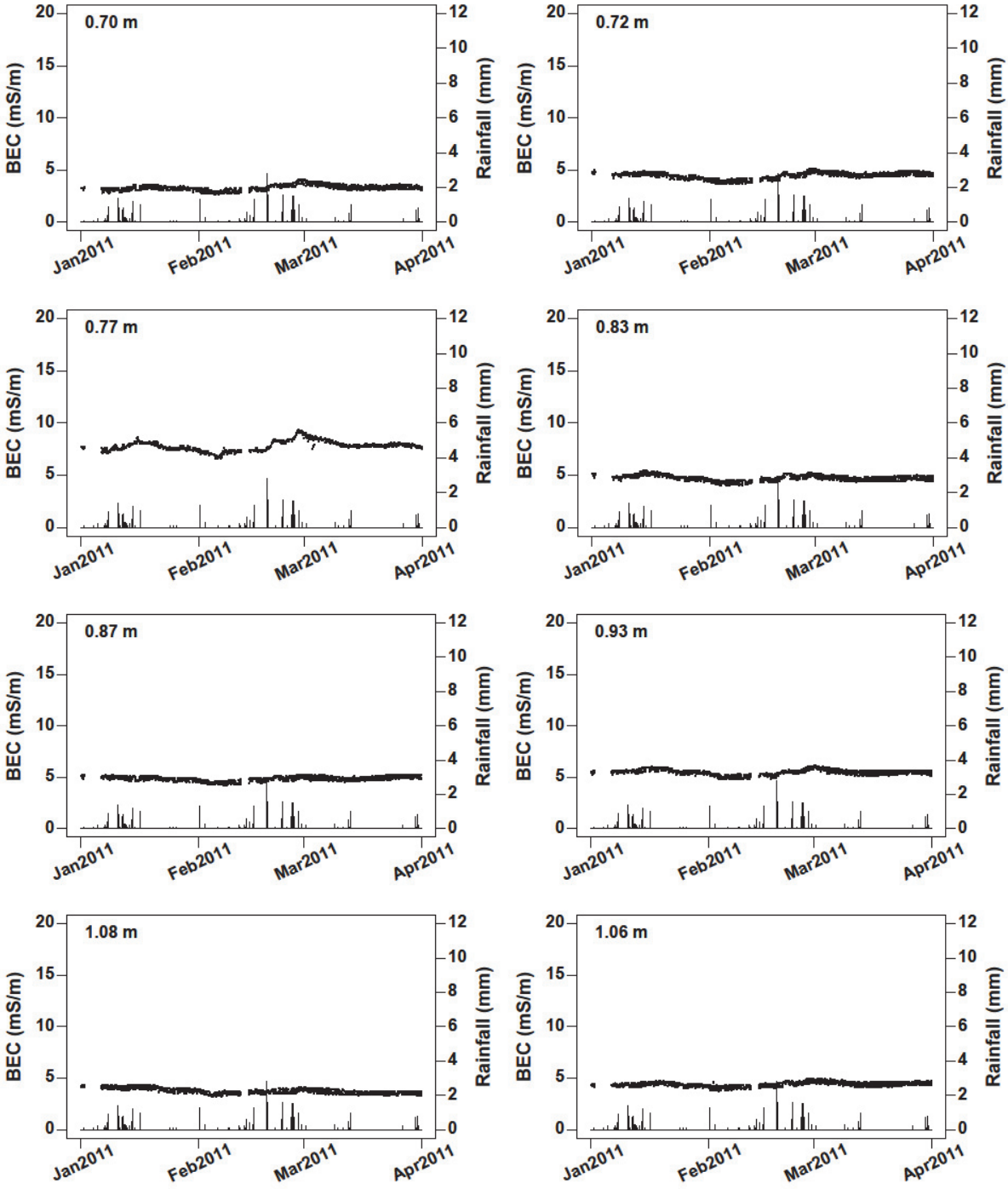



Figure 4.19 – TDR measured bulk electrical conductivity (BEC) during Winter 2011, from 0.70 and 1.08 m depth. The left column corresponds to array 1 and the right column to array 2.

Similar results to the ones shown in Figures 4.16 to 4.19 corresponding to Winter 2011 were also obtained for other seasons. In particular, rainfall was confirmed to be a major factor affecting the EM soil properties, especially the apparent permittivity.

However, an interesting behaviour was recorded during Summer 2011. As shown in Figures 4.20 and 4.21 the shallower probes responded only very slightly to rainfall events. Only probes at 0.42 and 0.59 m depth of array 2 seemed to increase as usual when rainfall occurred. Small increases were also visible at 0.60 m in array 1, although these are of little importance. The difference between arrays can at least partially be explained with differential infiltration paths of the water into the soil (Dekker et al., 1999; Zhou et al., 2002).

Since all the probes in the topsoil measured almost constant EM soil properties it is unlikely that these data were due to faulty equipment. A possible explanation is that the evapotranspiration was too high for the TDR probes to detect substantial changes in the soil conditions corresponding to rainfall events. After Spring 2011 the soil was very dry. This caused the grass to absorb water immediately after infiltration, especially because Summer is the grass growing season. The TDR monitoring station was able to take a measurement per probe per hour and this sampling rate might not have been sufficient to detect changes due to an increase in water content in the topsoil, within the grass root system.

Another possible, and perhaps concurrent, explanation is the formation of air gaps in the topsoil during dry conditions. If cracks and fissures formed in the topsoil along the length of the TDR probes, this would have caused the TDR to measure on average a smaller apparent permittivity and BEC.

It is important to note that this behaviour occurred only during the Summer and that the shallower probes measured a rise in apparent permittivity and BEC in Autumn 2011, corresponding to rainfall events (Figures 4.22 and 4.23). It is apparent that from November

2011 the rainfall had a greater effect on the soil EM properties. As shown in Figures 4.22 and 4.23, both apparent permittivity and BEC experienced a cumulative increase in the topsoil, indicating that the evaporation and the water absorption by grass were much reduced. It is the combination of high rainfall events and low evapotranspiration in the late Autumn that caused the EM soil properties to remain higher during the Winter seasons, despite the amount of rainfall during the Winter being small (see section 4.3.2.1 and 4.3.2.2).

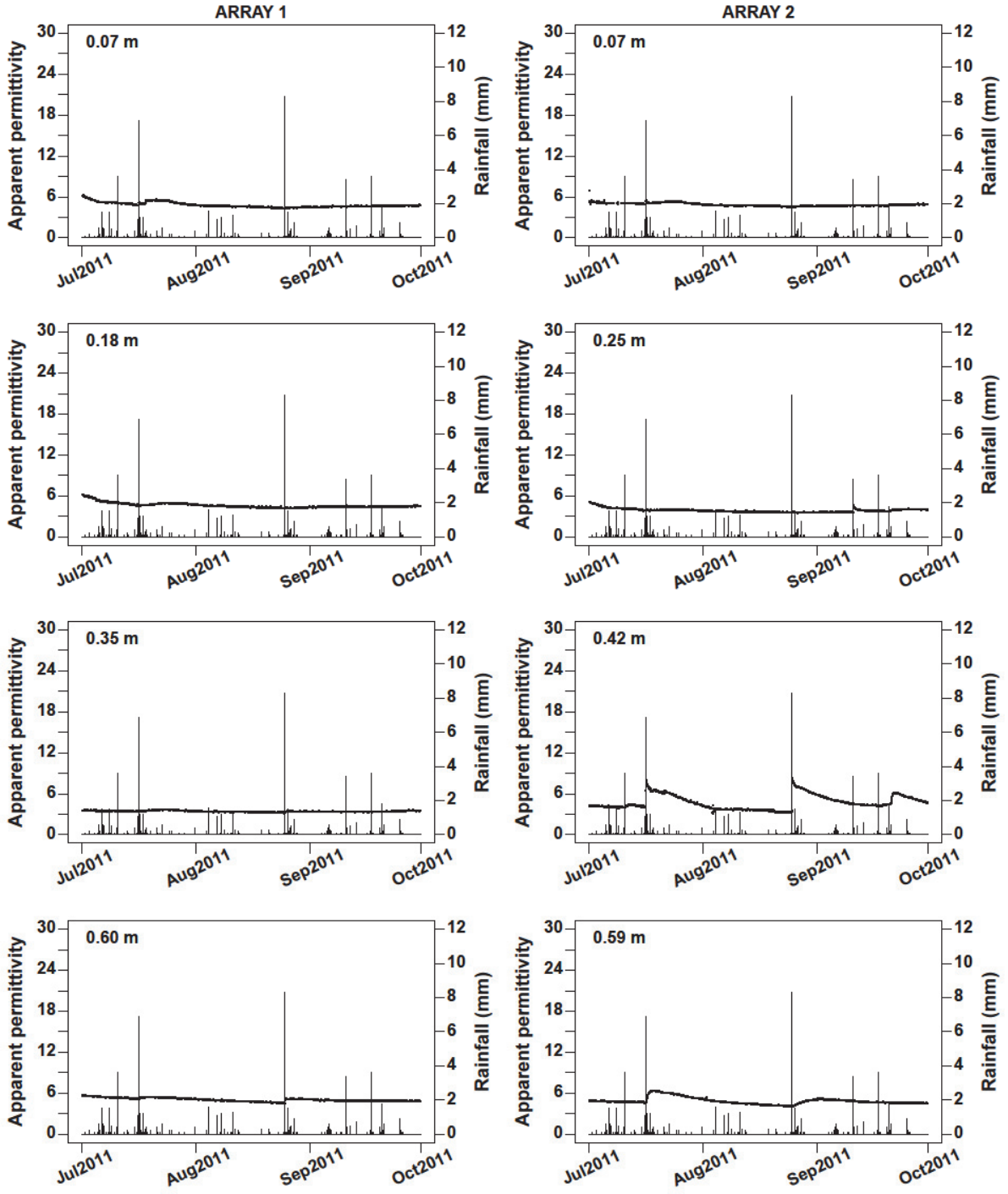



Figure 4.20 – TDR measured apparent permittivity during Summer 2011, from 0.07 and 0.60 m depth. The left column corresponds to array 1 and the right column to array 2.

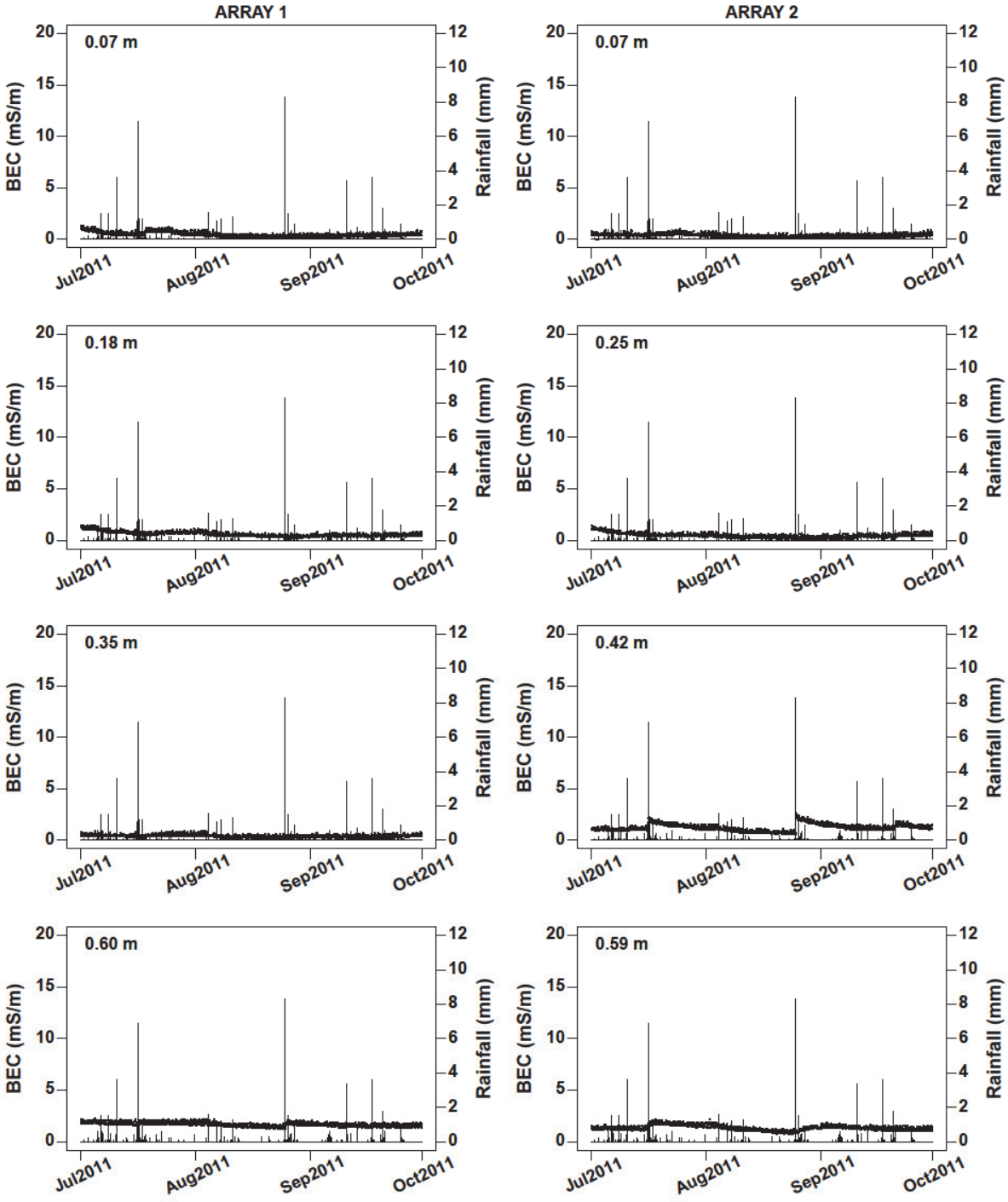



Figure 4.21 – TDR measured bulk electrical conductivity (BEC) during Summer 2011, from 0.07 and 0.60 m depth. The left column corresponds to array 1 and the right column to array 2.

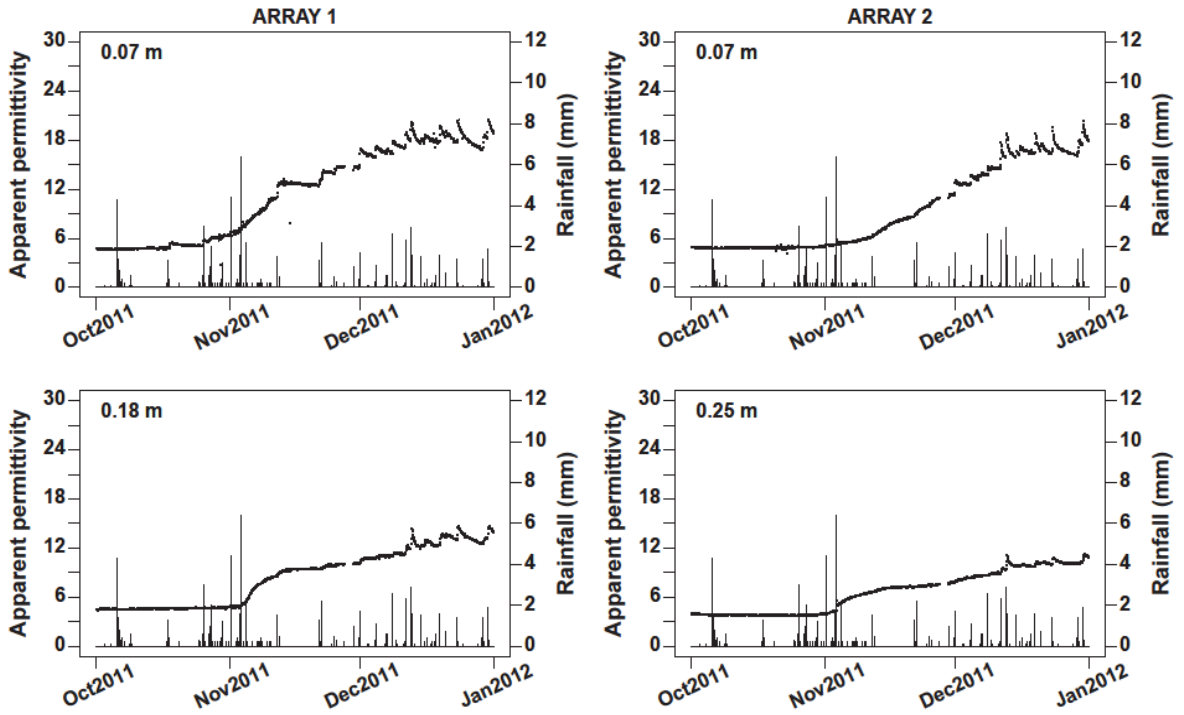



Figure 4.22 – TDR measured apparent permittivity during Autumn 2011, from 0.07 and 0.25 m depth. The left column corresponds to array 1 and the right column to array 2.

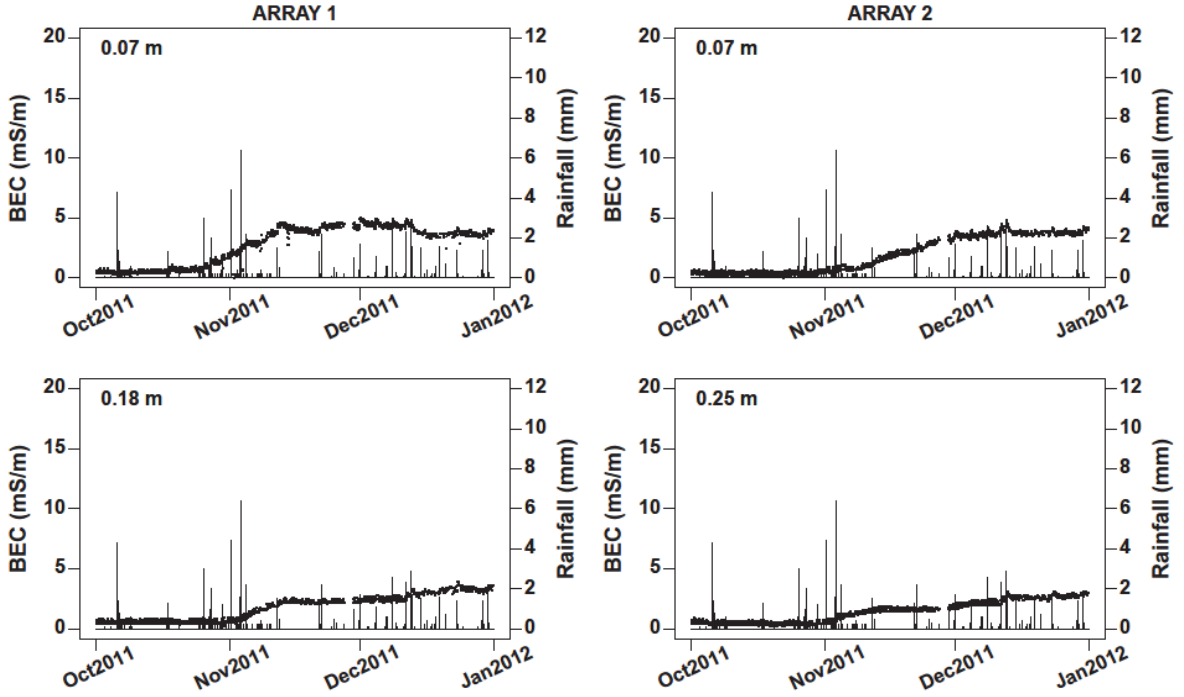



Figure 4.23 – TDR measured bulk electrical conductivity (BEC) during Autumn 2011, from 0.07 and 0.25 m depth. The left column corresponds to array 1 and the right column to array 2.

### 4.3.2.3. Variation of temperature

Figure 4.24 shows the hourly temperature variation of air and soil at three different depths, during the entire period of field monitoring. The temperature in Spring 2012 was lower than in Spring 2011, with the exception of a short period of warm and dry conditions occurring in May 2012. A sinusoidal pattern is clearly visible indicating the presence of a seasonal effect. This pattern was expected and has been shown by other authors for other soils at comparable depths such as wetlands (Musgrave and Binley, 2011), expansive clayey soils (Rajeev et al., 2012) and poorly developed organic and gravelly soils (Skierucha et al., 2012). The extent of this seasonal variation varies depending on the location and on the weather conditions. However, the results shown in Figure 4.24 and in the literature suggest that the soil temperature of the shallow subsurface (up to 1 m depth) behaves relatively homogeneously. The temperature variation measured in soil, even at shallow depth, was always smaller than in air. Despite recording peaks of extreme temperatures in air (e.g., approximately –10 °C in December 2010 and approximately 28 °C in October 2011), the soil temperature did not vary significantly. However, a slightly greater variation was recorded by the shallower temperature sensor at 0.16 m. The limited variation of the soil temperature with increasing depths is a well known phenomenon and has been reported by other authors (e.g., Mohanty et al., 1998; Lavelle and Spain, 2003; Comas et al., 2008). According to Lavelle and Spain (2003), the uppermost soil layer (up to approximately 0.1 m) is the most affected by changes in the air temperature. The seasonal variation of the soil temperature is greatly reduced at depths of a few metres, regardless of the soil type.

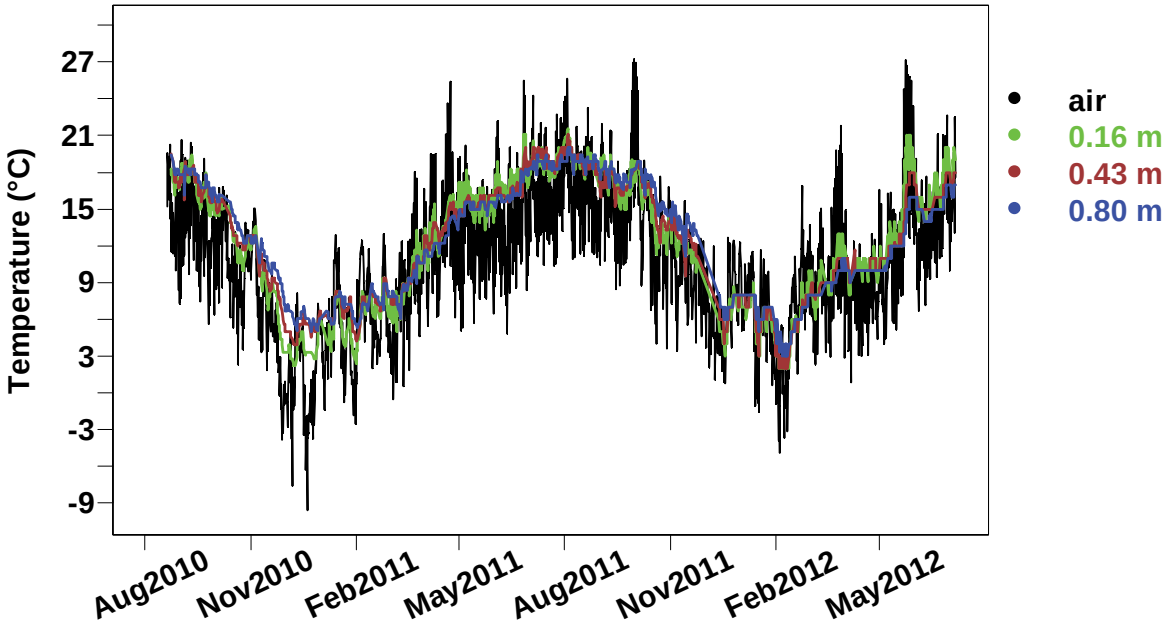



Figure 4.24 – Variation of hourly soil and air temperature during the entire period of field monitoring.

Table 4.4 shows the basic statistics of the temperature sensors during the entire period of field monitoring. The three temperature probes positioned at different depths recorded similar values, with a mean temperature of approximately 12 °C. No subzero temperatures were recorded in the soil during the period of monitoring.

Table 4.4 – Basic temperature statistics calculated over the entire period of field monitoring.

| | temperature (°C) | | |
|---|---|---|---|
| **probe** | **min** | **max** | **mean** |
| air | -9.6 | 27.8 | 10.1 |
| 0.16 m | 2.0 | 21.1 | 12.3 |
| 0.43 m | 3.0 | 20.0 | 12.4 |
| 0.80 m | 2.0 | 21.4 | 12.2 |

Figures 4.25 and 4.26 show in more detail the variation of soil and air temperature for Winter and Summer 2011. A sinusoidal pattern corresponding to diurnal variations is

visible, the extent of which is greater in air than in soil. Interestingly, the total variation during the Winter was greater than during the Summer because of the presence of alternating periods of relatively colder and warmer conditions. A delay between the increase in air temperature and the rise in soil temperature is noticeable, particularly in Winter (Figure 4.25). A more in depth analysis of the variation of the soil temperature in relation to the air temperature is described in section 4.4.2.2. Temperatures are higher in the Summer than in Winter, however it is important to note that local fluctuations within the same season can cause the soil temperature to vary quite significantly, as shown in Figure 4.25.

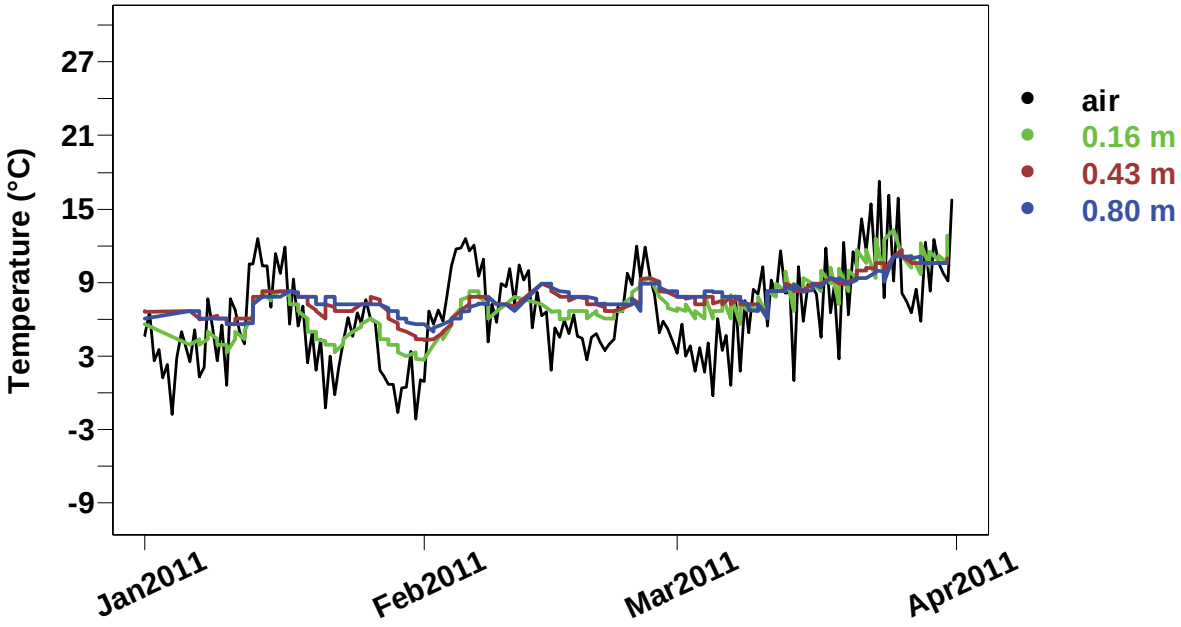



Figure 4.25 – Variation of soil and air hourly temperature during Winter 2011.

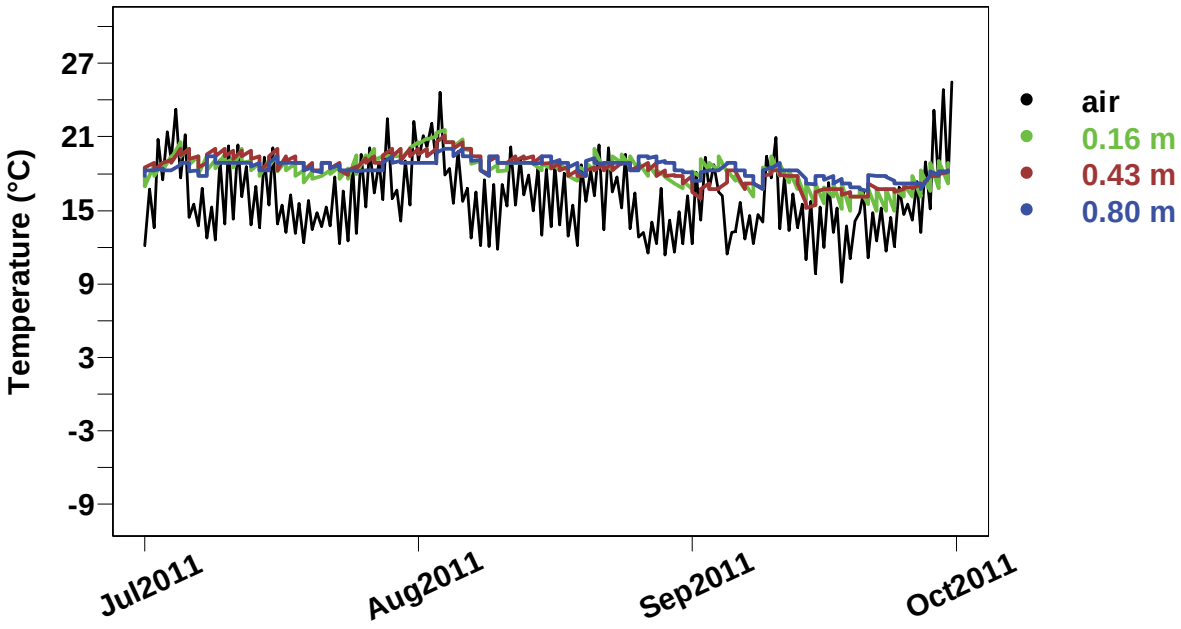



Figure 4.26 – Variation of soil and air hourly temperature during Summer 2011.

### 4.3.3. Daily variations

As shown in section 4.3.2.2 the soil EM properties varied significantly during the seasons. In order to analyse possible diurnal variations of the soil properties, two periods of a few days were selected corresponding to dry and wet conditions occurring in Spring 2011 and Spring 2012 respectively. The data are presented in Figures 4.27 to 4.30, for the probes of array 1. Air and soil temperature at different depths are also shown.

The selected dry event occurred in April 2011 after a number of weeks of dry and warm conditions and this is reflected by the low values of soil EM properties in Figures 4.27 and 4.28. Interestingly, these values remained approximately constant during the investigated three-day period, showing no dependency to temperature variations. BEC showed more variability, but no clear dependency to temperature is visible from Figures 4.27 and 4.28. It is important to note that a marked dependency of BEC to temperature was in fact recorded for shallow probes for other periods, for example in March 2011 (see section 3.3.4, Figure 3.36). However, it is apparent from Figures 4.27 and 4.28 that this relationship was not consistent. Despite large fluctuations of air temperature, the soil temperature varied only marginally and remained constant deeper in the soil profile.

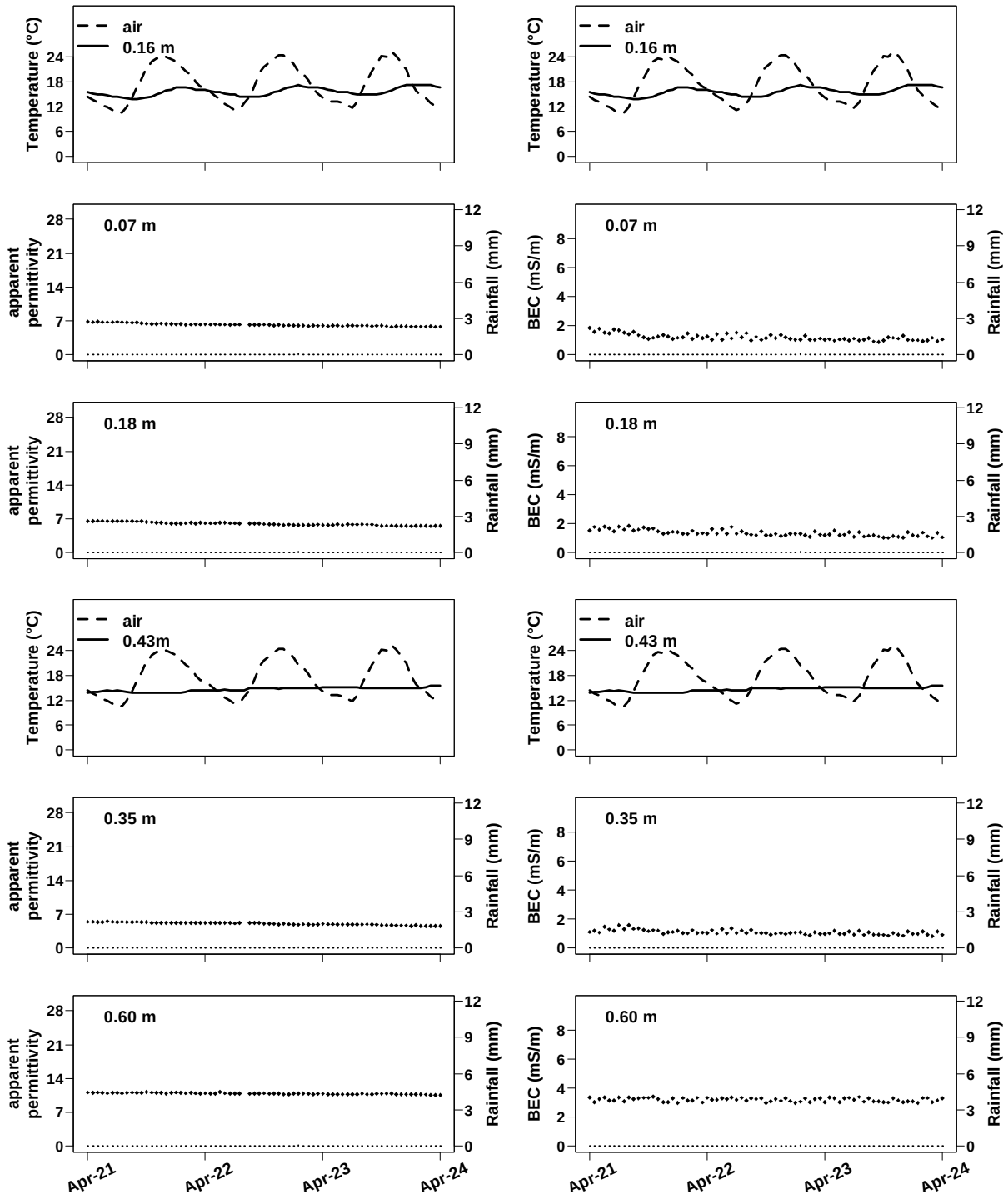



Figure 4.27 – Daily variation of the soil parameters (apparent permittivity, left and BEC, right) in the upper part of the soil profile for a selected period of dry conditions occurring in Spring 2011. [Note: the thin dots represent the rainfall, the thick dots are the apparent permittivity or the BEC]

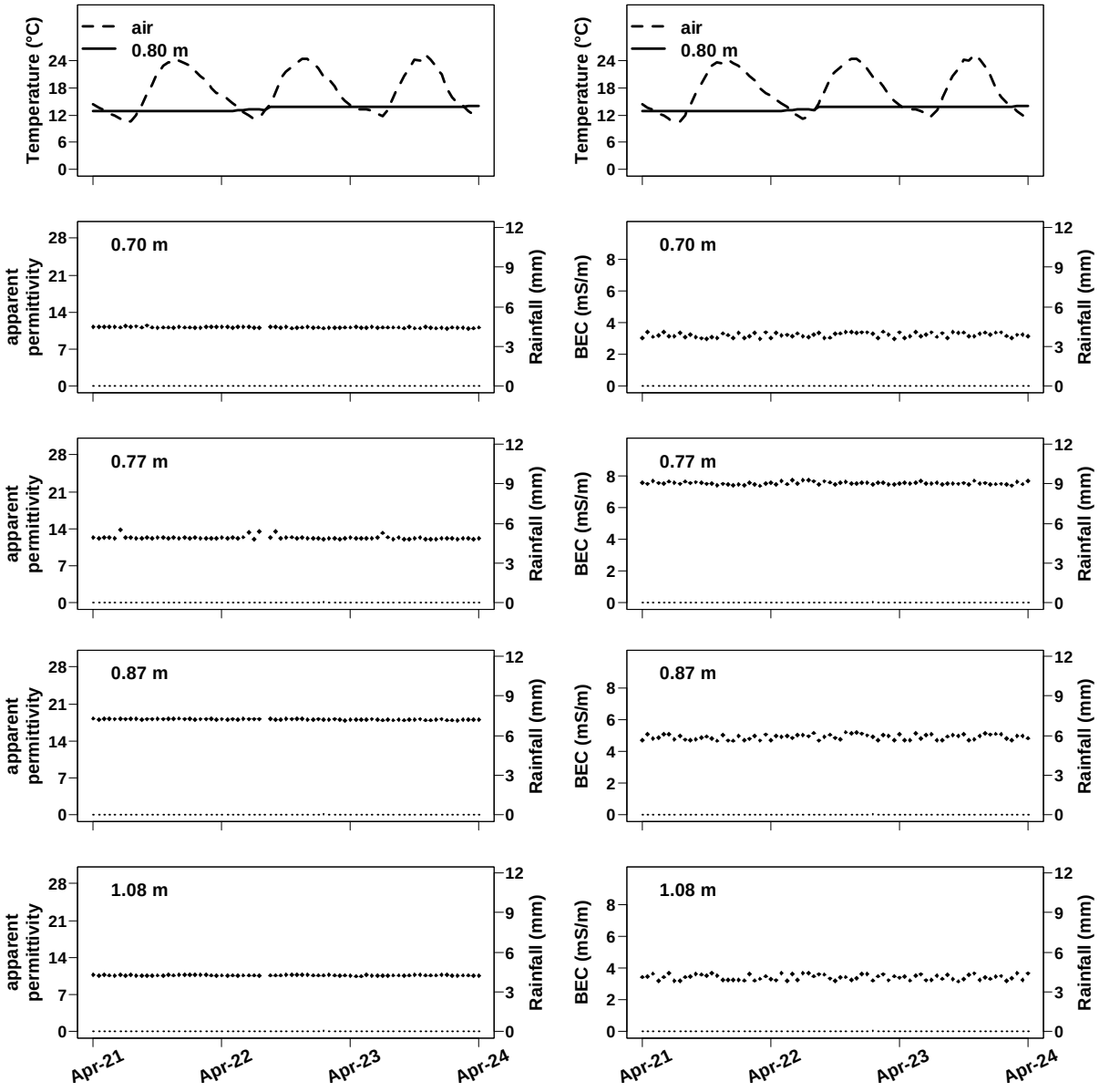



Figure 4.28 – Daily variation of the soil parameters (apparent permittivity, left and BEC, right) in the lower part of the soil profile for a selected period of dry conditions occurring in Spring 2011. [Note: the thin dots represent the rainfall, the thick dots are the apparent permittivity or the BEC]

The selected wet event corresponding to a four-day period in April 2012 showed a clear dependency of the soil EM properties to rainfall. In particular, a significant rainfall event occurring on the 18$^{th}$ of April 2012 caused the apparent permittivity and BEC to rise considerably. As shown in Figures 4.29 and 4.30, the water reached a depth of 0.20 m several hours after the rainfall event. The values of the deeper probes remained almost constant after more than 24 hours from the rainfall event, indicating that the water stopped in the upper part of the soil profile or took longer to infiltrate to greater depths. Significantly, Figures 4.29 and 4.30 show greater variability of BEC, despite the temperature recorded by the temperature sensors remaining approximately constant. This can be due to inaccuracies associated with the TDR and the temperature measurements and possibly to unknown external factors. However, the magnitude of this variation was small and not significant at all depths.

It is worth mentioning that the presence of a diurnal cycle for temperature but not for soil water was also reported in the literature for other soil types. For example, Mohanty et al. (1998) reported a lack of a diurnal variation for soil water for a fine sandy loam. However, as explained in Chapter 2, the dependency of the soil water to temperature fluctuations is very complex. Wraith and Or (1999) reported of contradictory studies, some showing a greater dependency of the apparent permittivity to temperature in fine-grained soils (Verstricht et al., 1994), while others showing a greater dependency in sandy soils (Halbertsma et al., 1995).

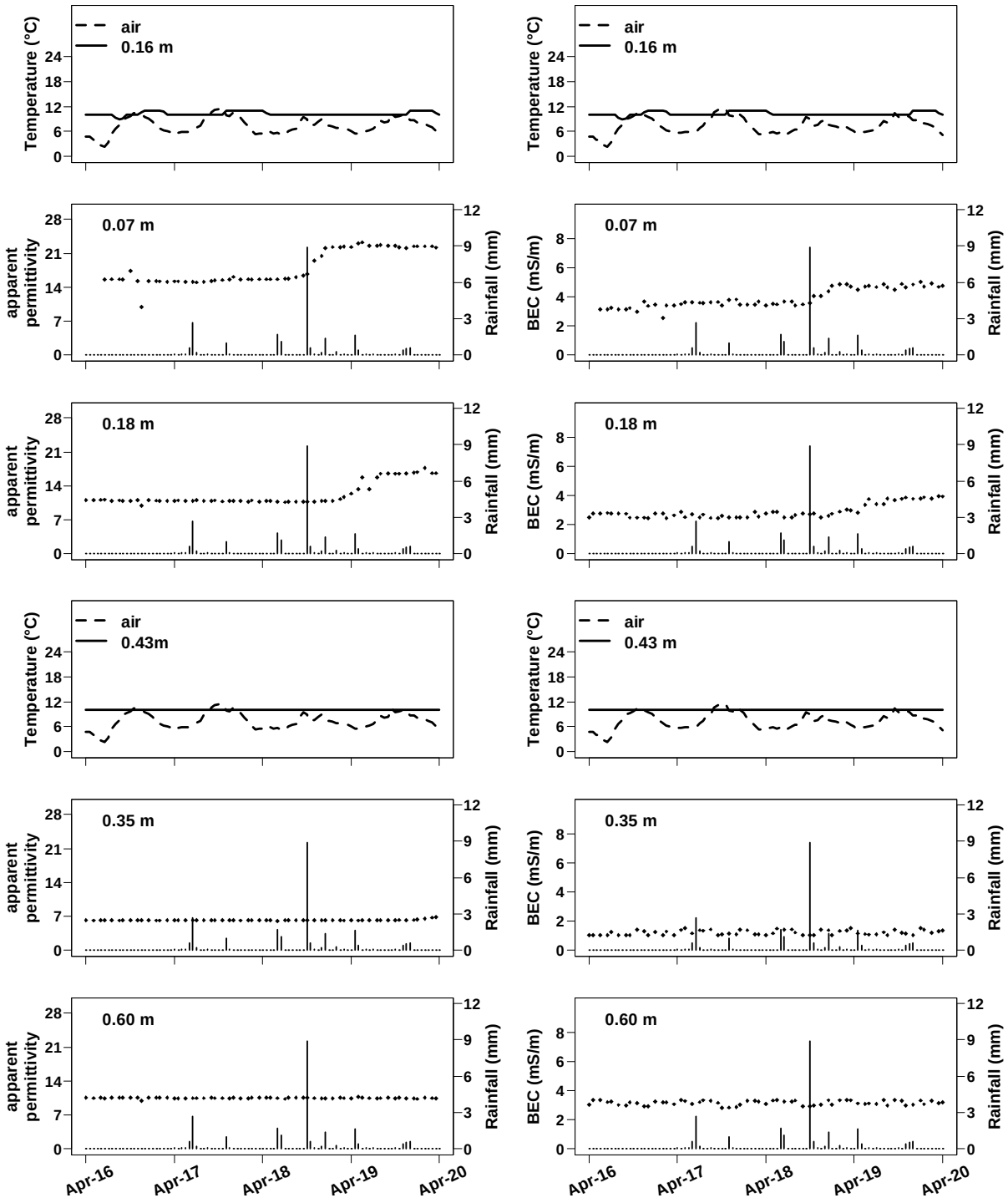



Figure 4.29 – Daily variation of the soil parameters (apparent permittivity, left and BEC, right) in the upper part of the soil profile for a selected period of wet conditions occurring in Spring 2012.

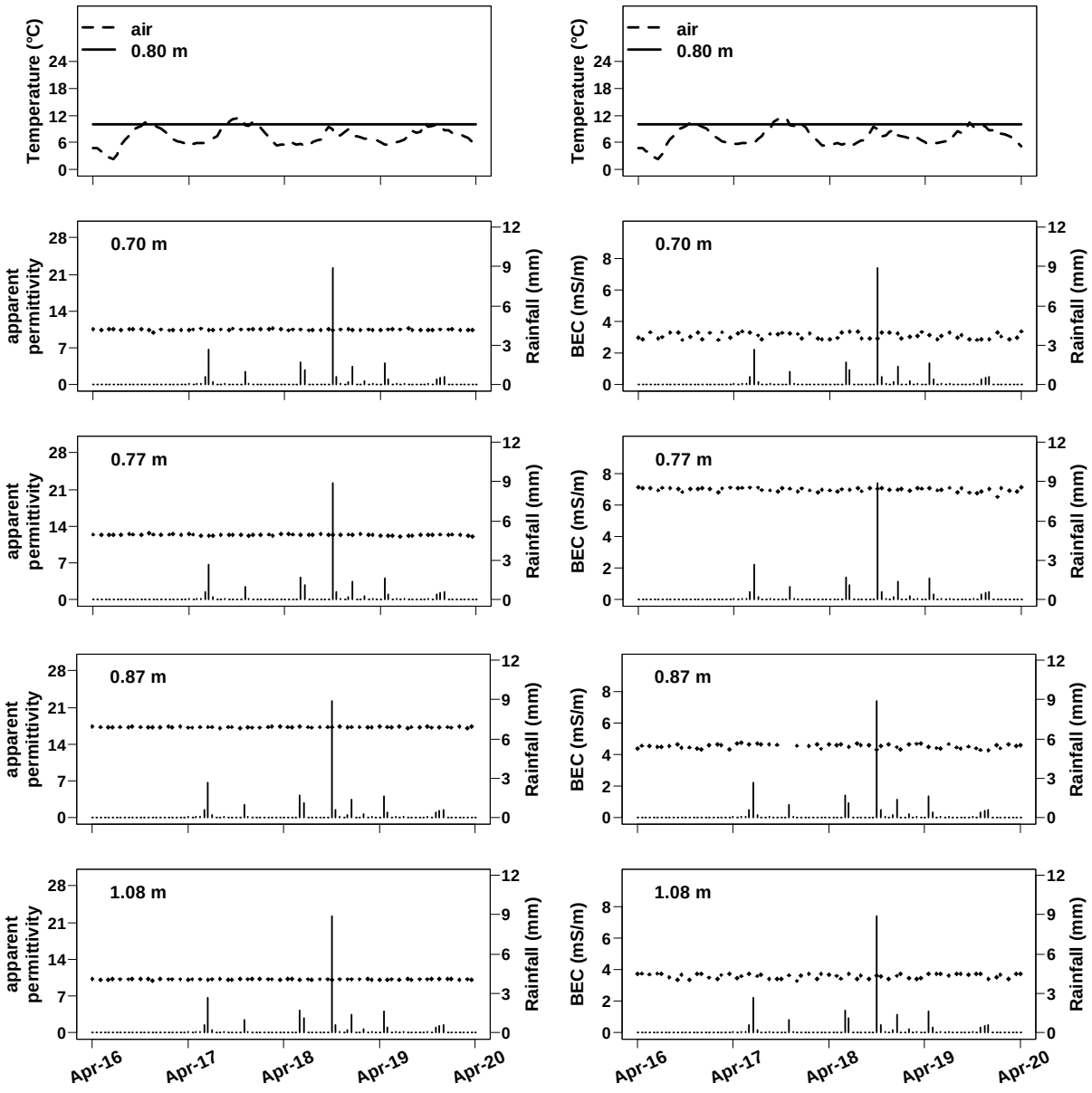



Figure 4.30 – Daily variation of the soil parameters (apparent permittivity, left and BEC, right) in the lower part of the soil profile for a selected period of wet conditions occurring in Spring 2012.

### 4.3.4. Field monitoring: summary

The previous sections described the seasonal and daily variation of the weather parameters, soil EM properties and temperature obtained from the monitoring conducted at the University of Birmingham. A period of approximately 22 months was analysed, where wet and dry conditions occurred. The main findings were:

- The weather parameters showed significant seasonal variation, with sinusoidal patterns for temperature and solar radiation. Rainfall varied significantly during the monitoring period. In particular, Spring 2011 and Spring 2012 showed opposite conditions, the first being very dry, the second very wet.
- The soil EM properties and temperature varied significantly with seasons. This variation was highly dependent on the amount of rainfall, in particular for apparent permittivity. However, BEC showed smaller variability even corresponding to rainfall events because of the sandy and gravelly nature of the soil. The recorded minima and maxima values were, respectively, approximately 3 and 29 for apparent permittivity, and approximately 0.01 mS/m and 18 mS/m for BEC.
- The topsoil and the deeper horizon with slightly higher percentage of fines showed greater variability in soil EM properties.
- The shallow TDR probes installed in the grass root system did not measure a substantial increase in the soil EM properties during Summer 2011. This is thought to be due to the high evapotranspiration and the formation of air gaps during that period.
- Despite a significant seasonal variation in air temperature the soil temperature did not reach extreme values (e.g., no subzero temperatures were measured) and remained relatively constant at different depths, up to a depth of approximately 1 m. However, fluctuations in air temperature during Winter caused the soil temperature

to vary quite significantly in the same season, up to 3-4 °C. Over the monitoring period, the soil temperature varied between 2 °C and 21 °C.

- Both apparent permittivity and BEC of the soil studied did not have a diurnal variation cycle. Apparent permittivity was largely independent to temperature variations. BEC showed greater variability but no clear relationship with temperature was found. The major influencing factor causing the soil EM properties to vary was rainfall.

# 4.4. FACTORS AFFECTING THE SOIL ELECTROMAGNETIC PROPERTIES

## 4.4.1. Introduction

This section describes the results of the statistical analyses carried out on the soil data collected in the field with the aim of identifying the relationships between parameters and their influence in determining the EM behaviour of the soil. The analyses include time-domain cross correlation, simple correlations and principal component analysis (PCA). An empirical calibration relating the apparent permittivity to the volumetric water content is also shown in this section. A summary of the main results is included at the end of the section.

## 4.4.2. Time-domain cross correlation

As explained in section 4.3, rainfall plays a major role in determining the EM properties of the soil. Although time plots visualise the dependency between EM soil properties and rainfall events, a more analytical approach involving time-domain cross

correlation can be used to demonstrate whether there is a lagged linear association between two time series observations (Cowpertwait, 2006). This analysis is useful to quantify time lags between events, in this case, between rainfall and soil EM properties and between air temperature and soil EM properties. For this analysis a wet and a dry event were selected.

### 4.4.2.1. Selected rainfall event

A rainfall event occurring in February 2011 was selected, corresponding to a cumulative rainfall of 10.2 mm in 10 hours (Figure 4.31).

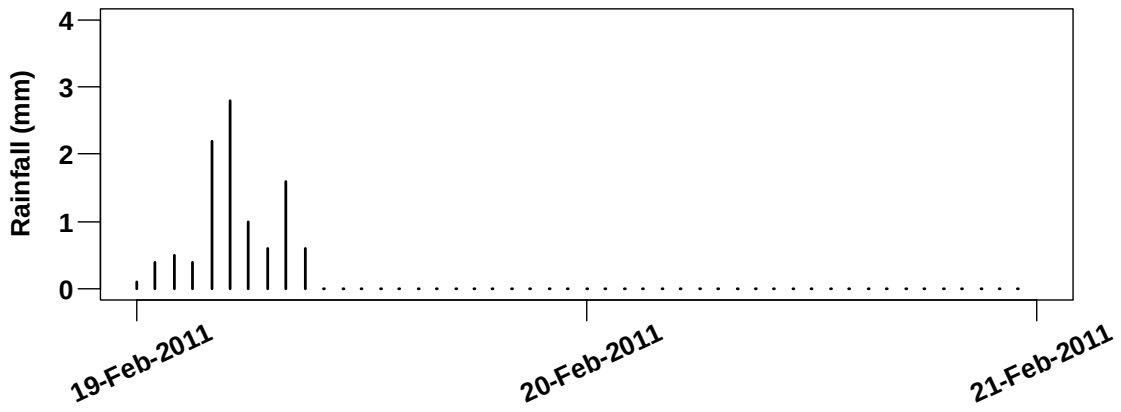



Figure 4.31 – Selected rainfall event occurring in February 2011, corresponding to a cumulative rainfall of 10.2 mm in 10 hours.

Figures 4.32 and 4.33 show the correlograms of the hourly apparent permittivity measured by array 1 against the corresponding hourly rainfall. The plots show two horizontal lines representing the 10 % significance level for the statistical test (i.e., correlations falling outside this range are significantly different from zero). As it can be seen there was a significant positive correlation between rainfall and apparent permittivity for most of the probes, with different time lags depending on the depth. The probes at

0.07 m and 0.18 m showed clear positive correlations with a time lag smaller than 10 hours, while probes at 0.70-0.87 m depth showed significant positive correlations after approximately 36 hours. Interestingly, probes at 0.35 m and 0.60 m, in the soil horizon almost completely lacking in fines content (section 4.2), did not show significant correlations with rainfall. However, a pattern was still distinguishable even for these probes.

The negative correlation occurring during and immediately after the rainfall event (Figures 4.32 and 4.33) is thought to be caused by the tendency of the soil to lose water during dry conditions through evapotranspiration and percolation. Therefore rainfall remained negatively correlated to the apparent permittivity until the water infiltrating into the soil reached the depth of the TDR probes.

Similar results were obtained for the probes of array 2 and for BEC (see appendix C), although the time lags were not always consistent. This was due to differential infiltration pattern of the water and to the actual time lags between apparent permittivity and BEC measurements. However, this analysis confirmed that rainfall is a major influencing factor affecting the soil EM properties. In addition, it shows that there was a time lag of several hours before the soil conditions changed because of rainfall. The absolute values of the time lags depend on the amount of rainfall and intensity in addition to the initial soil conditions (Zhou et al., 2002). Due to this complexity no attempts were made to quantify these lags more accurately. However, lags of several hours were expected for sandy and gravelly soils, which typically have a saturated hydraulic conductivity ranging between 0.01 and 1 cm/s (Chapuis, 2004).

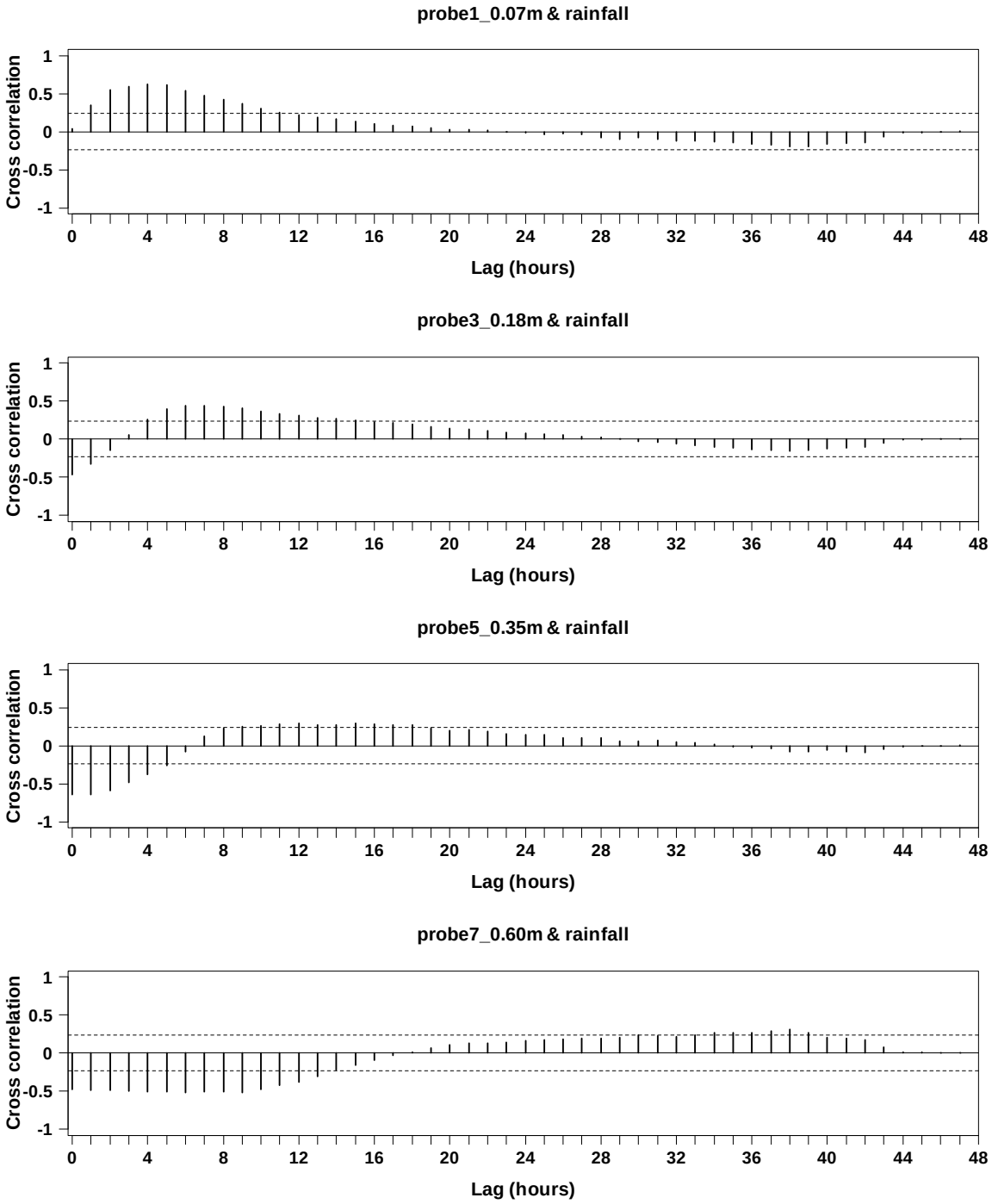



Figure 4.32 – Time-domain cross correlation between the apparent permittivity measured by the TDR probes in array 1, up to 0.60 m depth, and a rainfall event occurring in February 2011. [Note: the horizontal dashed lines represent the limits above which the absolute cross correlations are significant with a confidence level of 90 %]

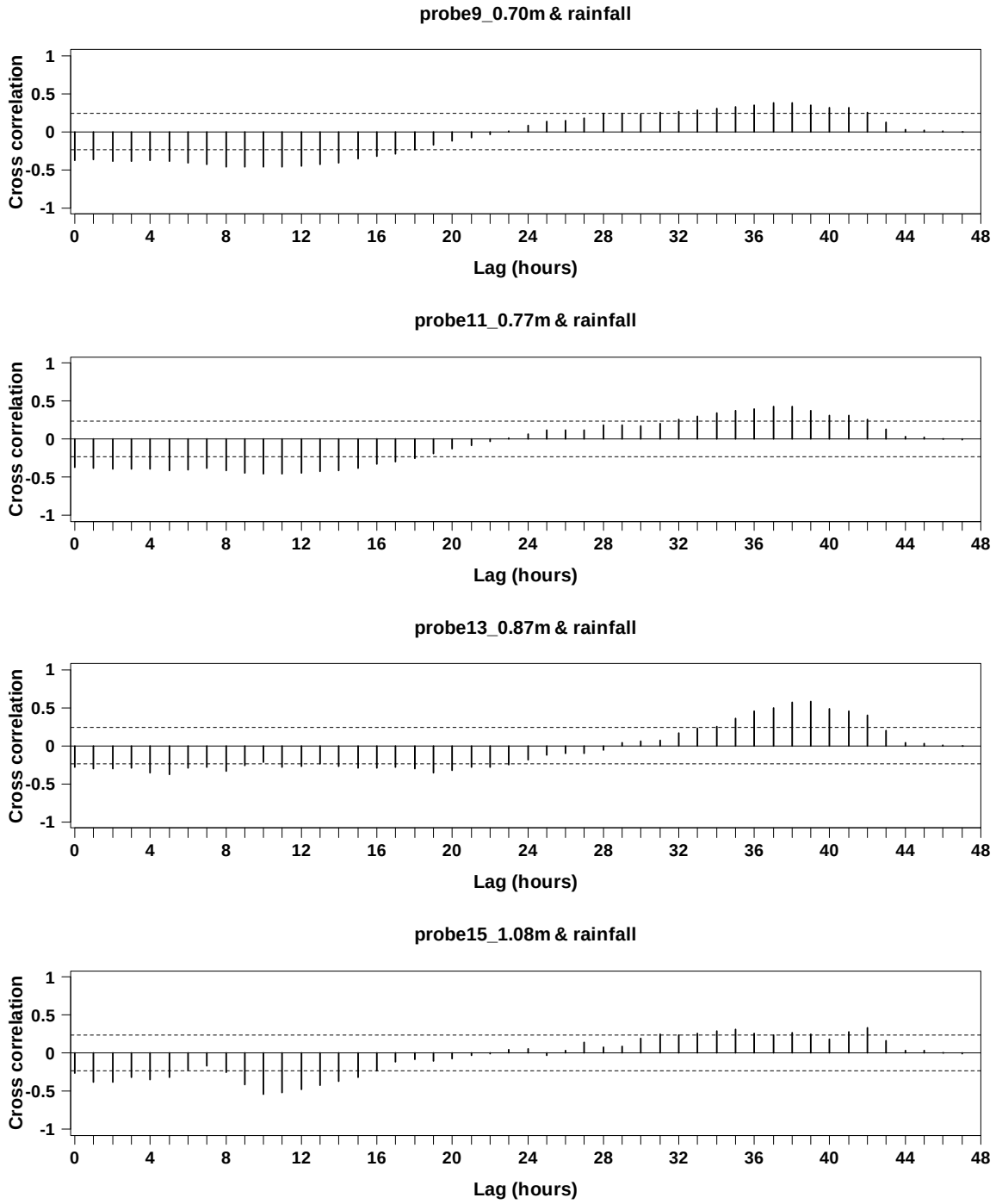



Figure 4.33 – Time-domain cross correlation between the apparent permittivity measured by the TDR probes in array 1, from 0.70 to 1.08 m depth, and a rainfall event occurring in February 2011. [Note: the horizontal dashed lines represent the limits above which the absolute cross correlations are significant with a confidence level of 90 %]

### 4.4.2.2. Selected dry event

In order to verify the existence of possible lagged correlations between air temperature and the soil parameters a dry day (21st April 2011) showing large temperature fluctuations was selected. Figure 4.34 shows the diurnal variation of air and soil temperature. As visible, the soil temperature did not vary significantly compared to the air temperature. A time lag of approximately 4 hours between the air temperature and the soil temperature at different depths was confirmed by the correlations shown in Figure 4.35. The deeper temperature sensor at 0.80 m did not show significant correlations. It is well known that wet soils need larger amounts of energy than dry soils in order to heat up because water has a large heat capacity[10] (Foth, 1990).

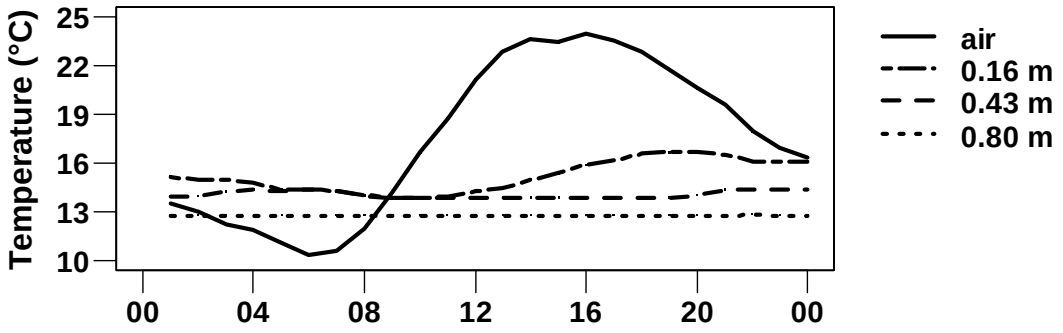



Figure 4.34 – Diurnal variation of air and soil temperature for a selected dry day (21st April 2011).

[10] In order to increase the temperature of 1 g of water by 1 °C it is necessary to provide 1 calorie of heat energy. One gram of a dry soil requires approximately 0.2 calories for its temperature to increase by 1 °C (Foth, 1990).

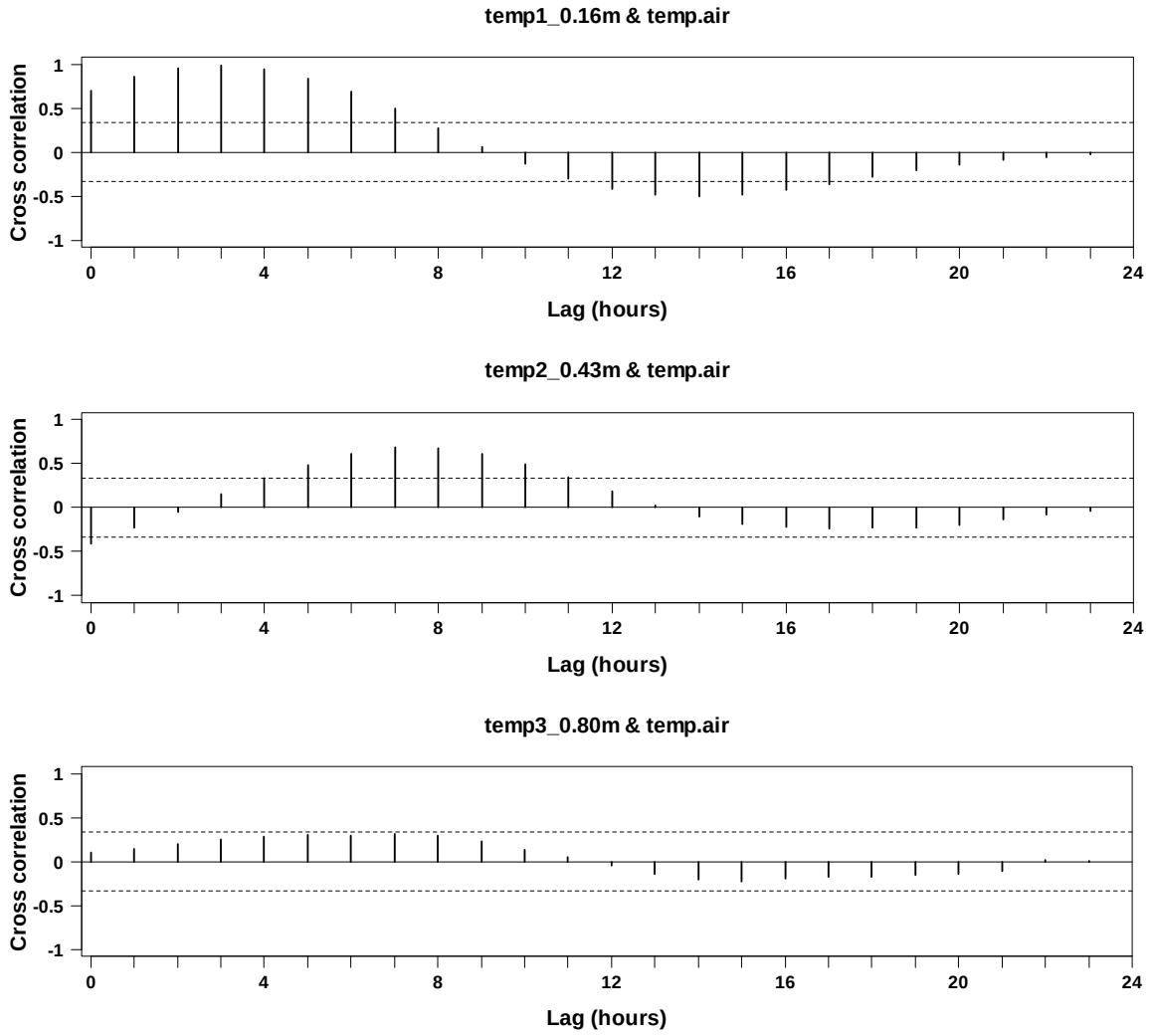



Figure 4.35 – Time-domain cross correlation between the soil temperature at different depths and the air temperature of the 21st April 2011. [Note: the horizontal dashed lines represent the limits above which the absolute cross correlations are significant with a confidence level of 90 %]

Figures 4.36 and 4.37 show the correlograms of BEC measured by array 1 against air temperature. No visible correlations were observed, confirming that the air temperature only had a minor impact in determining the soil EM properties of the studied soil. Similar results were obtained for apparent permittivity (see appendix C).

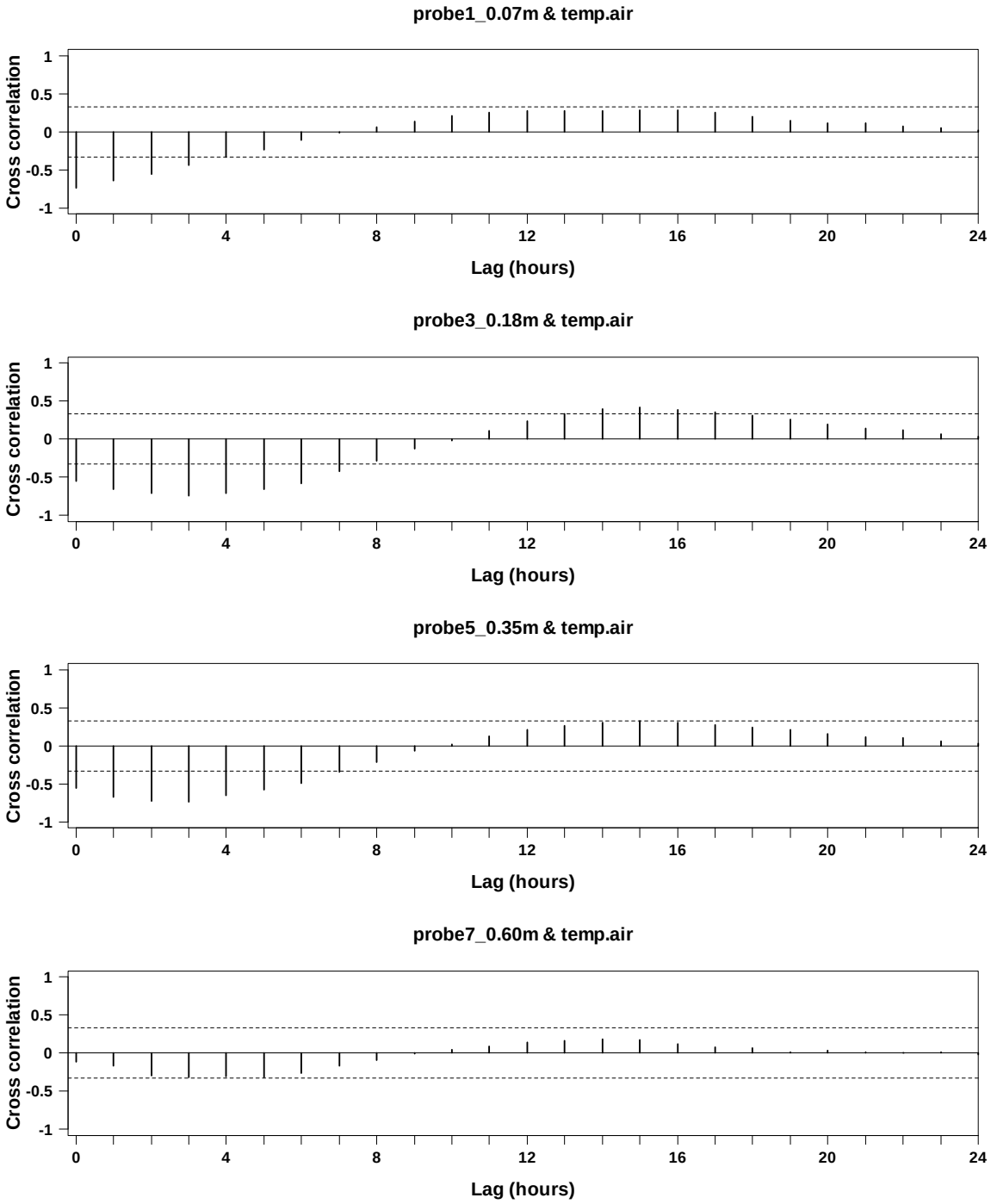



Figure 4.36 – Time-domain cross correlation between BEC measured by the TDR probes in array 1, up to 0.60 m depth, and the air temperature of the 21st April 2011. [Note: the horizontal dashed lines represent the limits above which the absolute cross correlations are significant with a confidence level of 90 %]

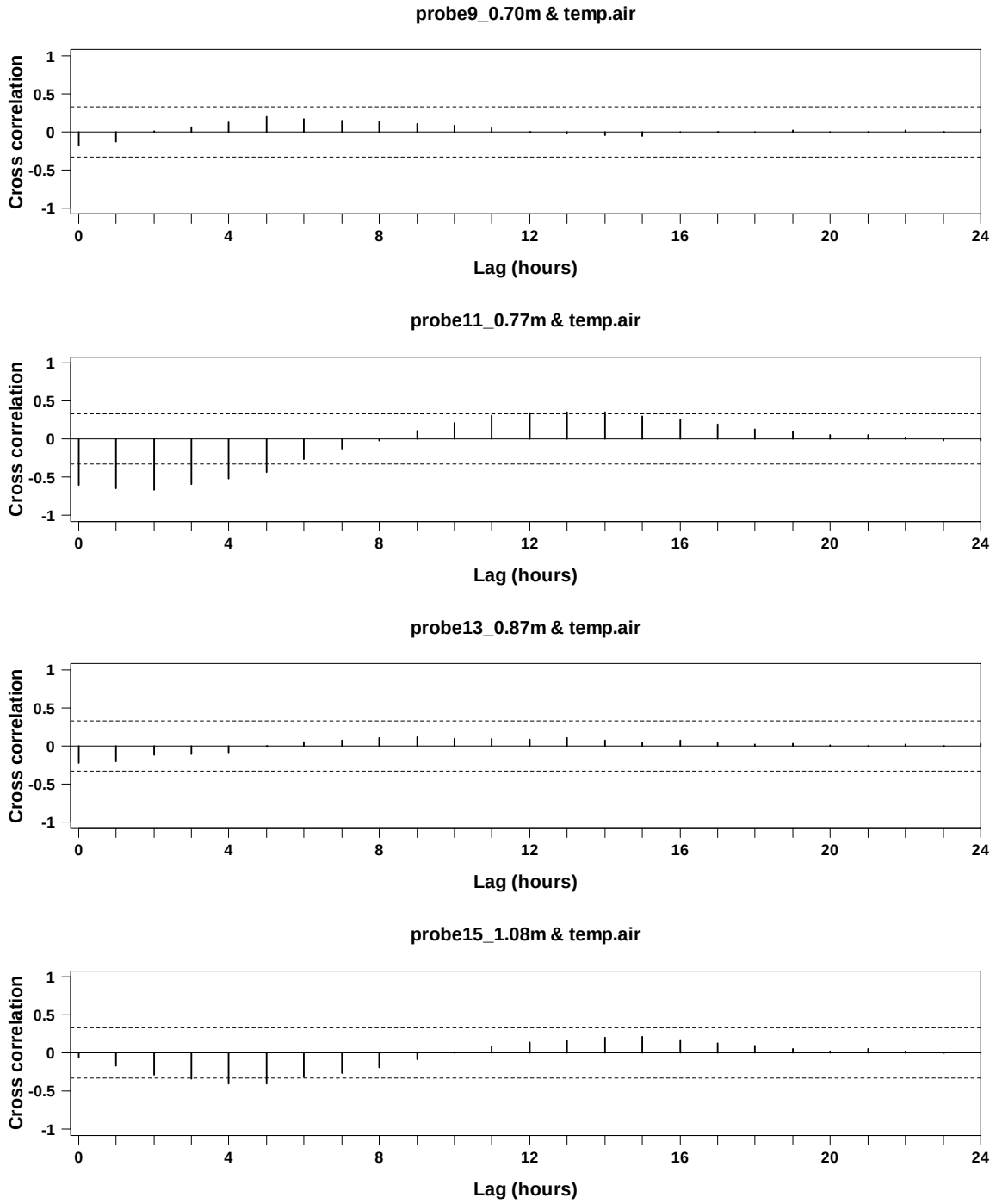



Figure 4.37 – Time-domain cross correlation between BEC measured by the TDR probes in array 1, from 0.70 to 1.08 m depth, and the air temperature of the 21st April 2011. [Note: the horizontal dashed lines represent the limits above which the absolute cross correlations are significant with a confidence level of 90 %]

### 4.4.3. Correlation between parameters

This section describes the relationships between the soil (and weather) parameters. Correlation coefficients were calculated between pairs of monitored soil properties and a principal component analysis was performed on all the measured soil parameters (Adler, 2010; Todeschini R., 1998).

Figure 4.38 shows the correlation coefficients between the daily means of apparent permittivity, BEC and temperature, for the entire period of field monitoring and for the TDR probes of both arrays (see Table 3.8 or Table 4.5 later in this section for information on the probe depths and identifiers). Since only three temperature sensors were used, each TDR probe was associated with the closest temperature sensor in terms of depth. In order to perform this analysis, all missing values were removed and only the available daily data for each parameter were used. Because the EM soil parameters were not normally distributed (see section 4.3.2.2) the Spearman correlation was used, since it does not make any assumptions about the underlying distribution (Adler, 2010).

A strong positive correlation between apparent permittivity and BEC is visible. Similar levels of correlations were described by other authors, between BEC and volumetric water content (e.g., Kachanoski et al., 1988). In agreement with the information reported by Wraith and Or (1999), the apparent permittivity seems to be inversely correlated with temperature. The apparent permittivity of free liquid water is known to decrease with increasing temperature, but higher temperatures could release a portion of bound water and therefore cause an increase in the apparent permittivity (see section 2.4.2). The results shown in Figure 4.38 suggest that the first mechanism was dominant in the soil studied and indicates that the bound water fraction was small. BEC shows a small negative correlation with temperature. This indicates that BEC was more affected by the amount of water in the soil (described here by the apparent permittivity) than by temperature.

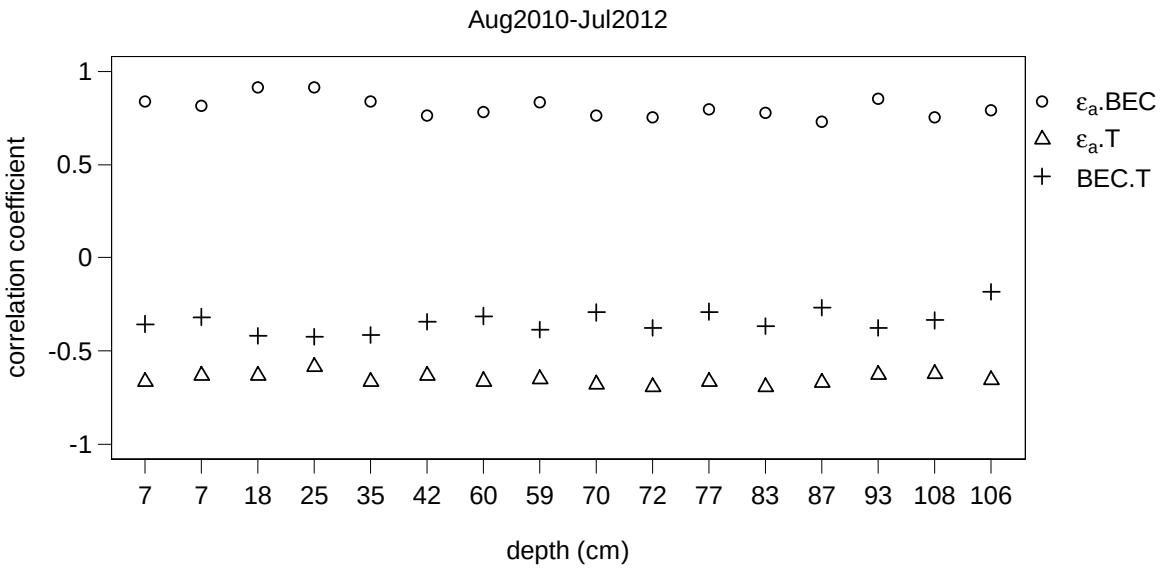



Figure 4.38 – Correlation coefficients calculated between pairs of soil parameters for the entire period of field monitoring and for all the TDR probes.

Despite the evident relationships shown in Figure 4.38, the measured soil parameters showed complex interactions depending on the soil conditions. Figures 4.39 and 4.40 show the correlation coefficients between the soil variables for Spring 2011 and Spring 2012, respectively. During dry conditions (Spring 2011) it seems that the negative correlation between apparent permittivity and temperature was dominant, and therefore BEC also showed a strong negative correlation with temperature. In other words, BEC was most affected by the amount of water. During wet conditions (Spring 2012) BEC showed an opposite correlation with temperature. A possible explanation is that under wet conditions BEC became less dependent on the amount of water and was also affected by the soil temperature. Apparent permittivity did not show an evident correlation with temperature during Spring 2012. However, the relationship was slightly positive and hence very different from the negative relationship found in Spring 2011. The same analysis conducted for the other seasons showed a mixed response, making it difficult to derive absolute conclusions.

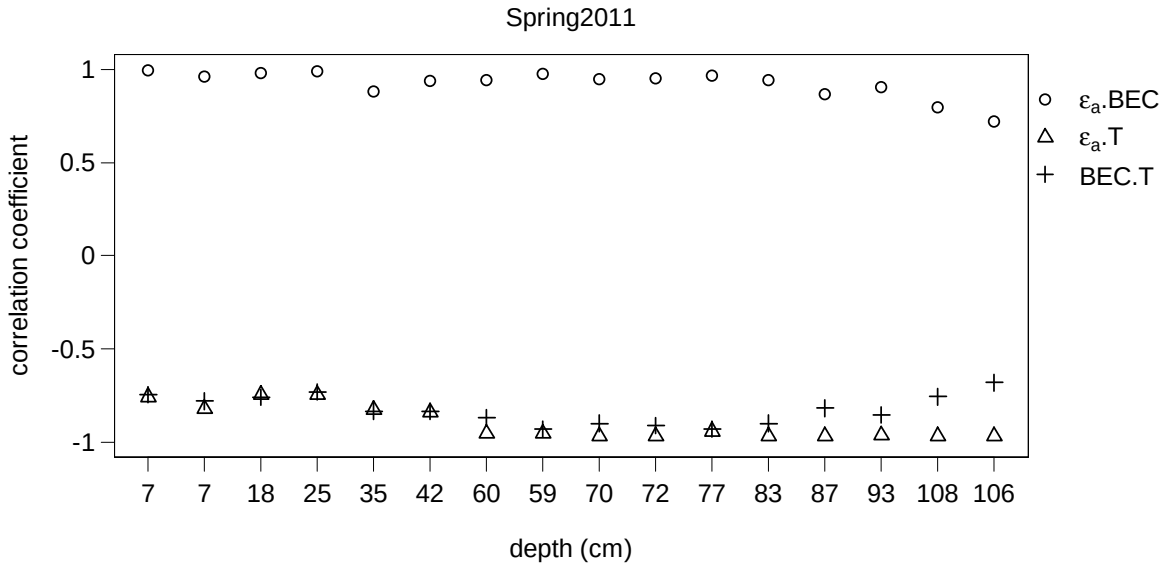



Figure 4.39 – Correlation coefficients calculated between pairs of soil parameters for Spring 2011 and for all the TDR probes.

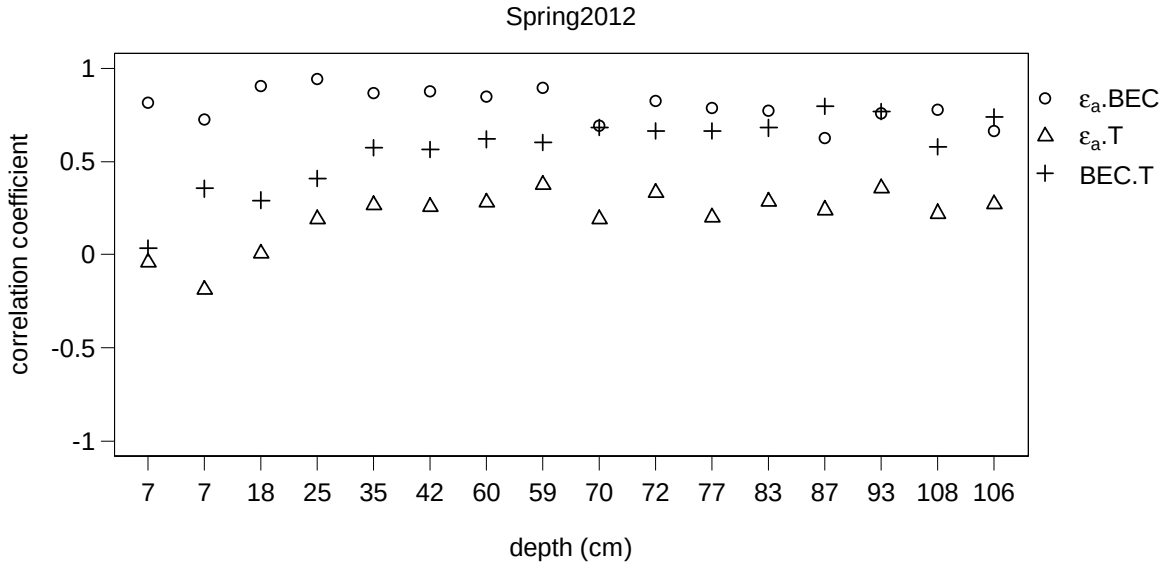



Figure 4.40 – Correlation coefficients calculated between pairs of soil parameters for Spring 2012 and for all the TDR probes.

Another way of visualising the relationships between parameters is by means of a matrix of scatterplots. In this type of plot the variables are placed on the diagonal of a matrix and define the axes for each scatterplot in the matrix. For example, the top-right scatterplot shows the relationship between the variable on the bottom-right of the matrix, which forms the x-axis, and the variable on the top-left of the matrix, which forms the y-axis. The scatterplots on the upper-right of the matrix diagonal show the same relationships of the scatterplots on the bottom-left of the matrix diagonal, but with inverted axes. For example, the scatterplot on the bottom-left corner of the matrix shows the same relationship shown on the top-right scatterplot, but with inverted axes.

Figures 4.41 to 4.43 show the scatterplot matrix between apparent permittivity, BEC (mS/m) and temperature (° C) for each main soil horizon. Each colour corresponds to a different season. The data represent the daily means over the entire period of field monitoring, therefore each season contains the data obtained in 2010, 2011 and 2012[11]. Generally it can be noted that apparent permittivity and BEC were positively correlated during all seasons and for each soil horizon. The situation is more complex when comparing the soil EM properties with temperature. No consistent pattern with seasons was visible. It appears that there was no clear seasonal relationship between soil EM properties and temperature.

[11] Appendix C shows the scatterplot matrices calculated only for 2011.

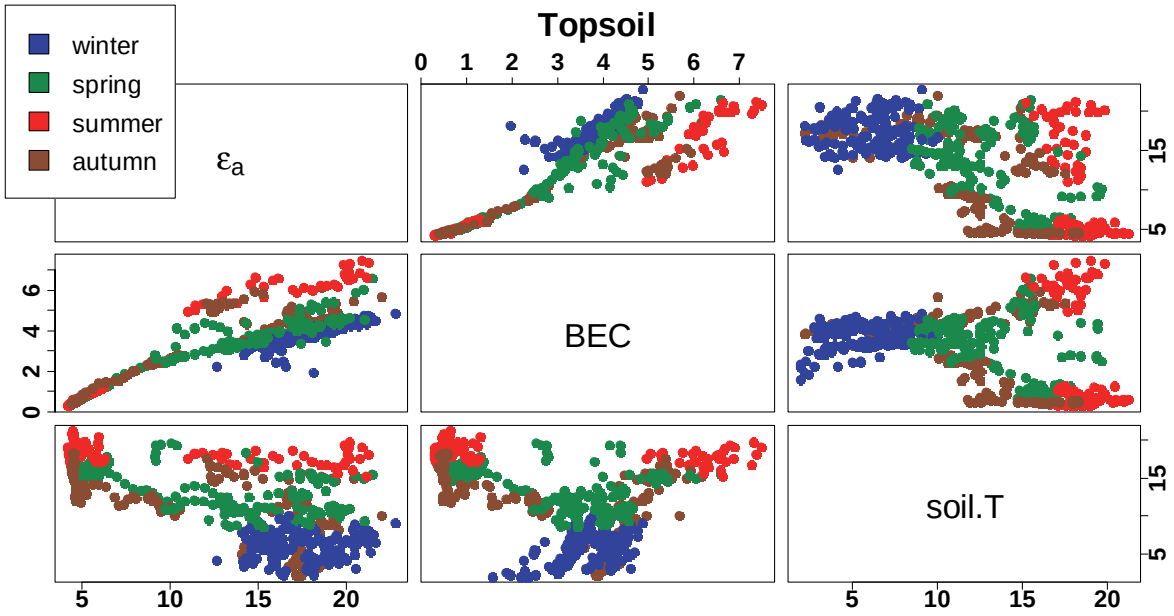



Figure 4.41 – Scatterplot matrix of the topsoil apparent permittivity, BEC (mS/m) and soil temperature, soil.T (° C), for the entire period of field monitoring.

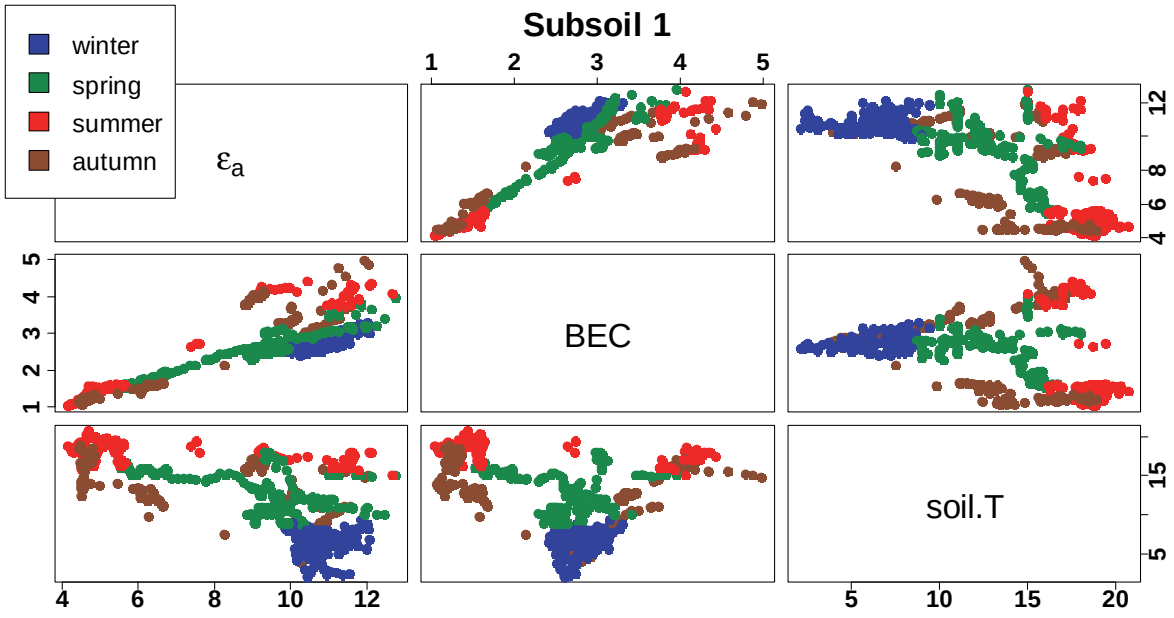



Figure 4.42 – Scatterplot matrix of the shallow subsoil (subsoil 1) apparent permittivity, BEC (mS/m) and soil temperature, soil.T (° C), for the entire period of field monitoring.

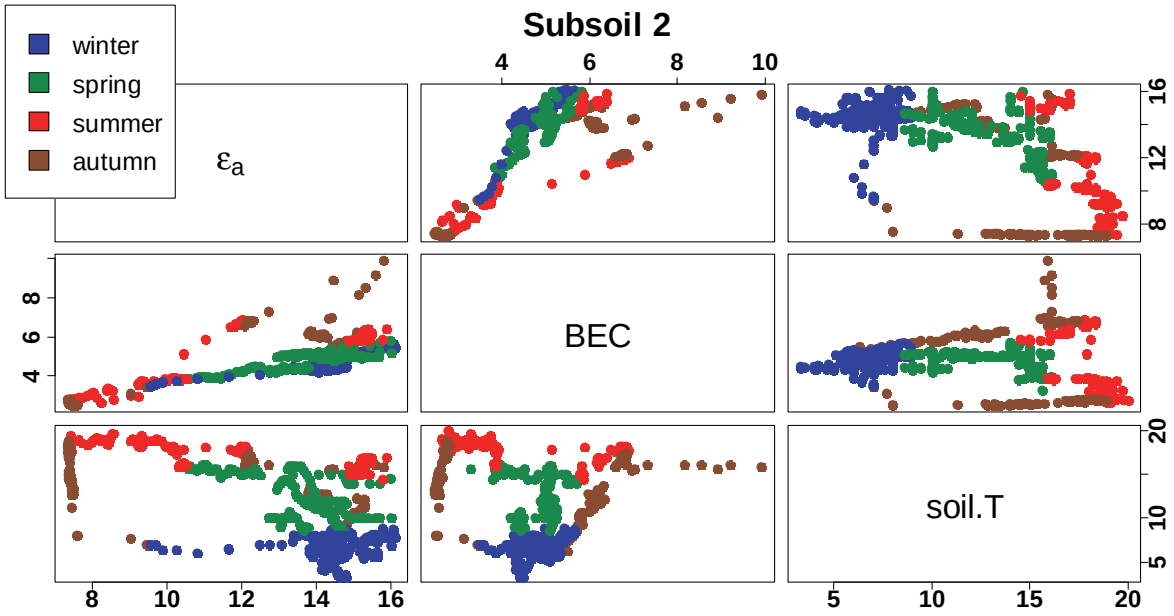



Figure 4.43 – Scatterplot matrix of the deep subsoil (subsoil 2) apparent permittivity, BEC (mS/m) and soil temperature, soil.T (° C), for the entire period of field monitoring.

Table 4.5 shows the data used for the principal component analysis. Columns with probe ID and depth were not used in the PCA but were added to Table 4.5 for the sake of clarity. In order to show the general relationship between parameters, the mean of the apparent permittivity, BEC and soil temperature calculated over the entire period of field monitoring were used, together with the results from the laboratory analyses on soil samples. Due to only three bulk soil horizons being tested in the laboratory (see section 4.2), and probes 3 and 4 were buried at a transition depth between topsoil and subsoil 1 (see section 4.2), these two probes were assumed to have average particle size distribution, OM and pH obtained from the values in the topsoil and subsoil 1. A temperature value was associated to each TDR probe depending on their depth. The R function *prcomp* was used to perform the PCA.

Table 4.5 – Matrix of the data used to perform the principal component analysis (probe ID and depth excluded).

| probe ID | depth (m) | $\varepsilon_a$ | BEC (mS/m) | soil.T (°C) | gravel (%) | sand (%) | clay (%) | OM (%) | pH |
|---|---|---|---|---|---|---|---|---|---|
| 1 | 0.07 | 15.80 | 3.56 | 12.91 | 1 | 87 | 6 | 4.7 | 5.9 |
| 2 | 0.07 | 15.35 | 4.45 | 12.91 | 1 | 87 | 6 | 4.7 | 5.9 |
| 3 | 0.18 | 12.16 | 3.09 | 12.91 | 24 | 68 | 4 | 2.8 | 6.1 |
| 4 | 0.25 | 10.14 | 3.14 | 12.91 | 24 | 68 | 4 | 2.8 | 6.1 |
| 5 | 0.35 | 6.57 | 1.42 | 13.05 | 48 | 48 | 2 | 0.9 | 6.4 |
| 6 | 0.42 | 7.17 | 1.99 | 13.05 | 48 | 48 | 2 | 0.9 | 6.4 |
| 7 | 0.60 | 10.88 | 3.49 | 13.05 | 48 | 48 | 2 | 0.9 | 6.4 |
| 8 | 0.59 | 8.16 | 2.51 | 13.05 | 48 | 48 | 2 | 0.9 | 6.4 |
| 9 | 0.70 | 10.43 | 3.43 | 13.12 | 48 | 48 | 2 | 0.9 | 6.4 |
| 10 | 0.72 | 10.71 | 3.74 | 13.12 | 48 | 48 | 2 | 0.9 | 6.4 |
| 11 | 0.77 | 12.31 | 7.57 | 13.12 | 34 | 57 | 5 | 1.3 | 6.3 |
| 12 | 0.83 | 11.50 | 4.00 | 13.12 | 34 | 57 | 5 | 1.3 | 6.3 |
| 13 | 0.87 | 16.21 | 5.22 | 13.12 | 34 | 57 | 5 | 1.3 | 6.3 |
| 14 | 0.93 | 14.71 | 4.89 | 13.12 | 34 | 57 | 5 | 1.3 | 6.3 |
| 15 | 1.08 | 10.13 | 3.94 | 13.12 | 34 | 57 | 5 | 1.3 | 6.3 |
| 16 | 1.06 | 10.24 | 3.26 | 13.12 | 34 | 57 | 5 | 1.3 | 6.3 |

Figure 4.44 shows the result of the PCA conducted on all the measured soil properties (i.e., apparent permittivity, labelled ε in the figure, bulk electrical conductivity, BEC (mS/m), soil temperature, soil.T (°C), pH, organic matter, OM (%), amount of clay, sand and gravel (%)). Figure 4.44a is the typical output of a PCA (often called a 'biplot') and it shows the original soil parameters and the objects (i.e., probe IDs) plotted in a new coordinate system described by two new variables named principal components (i.e., PC1 and PC2 in Figure 4.44) [12].

In this case, PCA is useful to show correlations between variables and to visualise the TDR probes in a single plot. Parameters placed closely in the biplot (i.e., small angles between the corresponding arrows) are positively correlated; parameters placed at opposite

[12] The PCA consists of a mathematical procedure that produces a rotation of the original data that as a result are seen in a new coordinate system identified by new variables named principal components. Each principal component describes a portion of the total variance in the data.

positions (i.e., approximately 180 ° angles between the corresponding arrows) are negatively correlated and orthogonal parameters (i.e., approximately 90 ° between the corresponding arrows) are not correlated. In order to make the plot clearer, an exaggeration factor was applied and therefore the length of the arrows does not correspond to the actual loadings (i.e., the contribution of the original variables to the principal components).

As expected, the organic matter is negatively correlated with pH and the percentage of gravel (opposite positions in the new coordinate system in Figure 4.44a). Also, the clay percentage is negatively correlated with the percentage of gravel. However, it is interesting to note that clay and sand percentages do not show a negative correlation. This is because of the large amount of gravel. In very gravelly soils, such as the one investigated, a low clay content does not necessarily correspond to a higher sand content. The soil EM properties, in particular the apparent permittivity, showed positive relationship with the percentage of clay (close positions in the new coordinate system), in accordance with the theory described in Chapter 2 and as reported by other authors for volumetric water content (e.g., Kachanoski et al., 1988; Johnson et al., 2001). This analysis was conducted on the mean values obtained during the entire period of field monitoring. However, it demonstrates that generally there was no clear relationship between the soil EM properties and temperature (variables placed approximately orthogonally in the new coordinate system). However, BEC seemed to be slightly more influenced by temperature than apparent permittivity.

Figure 4.44a also gives an immediate visualisation of the probes in relation to the soil parameters. In the new coordinate system, the probes that appear closest to the soil parameters were more influenced by them. It is clear that the shallower probes (i.e., probes 1 to 4) were most affected by the organic matter and by the percentage of sand (the topsoil was rich in sand particles and lacked almost completely gravel particles, see section 4.2). The intermediate probes (i.e., probes 5 to 10) were most affected by the dominant gravelly

fraction, and the deeper probes (i.e., probes 11 to 16) by BEC. The position of the probes is also useful to identify possible clusters and outliers in the data. In this case, probes 1 and 2 corresponding to the topsoil are clearly placed further from the other probes, indicating differing soil properties. Probes 11 to 16 indicate the presence of a more conductive soil horizon.

Figure 4.44b shows the variance explained by each principal component. The principal components are ranked according to their explanation of the variance in the data (i.e., the first principal component explains a higher variance compared to the second principal component, which in turn explains a higher variance than the third principal component, etc.). In this case, the first two components describe approximately 90 % of the variability in the data therefore the other components were safely neglected. Hence, the new coordinate system defined by the first two principal components (Figure 4.44a) is sufficient to describe the data and their relationships.

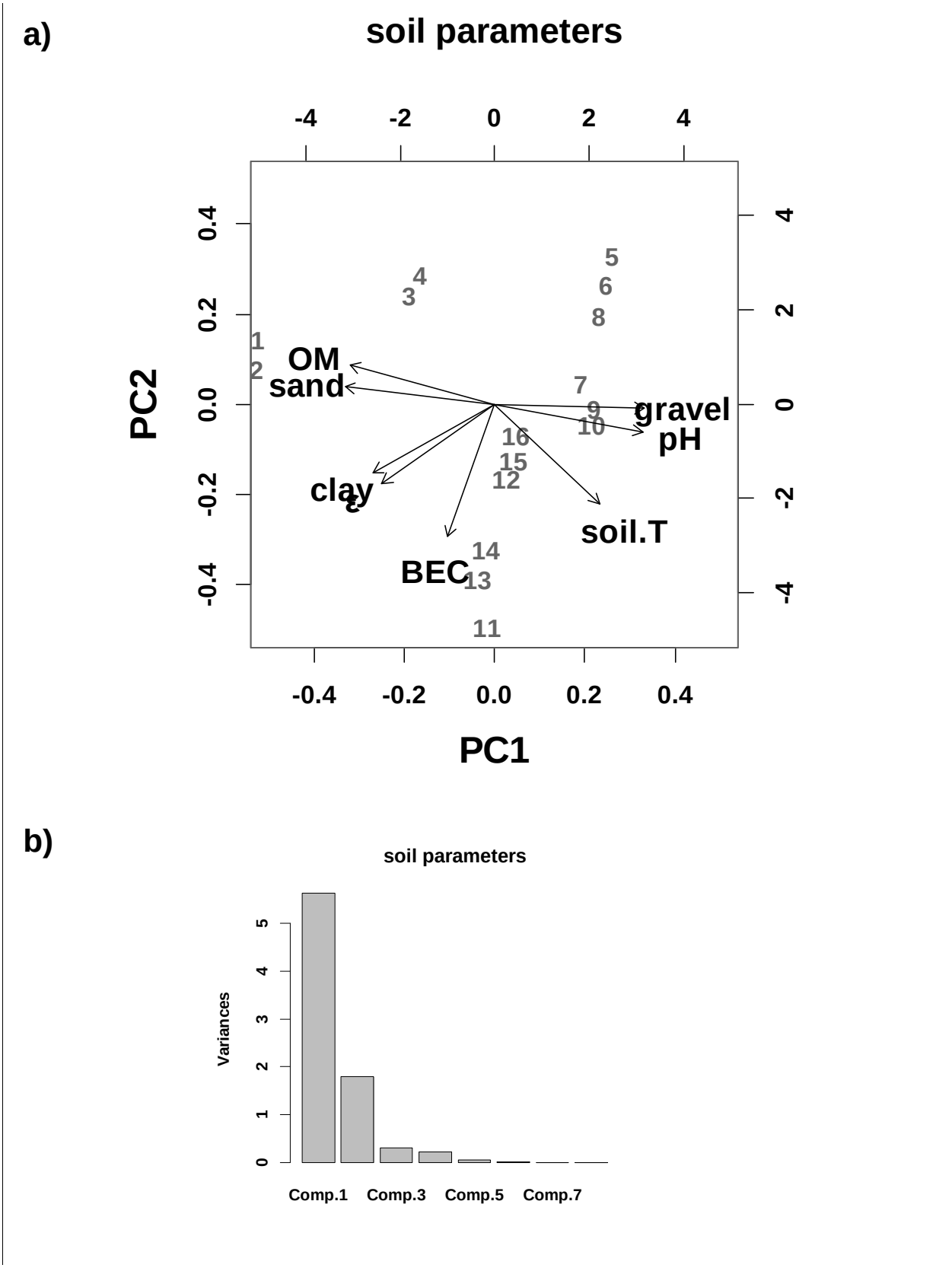



Figure 4.44 – (a) Biplot and (b) scree plot of the principal component analysis conducted on the measured soil properties.

### 4.4.4. Empirical calibration (apparent permittivity *versus* volumetric water content)

This section describes the results of an empirical calibration (apparent permittivity *versus* volumetric water content) identified in the laboratory for the University of Birmingham soil. Figure 4.45 shows the scatterplot matrix of the measured variables. As explained in section 4.4.3, each scatterplot is defined by the intersection of the variables on the diagonal of the matrix, which form the x- and y-axes. The scatterplots on the upper-right of the matrix diagonal show the same relationships of the scatterplots on the bottom-left of the matrix diagonal, but with inverted axes. The soil was tested at four discrete temperatures and at nine water contents (see section 3.3.6). Interestingly, despite previous authors reporting a linear relationship between the squared root of the apparent permittivity and the volumetric water content (Weiler et al., 1998; Gray and Spies, 1995), this did not seem to be the case for the soil studied (see the middle scatterplot at the far right in Figure 4.45, showing the relationship between the squared root of the apparent permittivity and the volumetric water content). For this reason a third order polynomial was preferred, as demonstrated later in this section. It was also found that the temperature did not have a significant impact on the apparent permittivity, except for the values close to saturation where a negative correlation is visible (i.e., soil apparent permittivity increases with decreasing temperature. See top scatterplot, second from the right in Figure 4.45). With the exception of the high apparent permittivity values (i.e., greater than approximately 15), the apparent permittivity remained constant at all the tested temperatures. This behaviour confirms the findings of the field monitoring that the temperature only has a minor impact on the apparent permittivity and that the dependency of the free water permittivity to temperature is the dominant mechanism in the soil studied. However, the laboratory data show that the apparent permittivity is more influenced by temperature at the higher water

contents, in contrast with the field data, which suggested a stronger relationship at the lower water contents (see Figure 4.39). A possible explanation for this behaviour is that deionised water was used in the laboratory and therefore the soil BEC (not measured) remained very low even at the high water contents. Apparent permittivity and BEC were consistently positively correlated (see section 4.4.3) and BEC showed a slight positive relationship with temperature during wet conditions in the field (see Figure 4.40). However, assuming a negligible BEC in the laboratory tests, this positive relationship, that would have affected the dependence of the apparent permittivity to temperature, was not prevailing. As a result, a negative correlation between apparent permittivity and temperature was still dominant in the laboratory tests at the high water content range.

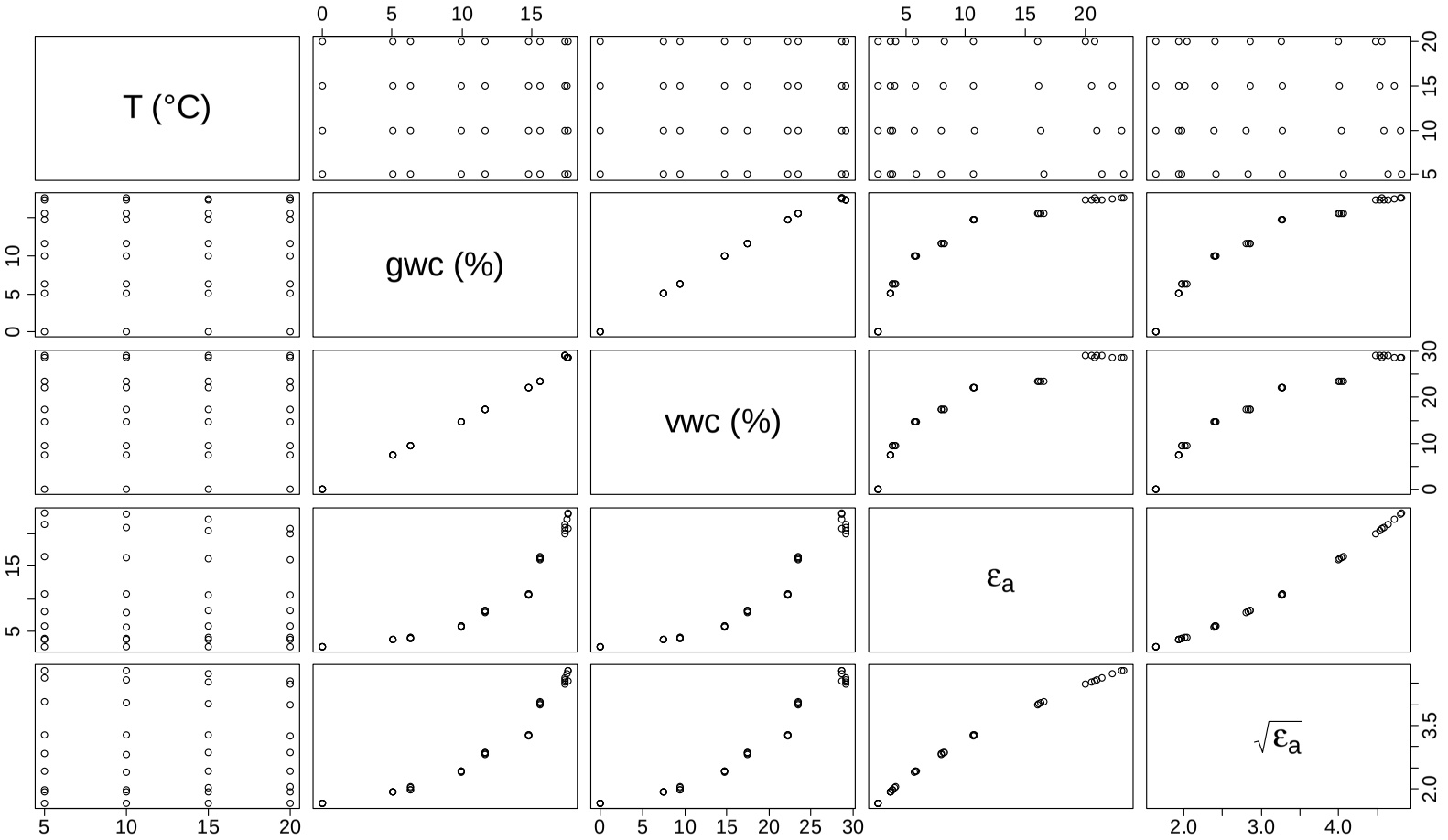



Figure 4.45 – Scatterplot matrix of the soil parameters measured during the empirical calibration: temperature, T, gravimetric water content, gwc, volumetric water content, vwc, apparent permittivity, $\varepsilon_a$.

Figure 4.46 shows the final empirical model based on all the data at the different water contents and temperatures shown in Figure 4.45 (further details on the model are provided in appendix D). Overall the adjusted $R^2$ is satisfactory (97.34 %) and the empirical model is more accurate than the commonly used Topp model (Equation (2.14)). As can be seen in Figure 4.46, there is a considerable variability in the measurements at the higher water contents. This was caused by temperature variations. The site specific empirical model is summarised by Equation (4.1):

$$VWC\ (\%) = \ -13.6937 + 6.9125 \times \varepsilon_a \ - \ 0.4311 \times \varepsilon_a^2 + 0.0094 \ \times \varepsilon_a^3 \qquad (4.1)$$

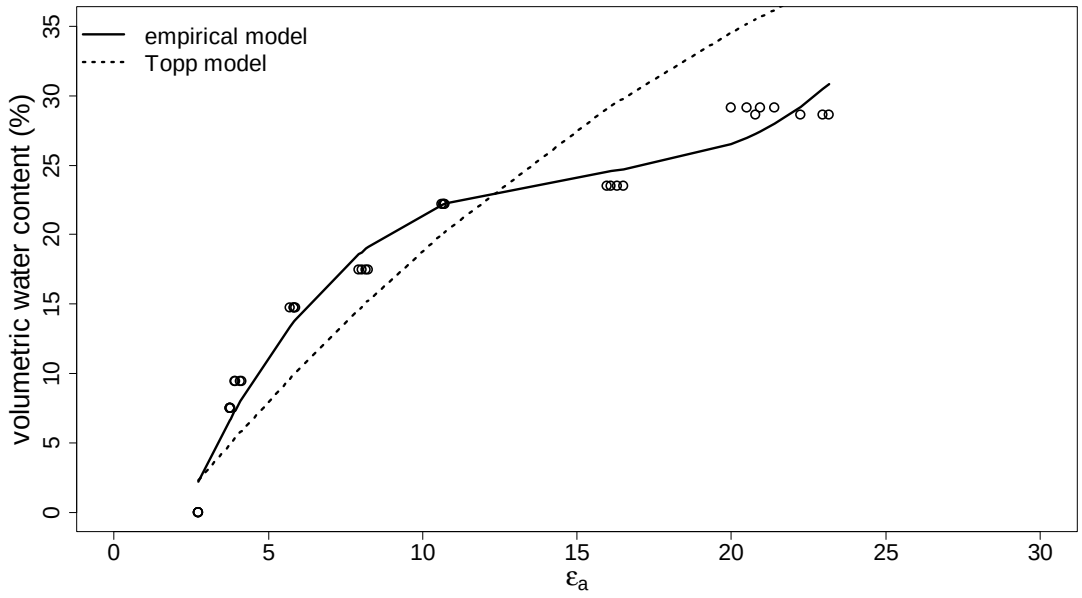



Figure 4.46 – Site specific polynomial model ($R^2$ = 97.34 %) relating the soil volumetric water content to the apparent permittivity measured by TDR.

Attempts were made to include the temperature as an additional variable in the model. However, the results of the Student statistical test showed that the coefficient of the temperature variable was not significantly different from zero.

Additional models were created at each fixed temperature. The results are shown in Figure 4.47 (the models summaries with the coefficients are reported in appendix D). For the soil studied, researchers have the option to use the most appropriate polynomial according to the soil temperature, if available. However, since temperature has only a minor effect on the apparent permittivity, Equation (4.1) can safely be considered a general model for the studied soil.

It has to be acknowledged that the models just described were based on measurements of disturbed soil samples and therefore might not fully represent the soil behaviour in the field. However, care was taken to create the most representative conditions by choosing the dry density (see Table 4.1), range of water contents and temperatures encountered in the field.

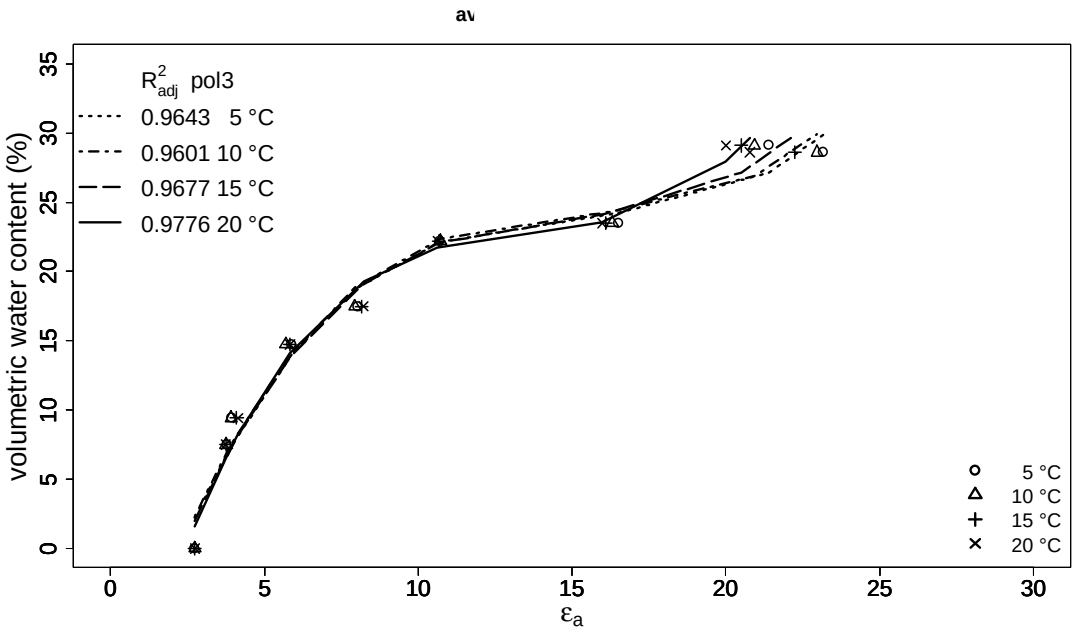



Figure 4.47 – Site specific polynomial models at the specific temperatures generally measured in the field.

### 4.4.5. Factors affecting the soil electromagnetic properties: summary

The previous sections described the results of statistical analyses conducted on the measured soil data. Time-domain cross correlations, simple correlations and principal component analysis were performed. In addition, an empirical calibration linking the apparent permittivity to the volumetric water content was shown. The results of these analyses can be summarised by the following points:

- The soil EM properties have been shown to be statistically correlated with rainfall events, with time lags of the order of several hours depending on the depth. The soil temperature was also correlated to air temperature with a time lag of a few hours, while the soil EM properties did not show lagged correlations with air temperature.
- Apparent permittivity and BEC were consistently positively correlated throughout the period of field monitoring.
- Complex relationships between soil EM properties and temperature were found. A general negative correlation was dominant, both in the field and in the laboratory. However, this was clear only during dry field conditions and was not consistent for all the seasons. Results from the PCA and from the empirical calibration confirmed the small dependency of the EM properties to temperature for the soil studied. However, it is worth noting that the laboratory and field data showed contrasting results. In the laboratory, apparent permittivity was more affected by the temperature at the higher water contents while in the field the negative relationship was a lot clearer during dry conditions. This behaviour could be attributed to the use of deionised water in the laboratory tests. However, a general negative correlation was observed for both cases, demonstrating that the amount of bound water of the soil studied was small.

- No reoccurring seasonal patterns of the relationships between soil EM properties were identified because of the large seasonal variability encountered during the monitoring period.
- Both apparent permittivity and BEC were positively correlated to the percentage of clay, confirming the important role clay has in determining the EM behaviour of the soil.
- The relationship between apparent permittivity and volumetric water content for the soil studied could be described by a third order polynomial.

# 4.5. SOIL SIMULATION WITH SPAW

## 4.5.1. Introduction

As explained in section 2.4.1.2 the SPAW (Soil-Plant-Air-Water) model allows the soil water content to be simulated from soil and weather input parameters (Saxton and Willey, 2006; Saxton and Rawls, 2006; Saxton et al., 2006; see also Table 2.1 and 2.2, and Figure 2.8). This section describes the application of the SPAW model to the University of Birmingham test site. For information on the input parameters refer to section 3.4. The results of the SPAW simulations are shown and compared to the data collected by TDR. In addition, the results of a sensitivity analysis conducted by varying the input soil water content are described. A summary is included at the end of the section.

## 4.5.2. SPAW results

This section describes the results obtained by the SPAW model for selected months, during the year 2011. It was found that the accuracy of the model generally decreased with

time and therefore the analysis was conducted by month and not by season (for simulations conducted by season see appendix E).

Figures 4.48 to 4.51 show the comparison of the daily volumetric water content simulated by SPAW and calculated by Equation (4.1) from the measured apparent permittivity, for selected months[13]. Rainfall is also shown. Overall the simulations matched relatively well the calculated data. Generally, the errors increased towards the end of the month, confirming that the SPAW model should be used with caution to model long periods of time based exclusively on initial inputs. Also, the errors were normally higher for the topsoil, where the SPAW model generally over predicted the soil water content, in particular during dry conditions. Higher errors corresponding to shallower depths were reported by other authors (e.g., Lenka et al., 2008). However, in this study, the higher errors were likely due to the fact that Equation (4.1) was developed on samples of subsoil and therefore the conversion between apparent permittivity and water content was expected to be less accurate for the topsoil. Interestingly, the SPAW model seemed to under predict the soil water content for the subsoil horizons. This suggests a potentially higher capacity of the subsoil to retain water, despite its sandy and gravelly nature.

[13] Examples of the comparison between simulated data and calculated using the Topp model (Equation (2.14)) are shown in appendix E. A comparison between Equation (2.14) and the Topp model is described later in this section.

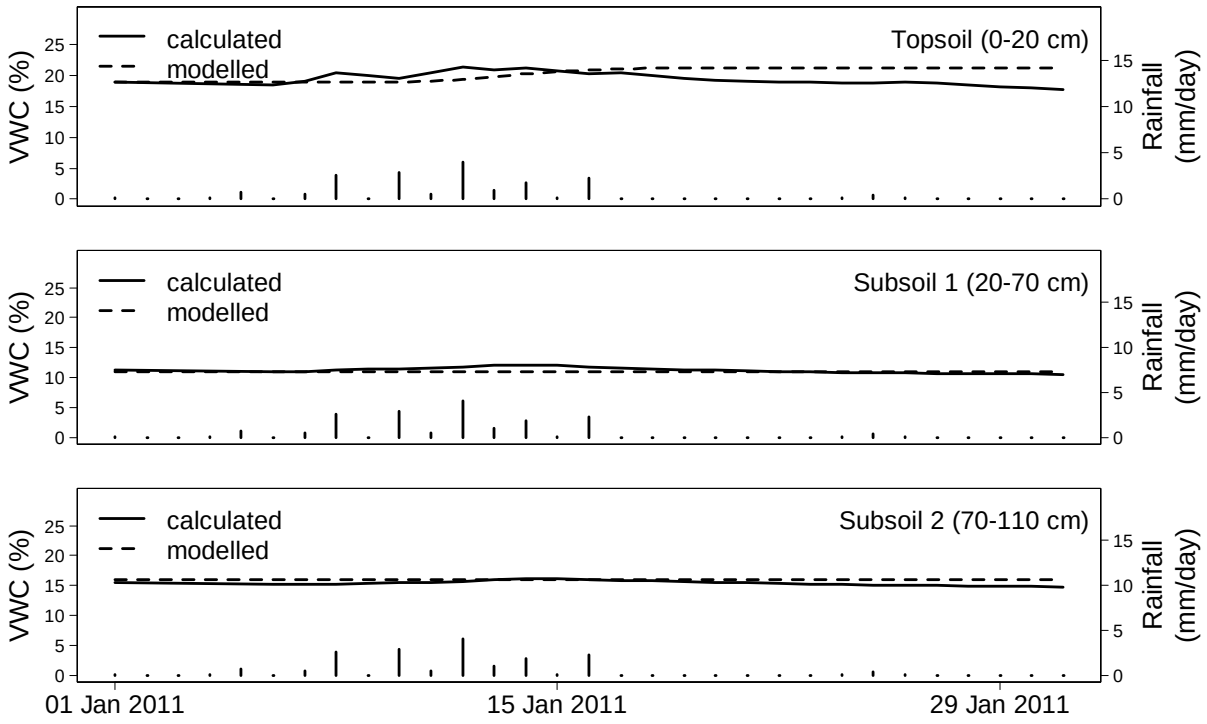



Figure 4.48 – Simulated (by SPAW) and calculated (by Equation (4.1)) daily volumetric water content for January 2011.

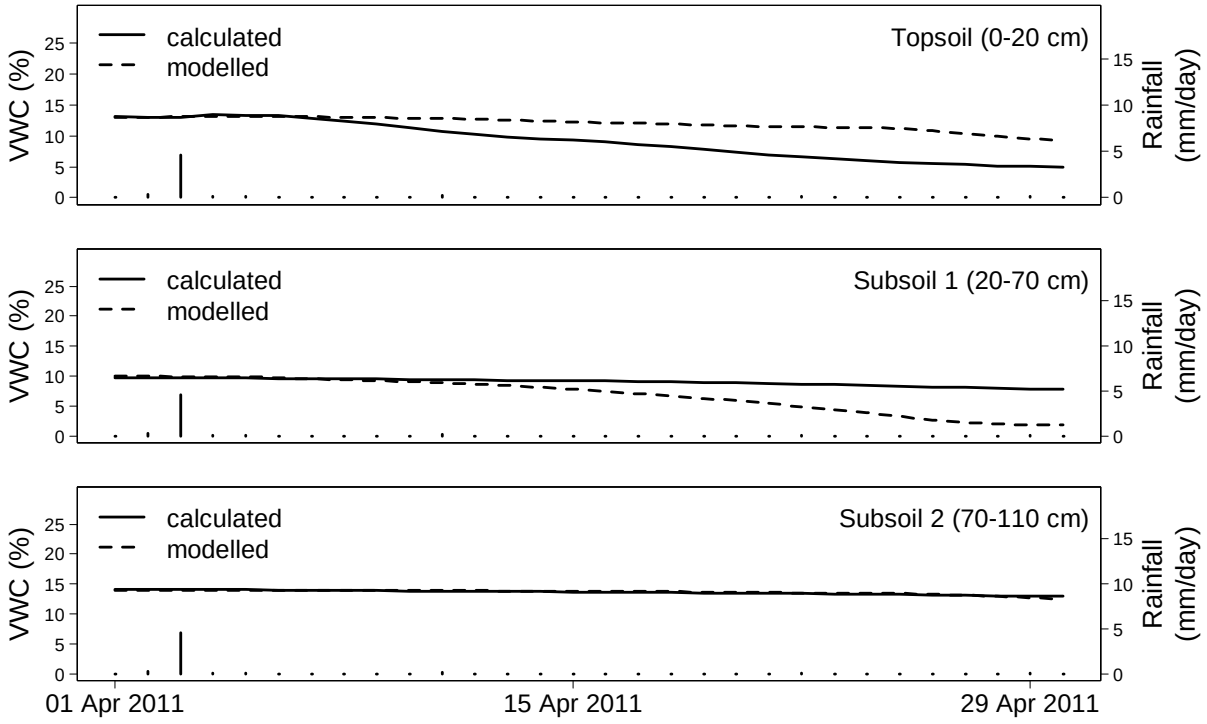



Figure 4.49 – Simulated (by SPAW) and calculated (by Equation (4.1)) daily volumetric water content for April 2011.

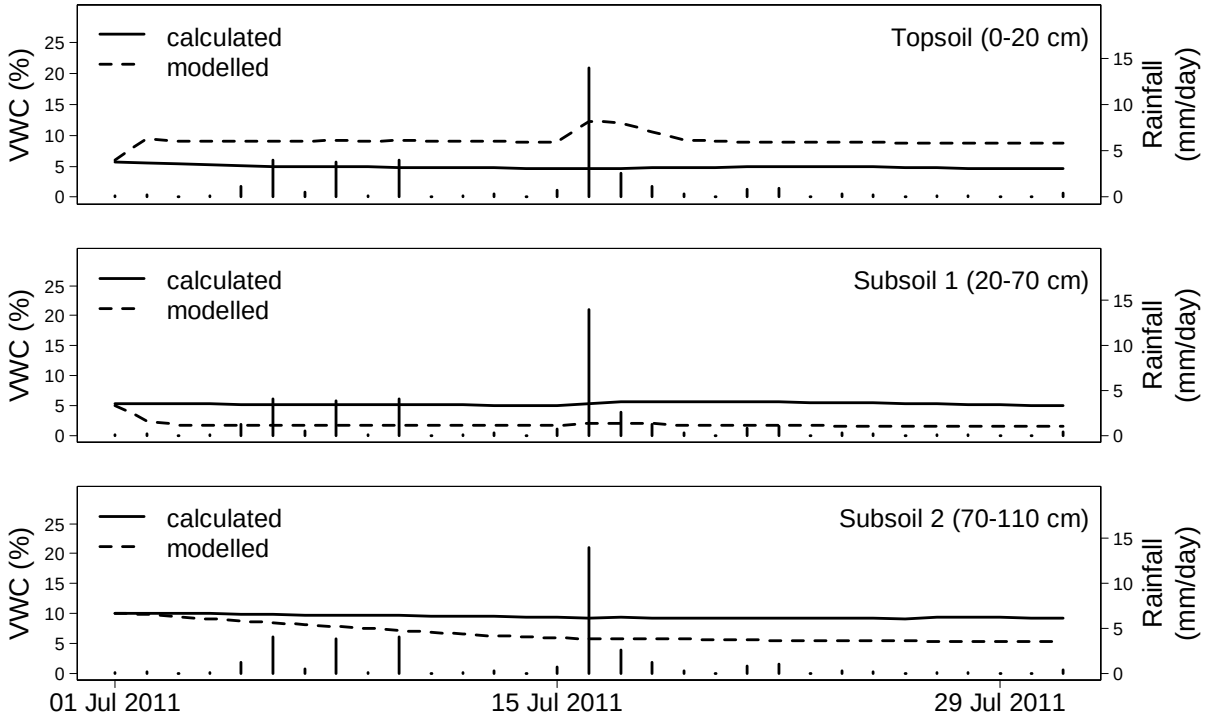



Figure 4.50 – Simulated (by SPAW) and calculated (by Equation (4.1)) daily volumetric water content for July 2011.

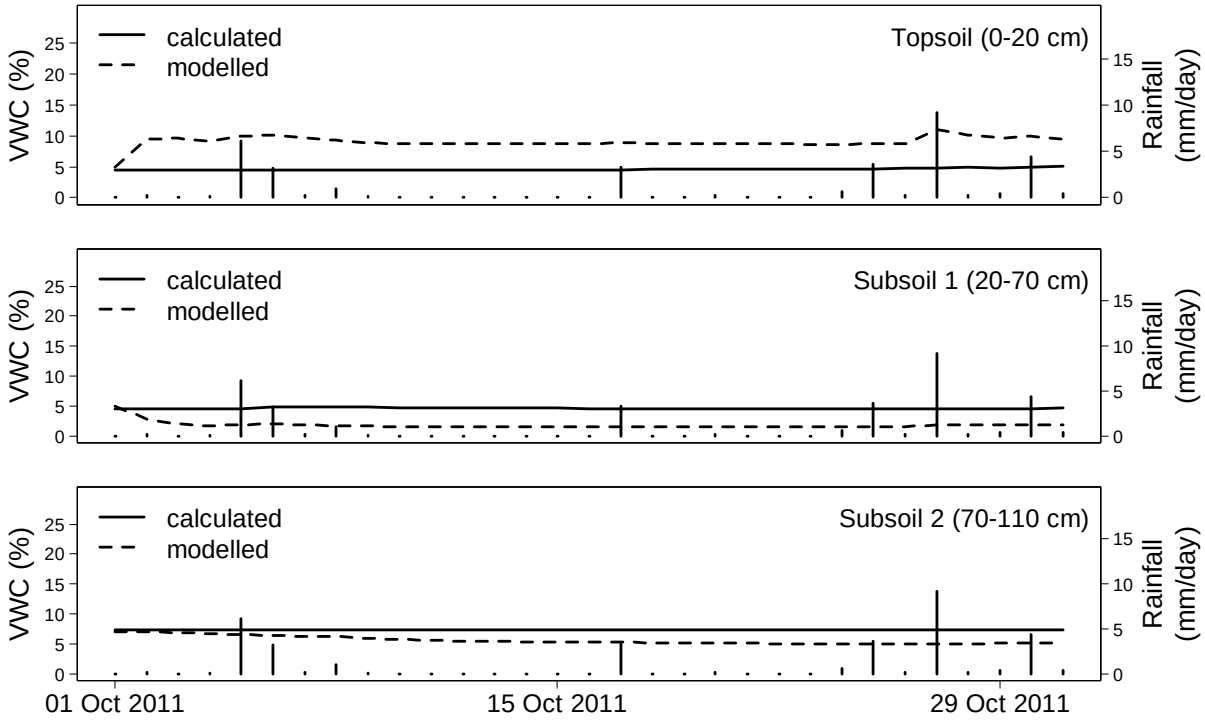



Figure 4.51 – Simulated (by SPAW) and calculated (by Equation (4.1)) daily volumetric water content for October 2011.

Figures 4.52 to 4.54 show the mean absolute difference and its standard deviation between simulated and calculated soil water contents for each soil horizon and for every month starting from October 2010 until June 2012. Bearing in mind that this is the mean error and that at certain times the errors could be smaller or higher, generally it can be seen that there were good matches during the entire period of field monitoring, with differences not greater than 0.1 $m^3/m^3$ of volumetric water content. Interestingly, the agreement was substantially better during the Winter months compared to the Summer months. This is probably due to the difficulty of modelling the complex interactions between soil and living organisms during the growing season. Also, as explained in section 4.3.2.2, the TDR data did not measure sensible increases in water content corresponding to rainfall events during the Summer months and hence this can also be the cause of the higher errors between the simulated and calculated data.

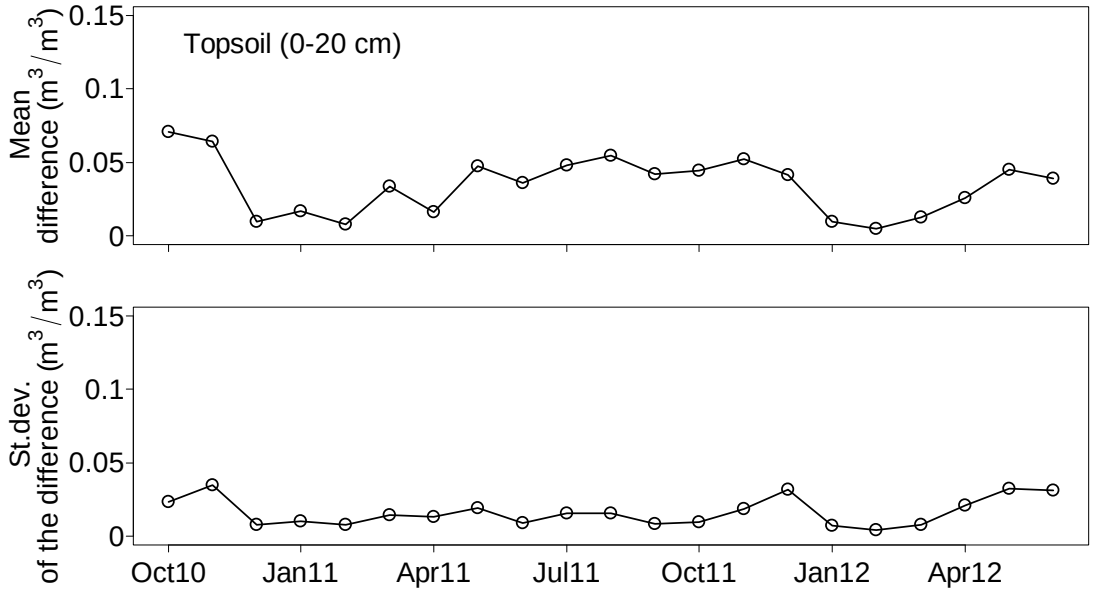



Figure 4.52 – Mean absolute difference (i.e., error) and its standard deviation between simulated and calculated soil water contents for the topsoil.

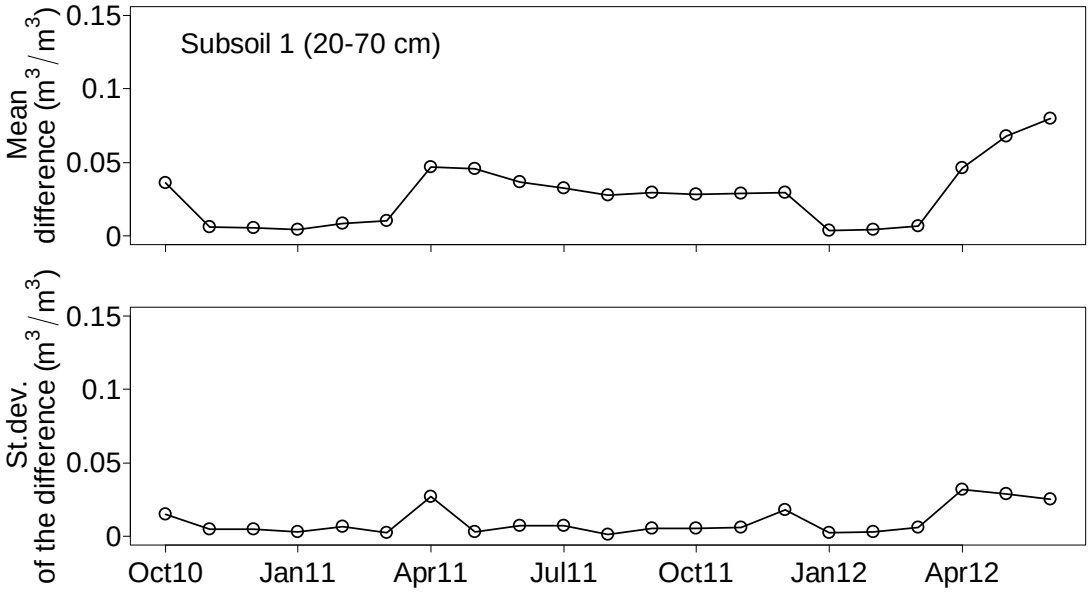



Figure 4.53 – Mean absolute difference (i.e., error) and its standard deviation between simulated and calculated soil water contents for the subsoil 1.

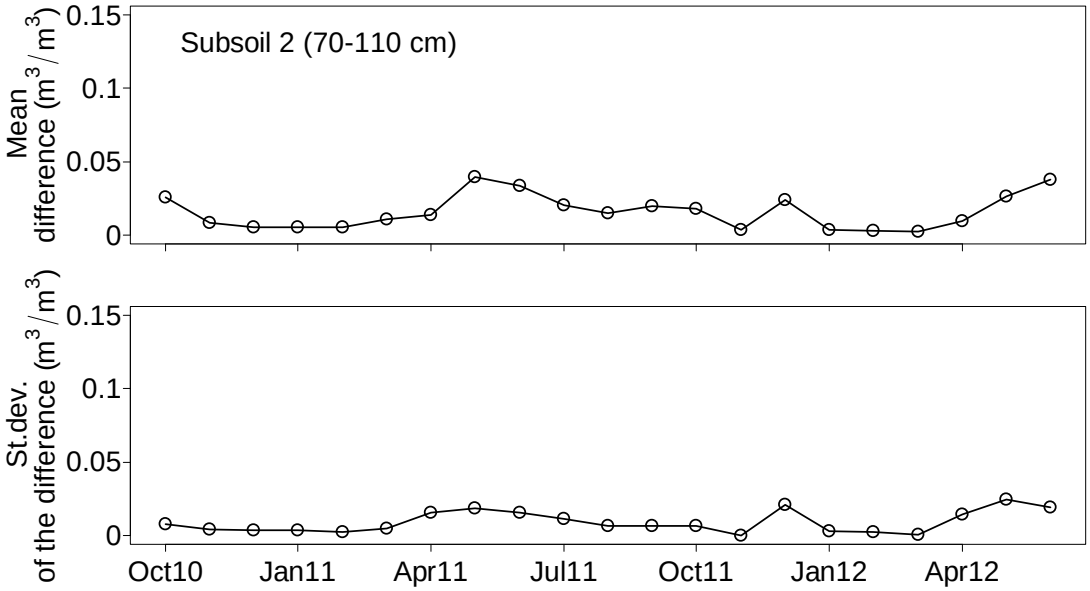



Figure 4.54 – Mean absolute difference (i.e., error) and standard deviation of the error between simulated and calculated soil water contents for the subsoil 2.

Table 4.6 shows the mean difference and its standard deviation between simulated and calculated soil water contents for all the simulated months, for both Equation (2.14) (Topp model) and Equation (4.1) (UoB empirical model). Both models produced decent

matches between the simulated and calculated data, with mean errors smaller than approximately 5 % of volumetric water content. However, noticeable better agreements were achieved by Equation (4.1) for the subsoil compared to the Topp model. This is a confirmation of the validity of Equation (4.1) for converting apparent permittivity to volumetric water content for the studied soil.

Table 4.6 – Mean difference and its standard deviation between simulated and calculated soil water content for the Topp model and the site specific UoB empirical model.

| **Topp model** | **topsoil** | **subsoil1** | **subsoil2** |
|---|---|---|---|
| **vwc error (%)** | 2.87 | 3.93 | 5.09 |
| **vwc st.dev. of the error (%)** | 1.72 | 1.64 | 1.88 |
| **UoB empirical model** | | | |
| **vwc error (%)** | 3.46 | 2.54 | 1.52 |
| **vwc st.dev. of the error (%)** | 1.68 | 0.96 | 0.85 |

## 4.5.3. SPAW sensitivity analysis

In order to study the sensitivity of the SPAW model to variations of the input parameters a sensitivity analysis was carried out by varying the initial soil volumetric water content by ±3 %. For example, if the initial volumetric water content was 10 %, the same simulation was run with inputs at 7 % and 13 %. The 3 % level was chosen because it is approximately twice the residual standard error of Equation (4.1) (see appendix D) and represents the confidence interval of the empirical model. Also, similar accuracy levels are reported in the literature for TDR and other techniques (e.g., Jones et al., 2002). However, for May, August, September, October and November 2011 (i.e., during very dry conditions) it was necessary to reduce the negative range from -3 % to -2 % or -1 %, in order to avoid internal software errors.

Figures 4.55 to 4.57 show the mean absolute difference of the SPAW output, when the input volumetric water content was varied by ±3 %. In general, the output did not vary substantially, remaining within 5 % of the water contents obtained with the original input. It is interesting to see that the SPAW results seemed to be significantly less sensitive to input variations when the initial volumetric water content was low (i.e., during dry conditions).

Due to the large number of inputs necessary to run the SPAW model, it was decided to conduct a sensitivity analysis only by varying the initial volumetric water content. A complete sensitivity analysis including variations of the other input parameters (i.e., weather parameters, soil geotechnical properties, crop type) was beyond the purposes of this study.

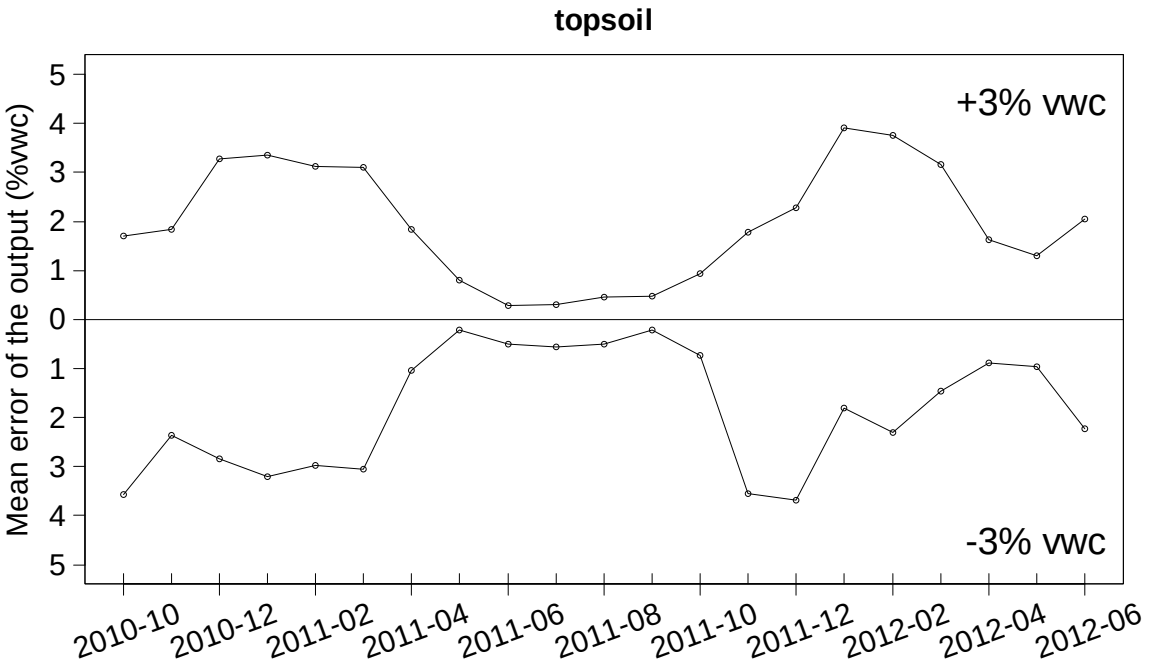



Figure 4.55 – Mean absolute difference of the SPAW output for the topsoil, when the input volumetric water content was changed by ±3 %.

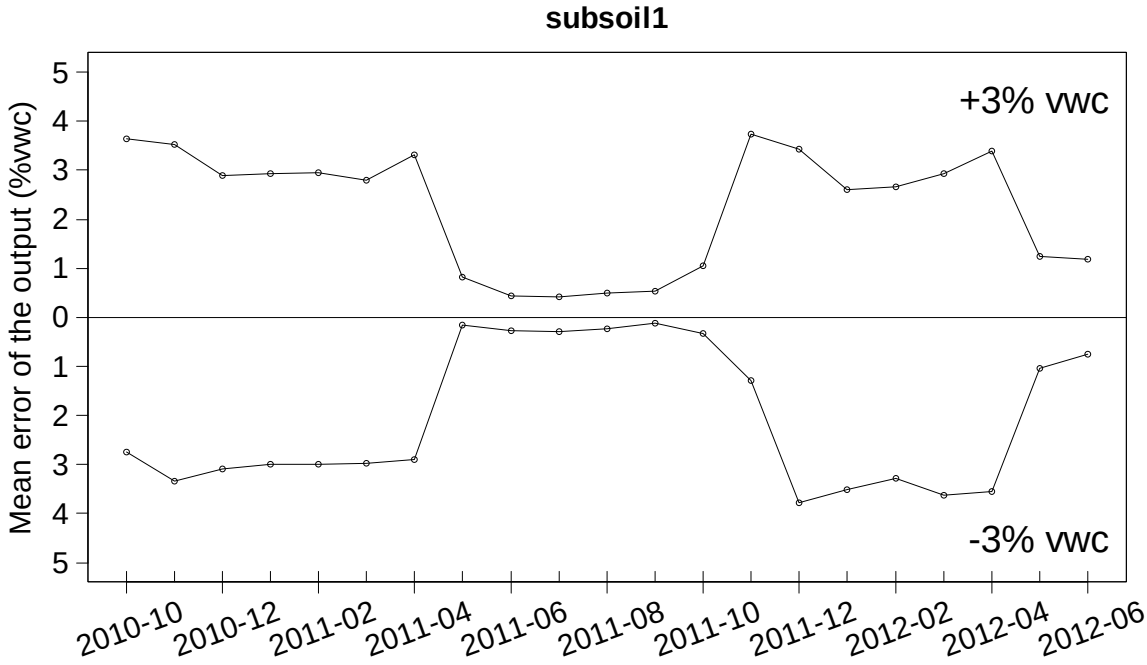



Figure 4.56 – Mean absolute difference of the SPAW output for the subsoil 1, when the input volumetric water content was changed by ±3 %.




Figure 4.57 – Mean absolute difference of the SPAW output for the subsoil 2, when the input volumetric water content was changed by ±3 %.

## 4.5.4. Soil simulation with SPAW: summary

The previous sections described the simulation of the volumetric water content with time by the SPAW model. Simulations were conducted by month and by soil horizon. Inputs included soil geotechnical parameters, weather parameters and crop type. A sensitivity analysis was conducted by varying the input volumetric water content of ±3 %. The main findings were:

- The simulated volumetric water content by SPAW matched reasonably well the calculated data by Equation (4.1) from the measured apparent permittivity. The mean difference between simulated and calculated values was smaller than 10 % and generally smaller than 5 %. Better agreement was achieved during the Winter months.
- The generally good agreement between the simulated and calculated data is a confirmation that the SPAW model is a reliable tool for simulating the soil water content, even in semi-natural anthropogenic soils. This result also validates the measurements obtained in the field by TDR.
- Equation (4.1) provided better agreement than the Topp model for the subsoil horizons. This is a confirmation of the validity of this equation for the studied soil and demonstrates the effectiveness of the SPAW model for selecting the most appropriate calibration model for the site.
- The SPAW model seemed to be relatively insensitive to ±3 % variations of the input volumetric water content, by providing results that differed less than 5 % compared to the original input. The sensitivity was very small during dry conditions, when the initial volumetric water content was low (< 10 %).

# 4.6. IMPACT OF WEATHER ON GPR

This section illustrates the results of the GPR surveys conducted at the University of Birmingham test site with the commercial GPR Detector Duo. In particular, B-scans corresponding to seasonal extreme conditions (e.g., wet, dry) and corresponding to rainfall events are shown. A comparison of the results obtained by GPR and TDR is also described. A summary is included at the end of the section.

## 4.6.1. GPR performance at extreme seasonal conditions

GPR surveys were conducted almost weekly from November 2010 until February 2012 (see section 3.3.7). During this period extreme wet and dry conditions occurred and the corresponding data were selected for analysis. Figures 4.58 and 4.59 show the B-scans obtained at these extremes for both the available frequencies (i.e., 250 MHz and 700 MHz). The images were taken on the 13$^{th}$ of January 2011 and on the 20$^{th}$ of August 2011, corresponding to wet and dry conditions, respectively. These extremes approximately corresponded to the coldest and warmest conditions recorded during the period of GPR monitoring. The raw data were processed by the commercial software GRED that came with the Detector Duo. A standard processing procedure was used involving vertical and horizontal bandpass filters, smoothed gain and moved start time. Fitting the hyperbola with its apex at approximately 5.2 m along the transect starting from the left was performed. This allowed the determination of a GPR apparent permittivity (i.e., average permittivity for the upper 0.5 m of soil) and the adjustment of the depths of the target. It is evident from Figures 4.58 and 4.59 that the quality of the images decreased substantially during wet conditions, for both frequencies. Six hyperbolae are relatively easily distinguishable during dry conditions. Starting from the left of the transect, hyperbolae are located at approximately 2 m, 4.2 m, 4.8 m, 5.2 m, 5.8 m and 6.5 m. The first pipe on the left, at 0.5 m

depth, corresponds to an existing pipe on the site. The images seem to suggest the presence of two pipes close-by. The other five metal and plastic pipes were deliberately installed (see section 3.3.7).

As it can be seen in Figures 4.58 and 4.59, the metal pipes at positions 4.2 m, 5.2 m and 6.5 m generated predominantly white hyperbolae in the grey scale system used by GRED. These were more clearly visible than the plastic ones (black hyperbolae at positions 4.8 m and 5.8 m), because of the greater contrast with the surrounding soil. The plastic pipes were even less recognisable during wet conditions. Conductive pipes such as metal pipes experience a phase shift of the reflected wave, while this does not occur with non conductive pipes with permittivity lower than the surrounding medium (e.g., air-filled plastic pipes; Daniels, 2004). This explains the different shades (black or white) observed for the two types of pipes shown in this study.

Interestingly, the pipes at the right of the transect, buried at approximately 1 m depth, were not clearly visible, especially at the high frequency and during wet conditions. This is likely due to the close proximity of the pipes, with the hyperbolae of the shallower pipes partially masking the reflections from the deeper ones. This phenomenon occurs frequently beneath roads, where pipes are often laid close to each other (Slob et al., 2009).

The signal became mostly noise between 2 and 3 m depth, depending on the frequency and the soil conditions. In addition to the EM loss caused by the material, which was low due to the low BEC, the abundance of cobbles of the dimension of few centimetres contributed to dissipate the signal through multiple reflections. Increased scattering due to the presence of cobbles, bricks and other object is a common problem in anthropogenic materials and can significantly reduce the rate of detection by GPR (Igel, 2008; Slob et al., 2009; Igel et al., 2011).

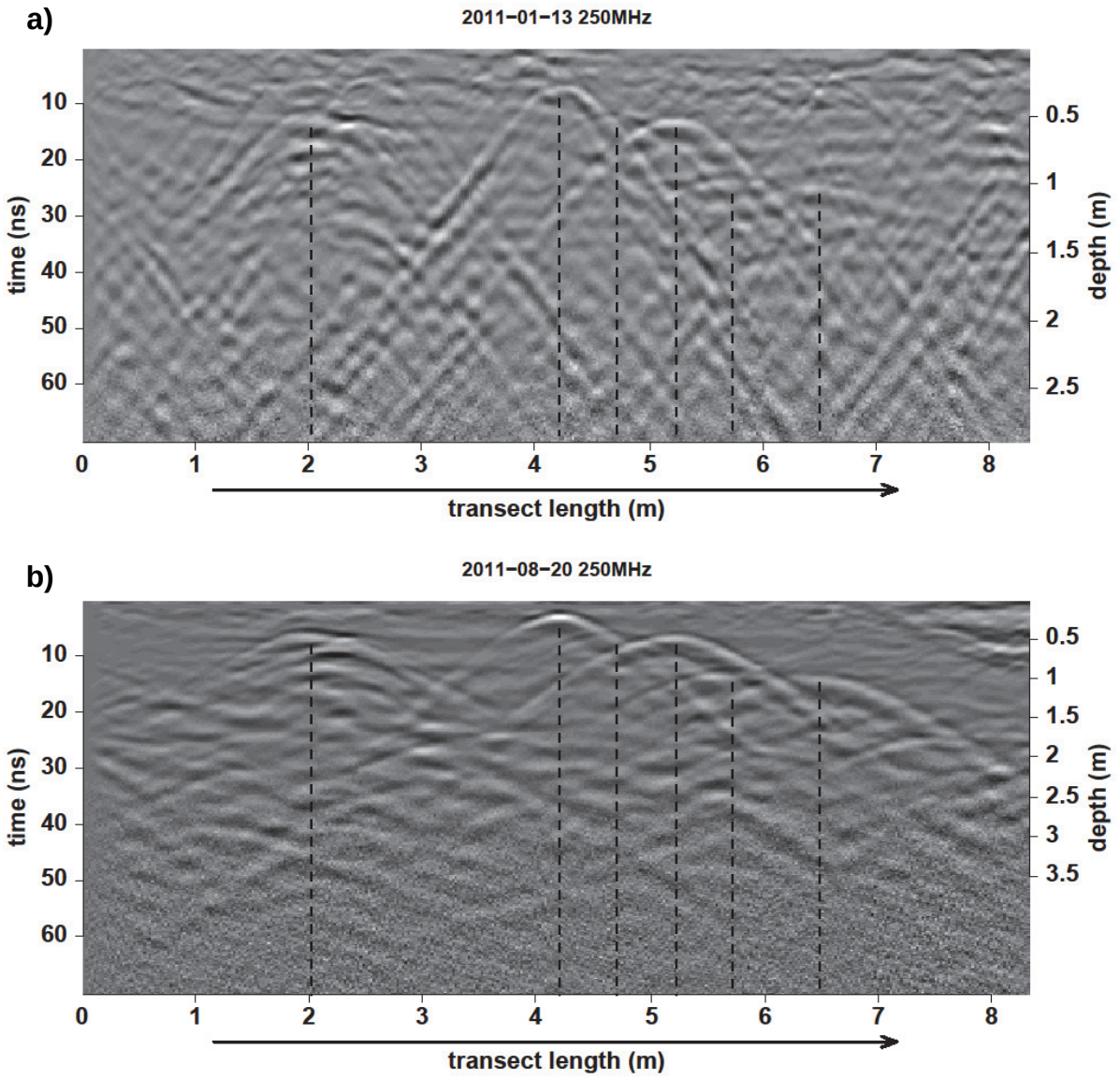



Figure 4.58 – B-scans obtained by the Detector Duo GPR at the University of Birmingham test site, corresponding to (a) wet and (b) dry extremes, with centre frequency of 250 MHz. [Note: the vertical lines approximately correspond to the apex of the hyperbolae.]

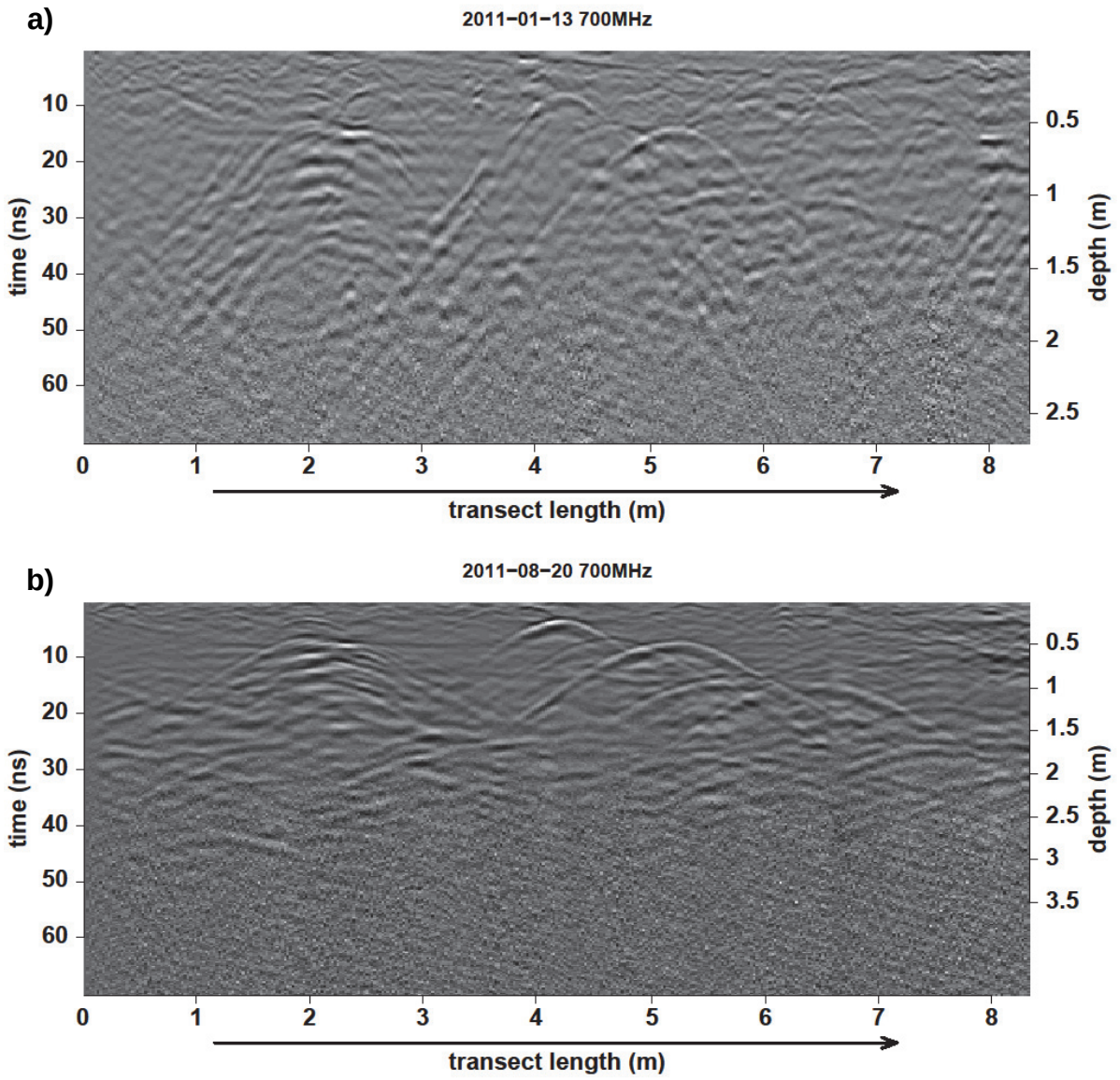



Figure 4.59 – B-scans obtained by the Detector Duo GPR at the University of Birmingham test site, corresponding to (a) wet and (b) dry extremes, with centre frequency of 700 MHz.

Table 4.7 shows the signal propagation velocity (m/ns) for the wet and dry extremes obtained after fitting the hyperbola at approximately 5.2 m along the transect (approximately 0.5 m depth), using the GRED software. Each value represents the mean of four fitted hyperbolae corresponding to individual GPR scans (each survey was repeated four times, see section 3.3.7). The apparent permittivity calculated by Equation (2.17) and the

corresponding standard deviations are also shown. The results for these two datasets indicate negligible velocity variation with frequency, confirming that the soil was not dispersive. The low standard deviations confirm that the method of analysis (i.e., fitting of hyperbolae) was reasonably precise despite involving subjective interpretation. A velocity variation was observed corresponding to wet and dry conditions, with a mean absolute difference of 0.055 m/ns.

Table 4.7 – Velocity and apparent permittivity with their standard deviations measured at wet and dry extremes by fitting the hyperbola of a metal target buried at approximately 0.5 m depth.

| | | | st.dev. | |
|---|---|---|---|---|
| | **wet (2011-01-13)** | **dry (2011-08-20)** | **wet (2011-01-13)** | **dry (2011-08-20)** |
| **velocity (m/ns) (250 MHz)** | 0.082 | 0.136 | 0.0005 | 0.0010 |
| **velocity (m/ns) (700 MHz)** | 0.082 | 0.137 | 0.0005 | 0.0006 |
| **apparent permittivity (250 MHz)** | 13.47 | 4.88 | 0.17 | 0.07 |
| **apparent permittivity (700 MHz)** | 13.47 | 4.83 | 0.17 | 0.04 |

The variation in velocity at extreme soil conditions has important implications for accurate target depth determination. Table 4.8 shows an example demonstrating the relevance of this issue. Assuming to have a pipe buried at 1 m depth, but for which a hyperbola cannot be fitted, an approximate permittivity (or propagation velocity) value is required in order to estimate the target depth. A typical permittivity value of 10 can be used. If the soil permittivity is actually 10, the estimated target depth would be correct and the vertical position of the target in the B-scan (i.e., pixel index in the vertical direction of the GPR image corresponding to 1 m depth) would be correct. In the GPR system used each pixel in the vertical direction corresponds to 0.25 ns (pixel time in Table 4.8). However, the

unit distance corresponding to each pixel in the vertical axis would change depending on the signal propagation velocity (pixel depth in Table 4.8). Therefore, other input permittivity values would cause the correct pixel index at 1 m depth to move up and down in the B-scan. But if the input permittivity is unknown and a typical value is used during wet or dry conditions, the estimated depth can be significantly offset. In this example, the variation against a typical input permittivity of 10 would be 0.142 m (14.2 %) and 0.426 m (42.6 %), for wet and dry conditions respectively. Comparable errors in depth estimation caused by lateral variations of water content were reported by Boll et al. (1996). This demonstrates the importance of both the spatial and temporal variations of the soil permittivity for accurate measurements of the target depths.

Table 4.8 – Variation of the estimated target depth (m) using different values of input permittivity: a typical value of 10, and the wet and dry extremes measured in the field by GPR at 250 MHz.

| input permittivity | velocity (m/ns) | pixel time (ns) | pixel depth (m) | pixel index at 1 m | estimated target depth (m) |
|---|---|---|---|---|---|
| 10.00 | 0.09487 | 0.25 | 0.01186 | 84 | 1.000 |
| 13.47 | 0.08174 | 0.25 | 0.01022 | 84 | 0.858 |
| 4.88 | 0.13580 | 0.25 | 0.01698 | 84 | 1.426 |

Table 4.9 shows the attenuation coefficient and the attenuation loss at 1 m depth[14] calculated by Equations (2.5) and (2.7). It is apparent that the attenuation loss remained low and independent of the soil conditions, although an increase was visible during wet conditions. This is explained by the low BEC of the soil.

[14] For this calculation, the apparent permittivity and BEC at 1 m depth were assumed to be the same as the values at 0.5 m depth. The apparent permittivity was calculated after fitting a hyperbola at 0.5 m depth because it was not possible to fit a hyperbola to the targets buried at 1 m depth.

Table 4.9 – Attenuation coefficient and attenuation loss at 1 m depth for the wet and dry extremes.

| | | GPR permittivity | TDR conductivity (mS/m) | attenuation loss at 1 m (dB) | attenuation coefficient (dB/m) |
|---|---|---|---|---|---|
| **2011-01-13** | **wet** | 13.47 | 3.60 | 3.21 | 1.60 |
| **2011-08-20** | **dry** | 4.88 | 0.66 | 0.98 | 0.49 |

The low attenuations in Table 4.9 do not explain the poorer quality of the GPR images obtained during wet conditions (Figures 4.58 and 4.59). A combination of the EM attenuation due to higher BEC and the increased multiple reflections caused by the larger amount of water in the soil are responsible for reducing the quality of the GPR results during wet conditions.

## 4.6.2. GPR performance before and after rainfall events

Three rainfall events spread over different seasons in 2011 were selected in order to study the impact of rain on the GPR results. GPR surveys were conducted before and after these rainfall events. Figures 4.60 and 4.61 show the B-scans obtained on the 4$^{th}$ of October 2011 and on the 6$^{th}$ of October 2011, corresponding to one of the selected rainfall events. A cumulative rainfall of 8.3 mm fell in 12 hours. It is apparent that wet soil produced additional multiple reflections that significantly reduced the quality of the images, particularly at the high frequency (Figure 4.61). The hyperbolae generated by the plastic pipes nearly disappeared after this rainfall event, confirming the increased difficulty of detection for this type of targets during wet conditions. Similar results were found for the rainfall event occurring in June 2011 (see appendix F). However, the situation was different in February 2011, when a similar rainfall event (10.2 mm in 10 hours) did not affect substantially the GPR images. As shown in Figures 4.62 and 4.63 the quality of the GPR images before and after a rainfall event were comparable. In this case, the multiple

reflections caused by infiltrating water were less visible since the soil conditions were already wet and homogeneous. Soil water heterogeneity is responsible for the deterioration of the GPR signals and was shown to significantly affect the GPR performance on low-conductive sandy soils by other authors (Igel, 2008; Igel et al., 2011).

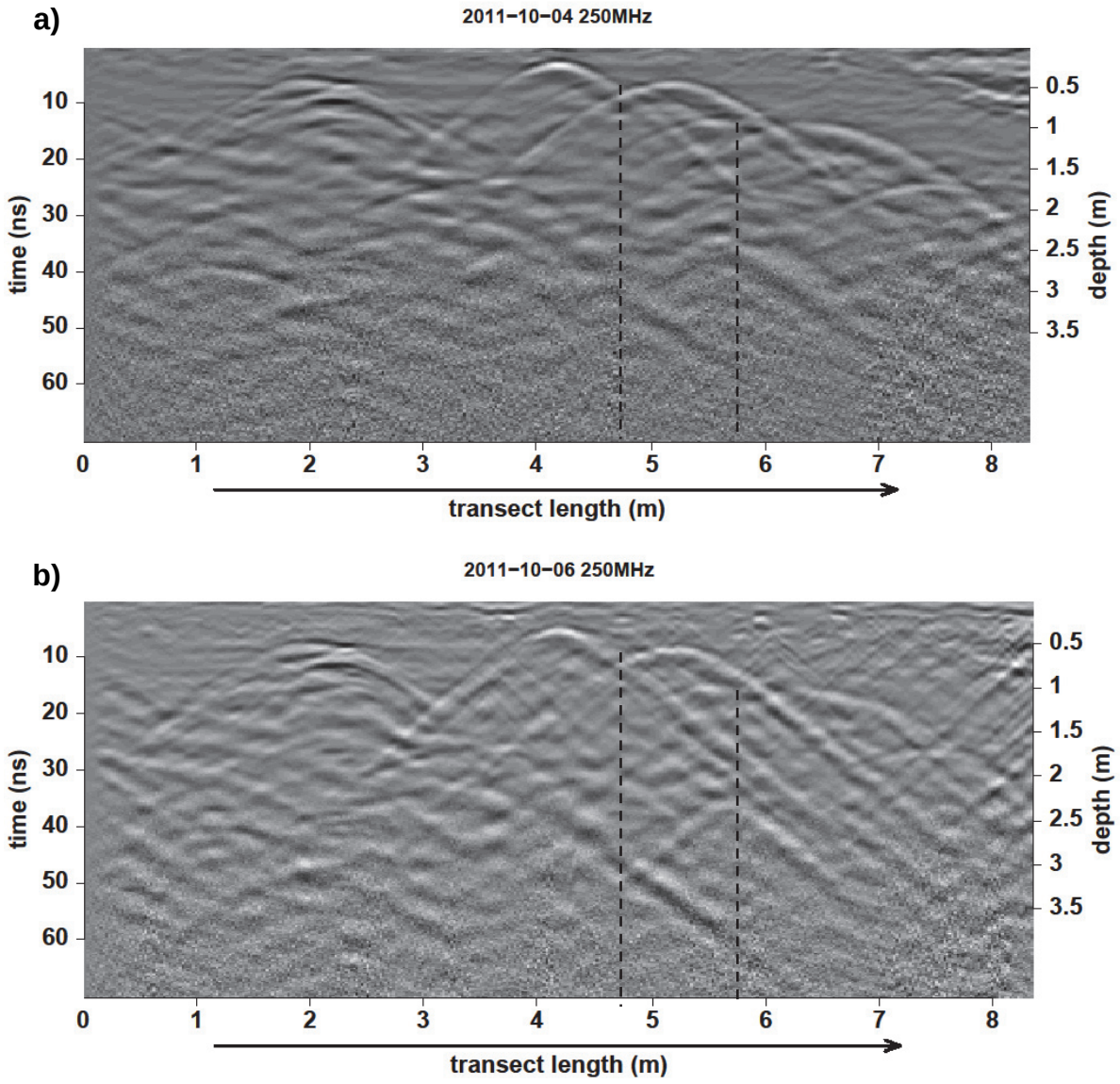



Figure 4.60 – B-scans obtained with a 250 MHz antenna on (a) the 4th of October 2011 and (b) on the 6th of October 2011, before and after a rainfall event, respectively. [Note: the vertical lines indicate the approximate position of the plastic targets.]

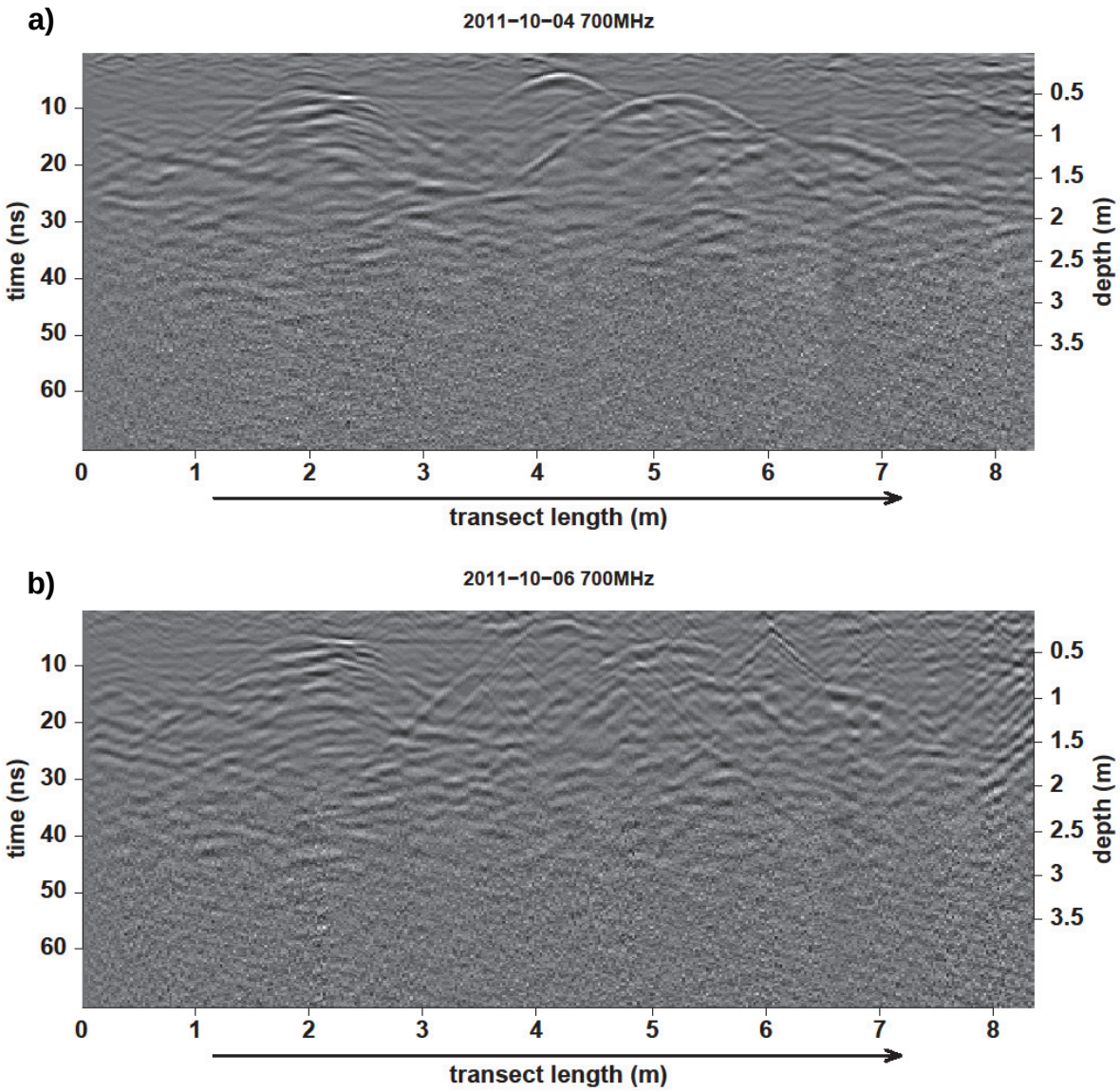



Figure 4.61 – B-scans obtained with a 700 MHz antenna on (a) the 4th of October 2011 and (b) on the 6th of October 2011, before and after a rainfall event, respectively.

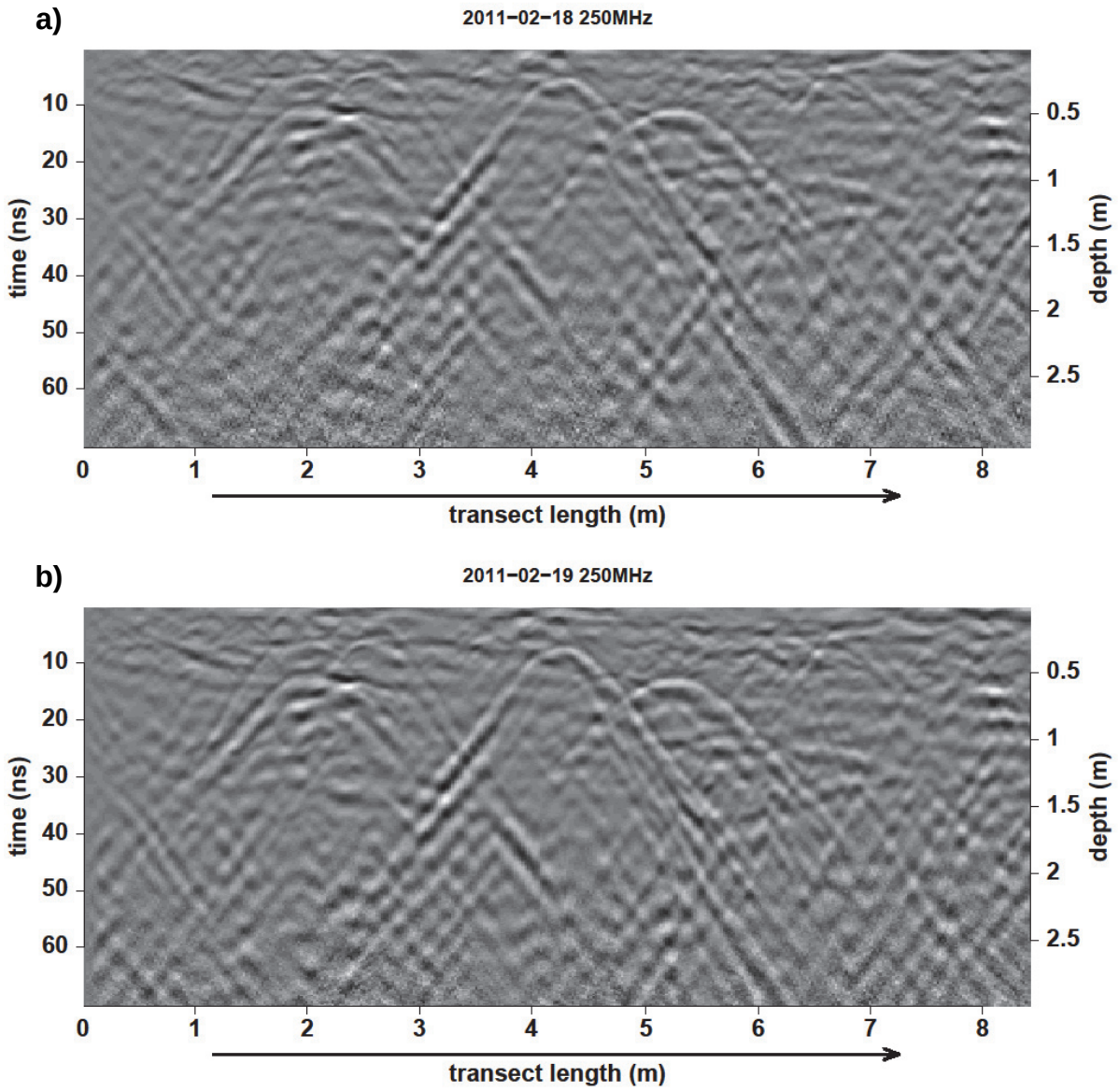



Figure 4.62 – B-scans obtained with a 250 MHz antenna (a) on the 18th of February 2011 and (b) on the 19th of February 2011, before and after a rainfall event, respectively.

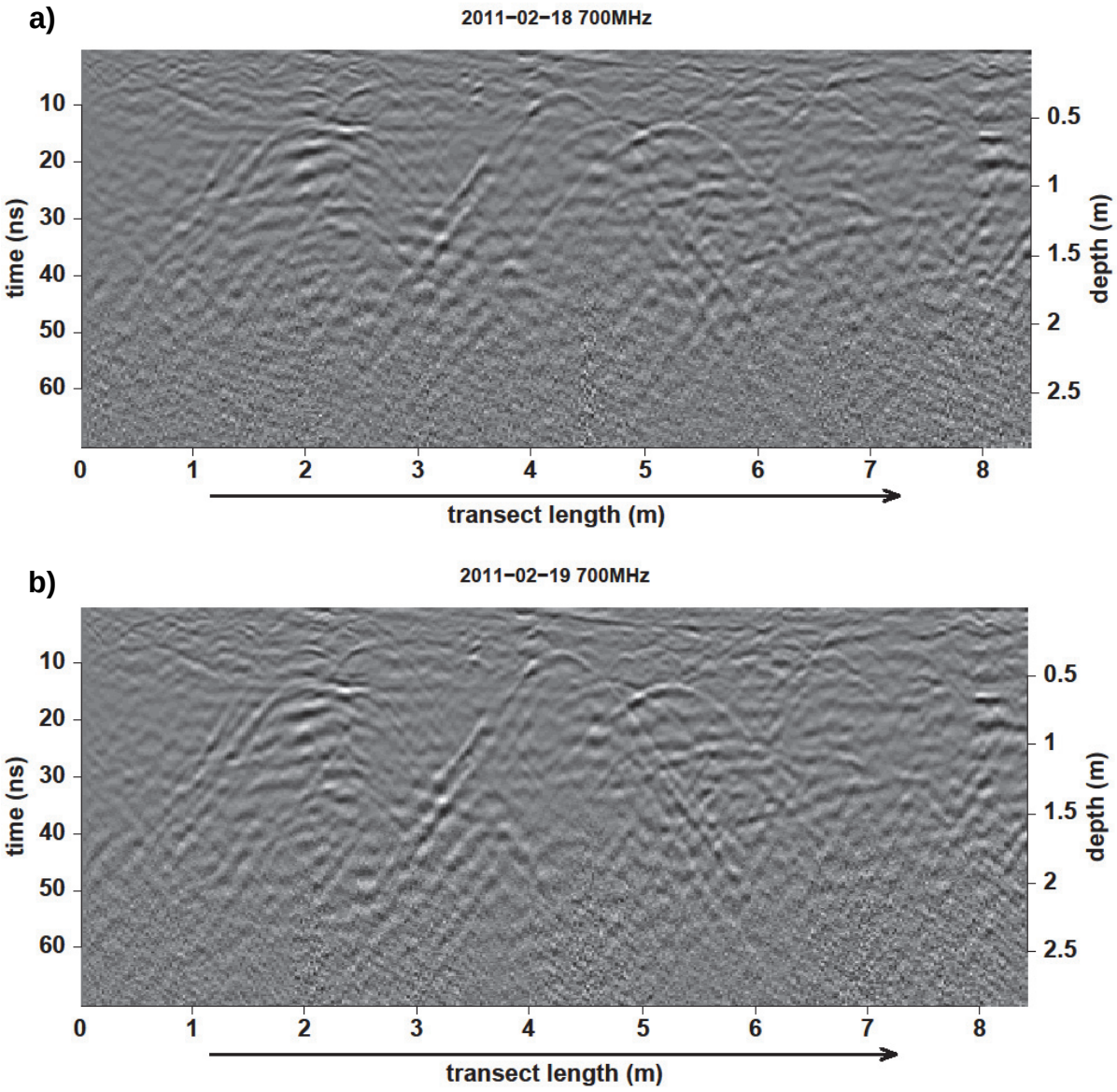



Figure 4.63 – B-scans obtained with a 700 MHz antenna (a) on the 18th of February 2011 and (b) on the 19th of February 2011, before and after a rainfall event, respectively.

Table 4.10 shows the variation in velocity and apparent permittivity before and after rainfall, for the three selected rainfall events. Both parameters did not change significantly, approximately 1 unit for apparent permittivity and 0.006 m/ns for propagation velocity. However, it has to be noted that these values correspond to the average values of the soil above the target buried at approximately 0.5 m depth. From these results it seems that the

soil conditions, for the purpose of utility detection and for a sandy soil, generally did not change dramatically after single rainfall events and that prolonged periods of rainfall or dry conditions were responsible for the seasonal changes in the soil. However, due to the limited number of selected rainfall events, it is not excluded that single, extreme rainfall events might have a larger impact on the soil conditions. In addition, as described above in this section, single rainfall events can decrease the quality of the B-scans, complicating the data interpretation.

Table 4.10 – Variation of velocity and apparent permittivity before and after three rainfall events occurring in 2011.

| **rainfall event 1 (10.2 mm in 10 hours)** | **2011-02-18** | **2011-02-19** | **difference** |
|---|---|---|---|
| velocity (m/ns) (250 MHz) | 0.085 | 0.081 | 0.004 |
| velocity (m/ns) (700 MHz) | 0.084 | 0.081 | 0.003 |
| apparent permittivity (250 MHz) | 12.38 | 13.63 | 1.25 |
| apparent permittivity (700 MHz) | 12.68 | 13.72 | 1.04 |
| **rainfall event 2 (16.8 mm in 20 hours)** | **2011-06-10** | **2011-06-14** | **difference** |
| velocity (m/ns) (250 MHz) | 0.120 | 0.113 | 0.007 |
| velocity (m/ns) (700 MHz) | 0.120 | 0.113 | 0.007 |
| apparent permittivity (250 MHz) | 6.28 | 7.05 | 0.77 |
| apparent permittivity (700 MHz) | 6.28 | 7.05 | 0.77 |
| **rainfall event 3 (8.3 mm in 12 hours)** | **2011-10-04** | **2011-10-06** | **difference** |
| velocity (m/ns) (250 MHz) | 0.132 | 0.124 | 0.008 |
| velocity (m/ns) (700 MHz) | 0.131 | 0.124 | 0.008 |
| apparent permittivity (250 MHz) | 5.20 | 5.85 | 0.65 |
| apparent permittivity (700 MHz) | 5.22 | 5.88 | 0.66 |

### 4.6.3. Comparison between TDR and GPR

Both TDR and GPR can measure an apparent permittivity. Other authors compared the TDR and GPR methodologies but generally made use of ground wave techniques or common midpoint methods (see section 2.5.4). In this study, a comparison between the values obtained by the TDR probes and the values obtained by fitting the hyperbolae of the

stainless steel pipes at depths of approximately 0.3 m, 0.5 m and 1 m was carried out. Hyperbolae were fitted for both GPR antennas and the mean value of the two frequencies was compared to the TDR data. Ten datasets were used, comprising the wet/dry extremes described in section 4.6.1, the rainfall events described in section 4.6.2, and warm/cold extremes corresponding to 27 July 2011 and 08 February 2012, respectively. The TDR probes were selected to approximately match the depth of the buried pipes and a mean value was used. The TDR data were selected corresponding to the time the GPR surveys were taken.

Table 4.11 shows the results of this analysis. Several apparent permittivity values by GPR are missing for the deeper pipe because of difficulties in identifying clear hyperbolae. The GPR results at frequencies of 250 MHz and 700 MHz were very similar and confirm that the soil was not very dispersive. This facilitated a direct comparison between the two techniques. In general, TDR and GPR provided analogous apparent permittivity values, with a mean absolute difference of 1.37. This confirmed that the TDR experimental setup was appropriate for detailed monitoring of the soil conditions. However, a closer look at the actual differences (i.e., tdr-gpr column in Table 4.11) shows that the TDR generally measured higher values of apparent permittivity during wet conditions, for apparent permittivity greater than 10. Conversely, it measured smaller values for apparent permittivity smaller than 10, corresponding to drier conditions.

Table 4.11 – Apparent permittivity values measured by fitting hyperbolae at different depths from GPR data and by TDR probes.

| date | pipe depth (m) | gpr (700MHz) | gpr (250MHz) | gpr mean | tdr | abs diff | tdr-gpr |
|---|---|---|---|---|---|---|---|
| 2011-01-13 | 0.3 | 14.06 | 13.90 | 13.98 | 16.97 | 2.99 | 2.99 |
| 2011-02-18 | 0.3 | 13.98 | 13.56 | 13.77 | 15.64 | 1.87 | 1.87 |
| 2011-02-19 | 0.3 | 15.18 | 15.08 | 15.13 | 18.30 | 3.17 | 3.17 |
| 2011-06-10 | 0.3 | 5.63 | 5.91 | 5.77 | 4.60 | 1.17 | -1.17 |
| 2011-06-14 | 0.3 | 6.87 | 6.90 | 6.88 | 5.88 | 1.00 | -1.00 |
| 2011-07-28 | 0.3 | 5.81 | 5.90 | 5.86 | 4.53 | 1.33 | -1.33 |
| 2011-08-20 | 0.3 | 5.09 | 5.09 | 5.09 | 3.97 | 1.12 | -1.12 |
| 2011-10-04 | 0.3 | 5.09 | 5.11 | 5.10 | 4.25 | 0.85 | -0.85 |
| 2011-10-06 | 0.3 | 5.81 | 5.72 | 5.76 | 4.67 | 1.09 | -1.09 |
| 2012-02-08 | 0.3 | 12.31 | 12.38 | 12.35 | 12.72 | 0.38 | 0.38 |
| 2011-01-13 | 0.5 | 13.47 | 13.47 | 13.47 | 16.71 | 3.24 | 3.24 |
| 2011-02-18 | 0.5 | 12.68 | 12.38 | 12.53 | 15.33 | 2.80 | 2.80 |
| 2011-02-19 | 0.5 | 13.72 | 13.63 | 13.68 | 17.63 | 3.96 | 3.96 |
| 2011-06-10 | 0.5 | 6.28 | 6.28 | 6.28 | 4.80 | 1.48 | -1.48 |
| 2011-06-14 | 0.5 | 7.05 | 7.05 | 7.05 | 5.87 | 1.18 | -1.18 |
| 2011-07-28 | 0.5 | 5.43 | 5.11 | 5.27 | 4.63 | 0.64 | -0.64 |
| 2011-08-20 | 0.5 | 4.83 | 4.88 | 4.86 | 4.06 | 0.80 | -0.80 |
| 2011-10-04 | 0.5 | 5.22 | 5.20 | 5.21 | 4.33 | 0.88 | -0.88 |
| 2011-10-06 | 0.5 | 5.88 | 5.85 | 5.87 | 4.70 | 1.17 | -1.17 |
| 2012-02-08 | 0.5 | 12.03 | 12.10 | 12.07 | 12.89 | 0.83 | 0.83 |
| 2011-01-13 | 1.0 | NA | NA | | 15.77 | | |
| 2011-02-18 | 1.0 | NA | NA | | 14.35 | | |
| 2011-02-19 | 1.0 | NA | NA | | 15.44 | | |
| 2011-06-10 | 1.0 | 6.87 | 6.58 | 6.72 | 7.36 | 0.64 | 0.64 |
| 2011-06-14 | 1.0 | NA | NA | | 7.75 | | |
| 2011-07-28 | 1.0 | 6.25 | 6.25 | 6.25 | 6.23 | 0.02 | -0.02 |
| 2011-08-20 | 1.0 | 5.74 | 5.69 | 5.72 | 5.56 | 0.16 | -0.16 |
| 2011-10-04 | 1.0 | 5.69 | 5.67 | 5.68 | 5.55 | 0.13 | -0.13 |
| 2011-10-06 | 1.0 | NA | NA | | 5.67 | | |
| 2012-02-08 | 1.0 | NA | NA | | 13.52 | | |
| | | | | | **mean:** | **1.37** | |

A possible explanation for this behaviour is as follows. GPR measures a bulk apparent permittivity, over a large sample of soil, whereas TDR measurements are limited to the dimensions of the probes, which can only be inserted in pockets of soils containing particles smaller than the separation between the rods. It is apparent that the TDR probes

used in this study were not able to measure bulk samples of soil including cobbles of the dimensions of a few centimetres. Because rocks have a low permittivity (e.g., Cassidy, 2008), this resulted in the TDR measuring larger apparent permittivity values than GPR, during wet conditions.

However, this explanation does not clarify why TDR measured lower values than GPR during dry conditions. As described in section 4.3.2.2, TDR seemed to not respond consistently to rainfall events during the Summer months (see Figure 4.20). It is believed that this is the reason why TDR values were smaller than the values measured by GPR. In section 4.3.2.2 this behaviour by the TDR probes was attributed to the high evapotranspiration of the soil and it was asserted that the sampling rate used in this study might not have been sufficient to detect more substantial increases in apparent permittivity corresponding to rainfall events. However, since GPR was able to measure higher apparent permittivity values, this explanation alone is not entirely satisfactory. However, it is also possible that air gaps formed along the length of the TDR probes during dry conditions that caused them to measure smaller apparent permittivity values. If this was the case, it would explain the higher GPR values because GPR was less sensitive to the formation of air gaps. It is believed that a combination of high evapotranspiration and formation of air gaps were responsible for these differences.

### 4.6.4. Impact of weather on GPR: Summary

The previous sections described how seasonal extremes and rainfall conditions affected the GPR surveys carried out with the Detector Duo GPR at the University of Birmingham test site. A comparison between apparent permittivity values measured by TDR and GPR was also shown. The main findings were:

- The quality of the GPR images was reduced during wet conditions, particularly at high frequency (e.g., 700 MHz). The hyperbolae from metal pipes were still identifiable for the pipes buried at shallow depth (approximately 0.5 m), but were often indistinguishable for the pipes buried at approximately 1 m depth. This was partially caused by the close positions between the targets, since the pipes buried at shallow depth partially masked the reflections of the deeper ones. Detection of the plastic pipes proved to be difficult during wet conditions.
- A velocity variation of 0.055 m/ns was observed between the wet and dry extremes occurring in 2011. This velocity variation can be significant if accurate target depths are needed. Based on the results of this study, the use of a typical apparent permittivity value of 10 during wet or dry extremes could have caused errors in depth determination greater than 40 % (or 0.40 m for a target buried at a depth of 1 m). The apparent permittivity measured after fitting hyperbolae was very similar for both GPR antennas (i.e., 250 MHz and 700 MHz). This demonstrated that the soil studied was not dispersive. The attenuation determined by BEC remained low (< 2 dB/m) during both wet and dry conditions. Multiple reflections caused by large cobbles and by water are thought to have played an important role in degrading the GPR signals and therefore the quality of the B-scans.
- The results from three rainfall events studies showed that apparent permittivity and velocity up to a depth of 0.5 m varied by approximately 1 unit and 0.006 m/ns, respectively. This demonstrated that in general these parameters do not change dramatically after single rainfall events and that prolonged periods of rainfall or dry conditions are responsible for their seasonal variation.
- TDR and GPR measured similar values of apparent permittivity, with a mean absolute difference of 1.37. TDR measured higher apparent permittivity values than

GPR during wet conditions and lower during dry conditions. The first behaviour was explained by the different sampling volume of the two techniques, with GPR measuring a bulk apparent permittivity including gravel and cobbles. The second behaviour was due to the fact that TDR did not measure significant increases in apparent permittivity corresponding to rainfall events during dry conditions (i.e., Summer 2011). Possible explanations for this latter phenomenon are the high evapotranspiration and the formation of air gaps along the TDR probes.

# CHAPTER 5: CONCLUSIONS AND RECOMMENDATIONS

## 5.1. CONCLUSIONS

This thesis described an application of TDR in the field, with the purpose of monitoring the EM soil properties that affect the performance of GPR for the detection of buried utilities. From the evaluation of the literature, a number of knowledge gaps were identified. It seemed apparent that despite a vast literature was available on both TDR and GPR, the study of anthropogenic soils in the field and for long time periods was largely missing. Furthermore, most of the past research investigated the variation of water content and not directly of the EM soil properties. Long-term monitoring by TDR combined with regular GPR surveys was deemed valuable in order to determine whether seasons and weather events have a significant effect on the GPR results.

To address these gaps, a field TDR monitoring station was developed at the University of Birmingham campus (UK) for monitoring the apparent permittivity and the bulk electrical conductivity (BEC) of a sandy anthropogenic soil. TDR and temperature probes were inserted at different depths, up to approximately 1 m from the surface, and the monitoring was conducted for almost two years, covering all seasons. Extreme dry and wet conditions occurring during this period were important for establishing the potential variation of the EM soil properties of the soil studied. Regular GPR surveys were conducted on specifically buried targets in the proximity of the TDR monitoring station in order to establish the effect of the soil conditions on the GPR surveys. Analyses of the data from the field monitoring and laboratory tests were carried out. In addition, the Soil-Plant-Air-Water

(SPAW) model was applied for simulating the variation of the soil water content for three main soil horizons. The main findings of this research can be summarised by the following points:

- It was found that the EM soil properties varied significantly with seasons and that their variation was highly dependent on the amount of rainfall, especially for apparent permittivity. BEC showed smaller variability due to the sandy and gravelly nature of the soil. The minima and maxima values measured by the TDR probes over the monitoring period were, respectively, approximately 3 and 29 for apparent permittivity, and approximately 0.01 mS/m and 18 mS/m for BEC. The soil horizons with higher organic content or fines content showed greater variability in the EM soil properties. This has important implications for the application of GPR on soils with these characteristics because the results could be highly dependent on the soil conditions at the moment of the survey. The results shown for the soil studied suggest that single rainfall events did not affect in a substantial way the EM soil properties, and that prolonged periods of dry and wet conditions were responsible for the more significant seasonal variation of the soil properties. These findings confirm that both the weather conditions and the soil composition are important in determining the EM behaviour of the soil.

- Both apparent permittivity and BEC of the soil studied did not show a diurnal variation cycle. The apparent permittivity was largely independent to temperature variations, BEC showed greater variability but no clear relationship with temperature was found. However, it is thought that these results can be different for other soil types, for example for soils with higher clay content, and that further field testing are

necessary to extend these findings. Although the soil investigated in this thesis was a single example of anthropogenic soil, it still provides an indication of the potential variation that can be encountered for similar soils in urban areas in the UK. However, care should be taken on generalising the results contained in this thesis to other types of urban soils, especially to clayey soils.

- Based on recent publications, a rigorous methodology was followed for the construction and calibration of the TDR monitoring station. Laboratory tests on the equipment showed its consistency, and the ability of measuring apparent permittivity and BEC with an accuracy of 2 % and 3 %, respectively, and a precision of approximately 2 % for both parameters. However, for materials with very low permittivity (e.g., air) and with a BEC smaller than 10 mS/m higher errors were found, but always remained smaller than 10 %. No evident temperature effect on the equipment was measured, and the introduction of two levels of multiplexers did not seem to reduce the accuracy of the TDR measurements. However, the cable lengths used in this study were short, approximately 4 m in total, and problems can arise if using longer cables. A comparison between manual analysis and automatic analysis of the TDR waveforms resulted in similar accuracies and improved precision by the automatic scripts. This proved very important due to the long-term nature of the monitoring described in this study. During the period of monitoring several gaps in the data occurred due to a number of reasons (e.g., problems with scripts, power supply). However, no major equipment failure happened during this period. Interestingly, the shallow TDR probes installed in the grass root system did not measure a substantial increase in the soil EM properties during Summer 2011. This

is thought to be due to the high evapotranspiration and the formation of air gaps during that period and not to faulty equipment.

- The field and laboratory data collected in this research allowed the determination of relationships between several soil parameters. As expected, it was found that the EM soil properties are statistically correlated with rainfall events, with time lags of the order of several hours up to several days depending on the depth. Apparent permittivity was consistently positively correlated to BEC. Both apparent permittivity and BEC were shown to depend on the water content and on the particle size distribution of the soil, in particular on the clay content. Contrasting relationships between EM soil properties and temperature were found. However, a general negative correlation seemed dominant. The relationship between apparent permittivity and volumetric water content for the soil studied was described by a third order polynomial.

- An existing simulation software (i.e., SPAW) was used for simulating the variation of the water content with depth over a predefined period of time for which the weather data were available. The simulated volumetric water content by the SPAW model matched reasonably well the calculated data from the measured apparent permittivity, with differences smaller than 10 % and generally smaller than 5 %. The agreement was improved when using a site specific empirical calibration relating the apparent permittivity to the volumetric water content, as compared to the commonly used Topp model. The use of the SPAW model can be regarded as a way of validating empirical calibrations using field data. The SPAW model was shown to

be relatively insensitive to ±3 % variations of the input volumetric water content, by providing results that differed less than 5 % compared to the original input.

- The variation in the EM soil properties were shown to affect the results of GPR surveys. In particular, the quality of the GPR images was reduced during wet conditions, making it more difficult to discriminate targets and to fit hyperbolae for velocity and depth estimations, especially for plastic pipes. The GPR images were generally poorer soon after rainfall events due to the presence of multiple reflections caused by water infiltrating in the soil. This was true when the soil was dry, for rainfall events occurring after dry periods. No significant deterioration of the GPR images was found for rainfall events occurring during wet conditions (i.e., when the soil was already wet). TDR and GPR measured similar values of apparent permittivity, with a mean absolute difference of 1.37. The differences were likely caused by the different sampling volumes of the two techniques and by the high evapotranspiration and formation of air gaps along the TDR probes during dry conditions.

- This study demonstrated that accurate knowledge of the soil apparent permittivity (or propagation velocity) is essential in order to accurately estimate the depth of the targets, if clear hyperbolae cannot be identified and fitted. The use of a typical soil apparent permittivity value during wet or dry conditions can cause significant errors in target depth determination, greater than 40 % (or 0.4 m for a target buried at a depth of 1 m). Whenever the TDR probes can be inserted in the ground, they could be used for providing information on the soil apparent permittivity.

# 5.2. RECOMMENDATIONS FOR FUTURE WORK

From the research described in this thesis a number of recommendations for future work became apparent. The methodology described could serve as a standard for future projects involving monitoring of the EM soil properties by TDR. The choice of using a netbook and a specifically developed Matlab script proved reliable. However, due to the high power consumption of the netbook, it is advisable for future projects to use dataloggers in combination with solar panels for more autonomous monitoring stations.

A more recent project, DART[15] (http://dartproject.info/WPBlog/), involving archaeological features, made use of a number of TDR monitoring stations based on the instrumentation layout developed in this work. DART is currently investigating a range of different soils found in rural areas in the UK by means of geophysical techniques, including TDR. These studies are a natural continuation of the work described in this thesis and should further improve our understanding of the variation of the EM soil properties in the field. Further field monitoring studies, in particular on clayey soils, should significantly extend our knowledge of the EM behaviour of soils in the field. Due to the peculiarity of urban soils (Craul, 1999) it would also be interesting to extend the type of monitoring described in this work to other soil types in urban areas, including soils buried beneath pavements and roads.

In order to improve the use of GPR for the detection of buried utilities, it is apparent that the seasonal variation of the EM soil properties and their dependency on the ground conditions should be taken into account. Efforts should be put into providing better estimations of the permittivity of the soil if accurate target depths are needed, particularly

15 DART: Detection of Archaeological Residues using remote sensing Techniques.

when clear targets are not visible. TDR can be used effectively for this purpose but only when the TDR probes can be inserted in the ground. In addition, the TDR probes can only measure shallow depths without the need of digging. An alternative approach is to predict the apparent permittivity of the soil from prior information of its geotechnical parameters. This option is currently being looked at by the Mapping The Underworld project (http://www.mappingtheunderworld.ac.uk/) through the development of a Knowledge Based System for the prediction of the soil EM properties based on existing information of the ground. Existing geotechnical databases such as the ones held by the British Geological Survey in the UK could be used for this purpose (Rogers et al., 2009; Foo et al., 2011).

# REFERENCES

Adler J. (2010) *R in a Nutshell – A Desktop Quick Reference*. Sebastopol, CA: O'Reilly Media Inc.

Allen R.G., Pereira L.S., Raes D. and Smith M. (1998) *Crop evapotranspiration – Guidelines for computing crop water requirements*. FAO Irrigation and drainage paper 56, FAO, Rome.

Anderson N., Croxton N., Hoover R. and Sirles P. (2008) *Geophysical Methods Commonly Employed for Geotechnical Site Characterization*. Transportation Research Circular E-C130, Washington: Transportation Research Board of the National Academies.

Annan A.P. (2008) "Electromagnetic Principles of Ground Penetrating Radar" In Jol, H. (ed.) *Ground Penetrating Radar Theory and Applications - Chapter 1*. Oxford: Elsevier. pp. 4-40.

Arora V.K. and Gajri P.R. (1996) Performance of simplified water balance models under maize in a semiarid subtropical environment. *Agricultural Water Management*, 31: 51-64.

Baker J.M. and Allmaras R.R. (1990) System for automating and multiplexing soil-moisture measurement by time-domain reflectometry. *Soil Science Society of America Journal*, 54 (1): 1-6.

Ball P. (1999) *H2O: A Biography of Water*. London: Phoenix.

Bechtold M., Huisman J.A., Weihermüller L. and Vereecken H. (2010) Accurate Determination of the Bulk Electrical Conductivity with the TDR100 Cable Tester. *Soil Science Society of America Journal*, 74 (2): 495-501.

Benson C.H. and Wang X. (2006) "Temperature-Compensating Calibration Procedure for Water Content Reflectometers" In *Proceedings of TDR 2006, Purdue University, West Lafayette, USA, September, p. 1-16.*

Bittelli M., Salvatorelli F. and Pisa P.R. (2008) Correction of TDR-based soil water content measurements in conductive soils. *Geoderma*, 143: 133-142.

Blonquist J.M., Jones S.B. and Robinson D.A. (2005) Standardising Characterization of Electromagnetic Water Content Sensors: Part 2. Evaluation of Seven Sensing Systems. *Vadose Zone Journal*, 4: 1059-1069.

Boll J., van Rijn R.P.G., Weiler K.W., Ewen J.A., Daliparthy J., Herbert S.J. and Steenhuis T.S. (1996) Using ground-penetrating radar to detect layers in a sandy field soil. *Geoderma*, 70: 117-132.

BS 1377-1, 1990, *Methods of test for soils for civil engineering purposes: Part 1: General requirements and sample preparation*. London: British Standards Institution.

BS 1377-2, 1990, *Methods of test for soils for civil engineering purposes: Part 2: Classification tests*. London: British Standards Institution.

BS 1377-3, 1990, *Methods of test for soils for civil engineering purposes: Part 3: Chemical and electro-chemical tests*. London: British Standards Institution.

BS 7755-3.4, 1995, *Soil quality – Part 3: Chemical methods – Section 3.4: Determination of the specific electrical conductivity*. London: British Standards Institution.

BS 5930:1999+A2, 2010, *Code of practice for site investigations*. London: British Standards Institution.

Campbell J.E. (1990) Dielectric properties and influence of conductivity in soils at one to 50 megahertz. *Soil Science Society of America Journal*, 54 (2): 332-341.

Cassidy N.J. (2007) "Frequency-Dependent Attenuation and Velocity Characteristics of Magnetically Lossy Materials" In *Proceedings of the 4th International Workshop on Advanced Ground Penetrating Radar, Naples, Italy, 27-29 July, p. 142-146.*

Cassidy N.J. (2008) "Electrical and Magnetic Properties of Rocks, Soils and Fluids" In Jol, H. (ed.) *Ground Penetrating Radar Theory and Applications - Chapter 2.* Oxford: Elsevier. pp. 41-72.

Castiglione P. and Shouse P.J. (2003) The Effect of Ohmic Cable Losses on Time-Domain Reflectometry Measurements of Electrical Conductivity. *Soil Science Society of America Journal*, 67: 414-424.

Castiglione P., Shouse P.J. and Wraith J.M. (2006) Multiplexer-Induced Interference on TDR Measurements of Electrical Conductivity. *Soil Science Society of America Journal*, 70: 1453-1458.

Chapuis R.P. (2004) Predicting the saturated hydraulic conductivity of sand and gravel using effective diameter and void ratio. *Canadian Geotechnical Journal*, 41: 787-795.

Chung C.C. and Lin C.P. (2009) Apparent Dielectric Constant and Effective Frequency of TDR Measurements: Influencing Factors and Comparison. *Vadose Zone Journal*, 8: 548-556.

Cole K.S. and Cole R.H. (1941) Dispersion and Absorption in Dielectrics 1. Alternating Current Characteristics. *Journal of Chemical Physics*, 9 (4): 341-351.

Comas X., Slater L. and Reeve A. (2008) Seasonal geophysical monitoring of biogenic gases in a northern peatland: Implications for temporal and spatial variability in free phase gas production rates. *Journal of Geophysical Research*, 113: G01012.

Cownie A. and Palmer L.S. (1952) The Effect of Moisture on the Electrical Properties of Soil. *Proceedings of the Physical Society. Section B.* 65 (4): 295-301.

# REFERENCES


Cowpertwait P.S.P. (2006) *Introductory Time Series with R*. Springer Science + Business Media, LLC.

Craig R.F. (2004) *Craig's Soil Mechanics*. 7th ed. London: Taylor & Francis.

Craul P.J. (1999) *Urban Soils: Applications and Practices*. UT: John Wiley & Sons Inc.

Curtis J.O., Weiss C.A. Jr and Everett J.B. (1995) *Effect of soil composition on dielectric properties*. Vicksburg, MS: U.S. Army Corps Eng. Waterways Exp. Station.

Curtis J.O. (2001) Water Effects on the Dielectric Properties of Soils. *IEEE Transactions on Geoscience and Remote Sensing*, 39 (1): 125-128.

Dalton F.N., Herkelrath W.N., Rawlins D.S. and Rhoades J.D. (1984) Time-Domain Reflectometry: Simultaneous Measurement of Soil Water Content and Electrical Conductivity with a Single Probe. *Science*, 224 (4652): 989-990.

Daniels D.J. (2004) *Ground Penetrating Radar*. 2nd ed. London: The Institution of Electrical Engineers.

DART, Detection of Archaeological Residues using remote sensing Techniques: http://dartproject.info/WPBlog/ [Accessed December 2012]

Davis J.L. and Annan A.P. (1989) Ground-Penetrating Radar for High-Resolution Mapping of Soil and Rock Stratigraphy. *Geophysical Prospecting*, 37: 531-551.

Debye P. (1929) *Polar Molecules*. New York: The Chemical Catalog Company.

Dekker L.W., Ritsema C.J., Wendroth O., Jarvis N., Oostindie K., Pohl W., Larsson M. and Gaudet J.P. (1999) Moisture distributions and wetting rates of soils at experimental fields in the Netherlands, France, Sweden and Germany. *Journal of Hydrology*, 215: 4-22.

De Loor G.P. (1968) Dielectric properties of heterogeneous mixtures containing water. *Journal of Microwave Power*, 3-2: 67-73.

Dirksen C. and Dasberg S. (1993) Improved calibration of time-domain reflectometry soil-water content measurements. *Soil Science Society of America Journal*, 57 (3): 660-667.

Dobson M.C., Ulaby F.T., Hallikainen M.T. and Elrayes M.A. (1985) Microwave dielectric behavior of wet soil – Part II. Dielectric mixing models. *IEEE Transactions on Geoscience and Remote Sensing*, 23 (1): 35-46.

Doolittle J.A. and Collins M.E. (1995) Use of soil information to determine application of ground penetrating radar. *Journal of Applied Geophysics*, 33: 101-108.

Doolittle J.A., Minzenmayer F.E., Waltman S.W., Benham E.C., Tuttle J.W. and Peaslee S.D. (2007) Ground-penetrating radar soil suitability map of the conterminous United States. *Geoderma*, 141: 416-421.

Doolittle J.A., Dobos R., Peaslee S.D., Waltman S.W., Benham E.C. and Tuttle J.W. (2010) Revised Ground-Penetrating Radar Soil Suitability Maps. *Journal of Environmental and Engineering Geophysics*, 15 (3): 111-118.

Evett S.R., Howell T.A., Steiner J.L. and Cresap J.L. (1993) "Evapotranspiration by Soil Water Balance Using TDR and Neutron Scattering" In *Proceedings of the National Conference on Irrigation and Drainage Engineering, Park City, UT, 21-23 July.*

Evett S.R. and Parkin G. W. (2005) Advances in Soil Water Content Sensing: The Continuing Maturation of Technology and Theory. *Vadose Zone Journal*, 4 (2): 986-991.

FAO/ISRIC/ISSS (1998) *World Reference Base for Soil Resources.* World Soil Resources Report, #84. Rome: FAO.

Ferre' P.A., Rudolph D.L. and Kachanoski R.G. (1996) Spatial averaging of water content by time domain reflectometry: Implications for twin rod probes with and without dielectric coatings. *Water Resources Research*, 32 (2): 271-279.

Foo K.Y., Hao T., Curioni G., Chapman D.N., Metje N. and Atkins P.R. (2011) "A Knowledge-based System for Evaluating the Impact of Soil Properties on the Performance of Utility Location Technologies: Design and Case-study" In *Proceedings of the ASCE International Conference on Pipelines and Trenchless Technology, Beijing, China, 26-29 October, p. 810-825.*

Foth H.D. (1990) *Fundamentals of Soil Science*. 8th ed. New York: John Wiley & Sons.

Fredlund D.G. and Xing A. (1994) Equations for the soil-water characteristic curve. *Canadian Geotechnical Journal*, 31 (3): 521-532.

Giese K. and Tiemann R. (1975) Determination of the complex permittivity from thin-sample time domain reflectometry improved analysis of the step response waveform. *Advances in Molecular Relaxation Processes*, 7 (1): 45-59.

Gijsman A.J., Jagtap S.S. and Jones J.W. (2003) Wading through a swamp of complete confusion: how to choose a method for estimating soil water retention parameters for crop models. *European Journal of Agronomy*, 18: 77-106.

Gong Y., Cao Q. and Sun Z. (2003) The effects of soil bulk density, clay content and temperature on soil water content measurements using time-domain reflectometry. *Hydrological Processes*, 17: 3601-3614.

Gray A.N. and Spies T.A. (1995) Water content measurement in forest soils and decayed wood using time domain reflectometry. *Canadian Journal of Forest Research*, 25: 376-385.

Greaves R.J., Lesmes D.P., Lee J.M. and Toksoz M.N. (1996) Velocity variations and water content estimated from multi-offset, ground-penetrating radar. *Geophysics*, 61 (3): 683-695.

Grote K., Hubbard S. and Rubin Y. (2003) Field-scale estimation of volumetric water content using ground-penetrating radar ground wave techniques. *Water Resources Research,* 39 (11): 5-1 – 5-13.

Halbertsma J., van den Elsen E., Bohl H. and Skierucha W. (1995) "Temperature effects on TDR determined soil water content" In *Proceedings of the Symposium: Time-Domain Reflectometry Applications in Soil Science, Research Center Foulum. Danish Inst. Of Plant and Soil Sci., Lyngby, Denmark, 16 September, p. 35-37.*

Hamburger F. (1930) Polar molecules, their contribution to energy loss in dielectrics. *Physical Review,* 35 (9): 1119-1124.

Hatzichristodulu V.C., Baker R.D. and Tellam J.H. (2002) *High Resolution Electrical Monitoring of Fluid Flow Through the Unsaturated Zone*. R&D Technical Report P2-042/TR1, Environment Agency.

Heimovaara T.J. and Bouten W. (1990) A Computer-Controlled 36-Channel Time Domain Reflectometry System for Monitoring Soil Water Contents. *Water Resources Research,* 26 (10): 2311-2316.

Heimovaara T.J. (1993) Design of triple-wire time-domain reflectometry probes in practice and theory. *Soil Science Society of America Journal,* 57 (6): 1410-1417.

Heimovaara T.J. (1994) Frequency domain analysis of time domain reflectometry waveforms 1. Measurement of the complex dielectric permittivity of soils. *Water Resources Research,* 30 (2): 189-199.

Heimovaara T.J., Focke A.G., Bouten W. and Verstraten J.M. (1995) Assessing temporal variations in soil-water composition with time-domain reflectometry. *Soil Science Society of America Journal,* 59 (3): 689-698.

Heimovaara T.J., Winter E.J.G., van Loon W.K.P. and Esveld D.C. (1996) Frequency-dependent dielectric permittivity from 0 to 1 GHz: Time domain reflectometry measurements compared with frequency domain network analyzer measurements. *Water Resources Research,* 32 (12): 3603-3610.

Herkelrath W.N., Hamburg S.P. and Murphy F. (1991) Automatic, Real-Time Monitoring of Soil Moisture in a Remote Field Area With Time Domain Reflectometry. *Water Resources Research,* 27 (5): 857-864.

Hess T. M. (1996) *Potential Evapotranspiration [DAILYET]*. Silsoe College. UK.

Hoekstra P. and Delaney A. (1974) Dielectric Properties of Soils at UHF and Microwave Frequencies. *Journal of Geophysical Research,* 79 (11): 1699-1708.

Howell T.A. and Evett S.R. (undated) *The Penman-Monteith Method. USDA-Agricultural Research Service & Production Research Laboratory,* Bushland, Texas, www.cprl.ars.usda.gov. [accessed May 2013]

Huisman J.A. and Bouten W. (1999) Comparison of calibration and direct measurement of cable and probe properties in time domain reflectometry. *Soil Science Society of America Journal*, 63 (6): 1615-1617.

Huisman J.A., Sperl C., Bouten W. and Verstraten J.M. (2001) Soil water content measurements at different scales: accuracy of time domain reflectometry and ground-penetrating radar. *Journal of Hydrology*, 245: 48-58.

Huisman J.A., Hubbard S.S., Redman J.D. and Annan A.P. (2003a) Measuring Soil Water Content with Ground Penetrating Radar: A Review. *Vadose Zone Journal*, 2 (4): 476-491.

Huisman J.A., Snepvangers J.J.J.C., Bouten W. and Heuvelink G.B.M. (2003b) Monitoring Temporal Development of Spatial Soil Water Content Variation: Comparison of Ground Penetrating Radar and Time Domain Reflectometry. *Vadose Zone Journal*, 2: 519-529.

Huisman J.A., Lin C.P., Weihermüller L. and Vereecken H. (2008) Accuracy of Bulk Electrical Conductivity Measurements with Time Domain Reflectometry. *Vadose Zone Journal*, 7 (2): 426-433.

IAEA (2008) *Field Estimation of Soil Water Content – A Practical Guide to Methods, Instrumentation and Sensor Technology*. Vienna: IAEA.

Igel J. (2008) "The Small-Scale Variability of Electrical Soil Properties – Influence on GPR Measurements" In *12th International Conference on Ground Penetrating Radar. Birmingham, UK, 16-19 June, CD-ROM.*

Igel J., Takahashi K. and Preetz H. (2011) "Electromagnetic Soil Properties and Performance of GPR for Landmine Detection: How to Measure, How to Analyse and How to Classify?" In *Proceedings of the 6th International Workshop on Advanced Ground Penetrating Radar. Aachen, Germany, 22-24 June, CD-ROM.*

Jenny H. (1941) *Factors of Soil Formation: A System of Quantitative Pedology*. New York: Dover publications.

Johnson C.K., Doran J.W., Duke H.R., Wienhold B.J., Eskridge K.M. and Shanahan J.F. (2001) Field-Scale Electrical Conductivity Mapping for Delineating Soil Condition. *Soil Science Society of America Journal*, 65: 1829-1837.

Jones S.B., Wraith J.M. and Or D. (2002) Time domain reflectometry measurement principles and applications. *Hydrological Processes*, 16 (1): 141-153.

Jones S.B., Blonquist J.M., Robinson D.A., Rasmussen V.P. and Or D. (2005) Standardizing Characterisation of Electromagnetic Water Content Sensors: Part 1. Methodology *Vadose Zone Journal*, 4: 1048-1058.

Jordan D. (2009) How Effective is Geophysical Survey? A Regonal Review. *Archaeological Prospection*, 16 (2): 77-90.

Kachanoski R.G., Gregorich E.G. and van Wesenbeeck I.J. (1988) Estimating spatial variations of soil water content using noncontacting electromagnetic inductive methods. *Canadian Journal of Soil Science,* 68: 715-722.

Kelleners T.J., Seyfried M.S., Blonquist J.M., Bilskie J. and Chandler D.G. (2005) Improved Interpretation of Water Content Reflectometer Measurements in Soils. *Soil Science Society of America Journal*, 69: 1684-1690.

Koppenjan S. (2008) "Ground Penetrating Radar Systems and Design" In Jol, H. (ed.) *Ground Penetrating Radar Theory and Applications - Chapter 3*. Oxford: Elsevier. pp. 73-97.

Laurent J.P, Ruelle P., Delage L., Zairi A., Ben Nouna B. and Adjmi T. (2005) Monitoring Soil Water Content Profiles with a Commercial TDR System: Comparative Field Tests and Laboratory Calibration. *Vadose Zone Journal*, 4: 1030-1036.

Lavelle P. and Spain A.V. (2003) *Soil Ecology*. Dordrecht: Kluwer Academic Publishers.

Ledieu J., De Ridder P., De Clerck P. and Dautrebande S. (1986) A method of measuring soil moisture by time-domain reflectometry. *Journal of Hydrology*, 88: 319-328.

Lenka N.K., Mohanty S., Singh K.K. and Chakravarty N.V.K. (2008) Performance Study of SPAW Model with Temperature-Derived $ET_0$ as Input in Place of Pan Evaporation under Wheat Crop in a Semiarid Subtropical Climate. *Journal of Irrigation and Drainage Engineering*, 134 (6): 730-736.

Lin C.P. (2003) Frequency Domain versus Travel Time Analyses of TDR Waveforms for Soil Moisture Measurements. *Soil Science Society of America Journal*, 67: 720-729.

Lin C.P., Chung C.C. and Tang S.H. (2007) Accurate Time Domain Reflectometry Measurement of Electrical Conductivity Accounting for Cable Resistance and Recoding Time. *Soil Science Society of America Journal*, 71: 1278-1287.

Lin C.P., Chung C.C., Huisman J.A. and Tang S.H. (2008) Clarification and Calibration of Reflection Coefficient for Electrical Conductivity Measurement by Time Domain Reflectometry. *Soil Science Society of America Journal*, 72 (4): 1033-1040.

Logsdon S.D. (2000) Effect of Cable Length on Time Domain Reflectometry Calibration for High Surface Area Soils. *Soil Science Society of America Journal*, 64: 54-61.

Logsdon S.D. (2005) Time Domain Reflectometry Range of Accuracy for High Surface Area Soils. *Vadose Zone Journal*, 4: 1011-1019.

Logsdon S.D. (2006) Experimental Limitations of Time Domain Reflectometry Hardware for Dispersive Soils. *Soil Science Society of America Journal*, 70: 537-540.

Malicki M.A., Plagge R. and Roth C.H. (1996) Improving the calibration of dielectric TDR soil moisture determination taking into account the solid soil. *European Journal of Soil Science,* 47 (3): 357-366.

Menziani M., Rivasi M.R., Pugnaghi S., Santagnelo R. and Vincenzi S. (1996) Soil volumetric water content measurements using TDR technique. *Annali di geofisica*, 34 (1): 91-95.

Menziani M., Pugnaghi S., Vincenzi S. and Santangelo R. (2003) Soil moisture monitoring in the Toce valley (Italy). *Hydrology and Earth System Sciences*, 7 (6): 890-902.

Metje N., Atkins P.R., Brennan M.J., Chapman D.N., Lim H.M., Machell J., Muggleton J.M., Pennock S., Ratcliffe J., Redfern M., Rogers C.D.F., Saul A.J., Shan Q., Swingler S. and Thomas A.M. (2007) Mapping the Underworld – State-of-the-art review. *Tunnelling and Underground Space Technology*, 22 (5-6): 568–586.

Metje N., Rogers C.D.F., Chapman D.N., Thomas A.M. and Parker J.M. (2008) "Minimizing Streetworks Disruption by Mapping the Underworld" In *Proceedings of Pipelines, American Society of Civil Engineers, Atlanta, UT, 22–25th July.*

MetOffice (2012): http://www.metoffice.gov.uk/climate/uk/stationdata/shawburydata.txt [Accessed October 2012]

Mironov V.L., Kosolapova L.G. and Fomin S.V. (2009) Physically and Mineralogically Based Spectroscopic Dielectric Model for Moist Soils. *IEEE Transactions on Geoscience and Remote Sensing*, 47 (7): 2059-2070.

Mitchell J.K. and Soga K. (2005) *Fundamentals of Soil Behavior*. 3rd ed. Hoboken, New Jersey: John Wiley & Sons Inc.

Mohanty B.P., Shouse P.J. and van Genuchten M.T. (1998) Spatio-temporal dynamics of water and heat in a field soil. *Soil & Tillage Research*, 47: 133-143.

Monteith J.L. (1965) Evaporation and Environment. *Symposium of the Society for Experimental Biology*, 19: 205-224.

Musgrave H. and Binley A. (2011) Revealing the temporal dynamics of subsurface temperature in a wetland using time-lapse geophysics. *Journal of Hydrology*, 396: 258-266.

MTU, Mapping The Underworld: http://www.mappingtheunderworld.ac.uk/ [Accessed May 2013]

Nadler A., Dasberg S. and Lapid I. (1991) Time Domain Reflectometry Measurements of Water-Content and Electrical-Conductivity of Layered Soil Columns. *Soil Science Society of America Journal*, 55 (4): 938-943.

Nelder J.A. and Mead R. (1965) A simplex method for function minimization. *Computer Journal*, 7 (4): 308-313.

Ollerton H.G. (2012) *A calibration of a soil for the estimation of water content using time-domain reflectometry*. MSc report, School of Civil Engineering, University of Birmingham, UK, August 2012.

Or D. and Wraith J.M. (1999) Temperature effects on soil bulk dielectric permittivity measured by time domain reflectometry: A physical model. *Water Resources Research*, 35 (2): 371-383.

ORFEUS, Optimised Radar to Find Every Utility in the Street: http://www.orfeus-project.eu/ [Accessed May 2013]

Penman H.L. (1948) Natural evaporation from open water, bare soil, and grass. Proceedings of the Royal Society of London A, 193: 120-146.

Peplinski N.R., Ulaby F.T. and Dobson M.C. (1995a) Dielectric Properties of Soils in the 0.3-1.3 GHz Range. *IEEE Transactions on Geoscience and Remote Sensing*, 33 (3): 803-807.

Peplinski N.R., Ulaby F.T. and Dobson M.C. (1995b) Corrections to "Dielectric Properties of Soils in the 0.3-1.3 GHz Range". *IEEE Transactions on Geoscience and Remote Sensing*, 33 (6): 1340.

Ponce V.M. and Hawkins R.H. (1996) Runoff Curve Number: Has It Reached Maturity? *Journal of Hydrologic Engineering*, 1 (1): 11-19.

Ponizovsky A.A., Chudinova S.M. and Pachepsky Y.A. (1999) Performance of TDR calibration models as affected by soil texture. *Journal of Hydrology*, 218: 35-43.

Rajeev P., Chan D. and Kodikara J. (2012) Ground-atmosphere interaction modelling for long-term prediction of soil moisture and temperature. *Canadian Geotechnical Journal*, 49: 1059-1073.

Rajkai K. and Ryden B.E. (1992) Measuring aerial soil moisture distribution with the TDR method. *Geoderma*, 52: 73-85.

Rao A.S. and Saxton K.E. (1995) Analysis of soil water stress for pearl millet in an Indian arid region using the SPAW model. *Journal of Arid Environments*, 29: 155-167.

Reece C.F. (1998) Simple method for determining cable length resistance in time domain reflectometry systems. *Soil Science Society of America Journal*, 62 (2): 314-317.

Rhoades J.D. and Vanschilfgaarde J. (1976) Electrical-Conductivity Probe for Determining Soil-Salinity. *Soil Science Society of America Journal*, 40 (5): 647-651.

Robinson D.A., Jones S.B., Wraith J.M., Or D. and Friedman S.P. (2003a) A Review of Advances in Dielectric and Electrical Conductivity Measurement in Soils Using Time Domain Reflectometry. *Vadose Zone Journal*, 2 (4): 444-475.

Robinson D.A., Schaap M., Jones S.B., Friedman S.P. and Gardner C.M.K. (2003b) Considerations for Improving the Accuracy of Permittivity Measurement using Time Domain Reflectometry: Air-water Calibration, Effects of Cable Length. *Soil Science Society of America Journal*, 67 (1): 62-70.

Robinson D.A., Schaap M.G., Or D. and Jones S.B. (2005) On the effective frequency of time domain reflectometry in dispersive and nonconductive dielectric materials. *Water Resources Research,* 41 (2): 239-261.

Rogers C.D.F. (2008) "Mapping the underworld to minimise street work" In Szot A. (ed.) *Underground Infrastructure of Urban Areas – Chapter 25*, London: Taylor & Francis Group. pp. 237-247.

Rogers C.D.F, Zembillas N., Metje N., Chapman D.N. and Thomas A.M. (2008) "Extending GPR Utility Location Performance – The Mapping The Underworld Project" In *12th International Conference on Ground Penetrating Radar. Birmingham, UK, 16-17 June.*

Rogers C.D.F, Chapman D.N., Entwisle D., Jones L., Kessler H., Metje N., Mica L., Morey M., Pospisil P., Price S., Raclavsky J., Raines M., Scott H. and Thomas A.M. (2009) "Predictive Mapping of Soil Geophysical Properties for GPR Utility Location Surveys" In *Proceedings of the 5th International Workshop on Advanced Ground Penetrating Radar. Granada, Spain, 27-29 May*.

Roth K., Schulin R., Fluhler H. and Attinger W. (1990) Calibration of Time Domain Reflectometry for Water Content Measurement Using a Composite Dielectric Approach. *Water Resources Research,* 26 (10): 2267-2273.

Royal A.C.D., Rogers C.D.F., Atkins P.R., Brennan M.J., Chapman D.N., Cohn A.G., Curioni G., Foo K.Y., Goddard K.F., Lewin P.L., Metje N., Muggleton J.M., Naji A., Pennock S.R., Redfern M.A., Saul A.J., Swingler S.G. and Wang P. (2010) "Mapping the Underworld: Location Phase II - Latest Developments" In *Proceedings of the International No-Dig 2010; 28th International Conference and Exhibition, Singapore, 8-10 November*.

Royal A.C.D., Rogers C.D.F., Atkins P.R., Chapman D.N., Curioni G., Foo K.Y., Hao T., Metje N., Moghareh Abed T., Shirgiri N. and Wazlan S. (2011) "Pipeline Engineering in the Ground: the Impact of Ground Conditions on Pipeline Condition and Maintenance Operations" In *Proceedings of the ASCE International Conference on Pipelines and Trenchless Technology, Beijing, China, 26-29 October.*

Saarenketo T. (1998) Electrical properties of water in clay and silty soils. *Journal of Applied Geophysics,* 40: 73-88.

Saxton K.E., Johnson H.P. and Shaw R.H. (1974) Modeling evapo-transpiration and soil moisture. *Transactions of American Society of Agricultural Engineers,* 17: 673-677.

Saxton K.E., Rawls W.J., Romberger J.S. and Papendick R.I. (1986) Estimating Generalized Soil-water Characteristics from Texture. *Soil Science Society American Journal*, 50: 1031-1036.

Saxton K.E. and Rawls W.J. (2006) Soil Water Characteristic Estimates by Texture and Organic Matter for Hydrologic Solutions. *Soil Science Society American Journal*, 70: 1569-1578.

# REFERENCES


Saxton K.E. and Willey P.H. (2006) "The SPAW model for agricultural field and pond hydrologic simulation" In Singh V.P. and Frevert D.K. (ed.) *Watershed models.* Boca Raton, Fl.: CRC Press. pp. 401–435.

Saxton K.E., Willey P.H. and Rawls W.J. (2006) "Field and pond hydrologic analyses with the SPAW model" In *ASABE Annual International Meeting, Paper No. 062108, Portland, Oregon, 9-12 July.*

Seger M., Cousin I., Besson A., Mafttei R., Andre' F., Lambot S., Thiesson J., Garfagnoli F., Moretti S., Steevens A., van Wesemael B., Samyn K., Richard G. and Grandjean G. (2010) *Report of calibration of the tested technologies integrated in the DIGISOIL mapping tool*. Report N°BRGM/FP7-DIGIOIL-D2.3; 88 pages.

Skierucha W., Wilczek A., Szyplowska A., Slawinski C. and Lamorski K. (2012) A TDR-Based Soil Moisture Monitoring System with Simultaneous Measurement of Soil Temperature and Electrical Conductivity. *Sensors*, 12: 13545-13566.

Slob E., Liu F., Pospisil P and Mica L. (2009) "Seasonal changes of soil geophysical properties, with applications to GPR utility location surveys" In *Proceedings of the 5th International Workshop on Advanced Ground Penetrating Radar, Granada, Spain, 27-29 May.*

Smith-Rose R.L. (1935) The electrical properties of soil at frequencies up to 100 megacycles per second; with a note on the resistivity of ground in the United Kingdom. *Proceedings of the Physical Society*, 47: 923-931.

Soil Survey Staff (1999) *Soil Taxonomy: A Basic System of Soil Classification for Making and Interpreting Soil Surveys*. 2nd ed. Washington, DC: USDA – Natural Resources Conservation Service.

Stangl R., Buchan G.D. and Loiskandl W. (2009) Field use and calibration of a TDR-based probe for monitoring water content in a high-clay landslide soil in Austria. *Geoderma*, 150: 23-31.

Take W.A., Arnepalli D.N., Brachman R.W.I. and Rowe R.K. (2007) "Laboratory and field calibration of TDR probes for water content measurement" In *Proceedings of OttawaGeo2007: The Diamond Jubilee: 60th Canadian Geotechnical Conference, Ottawa, Canada, 21-25 October.*

Thomas A.M., Chapman D.N., Rogers C.D.F., Metje N., Atkins P.R. and Lim H.M. (2008a) Broadband Apparent Permittivity Measurement in Dispersive Soils Using Quarter-Wavelength Analysis. *Soil Science Society of America Journal*, 72: 1401-1409.

Thomas A.M., Yelf R.J., Gunn D.A., Self S., Chapman D.N., Rogers C.D.F. and Metje N. (2008b) "The Role of Geotechnical Engineering for Informed Planning of GPR Surveys and Interpretation of Results in Fine-Grained Soils" In *12th International Conference on Ground Penetrating Radar. Birmingham, UK, 16-19 June, CD-ROM.*

Thomas A.M., Burrow M.P.N., Rogers C.D.F., Chapman D.N. and Metje N. (2008c) "Electromagnetic Characterisation of a Victorian Railway Embankment Fill Material" In 3rd *International Conference on Site Characterisation. Taipee, Taiwan, 1-4 April*

Thomas A.M., Chapman D.N., Rogers C.D.F. and Metje N. (2010a) Electromagnetic properties of the ground: Part I – Fine-grained soils at the Liquid Limit. *Tunnelling and Underground Space Technology*, 25: 714-722.

Thomas A.M., Chapman D.N., Rogers C.D.F. and Metje N. (2010b) Electromagnetic properties of the ground: Part II – The properties of two selected fine-grained soils. *Tunnelling and Underground Space Technology*, 25: 723-730.

Timlin D.J. and Pachepsky Y.A. (1996) Comparison of three methods to obtain the apparent dielectric constant from time domain reflectometry wave traces. *Soil Science Society of America Journal*, 60 (4): 970-977.

Todeschini R. (1998) *Introduzione alla chemiometria*. Napoli, IT: EdiSES s.r.l.

Topp G.C., Davis J.L. and Annan A.P. (1980) Electromagnetic Determination of Soil-Water Content: Measurements in Coaxial Transmission Lines. *Water Resources Research*, 16 (3): 574-582.

Topp G.C., Davis J.L. and Annan A.P. (1982a) Electromagnetic determination of soil-water content using TDR .1. Applications to wetting fronts and steep gradients. *Soil Science Society of America Journal*, 46 (4): 672-678.

Topp G.C., Davis J.L. and Annan A.P. (1982b) Electromagnetic determination of soil-water content using TDR .2. Evaluation of installation and configuration of parallel transmission-lines. *Soil Science Society of America Journal*, 46 (4): 678-684.

Topp G.C. and Davis J.L. (1985) Measurement of soil-water content using time-domain reflectometry (TDR) – a field evaluation. *Soil Science Society of America Journal*, 49 (1): 19-24.

Topp G.C., Yanuka M., Zebchuk W.D. and Zegelin S. (1988) Determination of Electrical Conductivity Using Time Domain Reflectometry: Soil and Water Experiments in Coaxial Lines. *Water Resources Research*, 24 (7): 945-952.

Topp G.C., Zegelin S. and White I. (2000) Impacts of the Real and Imaginary Components of Relative Permittivity on Time Domain Reflectometry Measurements in Soils. *Soil Science Society of America Journal*, 64: 1244-1252.

Topp G.C. (2003) State of the art of measuring soil water content. *Hydrological Processes*, 17: 2993-2996.

Topp G.C., Davis J.L. and Annan A.P. (2003) The Early Development of TDR for Soil Measurements. *Vadose Zone Journal*, 2: 492-499.

van Dam R.L., Borchers B. and Hendrickx J.M.H. (2005) Methods for prediction of soil dielectric properties: a review. *Proceedings of the Society of Photo-Optical Instrumentation Engineers*, 5794: 188-197.

van Genuchten M.TH. (1980) A Closed-form Equation for Predicting the Hydraulic Conductivity of Unsaturated Soils. *Soil Science Society of America Journal*, 44: 892-898.

Venables W.N., Smith D.M. and the R Development Core Team (2012) *An Introduction to R – Notes on R: A Programming Environment for Data Analysis and Graphics* – Version 2.15.1.

Verstricht J., Neerdael B., Meynendonckx P. and Volckaert G. (1994) "Clay moisture measurements in radioactive waste disposal research" In *Proceedings of Symposium on Time Domain Reflectometry in Environmental Infrastructure, and Mining Applications. Evanston, IL, 7-9 September, 337-348.*

Von Hippel A.R. (1954) *Dielectrics materials and applications*. Cambridge, MA: MIT Press.

Weast R.C. (1972) *Handbook of Chemistry and Physics*. 53rd ed. Cleveland, OH: Chemical Rubber Company.

Weast R.C. (1986) *Handbook of Chemistry and Physics*. 67th ed. Boca Raton, Fla.: Chemical Rubber Company.

Weiler K.W., Steenhuis T.S., Boll J. and Kung K.J.S. (1998) Comparison of ground penetrating radar and time-domain reflectometry as soil water sensors. *Soil Science Society of America Journal*, 62 (5): 1237-1239.

Wraith J.M. and Or D. (1999) Temperature effects on soil bulk dielectric permittivity measured by time domain reflectometry: Experimental evidence and hypothesis development. *Water Resources Research*, 35 (2): 361-369.

Wyseure G.C.L., Mojid M.A. and Malik M.A. (1997) Measurement of volumetric water content by TDR in saline soils. *European Journal of Soil Science*, 48: 347-354.

Yanuka M., Topp G.C., Zegelin S. And Zebchuk W.D. (1988) Multiple Reflection and Attenuation of Time Domain Reflectometry Pulses: Theoretical Considerations for Applications to Soil and Water. *Water Resources Research*, 24 (7): 939-944.

Zegelin S.J., White I. and Jenkins D.R. (1989) Improved Field Probes for Soil Water Content and Electrical Conductivity Measurement Using Time Domain Reflectometry. *Water Resources Research*, 25 (11): 2367-2376.

Zhou Q.Y., Shimada J. and Sato A. (2002) Temporal variations of the three-dimensional rainfall infiltration process in heterogeneous soil. *Water Resources Research*, 38 (4): 1030.

# APPENDICES

## APPENDIX A: genetic soil horizons

Over time, soils tend to form layers approximately parallel to the surface and with homogeneous characteristics. In the soil science terminology, these layers are called *horizons*, and are formed from a variety of pedogenetic processes predominantly driven by physical and chemical weathering. Seven major genetic horizons have been identified and are distinguished by capital letters (FAO/ISRIC/ISSS, 1998):

- **O**: uppermost horizons predominantly characterised by partially decomposed organic materials (e.g., litter, needles, moss, lichens). They are not saturated with water for prolonged periods of time.
- **H**: as the O horizons but they are saturated for prolonged periods of time.
- **A**: mineral horizons formed near the surface in which all or much of the original rock structure has been obliterated. They generally contain large amounts of humified organic matter mixed with the mineral fraction. They normally show a dark colour (e.g., brown, black).
- **E**: mineral horizons formed near the surface in which clay and components of iron and aluminium have leached, leaving a high concentration of sand and silt particles. They normally show a light colour (e.g., grey, white).
- **B**: mineral horizons formed deeper than O, H, A or E horizons in which all or much of the original rock structure has been obliterated. They are the result of pedogenetic processes such as the accumulation of clays and oxides, and the loss of carbonates. They generally show signs of weathering and the development of soil structure.

- **C**: mineral horizons that do not show the typical properties of the above horizons. They are only little affected by pedogenetic processes and are normally found just above the bedrock. They lack of soil structure.
- **R**: hard bedrock underlying the soil.

# APPENDIX B: time plots

**B1 – MetOffice historical weather data from year 2000 to 2012 (Shawbury weather station (MetOffice, 2012).**

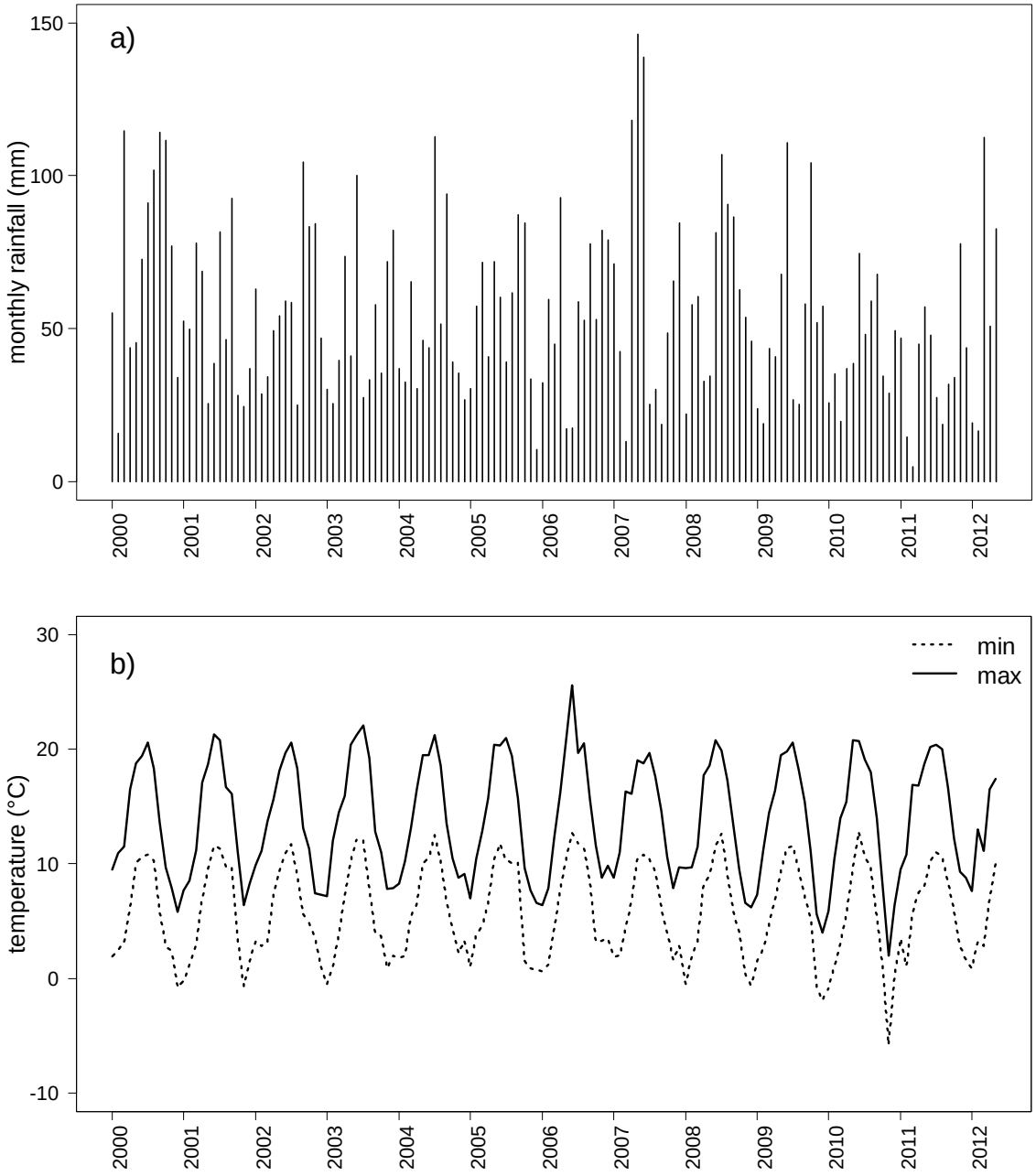



Figure B.1 – Historic rainfall data (a) and temperature maxima and minima (b) measured by the MetOffice weather station at Shawbury (UK).

**B2 – Example of unfiltered and filtered TDR data, by means of a median filter.**

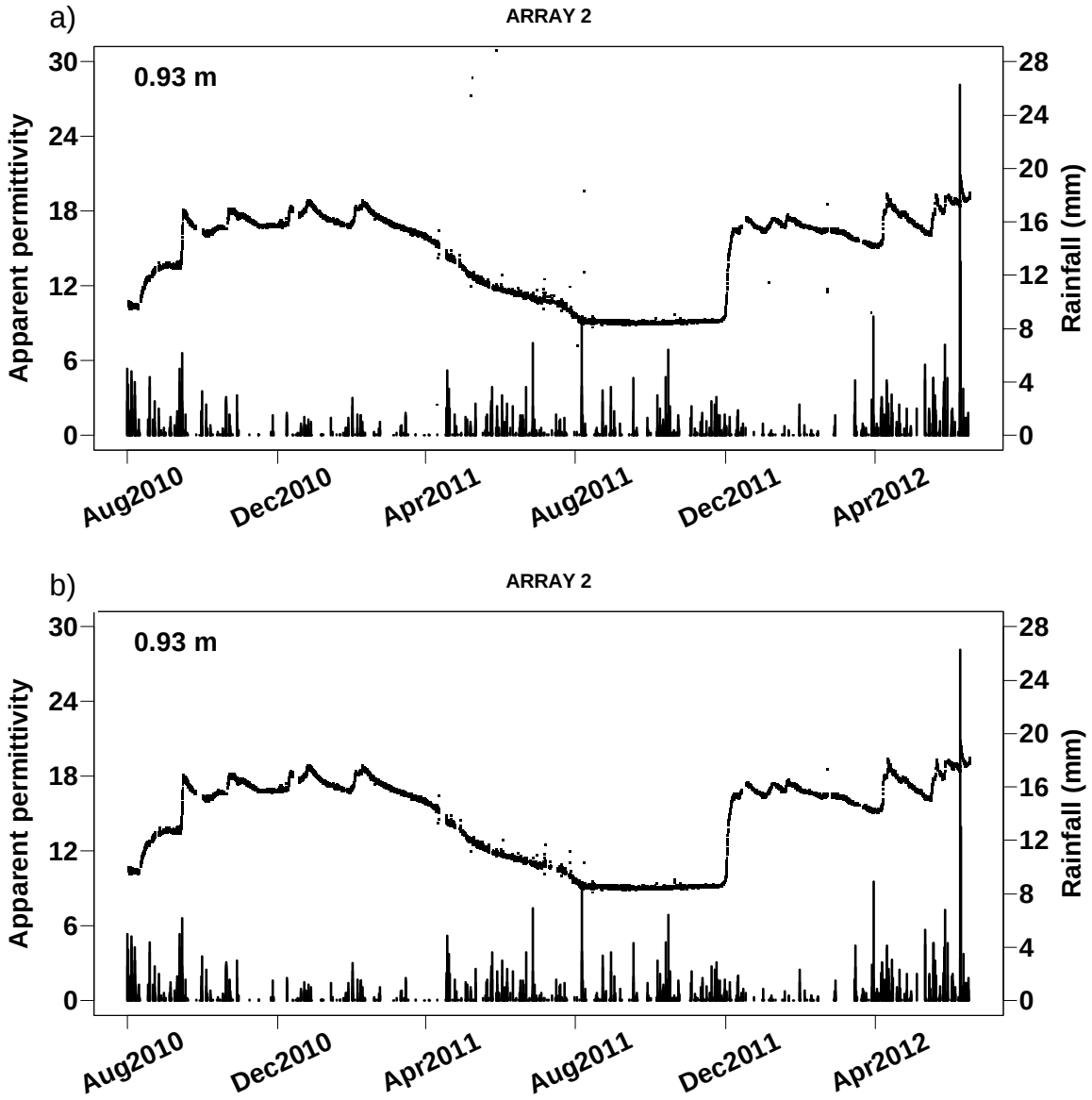



Figure B.2 – (a) Unfiltered and (b) filtered apparent permittivity data corresponding to a selected TDR probe.

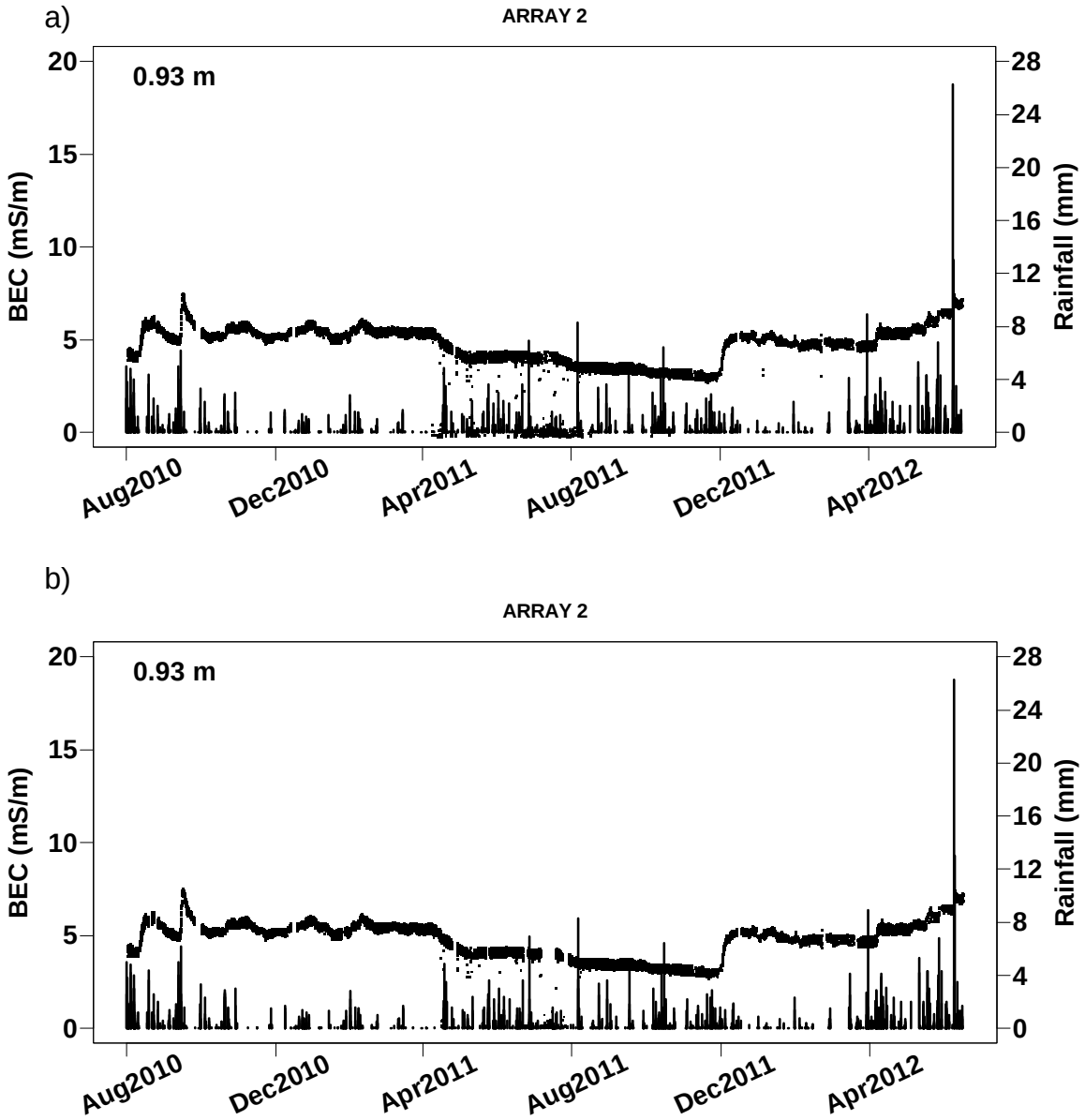



Figure B.3 – (a) Unfiltered and (b) filtered BEC data corresponding to a selected TDR probe.

# APPENDIX C: correlations between variables

**C1 – Time-domain cross correlation between the BEC measured by TDR probes in array 1 and a rainfall event occurring in February 2011.**

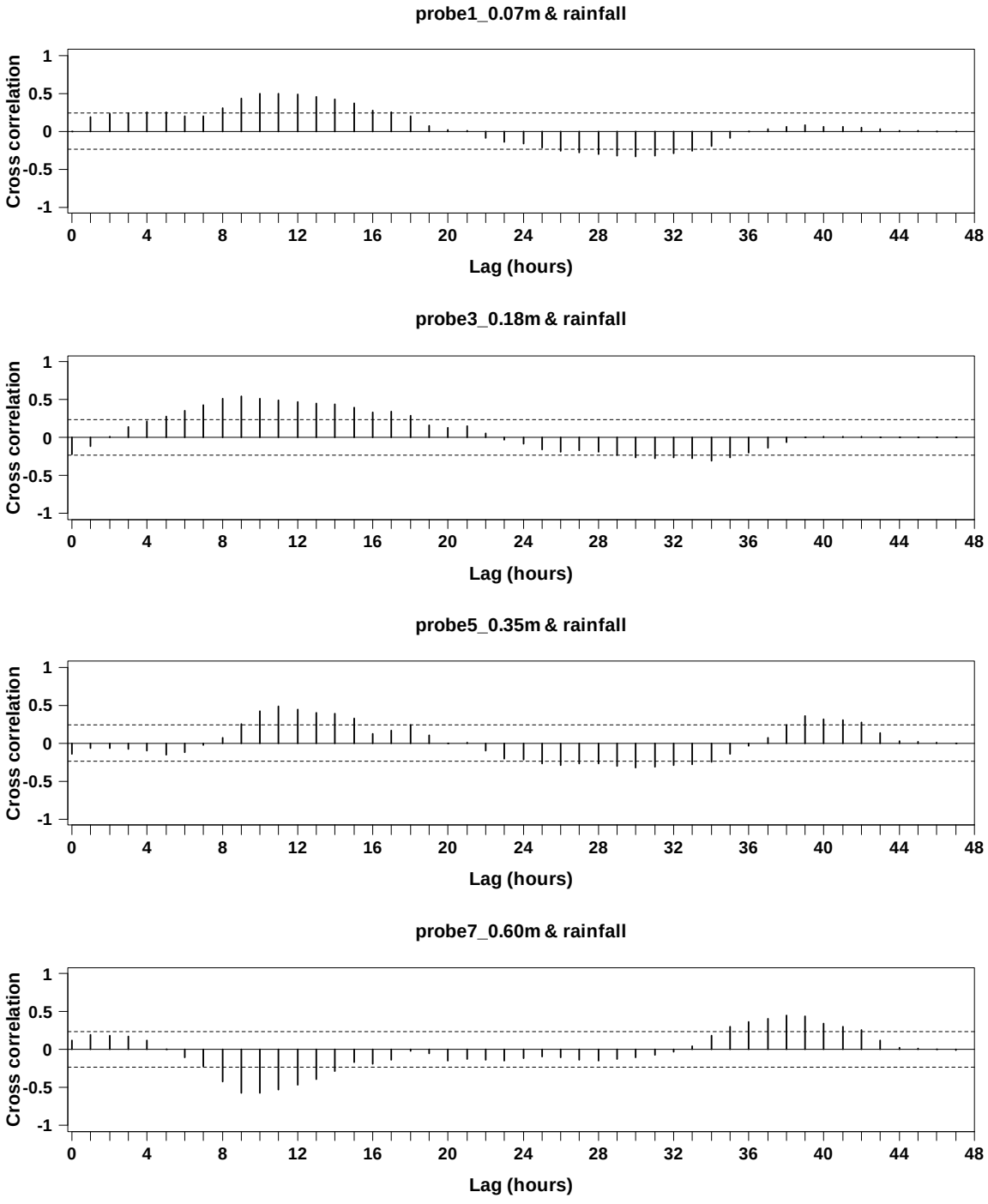



Figure C.1 – Time-domain cross correlation between the BEC measured by TDR probes in array 1, up to 0.60 m depth, and a rainfall event occurring in February 2011

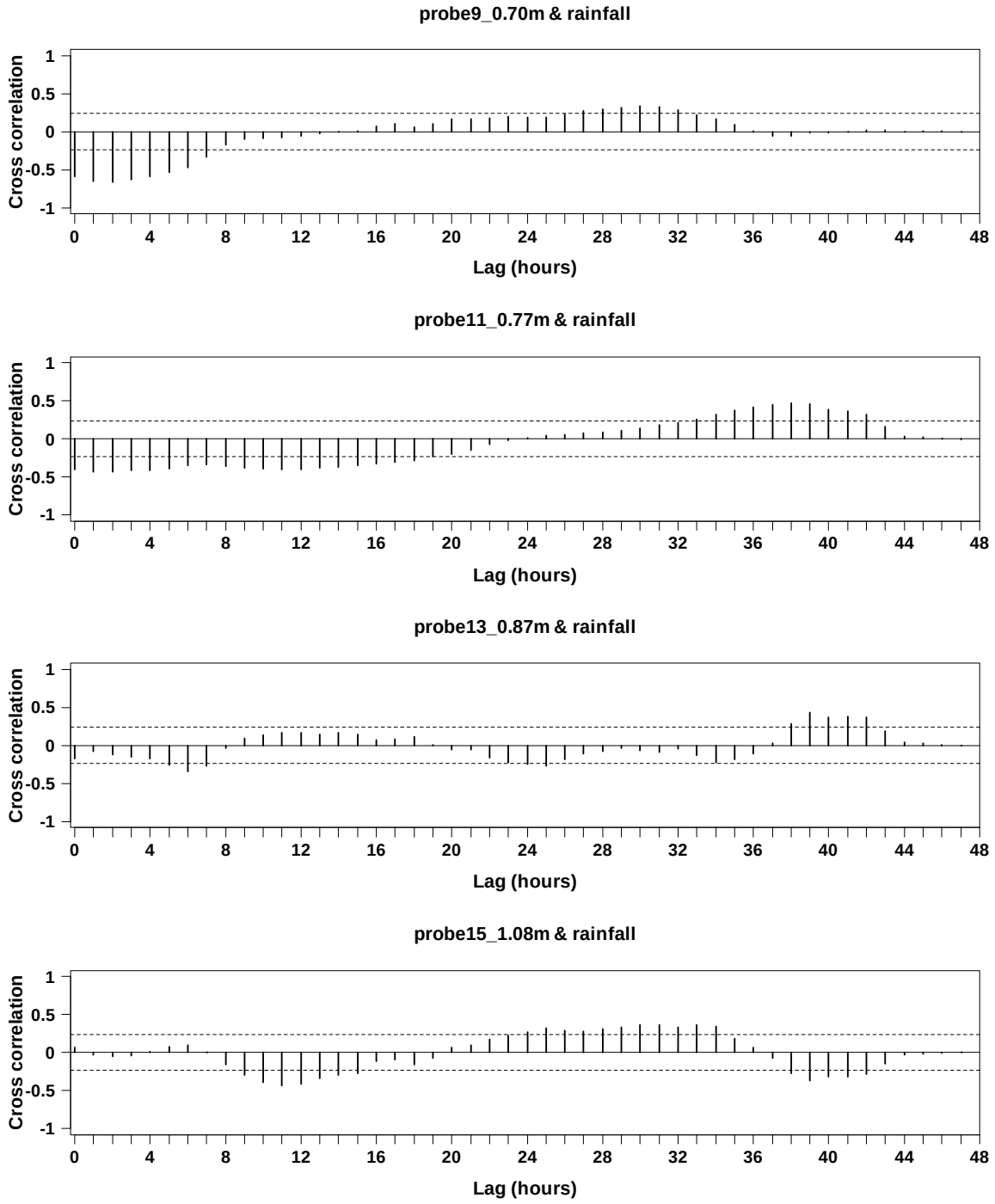



Figure C.2 – Time-domain cross correlation between the BEC measured by TDR probes in array 1, from 0.70 and 1.08 m depth, and a rainfall event occurring in February 2011

**C2 – Time-domain cross correlation between the apparent permittivity measured by TDR probes in array 1 and the air temperature of the 21st April 2011.**

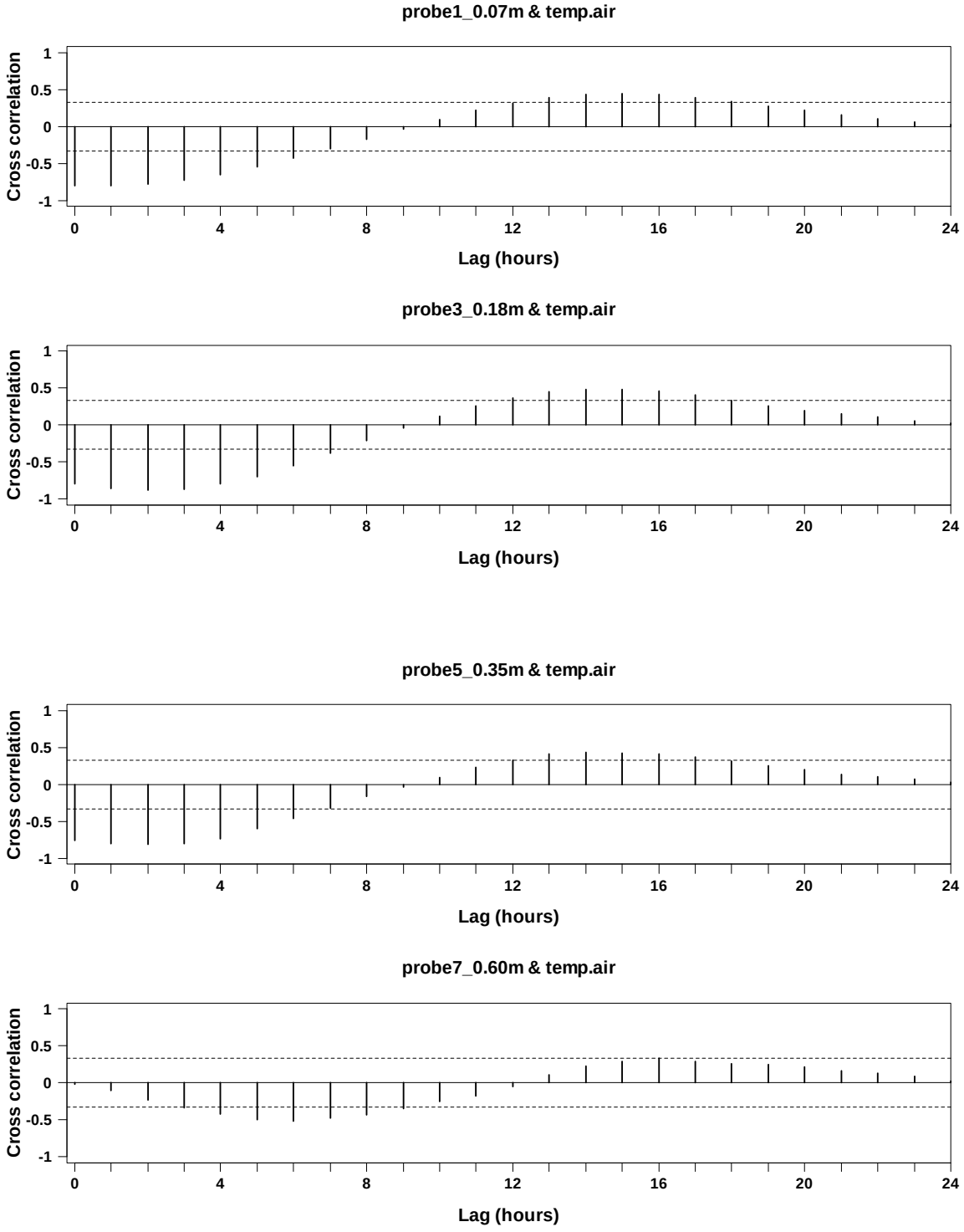



Figure C.3 – Time-domain cross correlation between the apparent permittivity measured by TDR probes in array 1, up to 0.60 m depth, and the air temperature of the 21st April 2011.

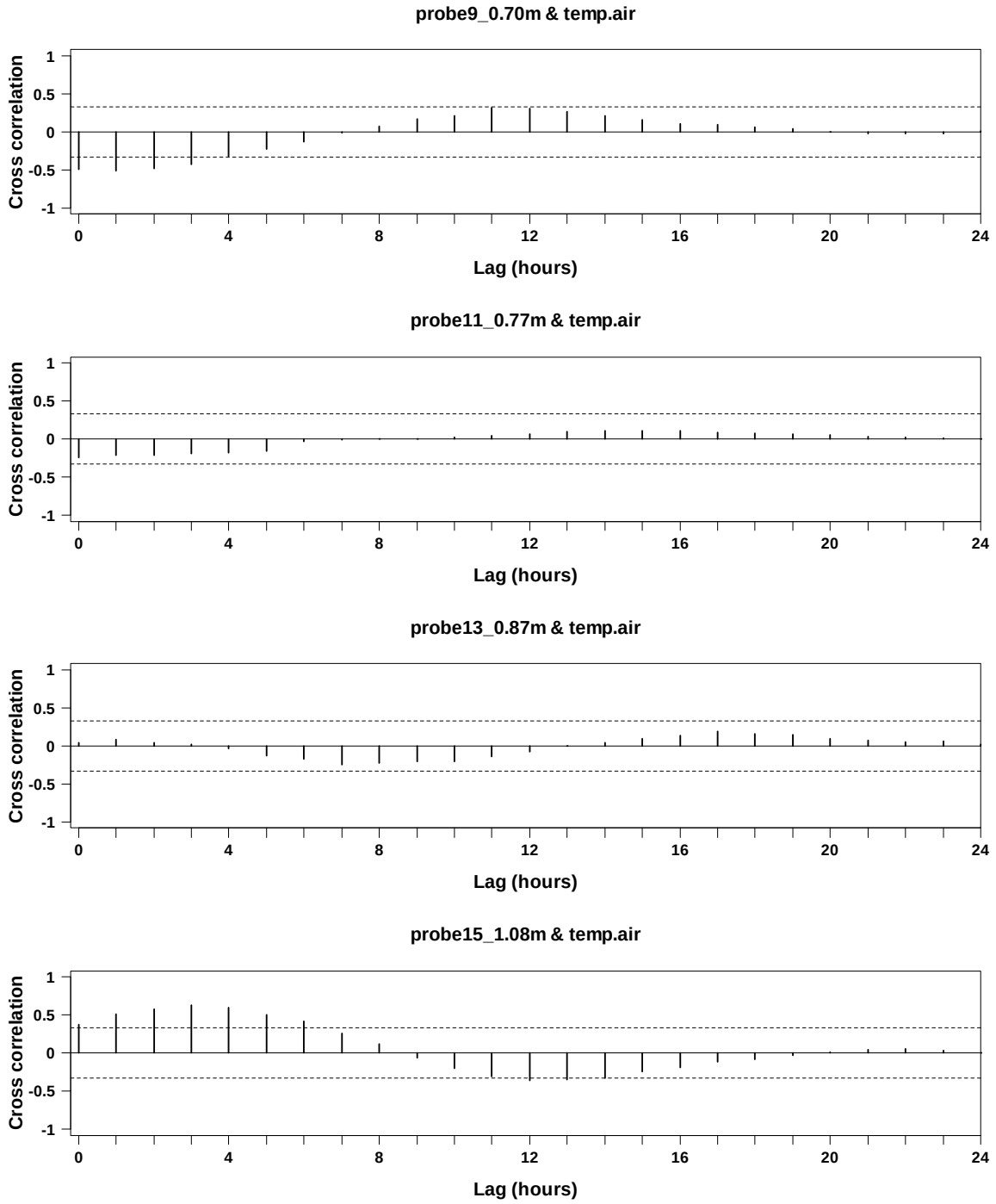



Figure C.4 – Time-domain cross correlation between the apparent permittivity measured by TDR probes in array 1, from 0.70 m and 1.08 m depth, and the air temperature of the 21st April 2011.

**C3 – Scatterplot matrix of the apparent permittivity, BEC (mS/m) and temperature (° C), for the year 2011.**

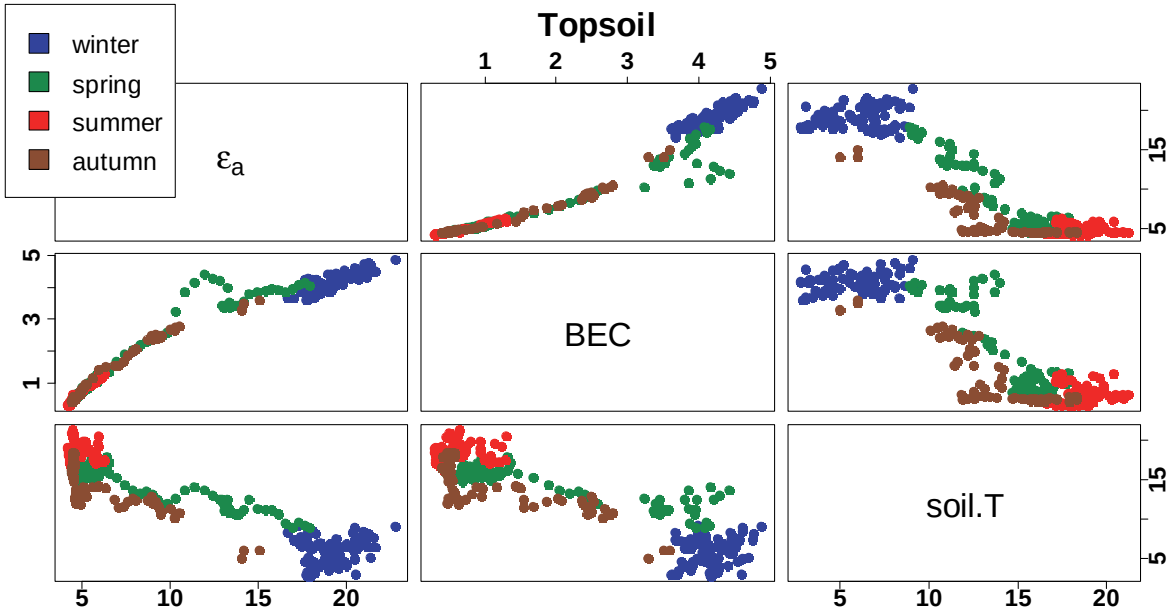



Figure C.5 – Scatterplot matrix of the topsoil apparent permittivity, BEC (mS/m) and temperature, soil.T (° C), for the year 2011.

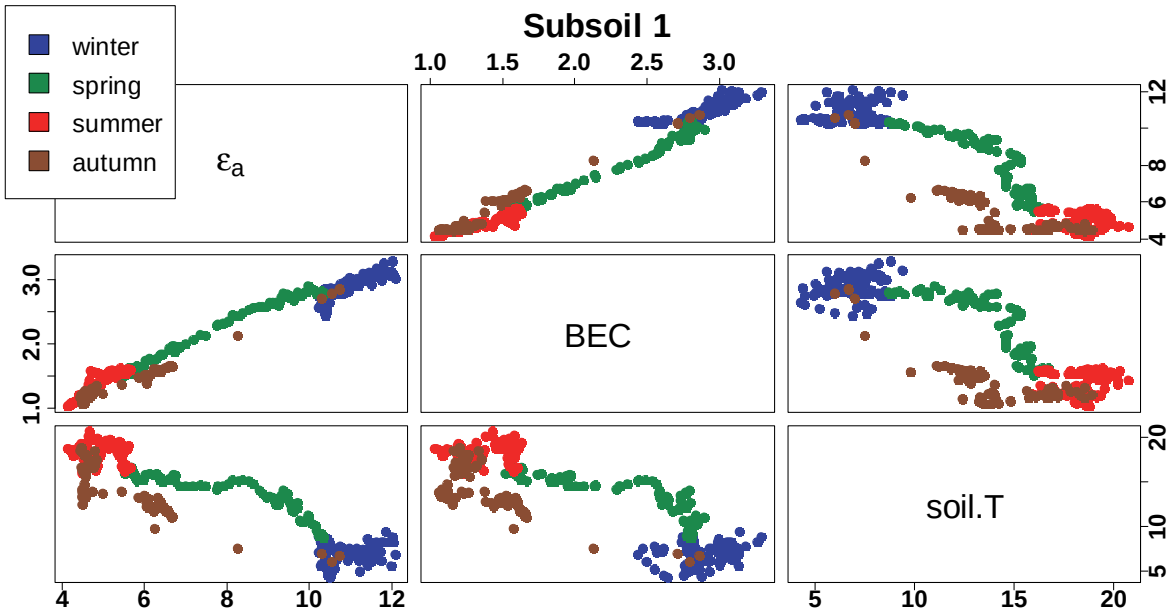



Figure C.6 – Scatterplot matrix of the subsoil 1 apparent permittivity, BEC (mS/m) and temperature, soil.T (° C), for the year 2011.

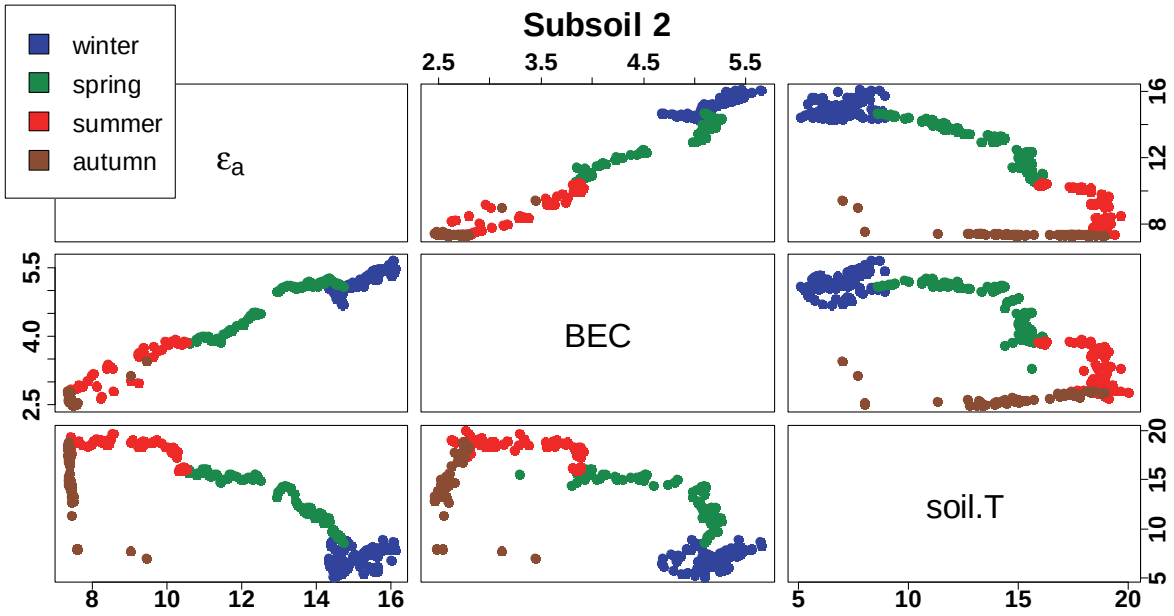



Figure C.7 – Scatterplot matrix of the subsoil 2 apparent permittivity, BEC (mS/m) and temperature, soil.T (° C), for the year 2011.

# APPENDIX D: empirical calibrations (apparent permittivity *versus* volumetric water content)

## D1 – Empirical calibration (all temperatures): model summary.

```
Call:
lm(formula = vwc ~ poly(Ea, 3, raw = T))

Residuals:
   Min     1Q  Median     3Q    Max
-2.2528 -1.1897  0.0473  1.1500  2.5983

Coefficients:
                    Estimate Std. Error t value Pr(>|t|)
(Intercept)         -13.693736   1.706443  -8.025 3.67e-09 ***
poly(Ea, 3, raw = T)1   6.912462   0.589617  11.724 4.04e-13 ***
poly(Ea, 3, raw = T)2  -0.433111   0.054468  -7.952 4.47e-09 ***
poly(Ea, 3, raw = T)3   0.009399   0.001450   6.484 2.70e-07 ***
---
Signif. codes:  0 ‘***’ 0.001 ‘**’ 0.01 ‘*’ 0.05 ‘.’ 0.1 ‘ ’ 1

Residual standard error: 1.553 on 32 degrees of freedom
Multiple R-squared: 0.9757,     Adjusted R-squared: 0.9734
F-statistic: 427.4 on 3 and 32 DF,  p-value: < 2.2e-16
```

## D2 – Empirical calibrations at specific temperatures: plot and summaries.

### 5 °C

```
Call:
lm(formula = vwc ~ poly(Ea, 3, raw = T))

Residuals:
      1       2       3       4       5       6       7       8       9
-2.19409  0.72054  2.00532  0.75345 -1.32869  0.04706 -0.71014  1.97533 -1.26879

Coefficients:
                    Estimate Std. Error t value Pr(>|t|)
(Intercept)         -13.922427   4.086506  -3.407  0.01911 *
poly(Ea, 3, raw = T)1   7.027724   1.406807   4.996  0.00412 **
poly(Ea, 3, raw = T)2  -0.444516   0.128801  -3.451  0.01821 *
poly(Ea, 3, raw = T)3   0.009616   0.003369   2.854  0.03564 *
---
Signif. codes:  0 ‘***’ 0.001 ‘**’ 0.01 ‘*’ 0.05 ‘.’ 0.1 ‘ ’ 1

Residual standard error: 1.882 on 5 degrees of freedom
Multiple R-squared: 0.9777,     Adjusted R-squared: 0.9643
F-statistic: 72.95 on 3 and 5 DF,  p-value: 0.0001507
```

## 10 °C

```
Call:
lm(formula = vwc ~ poly(Ea, 3, raw = T))

Residuals:
     1      2      3      4      5      6      7      8      9
-2.2846  0.6510  1.9320  1.1588 -1.3388 -0.1374 -0.8661  2.1852 -1.3000

Coefficients:
                    Estimate Std. Error t value Pr(>|t|)
(Intercept)         -13.913904   4.358332  -3.192   0.0242 *
poly(Ea, 3, raw = T)1   7.066313   1.507444   4.688   0.0054 **
poly(Ea, 3, raw = T)2  -0.447983   0.138287  -3.240   0.0230 *
poly(Ea, 3, raw = T)3   0.009726   0.003635   2.676   0.0440 *
---
Signif. codes:  0 ‘***’ 0.001 ‘**’ 0.01 ‘*’ 0.05 ‘.’ 0.1 ‘ ’ 1

Residual standard error: 1.987 on 5 degrees of freedom
Multiple R-squared: 0.9751,     Adjusted R-squared: 0.9601
F-statistic: 65.24 on 3 and 5 DF,  p-value: 0.0001977
```

## 15 °C

```
Call:
lm(formula = vwc ~ poly(Ea, 3, raw = T))

Residuals:
     1      2      3      4      5      6      7      8      9
-1.9547  0.9415  1.4511  0.9296 -1.5390  0.1408 -0.6913  1.9765 -1.2546

Coefficients:
                    Estimate Std. Error t value Pr(>|t|)
(Intercept)         -14.65594    4.10640  -3.569  0.01606 *
poly(Ea, 3, raw = T)1   7.27709    1.44236   5.045  0.00395 **
poly(Ea, 3, raw = T)2  -0.47234    0.13599  -3.473  0.01778 *
poly(Ea, 3, raw = T)3   0.01057    0.00368   2.873  0.03489 *
---
Signif. codes:  0 ‘***’ 0.001 ‘**’ 0.01 ‘*’ 0.05 ‘.’ 0.1 ‘ ’ 1

Residual standard error: 1.79 on 5 degrees of freedom
Multiple R-squared: 0.9798,     Adjusted R-squared: 0.9677
F-statistic: 80.78 on 3 and 5 DF,  p-value: 0.0001175
```

## 20 °C

Call:
lm(formula = vwc ~ poly(Ea, 3, raw = T))

Residuals:
```
      1       2       3       4       5       6       7       8       9
-1.57745  0.95066  1.20255  0.62654 -1.79466  0.46242 -0.04549  1.18978 -1.01434
```

Coefficients:
```
                    Estimate Std. Error t value Pr(>|t|)
(Intercept)          -16.969301   3.761800  -4.511  0.00634 **
poly(Ea, 3, raw = T)1   8.272300   1.380110   5.994  0.00185 **
poly(Ea, 3, raw = T)2  -0.587945   0.137461  -4.277  0.00788 **
poly(Ea, 3, raw = T)3   0.014326   0.003934   3.641  0.01488 *
---
Signif. codes:  0 ‘***’ 0.001 ‘**’ 0.01 ‘*’ 0.05 ‘.’ 0.1 ‘ ’ 1
```

Residual standard error: 1.491 on 5 degrees of freedom
Multiple R-squared: 0.986,	Adjusted R-squared: 0.9776
F-statistic: 117.2 on 3 and 5 DF,  p-value: 4.716e-05

# APPENDIX E: SPAW model

**E1 – Soil Water Characteristic Curves calculated by the SPAW model for the topsoil, subsoil 1 and subsoil 2, respectively.**

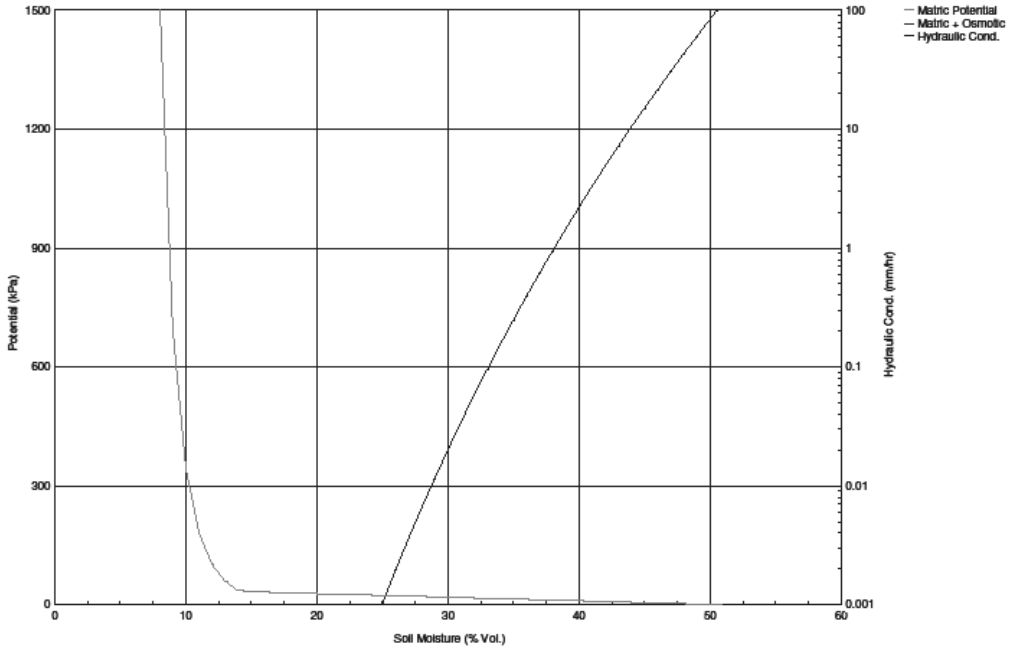



Figure E.1 – Soil Water Characteristic Curves calculated by the SPAW model for the topsoil.

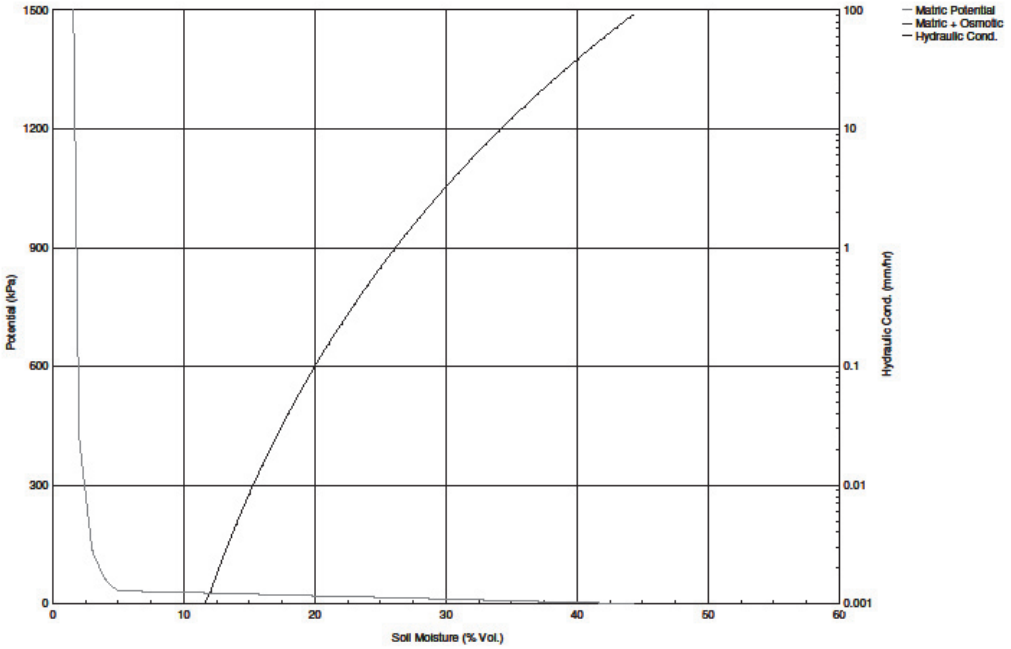



Figure E.2 – Soil Water Characteristic Curves calculated by the SPAW model for the subsoil 1.

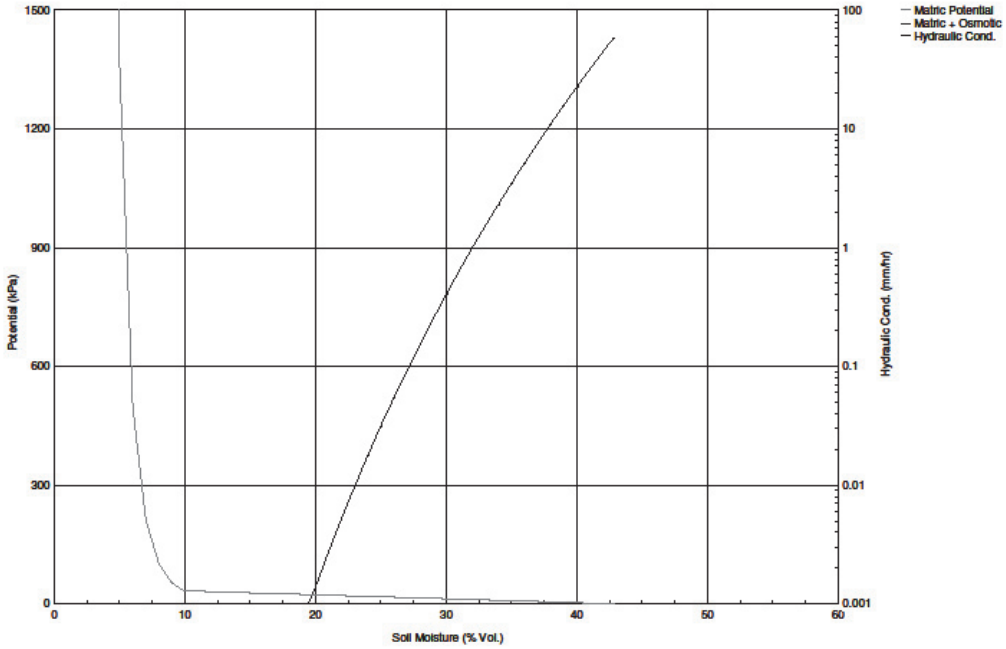



Figure E.3 – Soil Water Characteristic Curves calculated by the SPAW model for the subsoil 2.

**E2 – Simulated (by SPAW) and calculated (by the Topp model) daily volumetric water contents for selected months.**

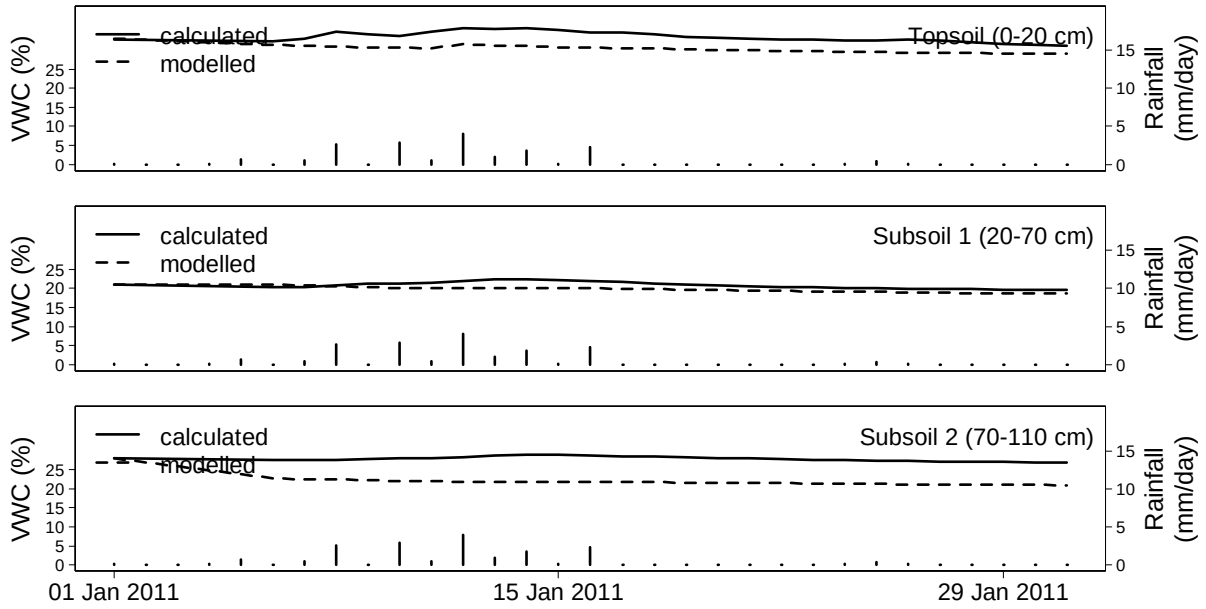



Figure E.4 – Simulated (by SPAW) and calculated (by the Topp model) daily volumetric water contents for January 2011.

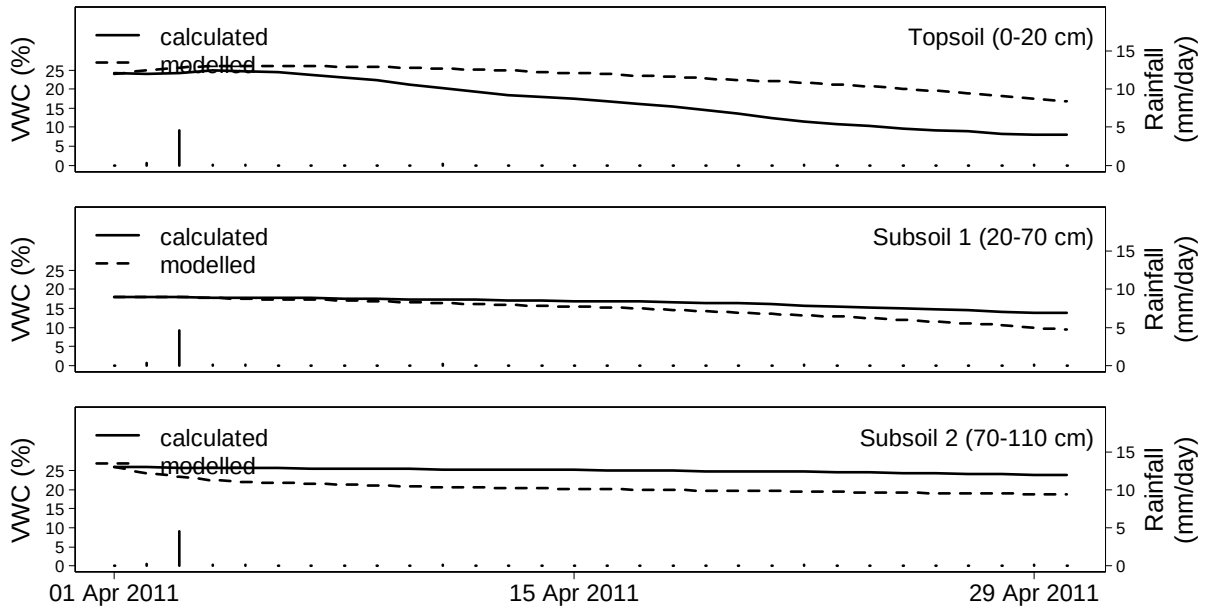



Figure E.5 – Simulated (by SPAW) and calculated (by the Topp model) daily volumetric water contents for April 2011.

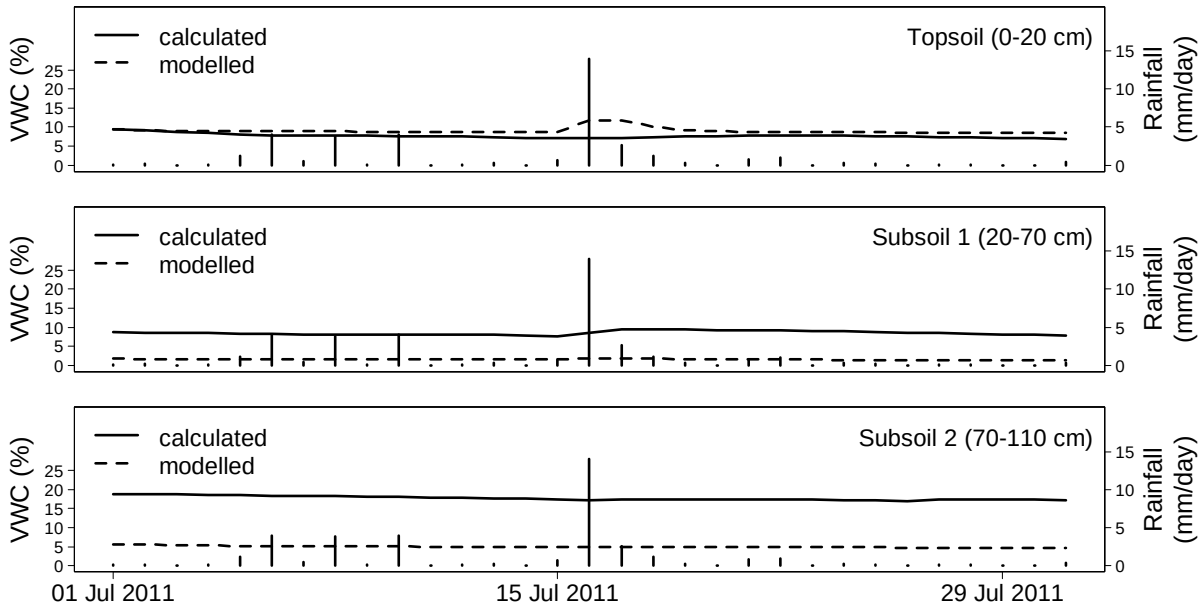



Figure E.6 – Simulated (by SPAW) and calculated (by the Topp model) daily volumetric water contents for July 2011.

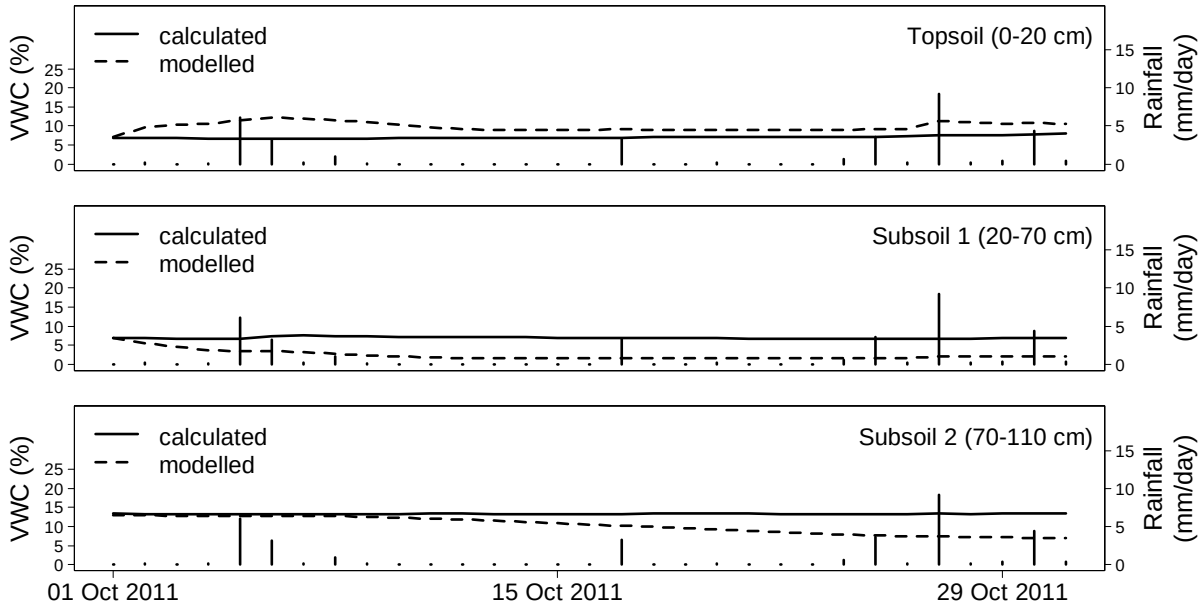



Figure E.7 – Simulated (by SPAW) and calculated (by the Topp model) daily volumetric water contents for October 2011.

**E3 – Simulated (by SPAW) and calculated (by Equation (4.1)) daily volumetric water contents for the 2011 seasons.**

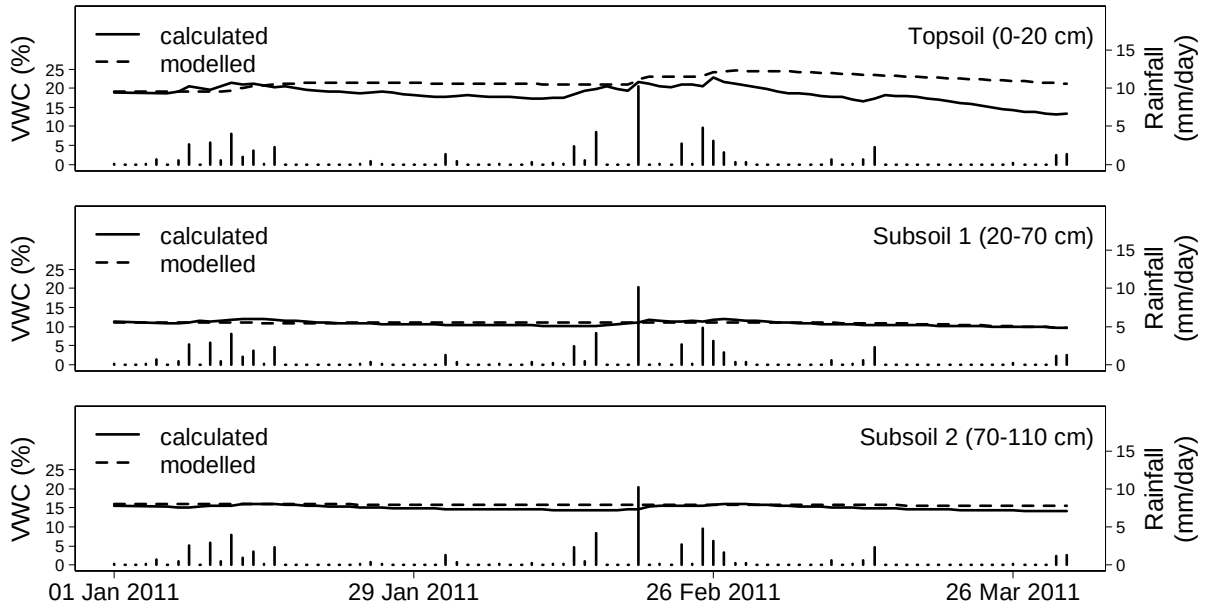



Figure E.8 – Simulated (by SPAW) and calculated (by Equation (4.1)) daily volumetric water contents for Winter 2011.

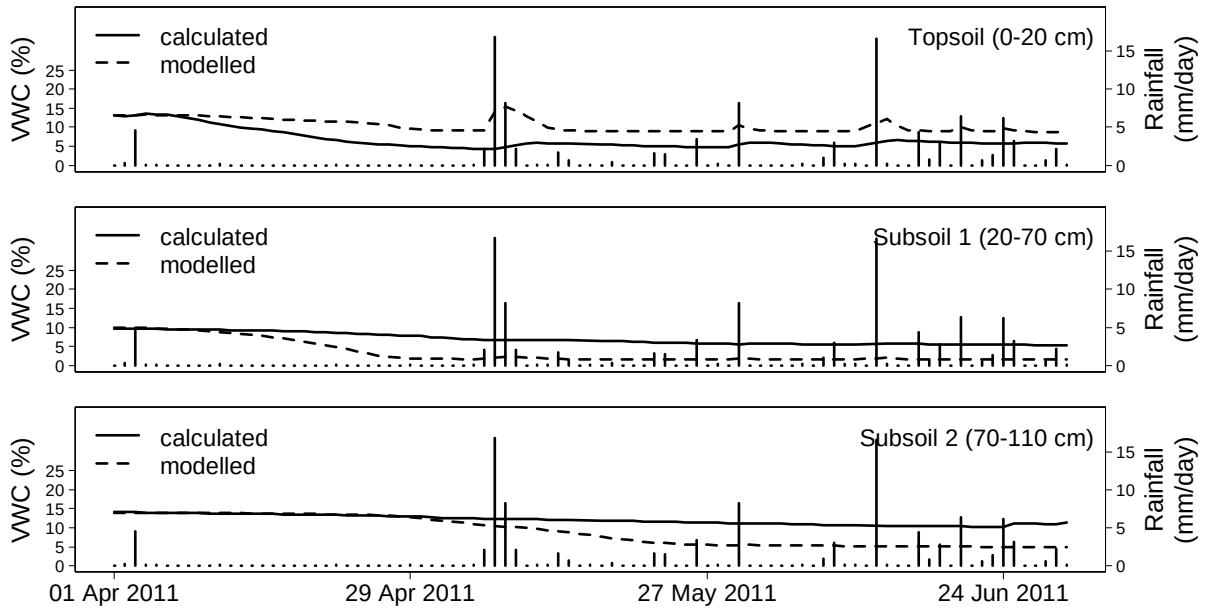



Figure E.9 – Simulated (by SPAW) and calculated (by Equation (4.1)) daily volumetric water contents for Spring 2011.

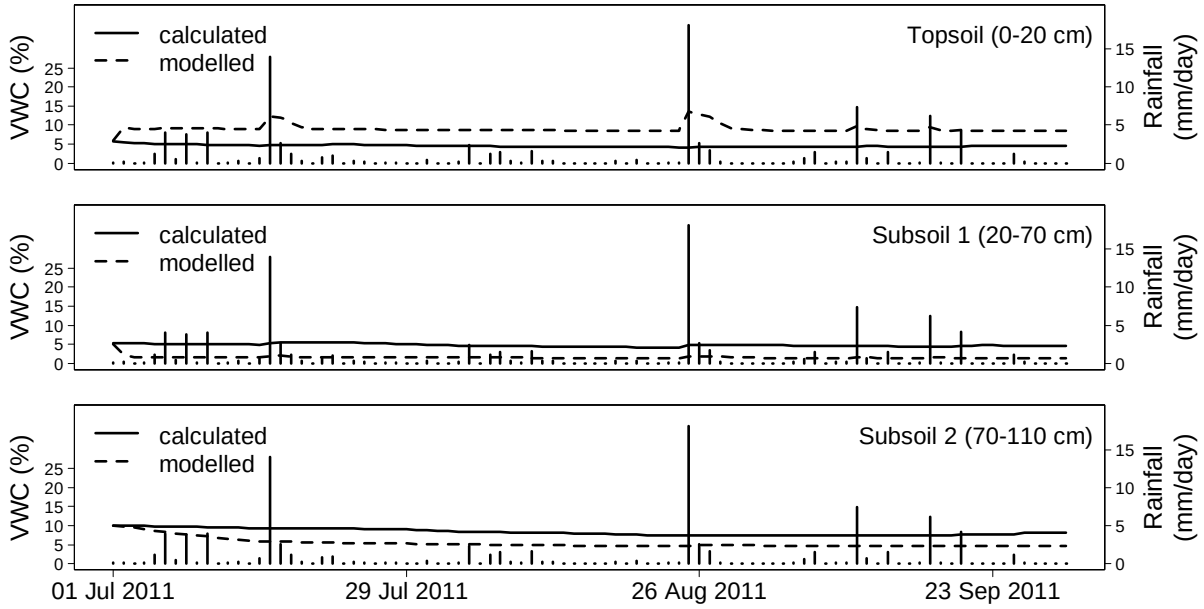



Figure E.10 – Simulated (by SPAW) and calculated (by Equation (4.1)) daily volumetric water contents for Summer 2011.

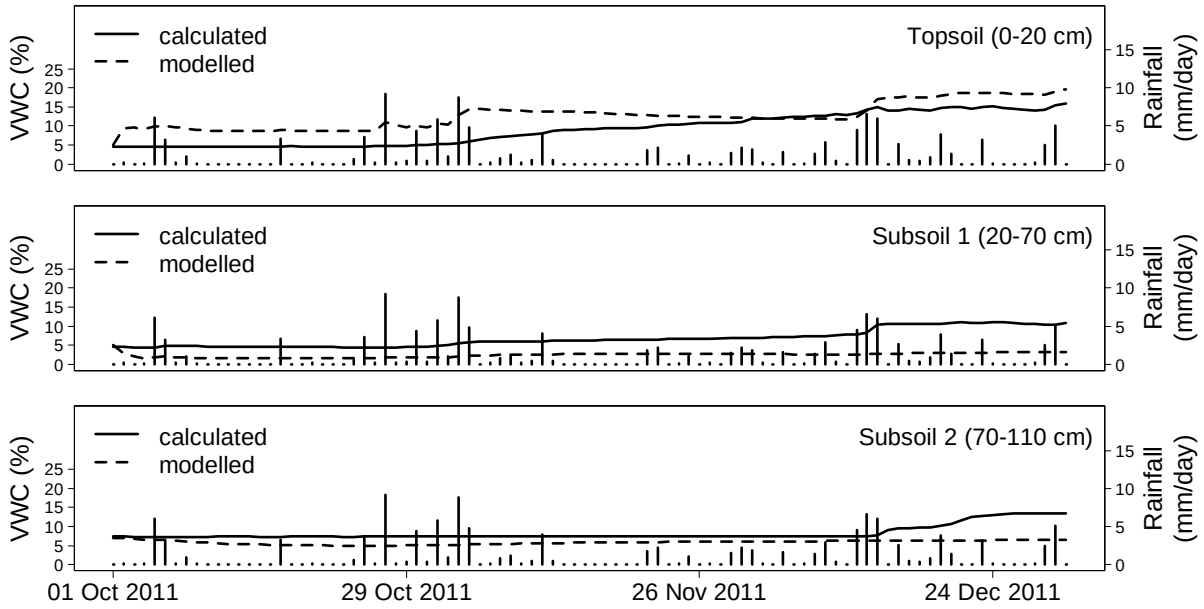



Figure E.11 – Simulated (by SPAW) and calculated (by Equation (4.1)) daily volumetric water contents for Autumn 2011.

# APPENDIX F: additional GPR results

**GPR B-scans obtained before and after a rainfall event occurring in June 2011.**

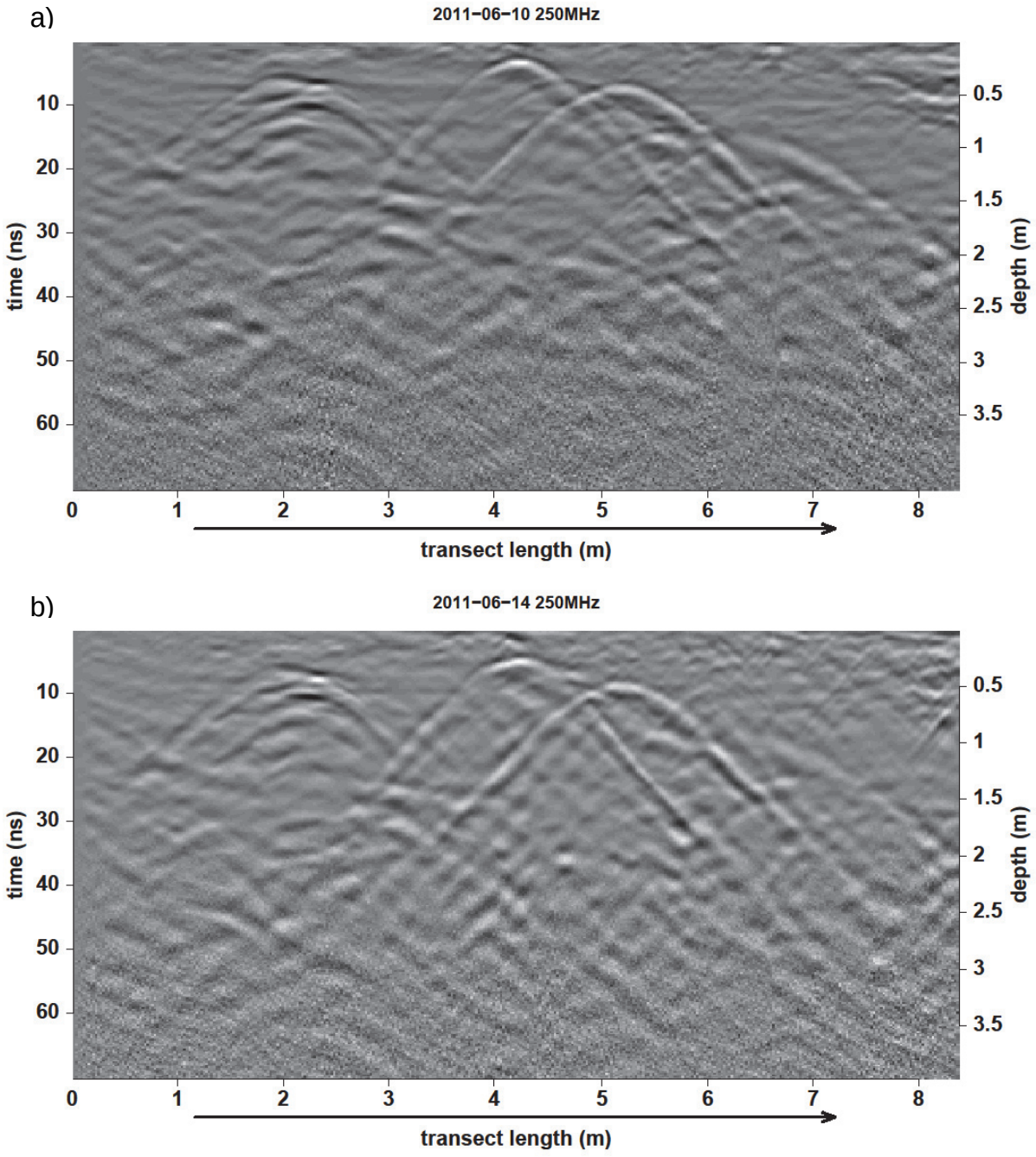



Figure F.1 – GPR B-scans obtained with a 250 MHz antenna (a) before and (b) after a rainfall event occurring in June 2011.

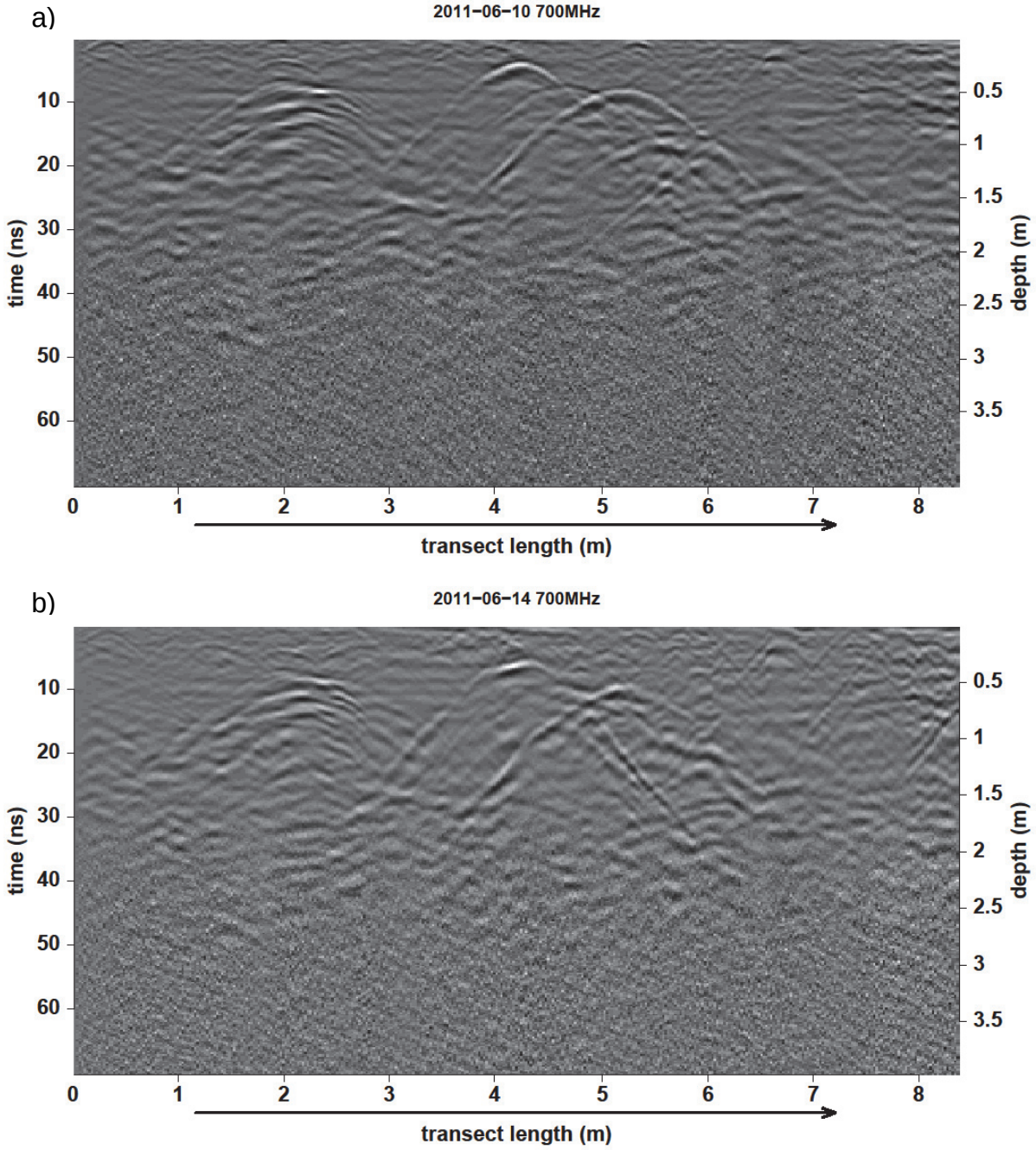



Figure F.2 – GPR B-scans obtained with a 700 MHz antenna (a) before and (b) after a rainfall event occurring in June 2011.